Universidade de São Paulo
Instituto de Astronomia, Geofísica e Ciências Atmosféricas
Departamento de Astronomia

Stefano Oliveira de Souza

A chrono-chemo-dynamical analysis of Globular Clusters: Looking for the fossils of the Galactic bulge/bar formation

Análise crono-químiodinâmica de aglomerados globulares:
Procurando por fósseis da formação da barra/bojo Galático

São Paulo
2024

Stefano Oliveira de Souza

A chrono-chemo-dynamical analysis of Globular Clusters: Looking for the fossils of the Galactic bulge/bar formation

Análise crono-químiodinâmica de aglomerados globulares:
Procurando por fósseis da formação da barra/bojo Galático

Thesis presented to Departamento de Astronomia of Instituto de Astronomia, Geofísica e Ciências Astmoeféricas, Universidade de Sao Paulo, as a partial requirement to get the title of PhD in Science..

Area: Astronomy
Advisor: Prof. Dr. Beatriz Barbuy
CoAdvisor: Dr. Angeles Pérez-Villegas

Versão Corrigida. O original encontra-se disponível na Unidade.

São Paulo
2024

À minha mãe!

Acknowledgements

Começo dedicando esta tese à minha mãe, Severina Florência de Oliveira, por ser a pessoa forte e determinada que ensinou a mim e aos meus irmãos (Christian e Fernanda) que a educação e dedicação ao trabalho são as únicas formas de ser uma pessoa digna. Esses são os pilares que sustentam esta tese.

Just like I am looking in this thesis for the fundamental bricks of the Galactic bulge, I can list here the keystones of this thesis. First, as cannot be different, my supervisor, Dr Beatriz Barbuy, since 19th September 2016, has believed in my potential as a researcher, always increasing my knowledge and opening the doors that made me reach where I am today. No one language in the world has an expression good enough to make you feel how much I am grateful for your orientation. Second, but not less important, Dr Angeles Pérez-Villegas, who co-supervisored this thesis. Sometimes, during the stress inherent in a doctorate, one needs someone they can trust with their frustrations, insecurities, fears, and anger or just someone to hear the most outlandish scientific ideas that cannot be said aloud and always result in a great idea. Thank you for being this person, always making me pursue my best, and most of all, for your friendship.

I cannot forget the fundamental bricks of this thesis. These people, in some way, have strengthened this thesis. Dr Leandro Kerber, who unofficially co-supervised my undergrad project, thank you for the advice and the scientific discussions to this day. Dr Marica Valentini, for welcoming me to AIP and for maintaining the successful collaboration since then. You both contributed in your own way to the resulting thesis. I am also grateful to Dr Josefina Montalban and Dr Cristina Chiappini for their patience and all the learning in our scientific discussions.

During all these years, I have met some people who have increased my vision of life and

also, in their way, contributed to the conclusion of this thesis. Here I list some of them: Dr Sergio Ortolani; Dr Eduardo Bica; Guilherme Limberg; Dr Gustavo Bruzual; Dr Anna Barbara Queiroz; Dr Raphael A. P. Oliveira; Dr Bruno Dias; Dr Francisco Maia; Dr Diego Bossini. I also would like to specially thank you to Dr Tatiana Moura (my P^3's friend!), Dr Guilherme Couto (AIP), and Dr Guillaume Guiglion (MPIA).

To the Professor Dr João Francisco, the evaluator of this thesis. Thank you for the advice and suggestions during our annual discussions. Also to the Professors Dr. Jorge Luis Melendez Moreno, Dr. Amancio Cesar Santos Friaça, Dr. Basilio Xavier Santiago, Dra. Cristina Chiappini Moraes Leite for the availability in evaluating this thesis as members of the committee. Thank you also to Dr. Marcos Dias for the wonderful classes of *Transporte de Energia em Astrofísica* (Undergrad), *Astrofísica Observacional* and *Atmosferas Estelares* (both graduation classes).

As a great person is supported by great friends, I am grateful to my *T-estrela* friends, in special to Rafael Bicudo for our 4-hour lunch with discussions about everything. A big thank you to my friend, Carol; without her advice, I would have taken more time to enter my undergrad course.

Like a hard drive, my memory is limited, and surely I will forget some people. If you reached this thesis, I would like to thank you for reading it.

Thank you to *Fundação de Amparo à Pesquisa do estado de São Paulo* (FAPESP), for the financial support under the PhD project: 2018/22044-3. To the *Programa de Apoyo a Proyectos de Investigación e Innovación Tecnológica* of the *Dirección General de Asuntos del Personal Académico* (DGAPA-PAPIIT) under the grants IA103122 and IA103224. And finally, to the *Deutsche Forschungsgemeinschaft* (DFG) under the project number: 428473034.

To the institutions: IAG-USP, Universidad Nacional Autonoma de Mexico (UNAM), and Leibniz-Institut für Astrophysik Potsdam (AIP).

This thesis was written in LaTeX with the IAGTESE class, for IAG theses and dissertations.

"*The only thing greater than the power of the mind is the courage of the heart.*"

John F. Nash

"*There's no such thing as the unknown, only things temporarily hidden.*"

James T. Kirk

"*There's a way out of every box, a solution to every puzzle; it's just a matter of finding it.*"

Jean-Luc Picard

"*Gott würfelt nicht*"

Albert Einstein

Resumo

Esta tese busca explorar de forma multifacetada os aglomerados globulares Galácticos (GCs) para desvendar suas implicações na formação e evolução do bojo e da barra da Via Láctea.

A fase inicial do estudo envolve uma análise meticulosa dos GCs Palomar 6 (Pal 6) e NGC 6355, localizados na região interna da Galáxia fortemente afetadas pela extinção. Realizamos a análise cronoquímio-dinâmica por meio de uma abordagem abrangente que combina informações químicas usando espectros FLAMES-UVES e APOGEE DR17, determinação de idade por meio de fotometria *HST* e análise orbital graças à astrometria *Gaia*. Notavelmente, Pal 6 e NGC 6355 foram identificados como pertencentes ao ramo *in-situ* da relação idade-metalicidade (AMR) dos GCs da Via Láctea. Pal6 foi inequivocamente confirmado como um aglomerado *in-situ* com uma idade de $12,4 \pm 1,0$ Gyr e metalicidade de [Fe/H]$= -1,10 \pm 0,09$. Por outro lado, o NGC 6355, com idade de $13,2 \pm 0,9$ Gyr e metalicidade de [Fe/H]$= -1,39 \pm 0,08$, apresenta características mais parecidas a de um aglomerado ex-situ, manifestadas por seu movimento retrógrado e composição química distinta.

A investigação se estende a uma coleção mais ampla de GCs com características semelhantes às de Pal 6 e NGC 6355, com o objetivo de revelar seus papéis na evolução Galáctica. Nossa descoberta destaca a importância dos GCs in-situ, caracterizados por composições moderadamente pobres em metais (MMP, [Fe/H]$< -1,0$) e idades que variam de $12,0$ a $13,4$ Gyr. Além disso, seus valores enriquecidos de [α/Fe] fornecem informações sobre os estágios iniciais do bojo. Dinâmicamente, os GCs *in-situ* do bojo exibem movimento prógrado e baixa energia total, indicando que estão fortemente ligados ao potencial da Galáxia. Além disso, a pesquisa investiga o histórico de formação dos primeiros aglomerados do bojo usando a AMR dos GCs MMP do bojo, rastreando suas origens até $13,69 \pm 0,12$

Gyr atrás. Além disso, o valor da taxa de enriquecimento químico encontrado é dez vezes maior do que o que melhor se ajusta ao ramo ex-situ, corroborando as previsões do rápido enriquecimento químico experimentado pelo bojo durante seus estágios iniciais.

Um aspecto fundamental da pesquisa envolve a exploração da interação entre os GCs e a barra Galáctica. Ao identificar uma estrela rica em N-Al presa dentro da barra, recuperamos seu provável GC original sendo o GC Terzan 5. Estimamos que a estrela foi completamente capturada do Terzan 5 há 315 ± 12 Myr pela barra, suavemente após várias interações. Essas descobertas lançam luz sobre a influência mútua da barra na evaporação dos GCs e das estrelas ricas em N e Al vindas de GCs que compõem a população de campo da barra Galáctica. Esse resultado é particularmente interessante porque é a evidência observacional para o modelo teórico que melhor explica a evaporação de Terzan 5 para atingir sua massa atual.

Em essência, esta tese representa um avanço significativo na arqueologia Galáctica, elucidando o papel fundamental dos GCs na formação do bojo da Galáxia e da estrutura e evolução química da barra. Desde a decifração das origens de aglomerados individuais até o desvendamento de padrões mais amplos de montagem Galáctica, a pesquisa oferece uma compreensão abrangente da complexa interação entre os GCs e a dinâmica evolutiva da nossa Galáxias.

Abstract

This thesis delves into the multifaceted exploration of Galactic globular clusters (GCs) to unravel their implications for the formation and evolution of the Milky Way bulge and bar.

The initial phase of the study involves a meticulous analysis of Palomar 6 (Pal 6) and NGC 6355, located within the inner parts of the Galaxy strongly affected by extinction. We performed the chrono-chemodynamical analysis through a comprehensive approach combining chemical information using FLAMES-UVES and APOGEE spectra, age determination via *HST* photometry, and orbital analysis thanks to *GAIA* astrometry. Notably, Pal 6 and NGC 6355 were identified as belonging to the in-situ branch of the age-metallicity relation (AMR) of Milky Way GCs. Pal6 was unequivocally confirmed as an in-situ cluster with a determined age of 12.4 ± 1.0 Gyr and a metallicity of [Fe/H]$= -1.10 \pm 0.09$. Conversely, NGC 6355, with an age of 13.2 ± 0.9 Gyr and metallicity of [Fe/H]$= -1.39 \pm 0.08$, exhibits characteristics indicative of an ex-situ cluster, manifested through its retrograde motion and distinct chemical composition.

The investigation extends to a broader collection of GCs with similar characteristics as Pal 6 and NGC 6355, aiming to unveil their roles in Galactic evolution. Our results highlight the significance of in-situ GCs, characterized by moderately metal-poor compositions (MMP, [Fe/H]< -1.0) and ages spanning from 12.0 to 13.4 Gyr. Also, their [α/Fe] enhanced values provide insights into the early stages of the bulge. Dynamically, in-situ bulge GCs exhibit prograde motion and low total energy, indicating that they are strongly bound to the Galaxy potential. Furthermore, the research delves into the formation history of early bulge clusters using the AMR of the MMP bulge GCs, tracing their origins back to 13.69 ± 0.12 Gyr ago. Also, the effective yield obtained is ten times larger than the one fitted to the ex-situ branch, corroborating predictions of the rapid chemical enrichment

experienced by the bulge during its early stages.

A pivotal aspect of the investigation involves exploring the interplay between GCs and the Galactic bar. By identifying an N-Al-rich star trapped within the bar, we recovered its probable parent cluster as Terzan 5. We estimated that the star was completely captured 315 ± 12 Myr ago by the bar from Terzan 5 smoothly after several interactions. These findings shed light on the mutual influence of the bar on the evaporation of GCs and the N-Al-rich stars came from GCs that compose the field population of the Galactic bar. This result is particularly interesting because it is the observational evidence for the theoretical model that better explains the evaporation of Terzan 5 to reach its present mass.

In essence, this thesis represents a significant advancement in Galactic archaeology, elucidating the pivotal role of GCs in shaping the Galaxy bulge and bar structure and chemical evolution. From deciphering the origins of individual clusters to unravelling wider patterns of Galactic assembly, the research offers a comprehensive understanding of the complex interplay between GCs and the evolving dynamics of our Galaxy.

List of Figures

List of Tables

Contents

Chapter 1

Introduction

The Galaxy formation and evolution: According to the ΛCDM hierarchical theory of galaxy formation, galaxies form from successive mergers of low-mass objects that are absorbed by more massive objects (Figure 1.1; Peebles, 1974; White and Rees, 1978; Kauffmann et al., 1993; Springel et al., 2006; Pfeffer et al., 2018). The less massive objects are gradually absorbed while orbiting the massive ones. The Milky Way (MW) contains remnants of this early history that can be divided into two groups: those still orbiting the Galaxy, with their structures entirely or almost intact (e.g. the Magellanic Clouds), and another group composed of objects that were already dissolved by the MW after several encounters and were completely accreted, remaining only their debris. The latter objects could have retained the dynamical signatures of their progenitor if the merger event had occurred during the evolution of the Galaxy. An example is Gaia-Sausage-Enceladus (GSE), known as the remnant of the last major merger of the MW with a dwarf galaxy (Belokurov et al., 2018; Helmi et al., 2018). The estimated merger time of GSE is ~ 8 Gyr (Gallart et al., 2019; Montalbán et al., 2021), therefore allowing the identification of its debris since they did not have enough time to change their dynamical properties completely.

The halo and bulge are the first components to be formed (Chiappini et al., 1997; Spitoni et al., 2023). They formed from the first major merger of massive objects called "building blocks". The proto-MW is then composed of a diffuse stellar halo and a spheroidal bulge. Pillepich et al. (2015) analysed the formation and evolution of the stellar components in Eris (Guedes et al., 2011), a 120 pc resolution cosmological hydrodynamic simulation of a late-type spiral galaxy of a $M_{vir} = 8 \times 10^{11}$ $M_{\odot}$ galaxy halo evolved from $z = 90$ until the present. In their simulation, star particles form in cold gas that reaches a limit density of $n_S F = 5$ atoms cm^{-3} following the initial mass function (IMF) from Kroupa et al. (1993)

with initial mass $m_* = 6 \times 10^3$ M$\odot$. We invite the reader to see the original paper by Pillepich et al. (2015) for more details regarding the simulation input parameters. The authors studied the relative contributions of in-situ and ex-situ star formation to each major Galactic component, and some simulation snapshots are shown in Figure 1.1 in the A, B, and C columns of panels.

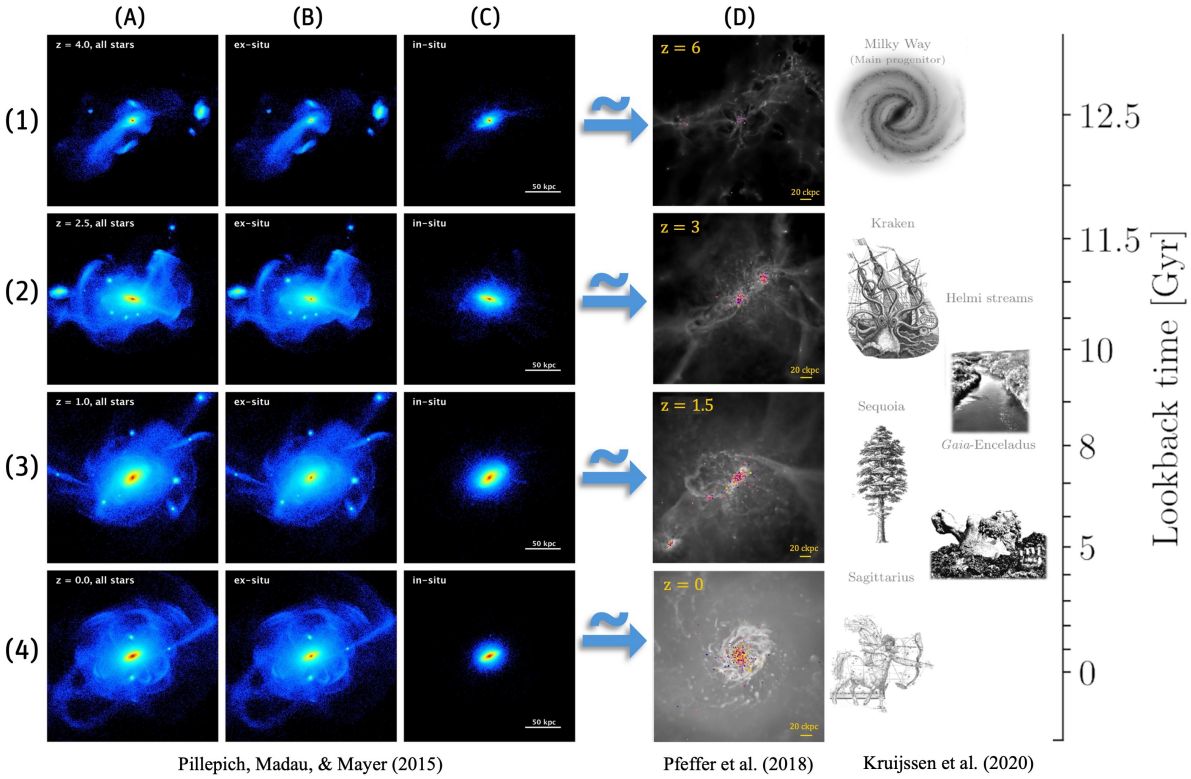

Figure 1.1: Galaxy formation and evolution through Eris (left) and E-MOSAICs (right) simulations. The columns from A to C show a random projection of Eris's stellar density field in a (240 comoving kpc)^3 box, from redshift $z \sim 4$ (row 1) to present time (row 4) taken from Pillepich et al. (2015) The columns B and C show only stars formed ex-situ and in-situ, respectively. Surface mass densities range from 100 to 10^8 M$\odot$ kpc^{-2}. The panels in column D are the zoom-in mock optical images of Gal004, an MW-like galaxy from the EAGLE Recal-L025N0752 simulation, taken from Pfeffer et al. (2018). The four panels from D1 to D4 show snapshots of the formation history of the galaxy and its star cluster population, where grey-scale shows the gas surface density and the points show positions of star clusters (with masses $> 5 \times 10^4$ M$_\odot$) coloured by metallicity (yellow for [Z/H]$= 0.5$, blue for [Z/H]$= -2.5$) and with point area scaling with cluster mass. On the right side are the pictures of the most studied merger events along the MW timeline obtained from Kruijssen et al. (2019). Their positions are approximately according to their merger time. The loockback time rule on the right is also approximately in agreement with the redshitf values of the snapshots.

After the first Gyrs of the proto-MW (row 1 in Figure 1.1), the Galaxy in-situ material forms the proto-bulge and the stellar halo (panel C1), while the ex-situ material contributes to the outer halo and the formation of the disc (panel B1). At this time, it is expected that the Galactic bar starts to form (~ 8 Gyr ago; Bovy et al., 2019; Wylie et al., 2022; de Sá-Freitas et al., 2023) from the instability of the disc. At redshift $z \sim 2$ (panels A2, B2, and

C2), the well-known merger events start to occur, as noticed by the overdensities orbiting the Galaxy, until approximately $z = 1$ (panels A3, B3, and C3) when the closest dwarf galaxies already were captured by the Galaxy. Some authors speculated the possibility of the Galactic bar starts to form indeed at this time ($\sim$ 3 Gyr ago; Nepal et al., 2024). Reaching the present day ($z = 0$, panels A4, B4, and C4), the simulation shows that approximately 70% of the Galaxy is composed of stars formed in-situ, being the majority of ex-situ stars located in the disc and the bulge. In contrast, in-situ stars dominate the inner 5 kpc from the centre.

As a globular cluster (GC) counterpart for the Eris simulations, Pfeffer et al. (2018) analysed the co-formation and evolution of spiral galaxies and their GC system using E-MOSAICs simulations (column D of Figure 1.1). The MOdelling Star cluster population Assembly In Cosmological Simulations within EAGLE project (E-MOSAICS; Pfeffer et al., 2018) combines the semi-analytic MOSAICS model of star cluster formation and evolution of Kruijssen et al. (2011, 2012) to the EAGLE simulations of galaxy formation (Schaye et al., 2015; Crain et al., 2015). The snapshots for redshifts from $z = 6$ to the present day are shown in panels from D1 to D4. The GCs are the coloured dots with colour codes based on the metallicity value from [Z/H]= 0.5 (yellow) to [Z/H]= -2.5 (blue). Interestingly, some GCs are forming already at redshift $z = 6$ ($\sim$ 13.0 Gyr, panel D1). At this time, the Galaxy is still in the phase of proto-Galaxy when the bulge and halo are forming (first infall Chiappini et al., 1997; Spitoni et al., 2023). Reaching the present day (panel D4), the GCs are mostly located in the inner regions of the Galaxy in agreement with the findings using Eris simulations (Pillepich et al., 2015). The first GCs present within the building blocks before the formation of the proto-MW could be considered as ***relics of the building blocks***, a new category of GCs with a crucial importance for the early Galaxy formation.

The system of GCs of the MW is composed of more than 200 objects (Bica et al., 2019), and a significant amount of new GCs was discovered in the direction of the Galactic bulge (Minniti et al., 2017; Garro et al., 2021, 2022). GCs are of the oldest objects of the Galaxy, reaching ages as old as the Galaxy (Forbes, 2020). Most of them are relics (remnants) of the merger process that occurred early in the Galaxy evolution timeline (Kruijssen et al., 2019; Callingham et al., 2022). Also, some of the most massive GCs like M54, $\omega-$Cen, NGC 6273, and NGC 6934 are considered to be the nuclear star clusters of the accreted dwarf galaxies Sagittarius, GSE, Kraken, and Helmi Streams, respectively (Pfeffer et al.,

2021). The age-metallicity relation (AMR) of the MW GCs shows a bifurcation that splits it into two main groups (Marín-Franch et al., 2009; Forbes and Bridges, 2010; Leaman et al., 2013; Kruijssen et al., 2019; Massari et al., 2019; Forbes, 2020; Limberg et al., 2022; Callingham et al., 2022): the steeper branch, in which older GCs are concentrated, is associated with an in-situ population; the broader component that includes very young to old ages is associated with accretion events. Also, in an analysis supported by chemistry and employing a steady Galactic mass model without non-axisymmetric components, it is possible to split the GCs, in total orbital energy E_T and angular momentum in the z-direction L_Z, into different progenitors to recover these accretion events (Massari et al., 2019; Callingham et al., 2022; Horta et al., 2023; Belokurov and Kravtsov, 2024) as in Figure 1.2. Also, since the majority of the relics of mergers are located in the Galactic halo, this analysis using the integrals of motion (like E_T and L_Z) is reliable because for these objects, for example, all the components mixed in the inner Galaxy are seen as pontual source of mass on the Galactic mass model[1].

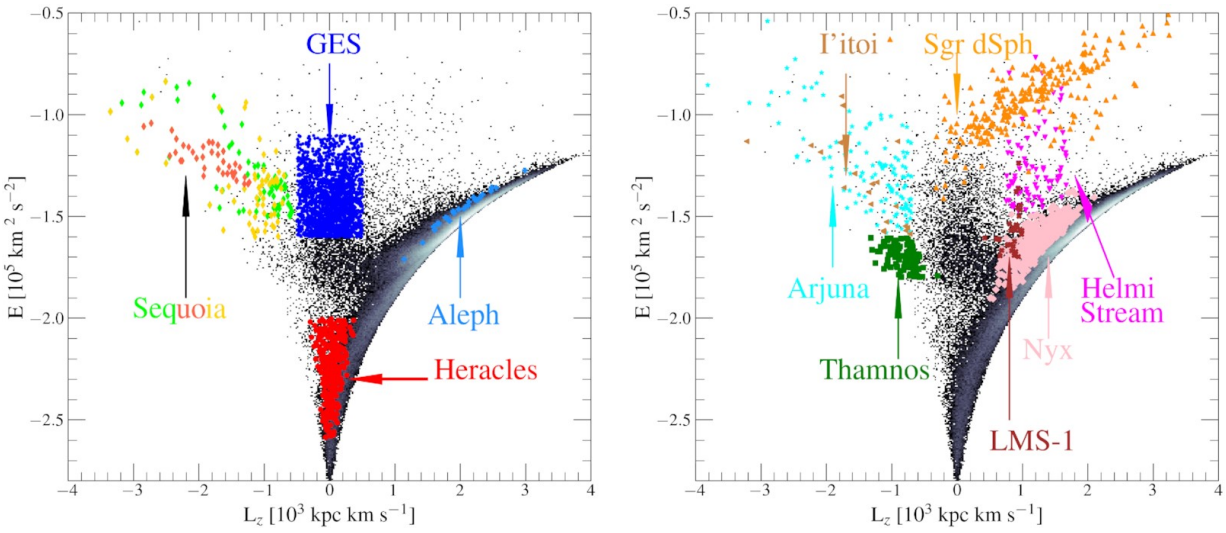

Figure 1.2: Distribution of the identified halo substructures in total orbital energy (E_T) vs angular momentum in the z-direction (L_Z). The black dots in background represent the parent sample selected by the authors. The coloured dots show the different structures studied by the authors. The figure is split into two panels for clarity. Taken from Horta et al. (2023).

According to Baade (1946), most stars in the inner part of the Galaxy are examples of population II, differing from disc stars which are type I. Even though the Galactic bulge is supposed to have been formed during the first phases of Galaxy formation, its origin is

[1] Newton's second theorem for gravitational potentials in spherical systems: *The gravitational force on a body that lies outside a spherical shell of matter is the same as it would be if all the shell's matter were concentrated into a point at its center.*

still under discussion. This early formation forms what is called "classical bulges", which are a spheroidal structure concentrated in the Galaxy. Nevertheless, secular evolution processes of the disc can originate what is known as "pseudo-bulges" via an instability of the disc leading to a bar formation. Ness and Lang (2016) provided with WISE photometry the picture of an X-shape structure in the bulge, indicating that the MW hosts a pseudo-bulge. The stars in a pseudo-bulge have characteristic kinematics and were observed to be cylindrically rotating, which means that the stars present similar velocities independent of their Galactic latitude (Ness et al., 2013). For instance, a spheroidal system presents high-velocity dispersion (dynamically hot) and latitude-dependent velocities. On the other hand, some studies have demonstrated the existence of a stellar population pressure supported, which is compatible with a spheroidal structure (Kunder et al., 2016; Queiroz et al., 2021; Razera et al., 2022). The Galactic bulge today appears to be mostly a pseudo-bulge with the presence of a less evident spheroidal structure (Barbuy et al., 2018a, and references therein).

Besides the dichotomy on the Galactic bulge origin, the complexity of the inner Galaxy relies on the fact that it also hosts material from the inner disc (Nogueras-Lara et al., 2023), from the inner halo (Pérez-Villegas et al., 2017), the MW nuclear star cluster (NSC; Nogueras-Lara, 2022), as well as from the other components passing through the inner Galaxy. Most of the stars in the bulge seem to be old stars, typical members of the type II stellar population (Baade, 1946). Following the oldest population of the Galactic halo, which can reach low metallicities as [Fe/H]~ -3, the Galactic bulge should host stars with similar metallicities since its stellar population is as old as the halo. However, the bulge metallicity distribution function peaks at -1.0 (Bica et al., 2016; Pérez-Villegas et al., 2020, , and Bica et al. accepted). These metallicities of about 10% of the solar one and 10 times larger than the halo indicate that the bulge may have been passed through a rapid chemical enrichment.

Kruijssen et al. (2020) analysed the MW GCs system to provide the first complete MW merger tree. They considered only the well-known major mergers Sagittarius stream, Sequoia, Kraken, Helmi streams, and GES (see the review by Helmi, 2020). These 5 merger events could have contributed to the Galaxy with at least 48 GCs (Massari et al., 2019; Kruijssen et al., 2019; Forbes, 2020; Callingham et al., 2022; Belokurov and Kravtsov, 2024). Nevertheless, the merger history is somewhat unknown for lookback times older

than 11.5 Gyr. At this lookback time, the GCs are located mainly in the bulge and the halo (Barbuy et al., 2018b; Kerber et al., 2019; Ortolani et al., 2019; Souza et al., 2020, 2021, 2023), both formed during the proto-Galaxy phase. Therefore, it is expected that the majority of the bulge GCs are members of the ***relics of the building blocks*** classification, and the other part, *in-situ* GCs formed during the formation of the Galactic discs (second infall; Chiappini et al., 1997; Spitoni et al., 2023, $1 - 3$ Gyr).

1.1 Globular Clusters

GCs are roughly spherical and extremely dense (e.g. of the order of a few parsecs; McLaughlin and van der Marel, 2005, Figure 1.3) self-gravitating objects composed of tens to hundreds of thousands stars born from the same primordial cloud at almost the same time, and because of that, all stars share the same age, chemical composition, and kinematics, but different values of mass. These characteristics define a simple/single stellar population (SSP; Renzini, 1986). Since a GC hosts stars with different masses, it means that there are stars of different evolutionary phases making them perfect laboratories of stellar evolution (e.g. Salaris et al., 2014). Also as a result of the meaning of SSP in GCs, they host the remnants of final stellar phase (e.g. white dwarfs and black holes) and exotic interaction systems (e.g. blue stragglers).

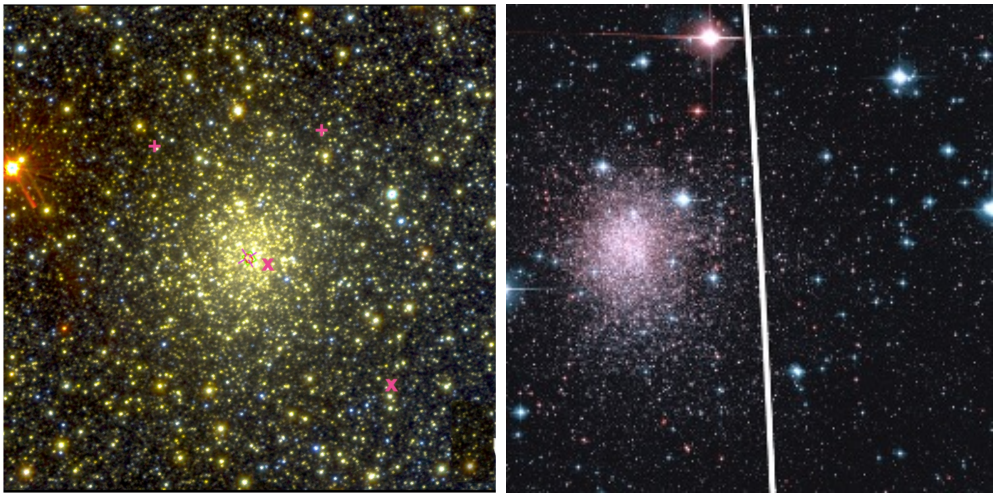

Figure 1.3: Examples of globular clusters. On the left panel is a view of the globular cluster UKS1 captured by the VVV survey (Fernández-Trincado et al., 2021). In the right panel is the globular cluster Terzan 5 combined F110W/F160W image captured with the WFC3 camera from HST.

1.1.1 Basic concepts

In principle, the stellar population within GCs follow the same initial mass function (IMF) as the entire universe (e.g. Chabrier, 2003), which shows that it is more common to form low-mass stars than massive ones. Upper panel of Figure 1.4 is a visual support for the following explanation. The majority of the stars of a GC are still in the main-sequence (MS), where a star is burning hydrogen (H) into helium (He) in its core. The star passes $\sim$ 90% of its life in this phase, but the stellar lifetime depends mainly on its mass: the most massive stars can evolve to the next phase in a few million years (Myr), while the less massive stars can remain in the MS for several billion years (Gyr, like the Sun, which is $\sim$ 4.6 Gyr old; Bonanno et al., 2002, and it is expected to evolve to the next phase when it has $\sim$ 10 Gyr).

When the star exhausts the hydrogen in its core, the core begins to contract while the outer envelope expands and cools down. At that moment, the star leaves the MS through the subgiant branch (SGB) to the red giant branch (RGB) phase. Here, the stellar core becomes inert until it reaches a high enough temperature to burn He. At the RGB phase, the H burning actually occurs in a shell around the core. The temperature at which He starts burning in the core is reached at the tip of the RGB with the He-flash, after which the stellar nucleus starts to convert He into carbon and oxygen.

After the RGB phase, the star enters the horizontal branch (HB) phase. This phase is characterized by a tight magnitude distribution that spreads horizontally in colour on the left side of the RGB along the colour-magnitude diagram (CMD). Initially, the morphology of the HB was credited to the overall metallicity of the GC, with the most metal-poor GCs displaying a wide and blue HB (left bottom panel of Figure 1.4). In contrast, the most metal-rich ones showed a narrow and redder HB (right bottom panel of Figure 1.4). Subsequent studies have found that some metal-poor GCs have red HB, but these GCs also have different ages. Consequently, the age of GC was also associated with the morphology of the HB. It was known as "the second parameter problem" (Sandage and Wildey, 1967; van den Bergh, 1967). In the last decades, some studies have increased the problem to a "third parameter problem" because, with the increased number of GCs observed, thanks mainly to the advent of *Hubble Space Telescope* (HST), the age and metallicity could not explain all the morphology of the HB. The most recent studies include the helium mass

fraction (Y) as a "third parameter" candidate (D'Antona and Caloi, 2004; Carretta et al., 2009; Legnardi et al., 2022; Johnson et al., 2023; Carini et al., 2024, among others).

Finally, the mass loss during the RGB phase is also an important parameter, not to explain the HB morphology but to set where a star will be in the HB region. When He is also exhausted in the core, the stellar core contracts, and He starts burning in the shell above the core, expanding the envelope and, consequently, the star. This phase is called the asymptotic giant branch (AGB) phase. At this phase, the star loses its entire envelope through massive stellar winds, finishing its life as a white dwarf.

1.1.2 Multiple stellar populations

The paradigm of GCs being examples of simple stellar populations has lost space with the evidence that all GCs host multiple stellar populations with distinct chemistry (see Gratton et al., 2004, 2012, , and references therein) and kinematics (Lardo et al., 2011; Richer et al., 2013; Cordoni et al., 2020). Harding (1962) observed $\omega-$Cen stars with anomalous enhancement in C abundances using the Cassegrain spectrograph at Radcliffe Observatory (1.88 meter telescope). He found the first CH strong star *globular-cluster like* because CH stars were considered field stars belonging to the population I. Later, Osborn (1971) observed the carbon molecule abundance (CN $\lambda = 4216$Å) for stars in two GCs: M5 and M10. He measured CN strength with the colour index $C(41-42)$ and compared it with surface gravity ($\log g$) colour index indicator $C(45-48)$. Two stars, one in each GC analysed, showed to be CN enhanced when compared with stars inside their clusters and stars with the same $\log g$ range.

In the past decades, Hartwick and McClure (1972) discovered the anomaly also in Nitrogen, Auer and Demarque (1977) observed the CNO abundances for M92 stars. Cohen (1978) analysed in turn five red giant stars in M13 and three in M3. They found that the chemical pattern of these stars is compatible with the observed for field stars, having, however, a large spread in Na. The works led by Kraft et al. also provided significant improvements in this field during the 80's and 90's. Kraft et al. (1982) analysed red giants in globular clusters, looking for C and N anomalies. They found that for M92, 40% of the analysed stars show [N/Fe] above +0.6, never observed in field stars. In Kraft et al. (1992), they found for M13, a depletion in O (< -0.4) followed by an enhancement in Na ($> +0.2$). All the results until that epoch were compiled in the review Kraft (1994). After

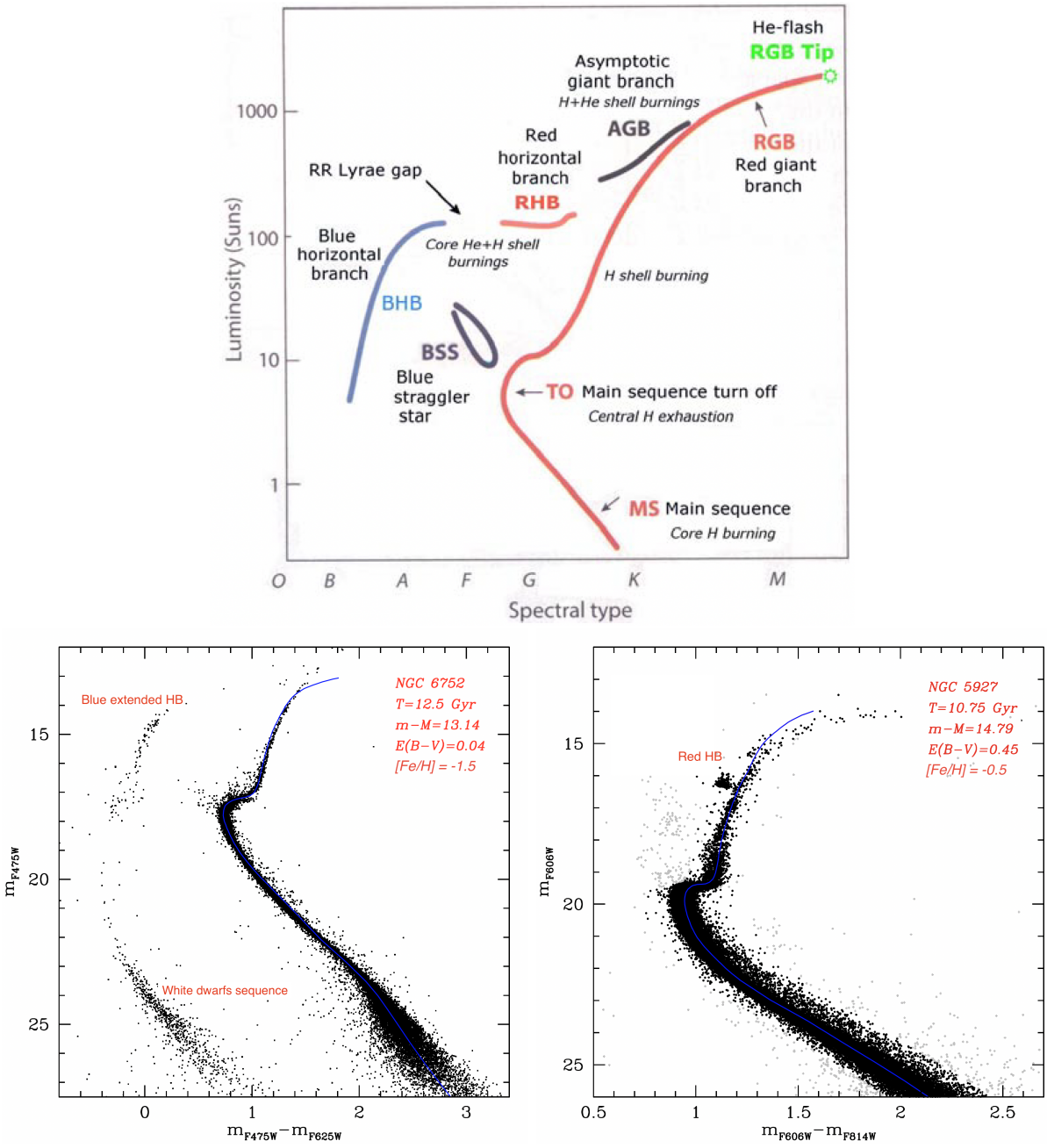

Figure 1.4: How the CMD diagram works. Upper panel: schematic CMD of a typical GC (https://sites.astro.caltech.edu/~george/ay20/eaa-globcl.pdf). The left and right panels represent two GCs, one metal-poor (NGC6752) and another metal-rich (NGC5927), respectively. The fundamental parameter of each cluster and the indication of the HB type and white dwarf sequence (for NGC6752) are displayed inside the CMD. The CMD was taken from https://people.smp.uq.edu.au/HolgerBaumgardt/globular/.

that, in Kraft et al. (1997), a wide spread in Al (> 1.0 dex) was observed for 11 giant stars in M13. Kraft et al. (1998) further analysed the GC NGC7006, trying to explain the wide and bluer HB of this cluster. They suggested that the enhancement in some elements of the proton capture chain could explain it. Later, Carretta et al. (2009) analysed 214 red giant stars of 19 GCs with UVES spectra. They demonstrated the (anti)correlations

among the CNO, α, and light elements. Figure 1.5 shows some of the (anti)correlations found by Carretta et al. (2009). The left panel is the anti-correlation between Na and O. The colours indicate the metalicity of the owner cluster from metal-rich (red) to metal-poor (blue). The middle panel shows the relation Al−Mg. It is interesting to note that the distribution of Mg is almost uniform, around 0.45. Finally, the right panel exhibits the almost uncorrelated relation between Si−Mg.

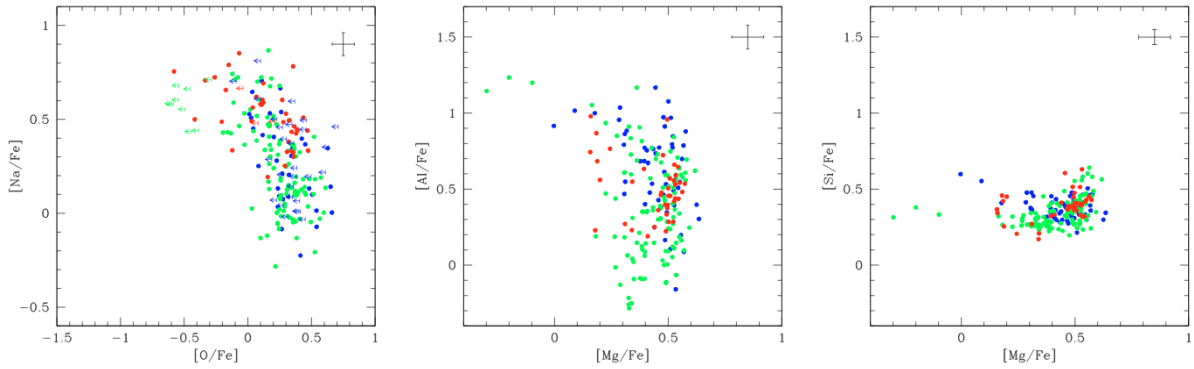

Figure 1.5: (Anti)Correlations for NaOSiAlMg abundances of 214 RGB stars of 19 GCs analysed with UVES spectra. *Left panel*: Na vs O anticorrelation. Stars are coloured according to cluster metallicity, from red stars of metal-rich clusters ($-1.1 <$ [Fe/H] < -0.4 dex), green giants of clusters of intermediate metallicity ($-1.8 <$ [Fe/H] < -1.1 dex) blue colours for stars in the most metal-poor clusters ($-2.4 <$ [Fe/H] < -1.8 dex). Arrows indicate upper limits in O abundances. *Middle panel*: Al vs Mg correlation. *Right panel*: Si vs Mg almost uncorrelated relation. (Carretta et al., 2009)

In parallel with the spectroscopic studies, many authors have found features compatible with those anomalous stars in the GCs CMDs. Lee et al. (1999) observed a metalicity distribution with at least four peaks and the presence of multiple structures on the RGB of ω−Cen CMD (Figure 1.6, upper-left panel). Pancino et al. (2002) further studied this CMD and associated the modes of metallicity with a multimodal distribution of Calcium (Ca) and carried out the split of those stars in which they called Multiple Stellar Populations (MPs, Figure 1.6 upper-right panel). Later, Bedin et al. (2004) with the Wide Field Camera (WFC) of HST demonstrated the presence of MPs on the entire CMD of ω−Cen (Figure 1.6 bottom panel). Interestingly, since α-elements are generated from core-collapse supernovae (SNe II) and Fe from type Ia supernovae, these elements together are stellar population indicators. Therefore, the multimodal metallicity distribution function of ω−Cen indicates that its is a complex object and more compatible with being the nuclear star cluster of a ancient dwarf galaxy(see the review Neumayer et al., 2020).

The photometric study of MPs in GCs has become very important through the UV

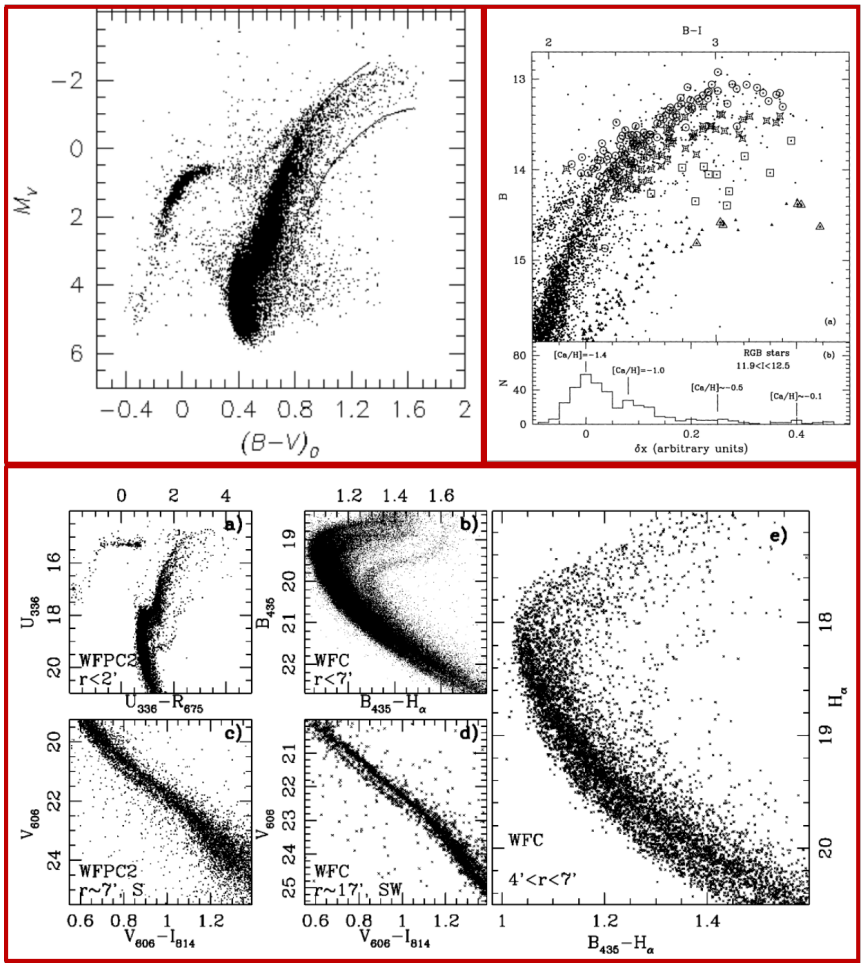

Figure 1.6: Sumary of first $\omega-$Cen photometry study of MPs. (*upper-left panel* : Lee et al. (1999)) CMD of $\omega-$Cen displaying several distinct RGBs. The outermost RGBs are overplotted by isochrones. (*upper-right panel* : Pancino et al. (2002)) RGB of $\omega-$Cen. Small-filled triangles are the main RGB. Large open circles are stars with $-1.5 < [Ca/H] < -1.3$, large open stars for ones with $-1.1 < [Ca/H] < -0.85$, large open squares are stars with $-0.65 < [Ca/H] < -0.40$, large open triangles with $[Ca/H] > -0.3$. The bottom histogram is the distribution of the distances from the fiducial line of the main RGB. Also, the mean [Ca/H] abundances for the prominent components of the RGB are marked. (*bottom panel* : Bedin et al. (2004)) CMDs of $\omega-$Cen using data from WFPC and ACS. The panels from **a** to **d** are zoom of distinct regions of CMD, and the panel **e** is a zoom to turn-off point.

data from the HST. The greatest improvement with HST was the high quality and the photometry depth, even in the UV bands. In the last decade, a great effort has been made to construct filters based on ultra-violet (UV) elemental abundance variation to the HST. This effort culminated in the HST UV Legacy Survey of Galactic Globular Clusters (Piotto et al., 2015). These allow us to obtain the separation of MPs in the entire CMD (all evolutionary stages). Figure 1.7 exemplifies the WFC3 UV filters conception. The UV filters F275W and F336W were thought to be perfect in the wavelength range of CN, NH, OH, and CH molecular bands. Many works have been devoted to characterising the MPs in the last decades. The most important characteristics are summarised in Piotto et al.

(2015), which analysed 57 known GCs in different regions of the Galaxy, and the recent reviews by Bastian and Lardo (2018a) and Milone and Marino (2022). It is worth noting that other studies have developed their own photometric systems in order to investigate the MPs phenomenon independently of HST (see right panel of Figure 1.7; Lee, 2017). Combining the HST UV filters, the resulting CMD in Figure 1.8 clearly show different stellar populations.

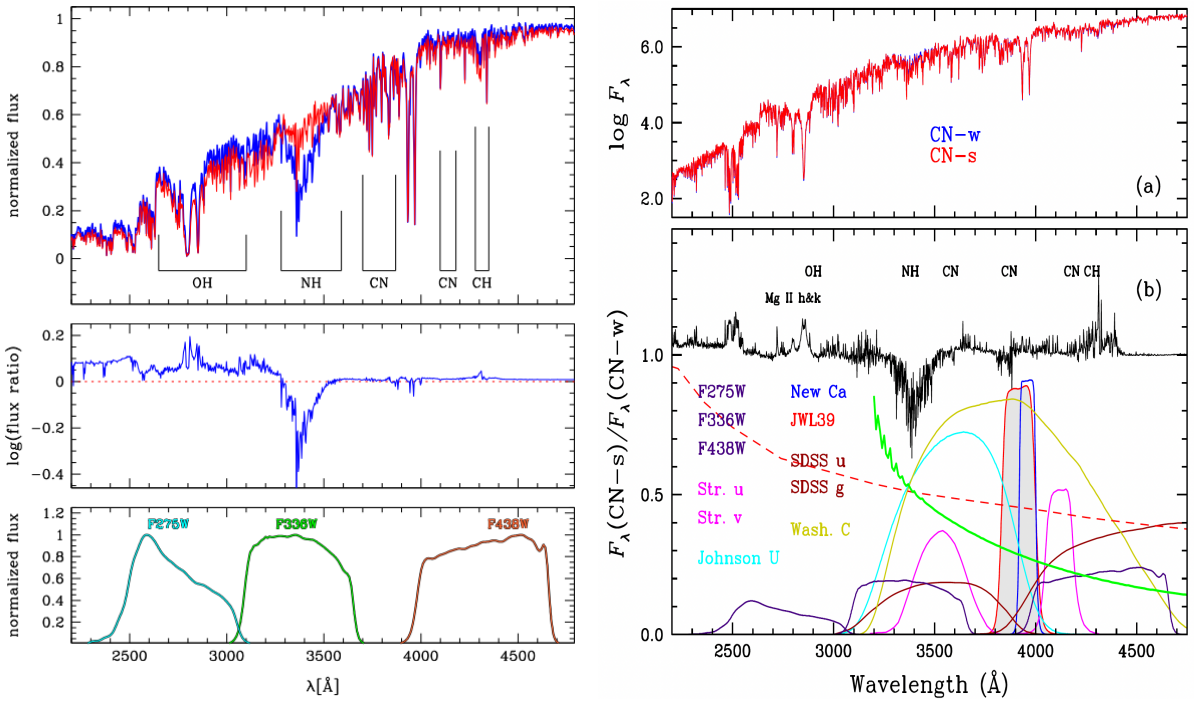

Figure 1.7: Left: HST UV passbands and molecular variations contrapart to build the UV WFC3 filters. *Top panel*: Observed NGC 6752 spectrum simulating the 1G star (red, depleted in N) and synthetic spectrum of a supposed third generation of NGC 6752 (blue, enhanced in N). *Middle panel*: Flux ratio between the observed and synthetic spectra from the upper panel. *Bottom panel*: Transmission curves of the WFC3/UVIS camera with the filters F275W, F336W, e F438W. Taken from (Piotto et al., 2015). Right: (a) Comparison of synthetic spectra for typical CN-w and CN-s RGB stars in GCs. (b) Flux ratio between the two spectra along with the transmission functions for the various filter systems used in the UV and in the blue part of the visible light. The red dashed line denotes the interstellar extinction curve for E(B−V)= 0.1 mag, and the green solid line represents the atmospheric extinction curve for Maunakea, given in units of mag/airmass. Taken from Lee (2017).

We know that most known GCs host from two (the majority; Milone et al., 2017) to many stellar populations (the case of $\omega-$Cen with 15 MPs; Tailo et al., 2016; Bellini et al., 2017; Latour et al., 2021). Also, it is known, from spectroscopy, that the first generation (1G) stars have a chemical composition similar to the primordial cloud which formed the GC and field stars. The second generation (2G) stars are depleted in C and O and enhanced in N, Na, Al, and helium mass fraction (Y; Carretta et al., 2009, 2012; Meszaros et al., 2020). On the other hand, the abundance of iron ([Fe/H]) almost has no variations,

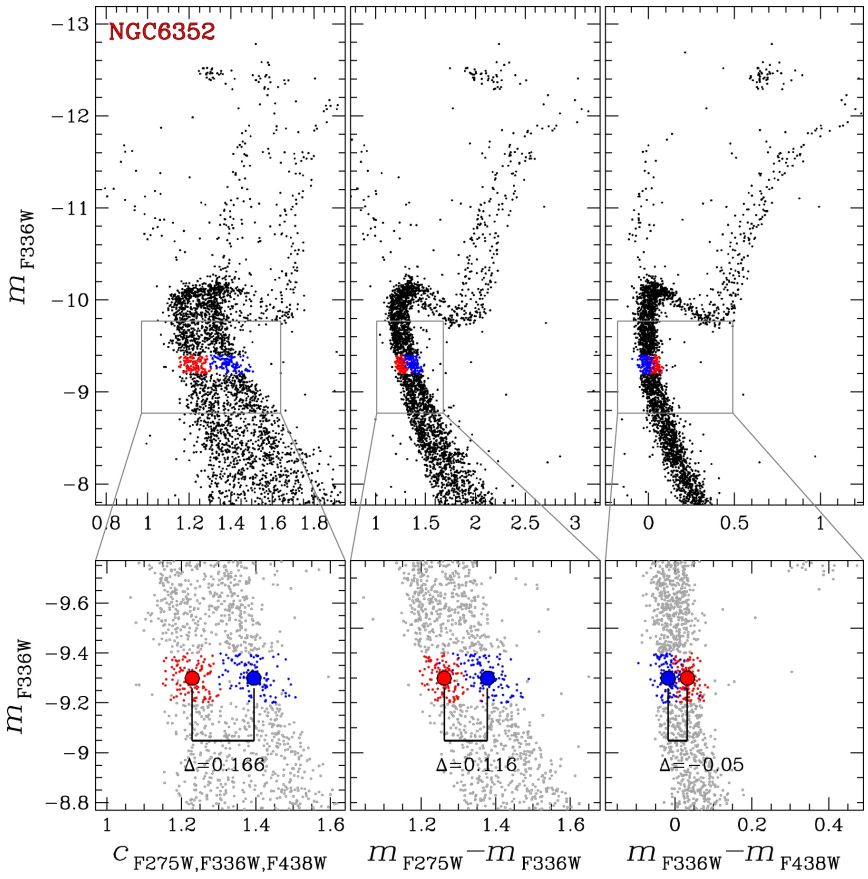

Figure 1.8: CMDs of NGC 6352 from GO-13297 data. m_{F336W} vs. $C_{F275W,F336W,F438W}$, defined as $(m_{F275W}-m_{F336W})-(m_{F336W}-m_{F438W})$ (left panels), m_{F336W} vs. $m_{F275W}-m_{F336W}$ (middle panels), and m_{F336W} vs. $m_{F336W}-m_{F438W}$ (right panels). Lower panels show a zoom of the MS. Red dots highlight 2G stars; blue dots 1G stars. Taken from Piotto et al. (2015).

pointing out a possible formation without accretion of SN yields, except for massive GCs as for example $\omega-$Cen and NGC 2808, since the winds from SN are excessively fast to be held by the GC gravitational potential(Piotto et al., 2015).

Although there are many works focused on MPs (see the reviews Bastian and Lardo, 2018a; Milone and Marino, 2022), their origin is still under debate. In general, we can divide the possible scenarios into two groups: GC interacting with an external object (Galaxy, for example) or an internal interaction among the stars of the GC. The first group is more compatible with massive GCs like $\omega-$Cen, probably the nucleous of a dwarf Galaxy accreted by the MW (e.g. Bekki and Freeman, 2003; Massari et al., 2019; Forbes, 2020; Limberg et al., 2022). On the other hand, Lee (2020) proposed that another massive GC, M22, were formed by the merger of two different GCs, reinforced by the bimodal [Fe/H] distribution that is observed.

The internal interactions aim to pollute the intracluster medium (ICM). These scenarios

are based on the stellar evolution of 1G stars. The most energetic contamination event of the medium is the final evolution of massive stars, the SNe. The shock wave caused by these events spreads with a velocity order of magnitudes greater than the typical escape velocity of GCs ($\sim 10 - 30$ km s^{-1}; Baumgardt and Makino, 2003). Therefore, the gravitational potential of the GC does not hold the reminiscent gas, preventing a new star formation event from this enhanced gas. This argument is compatible with the metallicity distribution function of the majority of GCs.

On the other hand, there are low energy events due to mass ejection from intermediate-mass stars (M~ 4M$_\odot$) and fast-rotating stars. During the RGB phase, the intermediate-mass stars experience a dredge-up process mixing the nucleosynthesis yields from the innermost shell to the outermost ones. After the RGB phase, the star reaches the AGB phase, in which phase a successive dredge-up process on the stellar atmosphere can occur. The atmosphere's inner shells are enhanced by C and O, while the outer ones are enhanced by N and helium mass fraction Y (Figure 1.9). During the AGB phase, several mass ejection events occur through stellar winds, polluting the medium. Finally, before reach the white dwarf phase, the complete stellar external shells of the star are ejected in the *post-AGB* phase. These AGB nucleosynthesis yields are contained by the GC mainly in the central region, which can be fuel to form 2G stars after the radiative cooling of the gas during ~ 100 Myr (D'Antona et al., 2016) up to ~ 500 Myr considering the massive binary interaction systems (Renzini, 2013; Renzini et al., 2015). The AGB scenarios can answer the question about the C, N, and O variations among the MPs. However, a huge amount of AGB stellar winds would be necessary to explain the predominance of 2G stars in some GCs (mass-bugdet problem; Milone et al., 2017; Bastian and Lardo, 2018a).

Another simple mass ejection event can occur due to high rotation in massive stars (fast-rotating massive stars - FRMS; Prantzos and Charbonnel, 2006). With the high rotational velocity, the mixing of the layers described for AGB can be reached even during the MS. An equatorial disc is formed from the external shells (Figure 1.10). The enriched material is then ejected to the ICM with enough low velocities to be held in the GC potential well and accumulate in the cluster centre in an interval of ~ 6 Myr (Decressin et al., 2007; Krause et al., 2013). At this time scale, most of the massive stars have reached SNe II, and the shockwave triggers a new star formation in the accumulated gas.

After the formation of the GC, remnants of the primordial cloud remain in the medium.

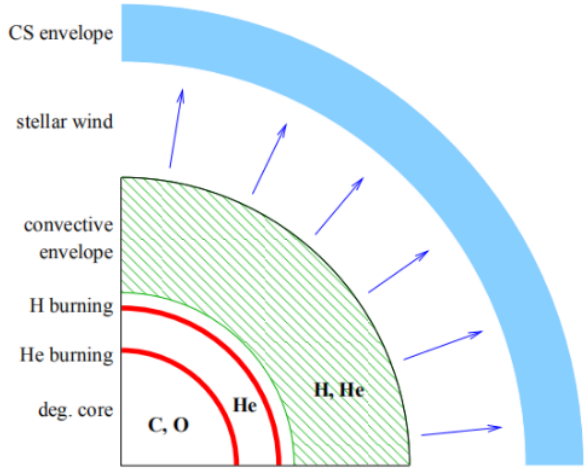

Figure 1.9: Schematic structure of an AGB star during its thermally pulsing phase demonstrated on notes from Pols (2011). The CO core is degenerate, very compact, and surrounded by two burning shells close together in mass coordination. The convective envelope, by contrast, is very extended and tenuous, having a radius $10^4 - 10^5$ times the size of the core. The strong stellar wind gradually erodes this loosely bound envelope, forming a dusty circumstellar envelope that runs to several hundreds of stellar radii. The convective envelope, stellar atmosphere and circumstellar envelope have a rich and changing chemical composition driven by nucleosynthesis processes in the burning shells in the deep interior.

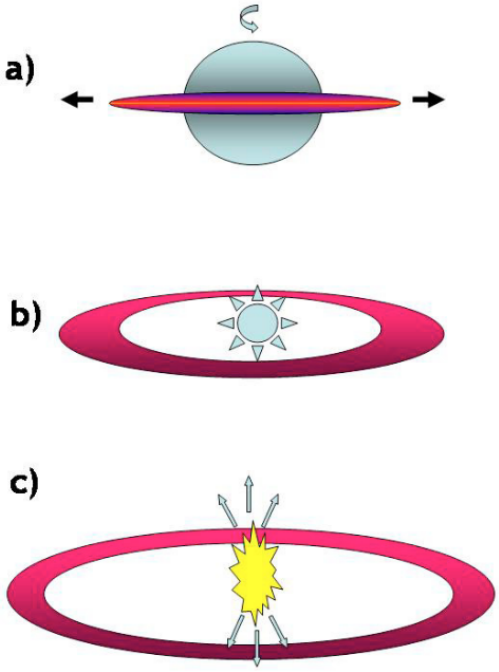

Figure 1.10: A schematic view of the FRMS scenario illustrates the possible ejection of stellar material at various evolutionary stages: a) During the main sequence, when the star rotates near or at critical velocity, the matter is predominantly ejected in the equatorial plane through an equatorial disc (pink ring) due to centrifugal acceleration; b) After the main sequence, the surface velocity is no longer critical, and the wind is primarily driven by radiation. This wind becomes isotropic rather than equatorial; c) If a supernova explosion occurs in a star that initially had a fast rotation, it may favour ejection through jets aligned along the rotational axis. Decressin et al. (2007)

The most massive stars in a GC are mainly in the central region. The supermassive stars (SMS, $10^3 M_\odot$; Gieles et al., 2018) are the main actors of this scenario. Due to their mass,

the SMSs attract the gas to their atmosphere. This process enriches the external shells and increases the stellar mass, consequently increasing the stellar winds ejecta due to the increment of luminosity. The SMS scenario predicts the pattern abundance present in MPs with no variation in [Fe/H]. Also, this scenario has two ways of observing MPs. The presence of MPs can be explained by the pollution of SMSs itself or the pollution of the medium by the mass ejection from SMSs stellar winds. The first approach meaning no age difference among the MPs. However, the second approach could result in multiple bursts of continuous star formation or with intervals of a few Myr (Figure 1.11).

Similarly, the lifetime of FRMS and AGB are fast enough to pollute the ICM, while low-mass stars are still in their pre-MS phase. These stars can pass through (at different timescales) the processed ejected gas and capture part of this material, forming an accretion disc. In this scenario, the star will enter the MS phase already with the chemical pattern of 2G stars but without the necessity of a new star formation burst. This scenario is called the "accretion disc scenario" (Bastian et al., 2013) and eliminates the mass-budget problem.

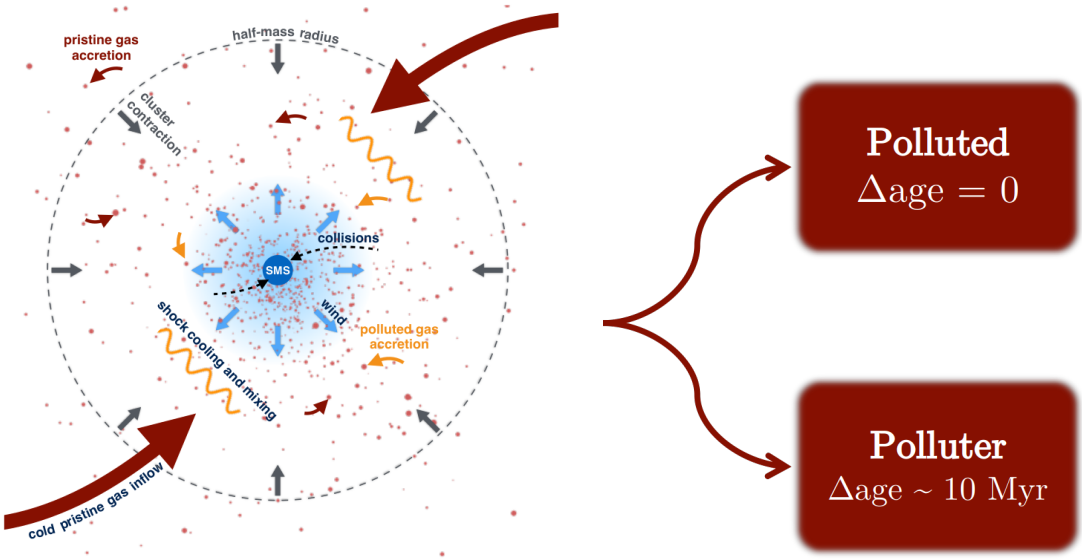

Figure 1.11: A schematic representation of the enrichment scenario described in Gieles et al. (2018): Cold, pristine gas accretes onto the stars within the cluster, causing the cluster to contract. The increased stellar density leads to stellar collisions, forming a Supermassive Star (SMS) at the cluster's centre. The SMS emits a wind enriched with hot hydrogen products, which interact with and mix into the inflowing gas. This mixed material then accretes onto the stars, enriching them with the yields from the SMS. Two main scenarios can occur from this: The falling gas can be captured by pre-existent stars, and the phenomenon observed today is a result of atmosphere pollution of these stars; the falling cold gas generates new stars through a new star formation event.

1.2 The chrono-chemo-dynamical analysis

This section presents the methodology developed along the Ph.D. project, called chrono-chemodynamical analysis. Besides the well-established chemodynamical interpretation of the data (e.g. Barbuy et al., 2018b; Queiroz et al., 2021), it is necessary to date the stellar objects to properly identify each subpopulation of a specific Galactic component (Queiroz et al., 2023). Here, we are deriving the age of GCs using the isochrone fitting method (Section 1.2.1). The chemical analysis is explained in Section 1.2.2, and the dynamics through orbital analysis is given in Section 1.2.3.

1.2.1 Fundamental parameters - SIRIUS code

We developed the `Python` code named `SIRIUS` (Souza et al., 2020), which stands for **S**tatistical **I**nference of physical pa**R**ameters of s**I**ngle and m**U**ltiple populations in **S**tellar clusters, to extract information on a stellar cluster from its CMDs. `SIRIUS` was designed to analyse stellar clusters, applied here both to synthetic data and to observed data. `SIRIUS` has already been successfully applied to derive the parameters of several GCs. In Kerber et al. (2019), we applied for HP 1 the isochrone fitting for a multi-band (K_S and J from Gemini-GSAOI+GeMS, and F606W from *HST*-ACS). For the GC ESO 456-SC38(Ortolani et al., 2019), we used the *HST* photometry in the filters F606W from ACS and F110W from WFC3, and FORS2@VLT photometry in V and I. We also applied `SIRIUS` for several GCs in different Galactic and extra-Galactic contexts (see more details in Chapter 5 and the list of publications in the Appendix A). A detailed description of the `SIRIUS` code flow-chart is presented in Figure 1.12.

The simple χ^2 isochrone fitting procedures do not necessarily represent a physical interpretation of a GC CMD since the best fit is the isochrone that seems most similar to the CMD, and many combinations of the parameters can fit the CMDs well as the best fit (minimum χ^2; D'Antona et al., 2018). The morphology of the isochrone depends on the age, metallicity, and helium abundance. Figure 1.13 illustrates the effects on the shape of isochrones due to the change in each parameter. The reddening $E(B-V)$ changes the location of the isochrone in the diagonal direction because it contributes to the apparent distance modulus $(m-M)_\lambda$ and to the apparent reddening $E(\lambda_1-\lambda_2)$, without varying the morphology of the isochrone (first panel of Figure 1.13). For high values of reddening and

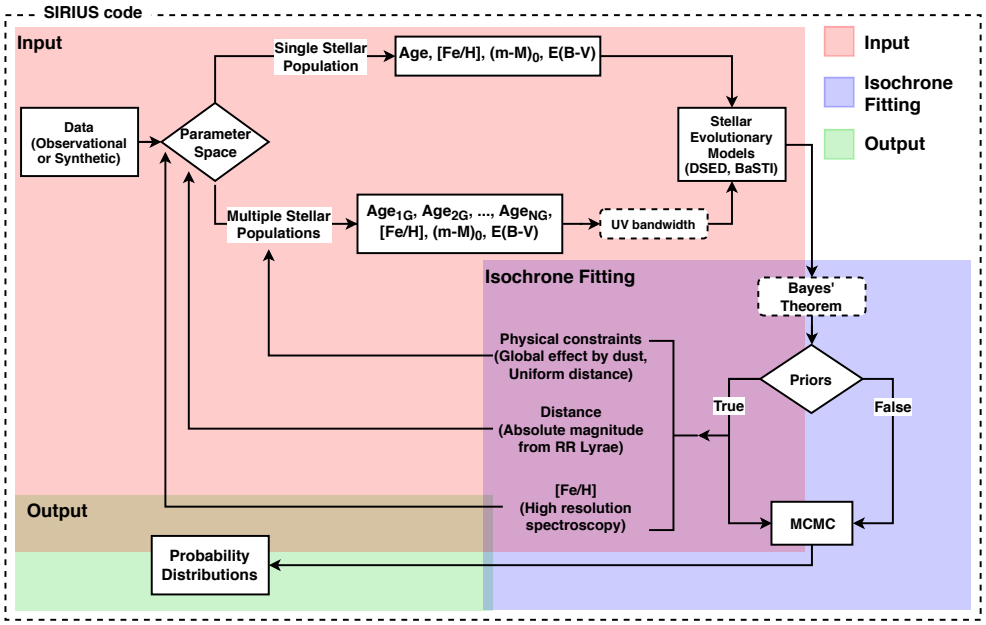

Figure 1.12: SIRIUS flow-chart shows the steps to perform the isochrone fitting. *Taken from* (Souza et al., 2020).

large passbands, a second-order correction from the effective temperature (e.g. Ortolani et al., 2017; Kerber et al., 2019), has to be taken into account during the isochrone fitting. A vertical displacement results from a change in distance modulus $(m-M)_0$ (second panel of Figure 1.13). Age essentially affects the position of the turn-off point (TO, third panel of Figure 1.13). The metallicity [Fe/H] has a complex effect on the isochrone, but more strikingly, by changing the slope of the RGB, with a sub-giant branch (SGB) and RGB steeper towards lower metallicities (fourth panel of Figure 1.13). A variation in Y changes the slope of the SGB and the location of the TO, shifting the isochrone to the bluer region of the CMD (last panel of Figure 1.13). It is worth noting that the above explanation is for the specific filter combination. Nevertheless, the behaviour of the variations on the isochrone morphology will be almost similar when the colour baseline is composed by the simple combination of two filters. The exceptions are the pseudocolours like UBI colour $((U-B)-(B-I))$.

SIRIUS , in principle, extract the fundamental parameters age, metallicities ([Fe/H], [M/H], or Z), distance to the Sun ($d_\odot$), reddening ($E(B-V)$), total-to-selective extinction ratio (R_V), and binary fraction. The code employs the Bayesian method of Markov Chain Monte Carlo (McMC) to obtain probability distributions for each parameter. The code compares the observed colour-magnitude diagram with synthetic colour-magnitude dia-

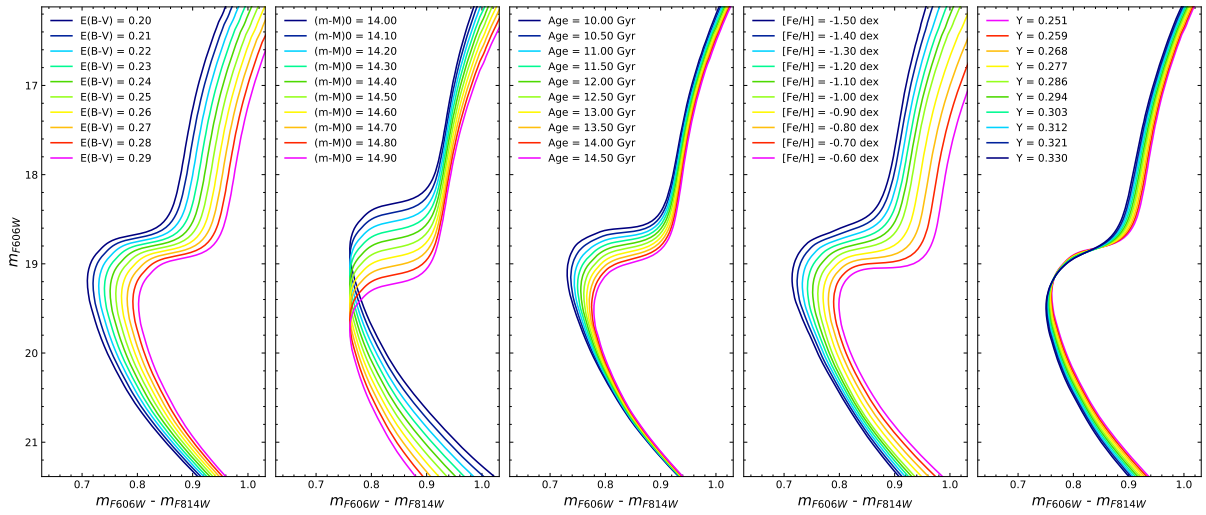

Figure 1.13: Graphical explanation of how the main five parameters change the morphology and position of the isochrone. The first panel shows the variation due to changes in $E(B-V)$, the second in $(m-M)_0$, the third in Age, the fourth in [Fe/H], and the last one in Y. *Taken from* (Souza et al., 2020)

grams constructed from each set of parameters randomly drawn during the fitting process. In the following, we describe the steps to construct the synthetic CMDs used to compare with observational CMDs that is visual explained in Figure 1.14.

To construct the synthetic diagrams, `SIRIUS` utilizes isochrones from the DSED[2] (Dartmouth Stellar Evolutionary Database - Dotter et al., 2008) and BaSTI[3] (A Bag of Stellar Tracks and Isochrones - Pietrinferni et al., 2006) databases, which initially spans ages between 10 Gyr and 15 Gyr with intervals of 0.1 Gyr, and metallicities between −2.30 and 0.0 with intervals of 0.01 dex. However, the code interpolates different isochrones during the fitting process to obtain the model with exact values. In this explanation, we employed a DSED isochrone with age equal to 13 Gyr and metallicity of [Fe/H]= −1.18 (panel **a** of Figure 1.14). These values are often observed in bulge GCs.

After interpolating in mass a sample of N random stellar mass, these values are then interpolated to obtain the corresponding magnitude values (panel **b** of Figure 1.14).. The code calculates the extinction coefficients following the total-to-selective parameter R_V of each iteration. The extinction law is interpolated from the curves of Cardelli et al. (1989), and the extinction coefficients for the specific magnitudes are obtained from this. Then, each absolute magnitude is converted to apparent magnitude as follows:

[2] http://stellar.dartmouth.edu/models/

[3] http://basti.oa-teramo.inaf.it/

$$m_\lambda = M_\lambda + (m - M)_0 + E(B - V) \times R_V \times R_\lambda \tag{1.1}$$

where (m-M)$_0$ is the intrinsic distance modulus, and R$_\lambda$ is the ratio between the extinction coefficient in band λ and in the V band A$_V$, computed in each iteration varying with R$_V$. Here, we are using a distance of d$_\odot$ = 7.52 and reddening E(B−V)= 0.14 (panel **c** of Figure 1.14).

A cut in magnitude is applied to remove stars with mass lower than 0.8M$_\odot$ and bigger than 3.0M$_\odot$ (panel **d** of Figure 1.14). These mass limits were select because they agree very well with fainter and brighter limits for most of the GCs observed with HST. A second cut is applied, however, adopting the initial mass function (IMF) of Chabrier (2003) (the code is also able to select other IMF), this step is in the panel **e** of Figure 1.14. A fraction of these mass values are associated with photometric binary stars (stars close enough to have their flux overestimated; panel **f** of Figure 1.14). While the first star has mass Mass$_A$, the hypothetical secondary star will have mass Mass$_B$ calculated as Mass$_B$ = q × Mass$_A$, where q is the mass ratio defined as:

$$q = q_{\rm min} + (1. - q_{\rm min}) \times NA(0., 1) \tag{1.2}$$

where $q_{\rm min}$ is the minimum mass ratio value, and NA(0,1) is a randomly chosen number uniformly between 0 and 1. The value of $q_{\rm min}$ is adopted as 0.6 as it is the minimum value to observe the effect of binaries in the CMD (Milone et al., 2023). The calculation of the final magnitude of binary stars is computed from the sum of the flux of each star:

$$m = -2.5 \log \left(10^{(-m_A/2.5)} + 10^{(-m_B/2.5)}\right) \tag{1.3}$$

With the synthetic diagram already with the apparent magnitudes, a luminosity function is applied to reproduce the observation conditions to which the data were subjected. The luminosity function is calculated as the number of stars in each magnitude bin. When applied to the synthetic diagram, some stars will be excluded to make the synthetic diagram more similar to the observed one in terms of the number of stars at each magnitude (panel **g** of Figure 1.14).

An error function is applied to spread the points that survived to all the cuts (panel **h** of Figure 1.14). The error function is derived from the observed data by calculating the

median error in magnitude bins and shifted to the position of the synthetic CMD from the turn-off point to ensure no bias in the position of the synthetic diagram relative to the observed one. Thus, whatever set of parameters is drawn, the error function will generate a synthetic CMD.

When the R_V is a free parameter, the isochrone fitting is performed simultaneously for the two CMDs, one of them must to be in the IR to reduce the effect of the extinction. Simultaneous fitting allows the determination of the extinction law since it will force the fit of a single set of distance and reddening for the two CMDs (Pallanca et al., 2021). Another advantage of this approach is determining an unbiased age using one specific photometric system.

As a proxy of distance, in some cases, we employ a prior to the distance according to the magnitude level of RR Lyrae stars (or the HB magnitude level). For each McMC interaction, the values of metallicity and reddening can be used to obtain the distance prior using the M_λ−[Fe/H] calibrations (e.g. Oliveira et al., 2022, for V and I magnitudes). This calculated distance is then compared with the distance value for the specific McMC interaction assuming a Gaussian distribution.

We used the `Python` library emcee (Foreman-Mackey et al., 2013) to perform the McMC. The likelihood function is an adaptation of Tremmel et al. (2013), which is basically a Poisson distribution comparing the number of observed and synthetic stars in a colour and magnitude bin. The adaptation includes a simple isochrone fitting component comparing the isochrone to the two-dimensional distribution of observed points. This change allows the code to reach the stability of the distance and reddening values more quickly. Meanwhile, the likelihood component that compares the synthetic diagram with the observed one allows for better age and binary fraction calculation.

As explained before, the age difference between the first and next generations is an important parameter to elucidate the origin of the MP phenomenon in GCs. From the methods to split the stellar populations, we can tag each star of the GC according to which population it belongs, separating each generation along the whole CMD.

Since the stellar evolutionary models available today do not consider the chemical pattern observed in GCs, the isochrone fitting for MPs must be performed in the optical and near IR filters.

We developed an algorithm to estimate the age difference between stellar populations

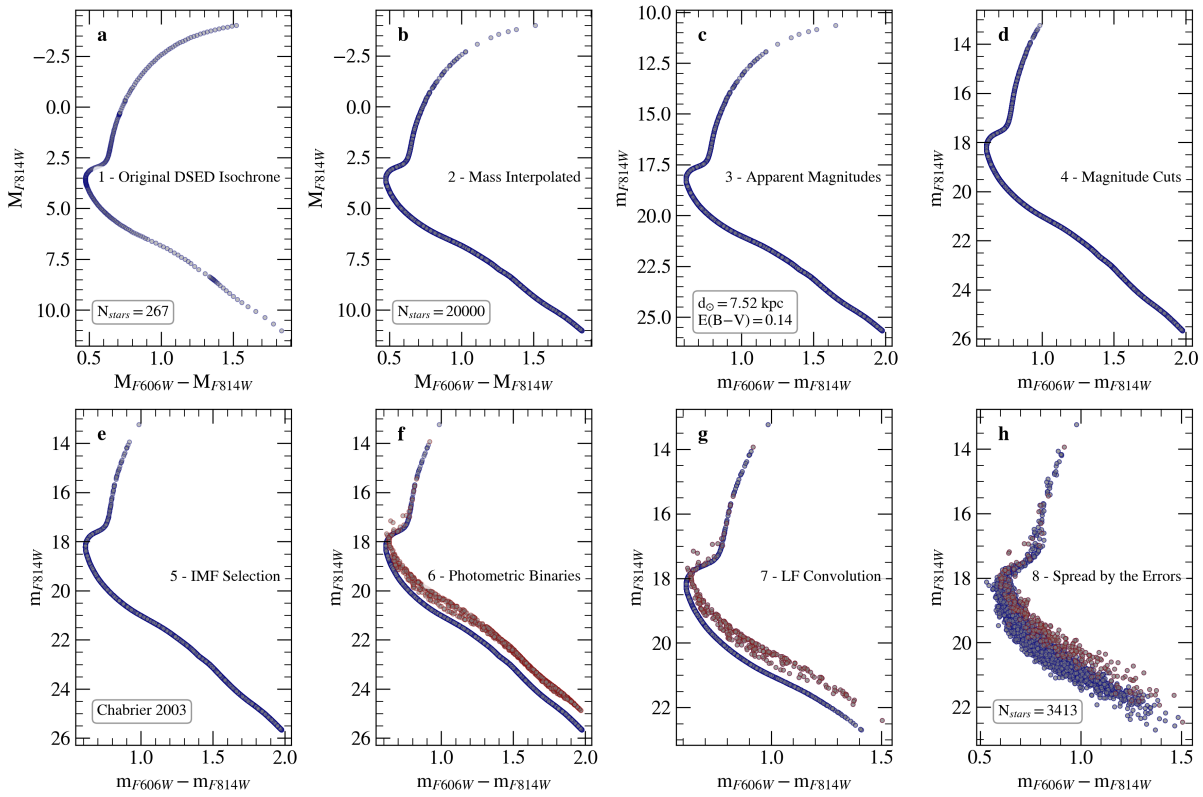

Figure 1.14: Visual explanation of the procedure to construct synthetic CMD. **a**: original DSED isochrone with age= 13 Gyr and [Fe/H]= −1.18. **b**: sample of 20,000 random mass values interpolated along the original isochrone. **c**: The panel's stars translated to apparent magnitudes, adopting a distance of 7.5 kpc and a reddening of 0.14. **d**: Selection of stars after the magnitude cut to mimic the photometric limits (in this case, HST). **e**: Selection of stars after applying the IMF. **f**: Draw photometric binaries uniformly sampled for the mass ratio between 0.6 (minimum value for observing the effect of binaries) and 1 (binaries with similar mass values). **g**: Sample of stars after the luminosity function selection. **h**: Final CMD with stellar magnitudes spread following an error function.

when they are split in the CMD. The algorithm considers each stellar population as an SSP. In the context of MPs, it is expected that the age derived using all stellar populations together is the weighted average age of each stellar population derived individually. The algorithm then fits the first stellar population[4] and applies the constraints of distance, reddening, and metallicity to the second (or subsequent) one(s). Hence, the unique free parameter among the stellar population is the age. This procedure considers that 1G stars are older than subsequent populations or they are coeval. The total likelihood $\ln \mathrm{P}(\mathrm{Model}|\mathrm{Data})$ is a linear combination of the priors and the likelihood of each generation with constrained by the likelihood of the entire CMD:

$$\ln \mathrm{P}(\mathrm{Model}|\mathrm{Data}) = \ln(\mathrm{priors}) + \sum_{i=1}^{N} \mathcal{L}(\,[\mathrm{i}]\mathrm{G}\,)_{\mathrm{all}}. \tag{1.4}$$

[4] Another possibility is to use the largest population.

where $[i]G$ is the i-th population of the cluster.

1.2.2 Chemical abundances - PFANT code

PFANT is a stellar spectral synthesis software written in Fortran and integrated into `Python` as PyFANT[5]. PFANT is a development effort of years (Spite, 1967; Barbuy, 1982; Cayrel et al., 1991; Barbuy et al., 2003; Coelho et al., 2005; Barbuy et al., 2018a) of the initial ABOND code by Monique Spite in 1967. The upper panel of Figure 1.15 shows the complete PFANT workflow indicating each sub-function, input, and output.

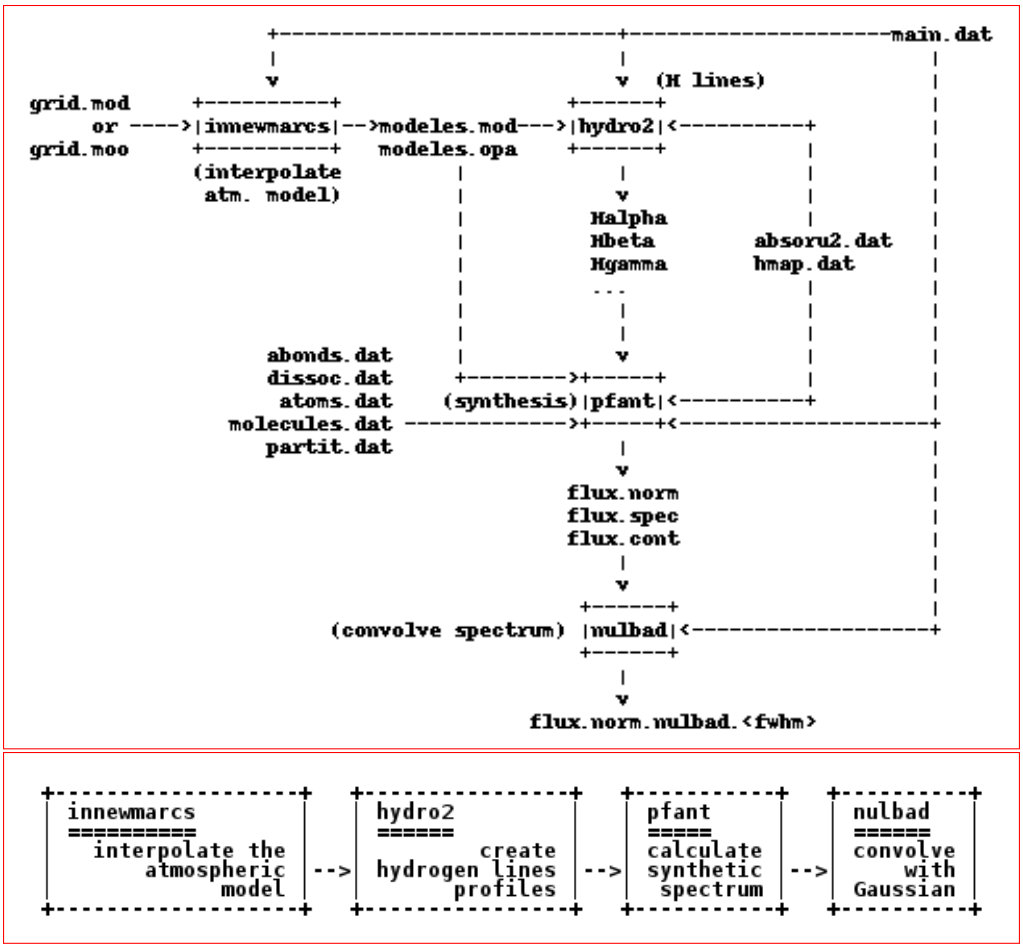

Figure 1.15: Spectral synthesis pipeline - Fortran programs (boxes) and their input/output files. CREDIT: J. Trevisan[6].

The PFANT spectral synthesis pipeline is shortly explained in the bottom panel of Figure 1.15. As the first step, PFANT interpolates (innewmarcs; Gustafsson et al., 2008) a 3D grid of atmospheric models (the file grid.mod in the upper panel of Figure 1.15 or

[5] https://trevisanj.github.io/pyfant/intro.html

[6] http://trevisanj.github.io/PFANT/reference.html

.moo for models containing opacities) to construct a new model for a given set of effective temperature, surface gravity, and metallicity contained within the limits of the grid. The inputs are specified in the main configuration file. The output is used to generate the hydrogen line profiles. After that, PFANT, a set of FORTRAN subroutines including the ABONDs (listed on the left of "pfant"instance in the full workflow, containing the input abundances), generates the synthetic spectra. The final step in the short workflow in Figure 1.15 is optional, and it convolves the synthetic spectra provided by PFANT with a Gaussian kernel.

We generate a sample of the synthetic spectra for each star with different abundances and the same atmospheric parameters. To obtain the best abundance value, we perform a chi-square minimisation algorithm that fits the different values to a spectrum region. When needed, a variation on the level of the continuum is taken into account. Figure 1.16 shows an example of the result obtained with this algorithm for the YI 6435.004Å line for a hypothetic star. The blue-shaded region represents the best-fit spectrum within 1σ, while the grey vertical stripe shows the fit region.

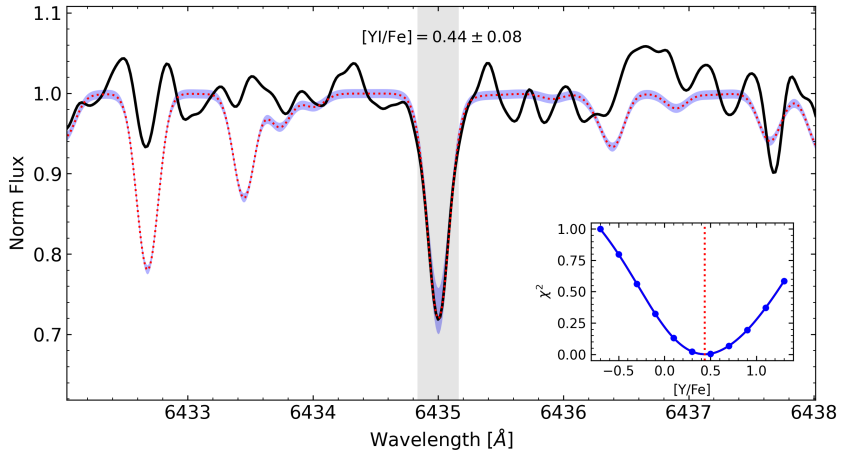

Figure 1.16: Fit to the YI 6435.004 Å line for a hypothetic star. The red dotted line is the synthetic spectrum, the blue strip represents the 1σ region, and the observed spectrum is the black solid line. The values of χ^2 are in the insert plot. The grey region represent the wavelength range to perform the fit, this region can be increased or decreased depending on the line.

1.2.3 Orbital analysis - Galactic potentials

Along this thesis, we employed three different Galactic potentials according to the need of each work in order to perform the orbit integration to obtain the orbital parameters apogalactic distance ($r_{\rm apo}$) and perigalactic distance ($r_{\rm peri}$), eccentricity (ecc =

$(r_{\rm apo} - r_{\rm peri})/(r_{\rm apo} + r_{\rm peri})$), and the maximum absolute height relative to the Galactic plane ($|Z|_{\rm max}$). In general, each Galactic potential has its numerical integrator code behind it. Therefore, the hard work for the thesis was to combine the numerical integrator with a `Python` -friendly environment responsible for deriving the errors on the orbital parameters from a Monte Carlo (MC) resampling of the initial conditions (IC) considering the errors on the observable parameters radial velocity, distance, and proper motions.

The orbital integration is crucial for analysing GCs in the context of Galactic components. Since all objects continually orbit the Galactic centre, they can pass very close to the centre and then move away tens of kpc from the centre. As a result, the current position of the GC does not completely reflect its orbital family. (Pérez-Villegas et al., 2020) derived the orbital parameters for 78 GCs and searched for substructures on different orbital parameters planes (left panels of Figure 1.17). With their classification, it is possible to calculate the probability of belonging to each Galactic component for any cluster: bulge/bar, thick disc, inner and outer halos. On the right panels of Figure 1.17 are the X-Y (top) and X-Z (bottom) projections for all GCs after classification. These panels show the importance of obtaining the classification considering the entire orbit because, for example, some GCs currently located within the bulge/bar region are actually passing by this region but belong to another component. These GCs are called intruders (e.g. Ortolani et al., 2019).

For all the cases, the Sun's position to the Galactic centre is $R_0 = 8.2$ kpc with circular velocity $V_0 = 241$ km s^{-1} (Gerhard et al., 2016). At the same time, the peculiar velocity of the Sun with respect to the local standard of rest (LSR) is adopted as $(U, V, W)_\odot = (11.1, 12.24, 7.25)$ km s^{-1} (Schönrich et al., 2010). The reference frame adopted aligned the Sun to the x-axis, which means $(x, y, z)_\odot = (8.2, 0.0, 0.02)$ kpc.

Pérez-Villegas et al. (2020).

This potential uses the Numerical Integrator of Galactic Orbits (NIGO; Rossi, 2015). Basically, this potential is composed of a exponential disc made by the superposition of three Miyamoto-Nagai potentials (Miyamoto and Nagai, 1975; Smith et al., 2015), a NFW density profile to model the dark matter halo (Navarro et al., 1997), and a triaxial Ferrers bar. For the details of each component, we refer to the original paper Pérez-Villegas et al. (2020). We also set up three values for the pattern speed of the bar: 40, 45, and 50 km

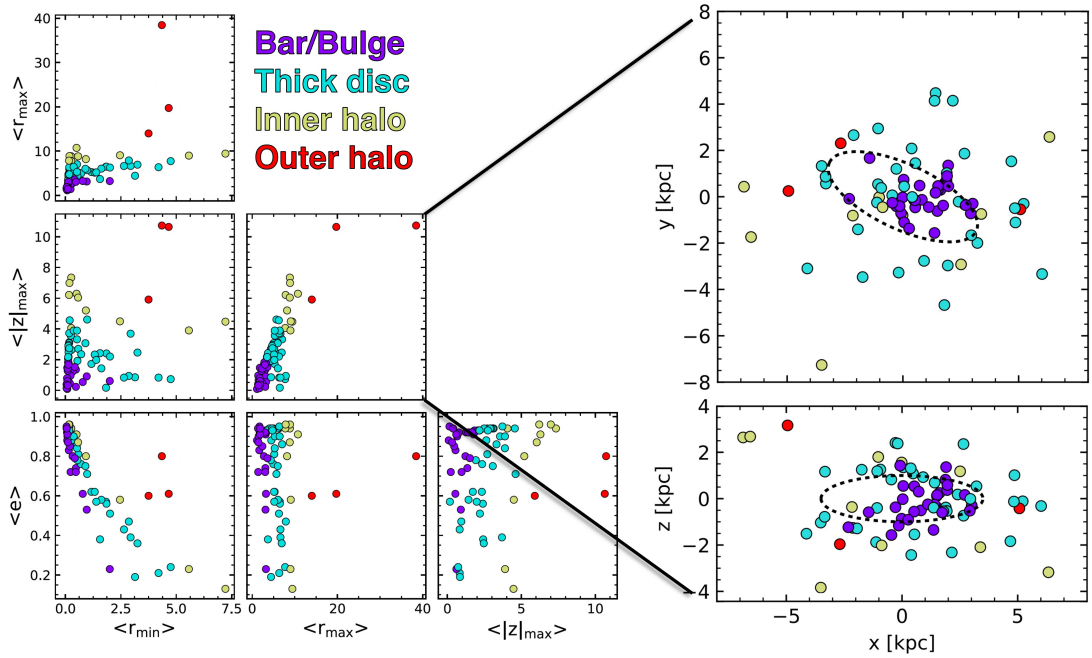

Figure 1.17: Orbital parameters are presented as functions of the median values of the perigalactic distance $< r_{\rm min} >$, the apogalctic distance $< r_{\rm max} >$, the maximum distance from the Galactic plane $< |z|_{\rm max} >$, and eccentricity $< ecc >$, for $\Omega_b = 40$ km s^{-1} kpc^{-1} (left panel). The four groups are identified asÂ bulge/bar (purple), thick disc (cyan), inner halo (green), and outer halo (red). In the right panel, the spatial distribution of the globular clusters (GCs) is shown in the x-y (top panel) and x-z (bottom panel) projections. The colours indicate the stellar component to which GCs are associated. The black dashed line shows the size of the Galactic bar. Modified from Pérez-Villegas et al. (2020)

s^{-1} kpc^{-1}.

McMillan (2017).

We used this potential with the `Python` package GalPy (Bovy, 2015) and the Action-based GAlaxy Modelling Architecture (AGAMA Vasiliev, 2019). Basically, this potential is composed of a spherical bulge (an axisymmetric approximation of Bissantz and Gerhard, 2002), two exponential stellar thick and thin discs, two components representing the H I and molecular gas discs (Dehnen and Binney, 1998), a dark matter halo (Navarro et al., 1997). For the details of each component, we refer to the original paper McMillan (2017). It is worth noting that there are no non-axisymmetric components on this potential, and it is supposed to be static, like the model used in Pérez-Villegas et al. (2020). Therefore, the total orbital energy and angular momentum perpendicular to the disc (in this case, the z-axis) are conserved along the entire orbits. This is the advantage of this potential. However, it has to be used carefully since the description of the inner Galaxy (interest of

the thesis) is not accurate.

Portail et al. (2017).

This potential possesses the most accurate description of the inner Galaxy. Firstly created by Portail et al. (2017), this model was adapted to be used in combination with AGAMA through an analytical approximation by Sormani et al. (2022). Now, the model was improved by Hunter et al. (2024) including more information about the inner Galaxy. The model is composed of the black hole (as a Plummer sphere Plummer, 1911), the MW nuclear star cluster (Dehnen, 1993), the nuclear stellar disc, the Galactic bars (the bar and the long bar Portail et al., 2017), the disc, and the dark matter halo using an Einasto (1969) model. For the details of each component, we refer to the original paper by Hunter et al. (2024).

1.3 Objectives and layout of the thesis

The goal of this thesis is to understand the connection between the evolution of GCs and the formation of the Galaxy itself. Which GCs have formed in-situ? Where and when were formed the early bulge clusters? Can we recover the building blocks using GCs? How old is the Galactic Bulge? Is there observational evidence for the contribution of GCs in the bar formation in terms of stellar population? In a more general view, we also studied the formation of stellar clusters to comprehend the mechanisms that lead to the multiple stellar population phenomenon observed in old clusters. How does the multiple stellar population phenomenon manifest? Is there an age difference among the different stellar populations? Is there a more probable formation scenario, or can it be a combination of different scenarios?

Another specific aim of the thesis is to develop the three areas of photometry, chemistry, and dynamics together. This objective has been successfully achieved and reflected in my publication list (see the complete list in Appendix A). The spectroscopic work was carried out using FLAMES-UVES and APOGEE. Besides the main work of Palomar 6 (Souza et al., 2021), NGC 6355 (Souza et al., 2023), and SOS1 (Souza et al. submitted), I contributed to another 19 papers including the following studies: Fernández-Trincado et al. (2020), Fernández-Trincado et al. (2021), Barbuy et al. (2021a), Romero-Colmenares

et al. (2021), Barbuy et al. (2021), Limberg et al. (2022), Razera et al. (2022), and Barbuy et al. (2023). For the dynamical side, we developed techniques to integrate the GC orbits and how to classify them in terms of the Galactic components and the GC evaporation in dwarf galaxies. The contributions were in the following studies: Pérez-Villegas et al. (2020), Razera et al. (2022), Barbuy et al. (2023), and Moreno-Hilario et al. (2024).

From the extra-galactic point of view, I have been involved in the VISCACHA Survey. VISCACHA (VIsible Soar photometry of star Clusters in tApii and Coxi HuguA; Maia et al., 2019, ; PI: B. Dias) is a photometric survey dedicated to observing star clusters in the Small and Large Magellanic Clouds (SMC and LMC) using the SOuthern Astrophysical Research (SOAR) telescope together with the SOAR Adaptive Module Imager. Inside VISCACHA, besides the work on the eMSTO in star clusters of the Magellanic Clouds (MCs), I have been involved in the determination of the fundamental parameters for the star clusters in specific studies where `SIRIUS` code was employed: Maia et al. (2019), Dias et al. (2021), Dias et al. (2022), Bica et al. (2022), Oliveira et al. (2023), and Parisi et al. (2024).

The thesis comprises six papers, of which I am the first author, being three already published and three submitted. The thesis also includes one Chapter containing all the important contributions to the age determination for GCs using different photometric systems. I was not the first author of these papers, but my contribution was crucial to the final results. The chapters essentially reproduce the papers as Chapters 2 to 8. Chapter 6 consists of discussions of chapters from 2 to 5. Finally, the thesis is divided into two parts:

Part I: Looking for the Galactic bulge/bar formation and evolution relic fossils.

In this part, we performed a comprehensive analysis of individual Globular Clusters. The difficulty of these studies is that all the clusters are towards the Galactic centre, having, therefore, substantial gas, dust, and stars in between the cluster and the observer and a huge amount of bulge field stars behind the cluster, contaminating its photometry.

- Chapter 2 reproduces almost integrally the paper *Photo-chemo-dynamical analysis and the origin of the bulge globular cluster Palomar 6* (Souza et al., 2021), where we analysed the GC Palomar 6 in terms of age, chemistry, and dynamics to provide insights of its origin regarding the progenitors of the Galaxy. We used data from

ESO FLAMES-UVES high-resolution spectrograph, HST photometry, and the state-of-the-art Galactic mass models.

- Chapter 3 contains the paper *Chrono-chemodynamical analysis of the globular cluster NGC 6355: Looking for the fundamental bricks of the Bulge* (Souza et al., 2023). In this paper, we present in more detail the chrono-chemo-dynamical approach we developed during this thesis. NGC6355 was previously classified as coming from the main bulge progenitor, we, however, show some arguments against this previous classification.

- Chapter 4 presents integrally the paper we submitted to Nature with some modifications due to the journal copyright rules. The modifications include the title and figures. The motivation for this paper comes from the analysis of a sample of stars observed by the Kepler satellite in the program K2. This paper results from my period at the *Leibniz-Institüt für Astrophysik Potsdam (AIP)* working with Dr. Marica Valentini. In this work, we found observation evidence for the contribution of Globular Clusters' evaporation for the Galactic bar formation and evolution, and also the observation constraints to the theory about the Globular Cluster Terzan 5.

- Chapter 5 includes the collection of papers whose results constitute part of this thesis but were not integrally performed by me. In this Chapter, we present the age determination of the NGC6558 age. This result was submitted to A&A titled as *GSAOI/Gemini and ACS/HST photometry of the globular cluster NGC 6558: A steep age-metallicity relation of the metal-poor bulge.*

- Chapter 6 compose the discussion on the results collected in the previous Chapters 2 to 5.

Part II: Supplementary studies – What drives the origin of multiple stellar populations in star clusters?

In this part, we studied the stellar populations within star clusters. The primary aim of this part is to understand how the multiple stellar populations in star clusters originate and evolve into the present phenomenon we observe today. To perform this analysis, we

compared the present phenomenon with the eMSTO observed in intermediate-age star clusters of the MCs within the VISCACHA collaboration.

- Chapter 7 reproduces integrally the scientific case of the paper *Self-consistent Analysis of Stellar Clusters: An Application to HST Data of the Halo Globular Cluster NGC 6752* (Souza et al., 2020), where we analysed the multiple stellar populations of the GC NGC6752 looking for a possible age difference among them. The motivation for this paper primarily came from the necessity of presenting the `SIRIUS` code to the community, but also an experiment to be incorporated within the collaboration *HST UV Legacy Survey for Galactic Globular Clusters*.

- Chapter 8 represents the paper *The VISCACHA Survey: The eMSTO for low mass star clusters* submitted to A&A and is under review. This paper aims to analyse the low mass regime ($\log Mass < 4.3$) for star clusters of the MCs. We are motivated by the lack of analysis of this mass regime in the literature because HST studies comprise only relatively high mass clusters.

Finally, Chapter 9 provides the conclusions of the thesis and presents the perspectives for future research.

Part I

Looking for the relic fossils of the Galactic bulge/bar formation and evolution.

Chapter 2

Palomar 6, an authentic bulge globular cluster

This chapter presents the description of the globular cluster Palomar 6, published in Souza et al. (2021).[1]

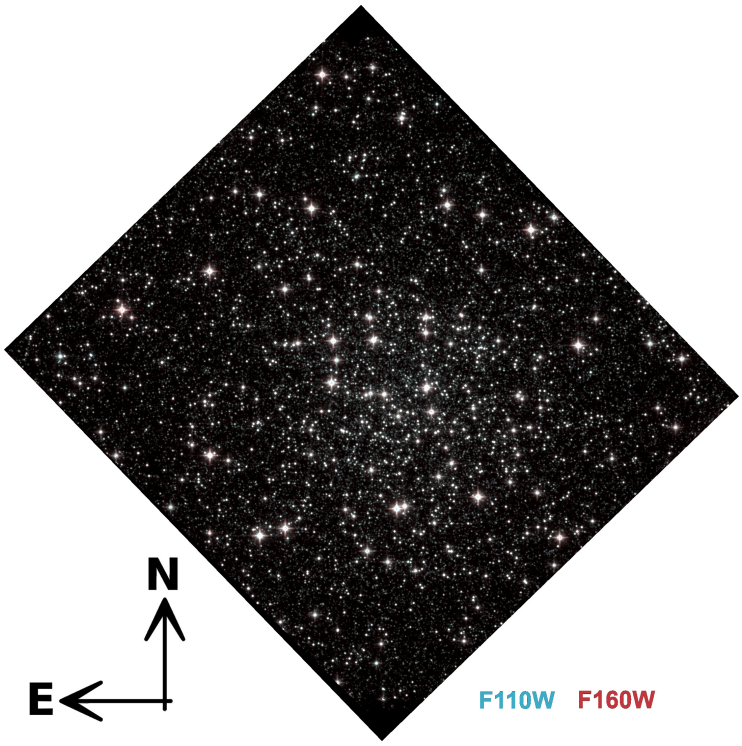

Figure 2.1: F110W/F160W combined colour image from HST for Pal 6.

[1] https://ui.adsabs.harvard.edu/abs/2021A%26A...656A..78S/abstract

2.1 Introduction

Palomar 6 (Pal 6) is a GC projected towards the Galactic bulge ($l = 2.10°$ and $b = 1.78°$), located in a highly-extincted region with $A_V > 4.3$ (Harris, 1996, 2010 edition)[2]. Despite that, the information about Pal 6 is conflicting, preventing further analysis, particularly concerning its distance and, consequently, the Galactic component to which Pal 6 should belong. Pal 6 has been considered to belong to the Galactic bulge due to its current position (Ortolani et al., 1995; Bica et al., 2016). In Lee et al. (2004) suggested that, based on its chemical and kinematic determinations, Pal 6 should belong to an internal component related to a contribution of the halo (inner halo). Pérez-Villegas et al. (2020) discussed the case of Pal 6 using a distance of $d_\odot = 5.8$ kpc (Baumgardt et al., 2019), and for their dynamical orbital analysis, they classified the cluster as a thick disc member. This result is opposite to Ortolani et al. (1995), who found a distance of $d_\odot = 8.9$ kpc placing Pal 6 in the Galactic bulge. Recently, Massari et al. (2019) presented a classification of clusters in terms of their plausible progenitors, indicating whether a cluster originates in a well-defined component of the Galaxy or if it came from one of the merger processes that occurred in the history of the Galaxy, besides other possibilities. They again indicated Pal 6 as an associated Low-Energy cluster based on the distance estimated by Baumgardt et al. (2019).

The controversy on which Galactic component Pal 6 is part is also due to an uncertain metallicity. The first Pal 6's metallicity estimation by Malkan (1981) from a reddening-free index resulted in [Fe/H]~ -1.30. Ortolani et al. (1995), from the V vs $V-I$ CMD based on data observed at the ESO NTT-EMMI, found [Fe/H] ~ -0.40 by the slope of the red giant-branch (RGB) and the presence of a red-horizontal-branch (RHB). Lee and Carney (2002) obtained [Fe/H] $= -1.22 \pm 0.18$ analysing the slope of the RGB on the near-infrared (NIR) CMD with NICMOS3 JHK bands. Spectroscopic analysis from the same authors using high-resolution NIR spectra of three RGB stars resulted in [Fe/H]$= -1.08 \pm 0.06$. Finally, a metallicity of [Fe/H]$= -1.0 \pm 0.1$ was confirmed by Lee et al. (2004) from a high-resolution spectroscopic analysis of five probable member stars observed with the CSHELL spectrograph at the NASA Infrared Telescope Facility.

[2] http://physwww.mcmaster.ca/ harris/mwgc.dat

2.2 Observations and data reduction

The UVES spectra were obtained using the FLAMES-UVES setup centred at 580 nm in the ESO Program 0103.D-0828 (A) (PI: M. Valentini). The ESO program was coordinated with the program GO11126 (PI: M. Valentini) for the Campaign 11 of the K2 satellite (K2 is the repurposed *Kepler* mission; Howell et al., 2014): the goal was to obtain asteroseismology for the giants in the proposed GCs. K2 observed four giants in Pal 6, but their UVES spectra were not collected due to clouds and strong winds that affected ESO observations. UVES spectra have a coverage ranging from 480 nm to 680 nm. Six giant stars of Pal 6 were observed, and the log of observations is given in Table 2.1. The JHK_S-combined image of Pal 6 is shown in Figure 1, obtained from the Vista Variables in the Via Lactea (VVV) survey (Saito et al., 2012).

The data were reduced using the ESO-Reflex software with UVES-Fibre pipeline (Ballester et al., 2000; Modigliani et al., 2004). After reduction, we have six spectra for each star. The corresponding spectra of each star were corrected by the radial velocity. To compute the radial velocities and the barycentric corrections, we used the python library `PyAstronomy` cross-correlating the spectra with the Arcturus spectrum (Hinkle et al., 2000).

The values of the heliocentric radial velocity of each spectrum and their mean are presented in Table 2.2. From these values, we calculate a mean heliocentric radial velocity for Pal 6 of 174.3 ± 1.6 km s^{-1}, excluding the stars `ID730` and `ID030` for which the radial velocities are very discrepant as compared with the other stars. Our mean radial velocity determination agrees with the recent value of 176.3 ± 1.5 km s^{-1} given by Baumgardt et al. (2019). Finally, each spectrum is normalised and combined through the median flux to get the final stellar spectrum.

For the photometric analysis, we used the HST data collected during the GO-14074 (PI: Cohen, Cohen et al., 2018) in F110W/F160W (WFC3/IR) and F606W (ACS/WFC) (first panel of Figure 2.2). Data were reduced using the pipeline described in Nardiello et al. (2018). We also followed their recipe (based on the quality-of-fit and photometric error parameters) to select well-measured stars and reject poor photometric measurements. Additionally, we selected the stars within a radius of 300 pixels from the cluster centre that is equivalent to a core radius (~ 0.66 arcmin; Harris, 1996, 2010). The cleaned CMD

is shown in the second panel of Figure 2.2, which contains the final selected stars.

Another critical effect in the photometric data is the differential reddening. Mainly for the clusters with a high reddening value, differential reddening increases the spread on the CMD. This is the case of Pal 6, which has an extinction of $A_V > 4$. We perform a reddening correction with a method similar to that described in Milone et al. (2012). The third panel of Figure 2.2 presents the final CMD after the reddening correction is applied, and the map of differential reddening is on the last panel of Figure 2.2. The contamination by field stars, combined with the high extincted region, results in low values of differential reddening. However, we obtained a more clear main sequence (MS) turn-off (TO) and sub-giant-branch (SGB) structures for the Pal 6 CMD.

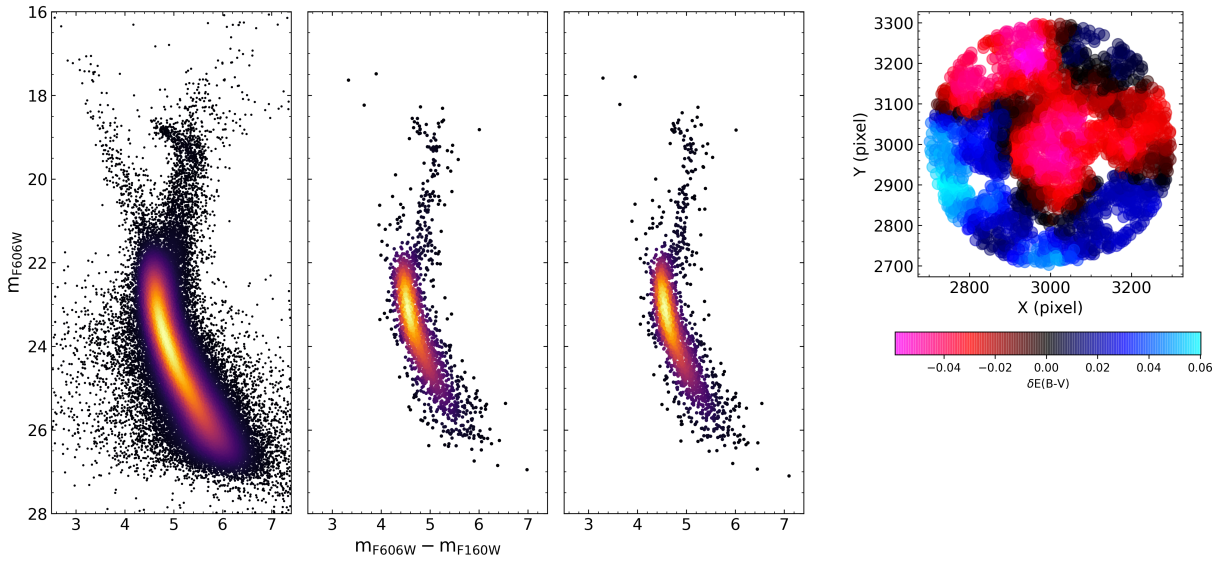

Figure 2.2: Procedure to obtain the photometry of Pal 6. First panel: HST photometry from Cohen et al. (2018). Second panel: Stars selected by the quality method within a ~ 0.66 arcmin radius from the cluster centre. Third panel: Differential reddening corrected CMD. Last panel: Differential reddening map.

We perform a membership analysis to determine which stars observed spectroscopically are members of Pal 6. We selected the Gaia Early Data Release 3 (EDR3; Gaia Collaboration et al., 2022) stars within $10'$ from the cluster centre (top-left panel of Figure 2.3). For the proper-motion distribution presented in the bottom-left panel of Figure 2.3, we applied the Gaussian Mixture Models (GMM; Pedregosa et al., 2011) clustering method to separate the cluster members from the field stars. The derived mean proper-motion for Pal 6 is $< \mu_\alpha^* >= -9.19 \pm 0.06$ mas yr^{-1} and $< \mu_\delta >= -5.30 \pm 0.05$ mas yr^{-1}, in excellent agreement with the new values computed by Vasiliev and Baumgardt (2021).

The membership probabilities are computed considering (both cluster and field distri-

butions, derived using GMM. See Bellini et al. (2009) for the mathematical description of the membership distribution. Once we have the membership probability, we cross-matched our sample stars with the Gaia data (Table 2.3), indicated as green stars in Figure 2.3. We found that two stars of our sample have zero membership probability (non-members), and four stars have probabilities above 80%. The non-member stars are the same with discrepant radial velocities (ID730 and ID030).

Table 2.1 - Log of the spectroscopic FLAMES-UVES observations of program 0103.D-0828 (A), carried out in 2019. The quoted seeing and airmass are the mean values along the exposures. In the last column is given the corresponding GIRAFFE setup, in which additional stars were observed

Date	UT	exp (s)	Airmass	Seeing (″)	GIRAFFE
Program 0103.D-0828 (A)					
2019-06-24	23:44:40	2400	1.810	0.87″	H13-1
2019-06-25	01:30:48	2400	1.190	0.85″	H13-3
2019-06-25	02:31:52	2700	1.057	0.95″	H14-1
2019-06-25	03:20:48	2700	1.012	0.91″	H14-2
2019-06-25	05:35:43	2700	1.097	0.93″	H14-3
2019-06-25	06:24:35	2700	1.223	0.93″	H14-4

2.3 Atmospheric Stellar Paramaters

The photometric effective temperature ($T_{\rm eff}$) and surface gravity ($\log g$) are derived from the $VIJHK_S$ magnitudes given in Table 2.4. For comparison purposes, we also obtained the effective temperature from the Transiting Exoplanet Survey Satellite (TESS) input catalogue (TIC; Stassun et al., 2018) for 5 of our six observed stars. We collected the 2MASS J, H, and K_S magnitudes from Skrutskie et al. (2006) and the VVV survey (Saito et al., 2012). Finally, according to Alonso et al. (1999), the colour $V-I$ is the best colour index to derive the effective temperature of giant stars. To get the $V-I$ colour for our sample, we employed the photometric systems relationships $G-V=f(G_{BP}-G_{RP})$ and $G-I=f(G_{BP}-G_{RP})$ from Gaia EDR3 (Riello et al., 2021).

Table 2.2 - Radial velocity obtained for each extracted spectra and the average value for each star.

Target	V_r^{hel} km s^{-1}	σ_{V_r} km s^{-1}	Target	V_r^{hel} km s^{-1}	σ_{V_r} km s^{-1}
730_1	−87.83	6.12	243_1	+172.80	6.06
730_2	−87.79	6.10	243_2	+172.34	6.38
730_3	−87.61	5.84	243_3	+172.50	6.18
730_4	−86.73	6.05	243_4	+172.85	5.87
730_5	−86.56	5.87	243_5	+172.84	6.00
730_6	−87.43	6.02	243_6	+173.02	6.54
730	**−87.33**	**2.65**	**243**	**172.73**	**2.61**
030_1	−62.94	6.34	785_1	+175.41	8.79
030_2	+14.63	9.36	785_2	+175.72	7.77
030_3	−32.31	9.82	785_3	+174.17	5.56
030_4	−56.20	6.81	785_4	+174.01	6.58
030_5	+14.36	8.82	785_5	+175.50	7.20
030_6	+14.86	12.0	785_6	+174.69	7.80
030	**−12.36**	**17.44**	**785**	**174.99**	**3.25**
145_1	+179.81	7.07	401_1	+170.16	6.12
145_2	+178.59	7.39	401_2	+170.82	7.13
145_3	+178.38	6.27	401_3	+169.62	6.82
145_4	+178.33	5.67	401_4	+168.72	6.18
145_5	+179.65	6.51	401_5	+170.87	6.06
145_6	+179.23	7.27	401_6	+171.00	6.34
145	**179.02**	**2.98**	**401**	**170.21**	**2.96**

Effective temperatures

Effective temperatures $T_{\rm eff}$ were derived from $V-I$, $V-K$, and $J-K$ using the colour-temperature calibrations from Casagrande et al. (2010). The VVV JHK colours were transformed into the 2MASS JHK_S system, using relations given by Soto et al. (2013). For Pal 6 the distance modulus of $(m-{\rm M})_0 = 13.87$, extinction ${\rm A}_V = 4.53$, and metallicity [Fe/H]$= -0.91$ were used (Harris, 1996, 2010 edition) to perform the reddening correction of the colours. Table 2.5 lists the derived photometric effective temperatures. The $< T_{\rm eff} >$ is the mean effective temperature considering only values below 5000 K.

Table 2.3 - Gaia EDR3 information about the observed stars; the last column shows the membership probabilities.

ID	$^{\dagger}\mu^*_\alpha$ (mas/yr)	μ_δ (mas/yr)	G (mag)	G_{RP} (mag)	$\mathcal{P}_{\rm memb}$ (%)
730	-6.18 ± 0.10	-2.61 ± 0.06	17.187	15.873	0
243	-9.32 ± 0.07	-5.37 ± 0.04	15.859	14.493	100
30	$+0.04 \pm 0.10$	-2.11 ± 0.06	16.913	15.820	0
785	-9.26 ± 0.14	-5.12 ± 0.08	17.598	15.997	97
145	-9.49 ± 0.12	-5.58 ± 0.07	17.141	15.788	93
401	-9.33 ± 0.08	-4.92 ± 0.05	16.430	15.056	83

$^{\dagger}\mu^*_\alpha = \mu_\alpha \cos\delta$.

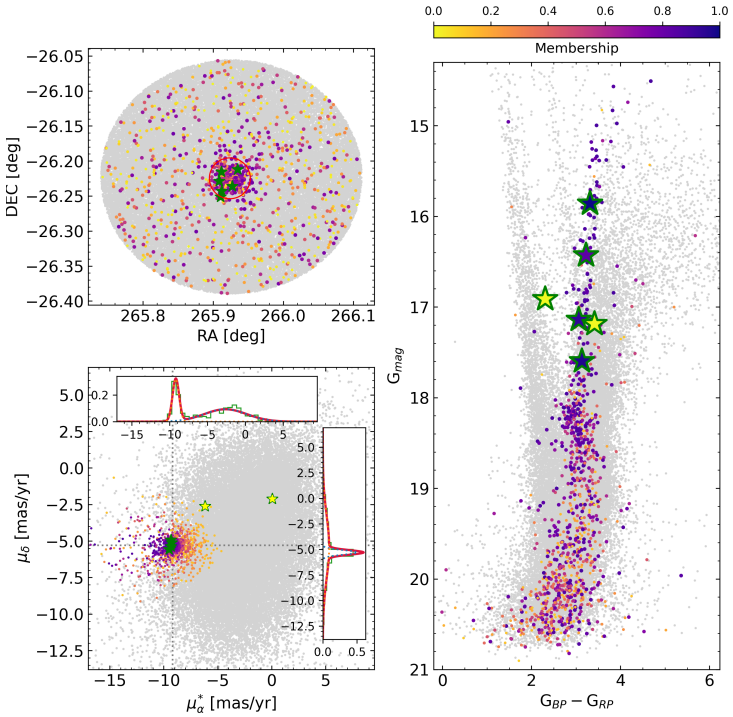

Figure 2.3: Proper motion analysis to obtain the cluster members. Top left panel: Sky distribution of stars within ten arcmins from the cluster centre. Left bottom panel: Vector point diagram with the cluster (colourful dots) and field (grey dots) stars, the green star symbols are the observed stars with FLAMES-UVES, and the insert plots show the density distributions found using GMM. Right panel: Gaia EDR3 G vs. $G_{BP} - G_{RP}$ CMD, the green stars symbols are the observed stars. From the left bottom and right panel, we can identify that two observed stars have zero membership probability **(yellow stars symbol)**.

Surface Gravities

To derive the photometric surface gravities $\log g$, we used the ratio $\log(g_*/g_\odot)$ where $\log g_\odot = 4.44$:

$$\log g_* = 4.44 + 4 \log \frac{T_{\rm eff}*}{T_\odot} + 0.4(M_{\rm bol} - M_{\rm bol\odot}) + \log \frac{M_*}{M_\odot}. \quad (2.1)$$

Table 2.4 - Identifications, coordinates, and magnitudes. JHK_s from both 2MASS and VVV surveys are given.

ID	ID	RA	DEC	K_P	V	$V-I$	J	H	K_S	J	H	K
	2MASS	(hh:mm:ss)	(dd:mm:ss)				2MASS			VVV		
730†	174338762612551	17 : 43 : 38.75	−26 : 12 : 55.2	16.05	18.29	3.22	13.43	12.23	11.83	13.22	12.21	11.82
243	174342502614101	17 : 43 : 42.51	−26 : 14 : 10.2	14.75	16.91	3.12	11.86	10.66	10.25	11.95	11.32	10.73
30†	174338622615013	17 : 43 : 38.47	−26 : 15 : 04.8	15.82	17.62	2.19	13.58	12.46	11.93	14.02	13.53	13.26
785	174344402612418	17 : 43 : 44.38	−26 : 12 : 42.5	16.44	18.56	2.94	13.35	12.36	11.87	13.65	12.77	12.37
145	174338892614359	17 : 43 : 38.86	−26 : 14 : 34.7	15.98	18.07	2.87	12.76	11.61	11.51	13.28	12.27	11.98
401	174338062613426	17 : 43 : 38.05	−26 : 13 : 42.7	15.28	17.43	3.03	12.55	11.46	11.08	12.52	11.45	11.23

† Stars are classified as non-members based on proper motion and radial velocities.

Table 2.5 - Atmospheric parameters derived from photometry using calibrations by Casagrande et al. (2010) for $V-I$, $V-K$, $J-K$ and spectroscopic analysis of Fe lines.

		Photometric parameters										Spectroscopic parameters					
			2MASS			VVV											
ID	T_{TESS} (K)	$T_{(V-I)}$ (K)	$T_{(V-K)}$ (K)	$T_{(J-K)}$ (K)	$T_{(V-K)}$ (K)	$T_{(J-K)}$ (K)	$<T_{eff}>$ (K)	BC_V	M_{bol}	$\log g$	T_{eff} (K)	$\log g$	[FeI/H]	[FeII/H]	[Fe/H]	v_t (km s^{-1})
730	3973	4267	4764	4240	4742	4534	4535	−0.721	−0.89	1.67	4857	1.40	−1.09	−1.10	−1.10	2.5
243	4323	4385	4592	4212	5024	5304	4385	−0.623	−2.18	1.09	4350	0.80	−0.93	−0.91	−0.92	1.0
30	5058	7610	5632	4103	8780	8095	4103	−0.093	−0.94	1.48	4800	1.50	−1.65	−1.61	−1.63	2.3
785	–	4659	4568	4601	5013	4985	4630	−0.446	−0.35	1.92	4860	2.40	−1.21	−1.20	−1.21	2.0
145	4865	4790	4676	5455	5120	4871	4790	−0.380	−0.77	1.81	4800	1.90	−1.31	−1.26	−1.28	2.5
401	4387	4511	4866	4634	5002	4888	4750	−0.534	−1.57	1.48	4500	1.50	−1.00	−0.99	−1.00	1.0

We adopted the values of $< T_{\rm eff} >$ from Table 2.5, $M_* = 0.85 M_\odot$, and $M_{\rm bol\odot} = 4.75$.

The derived values of the photometric $T_{\rm eff}$ and $\log g$ are given in the left columns of Table 2.5.

2.4 Abundance Analysis

We carried out a detailed abundance analysis using ionisation and excitation equilibrium to derive stellar parameters and line-by-line spectrum synthesis for the derivation abundance ratios.

2.4.1 Spectroscopic Stellar Parameters

To determine the final stellar parameters T_{eff}, log g, metallicity [Fe/H], and microturbulence velocity v_t of Pal 6, we measured the equivalent width (EW) for a list of FeI and FeII lines using DAOSPEC (Stetson and Pancino, 2008). To evaluate the impact of blending lines, we remeasured some lines with IRAF, mainly for FeII.

In the line list of Table B.1 are also given the adopted oscillator strengths ($\log gf$) for FeI lines obtained from VALD3 and NIST 3 databases (Piskunov et al., 1995; Martín et al., 2002), and for FeII lines from Meléndez and Barbuy (2009).

Using the MARCS grid of atmospheric models (Gustafsson et al., 2008), we extracted the 1D photospheric models for our sample. These CN-mild models consider $[\alpha/Fe] = +0.20$ for $[Fe/H] = -0.50$ while $[\alpha/Fe] = +0.40$ for $[Fe/H] \leq -1.00$. We adopted $\epsilon(Fe) = 7.50$ (Grevesse and Sauval, 1998) for the solar Fe abundance.

Adopting the mean photometric $<T_{eff}>$ and $\log g$ calculated in Section 2.3 as initial guesses, we derived the spectroscopic parameters. Through an iterative method, we obtained the excitation and ionisation equilibrium. The excitation equilibrium means a constant distribution of FeI vs χ_{exc} and is obtained iterating the value of T_{eff}. The similar values of [FeI/H] and [FeII/H] indicate that the ionisation equilibrium is reached by iterating in $\log g$. Finally, the microturbulence velocity v_t is obtained by imposing a constant distribution of FeI abundance vs. EW. Figure 2.4 shows the excitation and ionisation equilibrium for the four-member stars.

The derived spectroscopic parameters T_{eff}, $\log g$, [FeI/H], [FeII/H], [Fe/H], and v_t are presented in the right columns of Table 2.5. Based on the four-member stars, our metallicity determination is $[Fe/H] = -1.10 \pm 0.09$ dex. This metallicty is in excellent agreement with Lee and Carney (2002) and Lee et al. (2004) spectroscopic determinations, of $[Fe/H] = -1.08 \pm 0.06$ and -1.0 ± 0.1, respectively.

2.4.2 Spectrum Synthesis

We derived the abundance ratios for the elements C, N, O, Na, Mg, Al, Si, Ca, Ti, Zr, Ba, La, and Eu. We employed the PFANT code described in Barbuy et al. (2018a) for the spectrum synthesis. The basic atomic line list is from VALD3 (Ryabchikova et al., 2015). The solar abundances A(X) were taken from Grevesse et al. (2015).

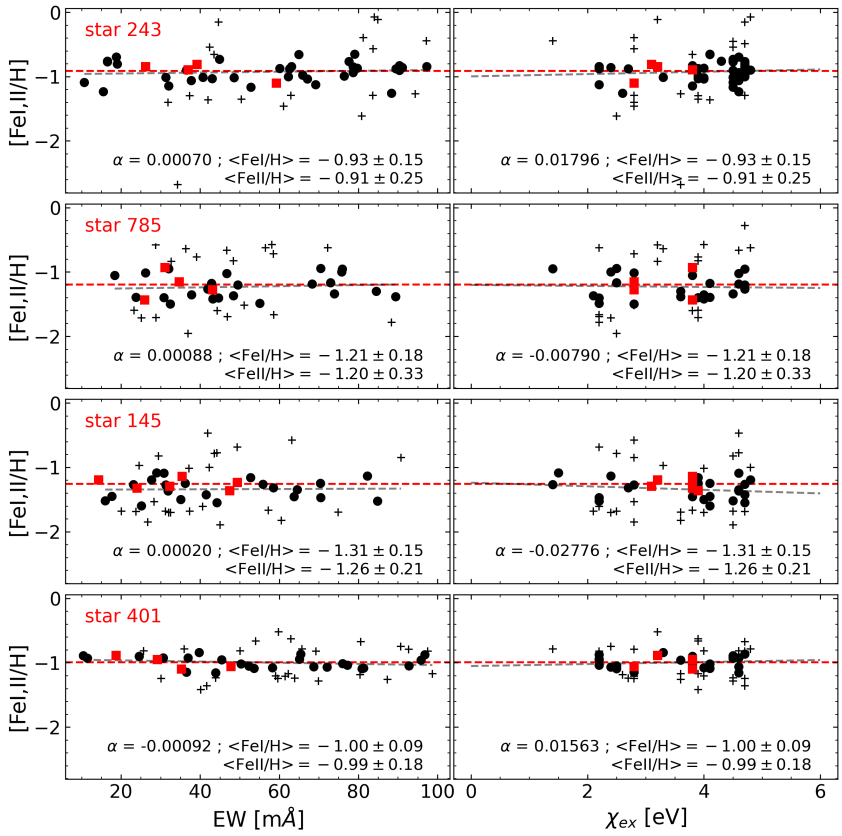

Figure 2.4: Excitation and ionisation equilibria of FeI and FeII lines for the four-member stars. The black dots are the values considered to compute the metallicity of FeI lines after a sigma-clipping of 1σ. The crosses are the omitted values. The red squares are the values of FeII lines. The α values show the slope of the trends of FeI lines.

The CNO abundances are listed in Table 2.6, as detailed below. For the odd-Z, α, and heavy elements, we used the line list from Barbuy et al. (2016). In Table B.2, we give the line-by-line abundances ratios of the odd-Z elements Na, Al, the α-elements Mg, Si, Ca, and Ti, neutron-capture dominant s-elements Y, Zr, La, Ba, and the r-element Eu. We do not measure Sr lines because they are faint in the observed spectra. The mean values for each star and the cluster mean (considering only the mean of the member stars) are given in Table 2.7.

CNO abundances

To measure the CNO abundances, we perform an iterative fitting of C, N, and O abundances. We use the extended $C_2(1,0)$ Swan molecular bandhead at 5635.3Å for the C abundance. We considered the average fit of the region (left panel Figure 2.5) and assumed the abundances as upper limits. For the oxygen (Figure 2.5) forbidden line at [OI]

6300.31Å , a selection among the original spectra where telluric lines did not contaminate the line was needed since most of the observations were contaminated, showing that these spectra seem to have been observed at too high airmasses. A few spectra showing a clean [OI] 6300.31Å line could be retrieved, and the oxygen abundance could be derived. The nitrogen abundance is derived from the CN(5,1) at 6332.2Å and CN(6,2) at 6478.48Å of the $A^2\Pi X^2\Sigma$ system bandheads (Figure 2.5). The derived abundances are listed in Table 2.6.

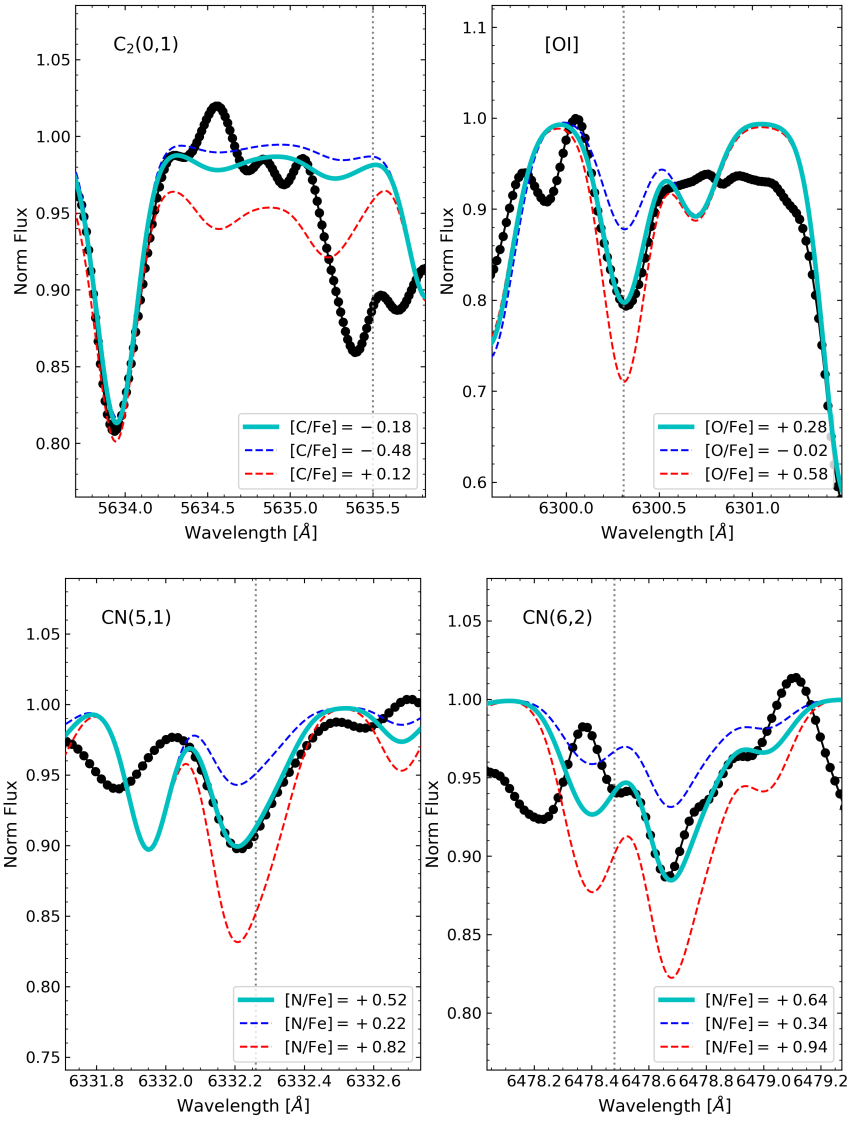

Figure 2.5: Example for star 243 line fit of the bandhead $C_2(0,1)$ (upper left), [OI] (upper right), N from CN(5,1) (bottom left), and CN(6,2) (bottom right). The solid cyan line is the best-fit abundance ratio, while the dotted lines are considering [X/Fe]=$[X/Fe]_{best} \pm 0.20$ (red, plus - blue, minus).

Table 2.6 - Carbon, nitrogen, and oxygen abundances [X/Fe] from C_2, CN bandheads, and [OI], respectively.

	[C/Fe]	[N/Fe]		[O/Fe]
Star	C_2	CN(5,1)	CN(6,2)	[OI]
	5635.50 Å	6332.26 Å	6478.60Å	6300.31 Å
730	$\leq +0.04$	—	+0.98	+0.37
243	≤ -0.18	+0.52	+0.64	+0.28
030	$\leq +0.00$	+0.82	+0.77	+0.16
785	$\leq +0.10$	+0.34	—	+0.38
145	$\leq +0.05$	+0.62	—	+0.42
401	≤ -0.12	+0.90	+0.74	+0.45

Odd-Z Elements

We derived the sodium abundances using three NaI lines, one in the blue arm at 5682.633Å . The blue-arm spectrum has a lower SNR than the red-arm one. Due to the lower SNR values in all stars, these lines show a higher noise. For this reason, the abundance ratios were derived essentially from the lines in the red arm, 6154.23Å and 6160.753Å . The aluminium abundances were derived from lines at 6696.185Å and 6698.673Å .

α-elements

The fast early enrichment of the proto-cluster gas by supernovae type II (SNII) can be seen through the abundances of α-elements O, Mg, Ca, Si, and Eu produced through the rapid neutron capture process. We obtained a consistent enrichment for all α-elements with a mean value of [α/Fe]= +0.35 with a dispersion of 0.06.

Figure 2.6 shows the line profile fitting of the MgI 6318.720Å, SiI 6142.494Å, CaI 5867.562Å, and TiI 6336.113Å for the member star 243. The cyan line represents the best fit. We also show the lines considering a variation of 0.20 dex plus (red) and minus (blue) concerning the best abundance.

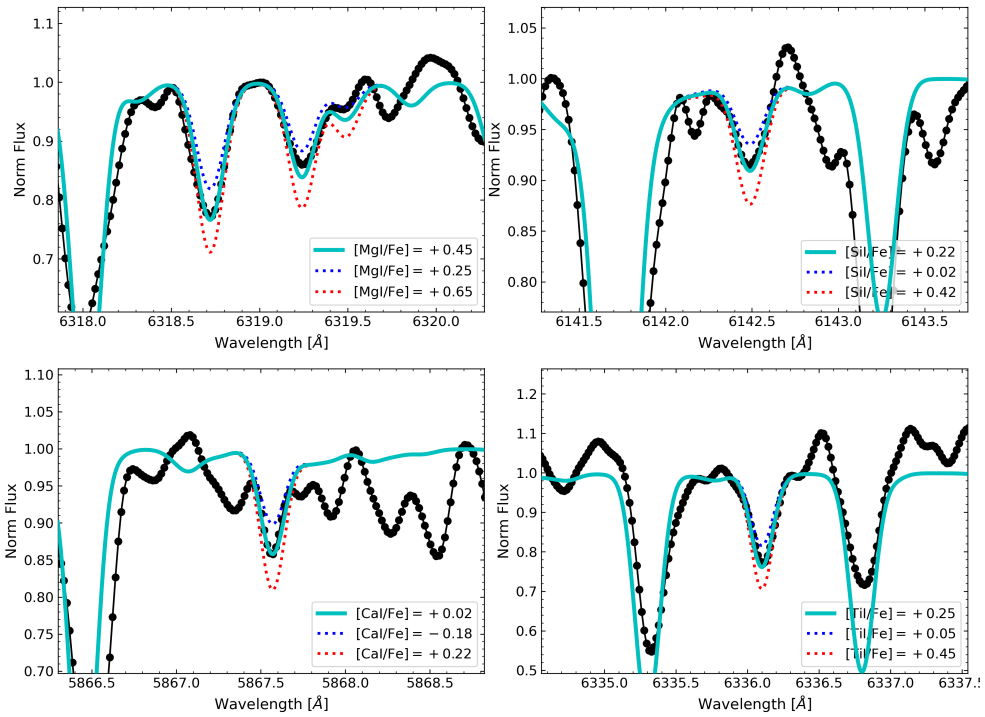

Figure 2.6: Same as Figure 2.5 for $\alpha-$elements Mg (top left), Si (top right), Ca (bottom left), and Ti (bottom right).

Heavy elements

We derive the heavy neutron-capture elements Y, Zr, Ba, La, and Eu abundances. The Eu abundance is essentially the reference for the r-process. We measured the YI 6435.004Å and the YII 6613.73Å lines. For the final [Y/Fe] values, we assumed that the ionised species of Y contributes 99% to the abundance. Figure 2.7 shows the line profile fitting of the YI 6435.004Å, BaII 6496.897Å, LaII 6390.477Å, and EuII 6437.640Å for the member star 243. The [Y/Fe] is systematically enhanced for Pal 6 and follows the same pattern observed for the bulge GCs with the same metallicity.

The barium abundance was measured considering only the BaII 5853.675Å and 6496.897Å lines. For zirconium, we fit four ZrI lines 6127.47Å, 6134.58Å, 6140.53Å, and 6143.25Å. We neglected ZrI's strong lines in the blue arm.

The lanthanum abundances are based on five LaII lines, located at 6172.72Å, 6262.287Å, 6296.079Å, 6320.376Å, and 6390.477Å. Finally, we adopted the lines of EuII 6437.6Å and 6645.1Å for the europium abundances.

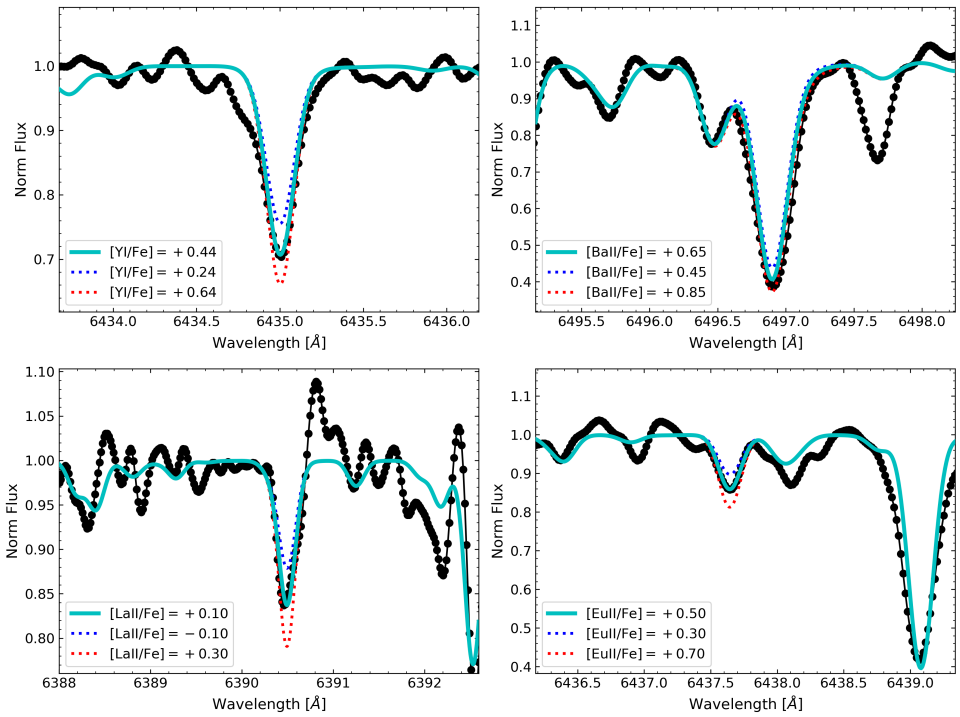

Figure 2.7: Same as Figure 2.5 for heavy-elements Y (top left), Ba (top right), La (bottom left), and Eu (bottom right).

Table 2.7 - Abundances in the six UVES sample stars. The mean abundance for the clusters is computed using only the four-member stars.

[X/Fe]	star 730	star 243	star 030	star 785	star 145	star 401	<Pal 6>
C	$+0.04 \pm 0.15$	-0.18 ± 0.15	$+0.00 \pm 0.15$	$+0.10 \pm 0.15$	$+0.05 \pm 0.15$	-0.12 ± 0.15	-0.04 ± 0.15
N	$+0.98 \pm 0.15$	$+0.58 \pm 0.16$	$+0.79 \pm 0.12$	$+0.34 \pm 0.15$	$+0.62 \pm 0.15$	$+0.82 \pm 0.08$	$+0.59 \pm 0.14$
O	$+0.37 \pm 0.15$	$+0.28 \pm 0.15$	$+0.16 \pm 0.15$	$+0.38 \pm 0.15$	$+0.42 \pm 0.15$	$+0.45 \pm 0.15$	$+0.38 \pm 0.15$
Na	$+0.29 \pm 0.22$	$+0.42 \pm 0.10$	$+0.17 \pm 0.26$	$+0.27 \pm 0.12$	$+0.40 \pm 0.12$	$+0.10 \pm 0.15$	$+0.30 \pm 0.12$
Al	$+0.44 \pm 0.12$	$+0.26 \pm 0.11$	$+0.49 \pm 0.10$	$+0.19 \pm 0.10$	$+0.11 \pm 0.14$	$+0.40 \pm 0.17$	$+0.24 \pm 0.13$
Mg	$+0.43 \pm 0.12$	$+0.40 \pm 0.09$	$+0.53 \pm 0.14$	$+0.25 \pm 0.08$	$+0.48 \pm 0.16$	$+0.30 \pm 0.17$	$+0.36 \pm 0.13$
Si	$+0.33 \pm 0.19$	$+0.37 \pm 0.16$	$+0.32 \pm 0.15$	$+0.38 \pm 0.15$	$+0.38 \pm 0.19$	$+0.41 \pm 0.17$	$+0.38 \pm 0.17$
Ca	$+0.30 \pm 0.26$	$+0.37 \pm 0.19$	$+0.11 \pm 0.35$	$+0.19 \pm 0.21$	$+0.28 \pm 0.17$	$+0.34 \pm 0.18$	$+0.29 \pm 0.19$
Ti	$+0.32 \pm 0.19$	$+0.44 \pm 0.11$	$+0.29 \pm 0.20$	$+0.27 \pm 0.21$	$+0.34 \pm 0.20$	$+0.32 \pm 0.18$	$+0.34 \pm 0.17$
Y	$+0.33 \pm 0.16$	$+0.23 \pm 0.10$	$+0.49 \pm 0.32$	$+0.84 \pm 0.13$	$+0.57 \pm 0.16$	$+0.09 \pm 0.15$	$+0.43 \pm 0.20$
Zr	$+0.76 \pm 0.17$	$+0.68 \pm 0.19$	$+0.65 \pm 0.13$	$+0.61 \pm 0.12$	$+0.74 \pm 0.24$	$+0.41 \pm 0.35$	$+0.61 \pm 0.22$
Ba	—	$+0.58 \pm 0.17$	—	$+0.23 \pm 0.15$	—	$+0.49 \pm 0.13$	$+0.43 \pm 0.18$
La	$+0.46 \pm 0.15$	$+0.24 \pm 0.13$	$+0.57 \pm 0.28$	$+0.69 \pm 0.12$	$+0.68 \pm 0.18$	$+0.24 \pm 0.16$	$+0.46 \pm 0.15$
Eu	$+0.43 \pm 0.12$	$+0.31 \pm 0.19$	$+0.49 \pm 0.12$	$+0.73 \pm 0.08$	$+0.74 \pm 0.13$	$+0.58 \pm 0.11$	$+0.59 \pm 0.13$

2.4.3 Errors

Spectroscopic parameter uncertainty is given in Table 2.8 for star 243. For each stellar parameter, we have adopted the usual uncertainties as for similar samples (Barbuy et al., 2014, 2016, 2018a): ±100 K in effective temperature, ±0.2 on gravity, and ±0.2 km s^{-1} on the microturbulence velocity. The sensitivities are computed by employing models with these modified parameters and recomputing lines of different elements considering changes of ΔTeff = +100 K, Δlog g= +0.2, Δv_t = 0.2 km s^{-1}. The given error is the difference between the new abundance and the adopted one. Uncertainties due to non-LTE effects are negligible for these stellar parameters, as discussed in Ernandes et al. (2018). The same error analysis and estimations can be applied to other stars in our sample. The abundance derivations from strong lines are, in general, avoided since they are too sensitive to stellar parameters and spectral resolution, as can be seen for the sensitivity of BaII lines of Table 2.8. On the other hand, the La lines are faint and are at least not affected by the same problem. Finally, it is essential to note that the main uncertainties in stellar parameters are due to uncertainties in the effective temperature, as seen in Table 2.5. The second most important source of error is the EWs, given the limited SNR of the spectra, estimated from the formula by Cayrel (1988): $\sigma_{EW} = 1.5\ \sqrt{FWHM.\delta_x}/(S/N)$, where δ_x is the pixel size.

2.4.4 Comparison with previous results

The metallicity derived in this work is in excellent agreement with the values derived by Lee and Carney (2002) ([Fe/H] = -1.08 ± 0.06) and Lee et al. (2004) ([Fe/H] = -1.0 ± 0.1) from high-resolution spectroscopy. It is also in good agreement with the Carretta et al. (2009) metallicity scale, where Pal 6 has [Fe/H] = -1.06 ± 0.09. The metallicity scale of Dias et al. (2016) gives a value of [Fe/H] = -0.85 ± 0.11 for Pal 6. For comparison purposes, we selected the stars of Dias et al. (2016) and calculated their membership probabilities. The stars Pal 6-9 and Pal 6-13 in their sample seem to be members of Pal 6 with metallicities [Fe/H] = -0.76 ± 0.18 and [Fe/H] = -1.14 ± 0.28, respectively. Therefore, we can suppose that the star Pal 6-13 is the most probable member of Pal 6. This fact shows Gaia's power, which was not available until very recently, and the stellar membership should be verified in all samples preceding the Gaia data.

Recently, Kunder et al. (2021) analysed Pal 6 in the context of the data release 16

Table 2.8 - Sensitivity in abundances due to variation in atmospheric parameters, for the star 243 considering uncertainties of ΔT_{eff} = 100 K, Δlog g = 0.2, Δv_t = 0.2 km s^{-1}, and the last column is the total error. The errors are to be added to reach the reported abundance.

Element	ΔT	Δlog g	Δv_t	$(\sum x^2)^{1/2}$
	100 K	0.2 dex	0.2 kms^{-1}	
(1)	(2)	(3)	(4)	(5)
[FeI/H]	−0.05	+0.03	+0.06	+0.08
[FeII/H]	+0.13	−0.15	+0.02	+0.20
[C/Fe]	+0.02	+0.02	+0.00	+0.03
[N/Fe]	+0.15	+0.10	+0.00	+0.18
[O/Fe]	+0.00	+0.05	+0.00	+0.05
[NaI/Fe]	+0.13	+0.05	+0.04	+0.15
[AlI/Fe]	+0.10	+0.03	−0.01	+0.10
[MgI/Fe]	+0.07	+0.03	+0.00	+0.08
[SiI/Fe]	+0.02	+0.12	+0.08	+0.14
[CaI/Fe]	+0.18	+0.10	−0.05	+0.21
[TiI/Fe]	+0.25	+0.09	−0.04	+0.27
[TiII/Fe]	−0.04	+0.10	−0.03	+0.11
[YI/Fe]	+0.13	+0.13	−0.12	+0.22
[YII/Fe]	+0.07	+0.08	−0.02	+0.11
[ZrI/Fe]	+0.22	+0.06	−0.12	+0.26
[BaII/Fe]	+0.05	+0.12	−0.16	+0.21
[LaII/Fe]	+0.08	+0.16	+0.07	+0.19
[EuII/Fe]	−0.01	+0.10	+0.00	+0.10

(DR16) of the Apache Point Observatory Galactic Evolution Experiment (APOGEE) survey for five observed stars. We inspected the membership probabilities of their sample. With our analysis, all stars are members of the cluster. Their mean radial velocity of 174.5 ± 1.5 is in agreement with our derivation. Their mean metallicity given by the three stars with good `ASPCAPFLAG` is [Fe/H] $= -0.92 \pm 0.10$, which is compatible within 1σ with our result.

We also have abundances for C, N, O, Na, Mg, Si, and Ca elements from APOGEE DR16. The CNO abundances are [C/Fe] $= -0.05 \pm 0.04$, [N/Fe] $= +0.31 \pm 0.27$, and [O/Fe] $= +0.22 \pm 0.05$. These values agreed with our results considering our derived errors, except for the carbon abundance, which is in excellent agreement with our determi-

nation. The abundances of α-elements [Mg/Fe] = $+0.34 \pm 0.03$, [Si/Fe] = $+0.22 \pm 0.07$, and [Ca/Fe] = $+0.20 \pm 0.03$, individually are following the results of Table 2.7. Additionally, the abundances of α-elements give a value of [α/Fe] = $+0.25 \pm 0.06$, which agrees with our UVES analysis. This value also agrees with Coelho et al. (2005) [α/Fe] = $+0.28 \pm 0.05$. Finally, only the two stars with `ASPCAPFLAG` $\neq 0$ have [Na/Fe] values with a mean of [Na/Fe] = $+0.35 \pm 0.10$. However, it is expected that Na should show variations due to the probable presence of first and second-generation stars, as discussed below.

2.4.5 s-process elements analysis

The presence of heavy elements in old stars can be explained through the r-process contribution to these elements, as the first suggested by Truran (1981). Otherwise, the early enhancement of heavy elements can be explained by the ignition of the s-process for the first generation of stars with high rotation, the fast-rotating massive stars (Chiappini et al., 2011; Cescutti et al., 2013, 2015; Frischknecht et al., 2016; Choplin et al., 2018). The rotation transports the ^{12}C from the internal layers to external ones to burn into ^{14}N and ^{13}C. The activation of the s-process occurs when the ^{14}N is converted into ^{22}Ne. Therefore, this mechanism does not predict carbon enhancements.

An alternative explanation is an s-process contribution within a binary system in which the main companion has gone through the asymptotic giant branch (AGB) phase (Beers and Christlieb, 2005; Sneden et al., 2008, and references therein). Due to the mass transfer from AGB, the second companion receives s-process yields (see discussion in Barbuy et al., 2021a).

The top panel of Figure 2.8 highlights the region for solar system r-process abundance ratio of [Eu/Ba]= $+0.60 \pm 0.13$ (Simmerer et al., 2004), that would characterise r-II stars. Otherwise r-I stars are defined to have $0.3 \leq$ [Eu/Fe] $\leq +1.0$ and [Ba/Eu] < 0, and r/s stars to have $0.0 <$ [Ba/Eu] $< +0.5$ (Beers and Christlieb, 2005). These ratios are shown for the present sample of stars in the bottom panel of Figure 2.8.

We also tentatively investigate the nature of heavy element enhancement through the diagnostic plots of Figure 2.8 using the [Zr/Ba] ratio. The use of [Zr/Ba] as presented by Siqueira-Mello et al. (2016) consisted in using [Y/Ba], and values from the six r-rich halo stars compiled in Sneden et al. (2008), as representatives of the main r-process, that have a mean of [Y/Ba] = -0.42 ± 0.12. On the other hand, Siqueira-Mello et al. (2016) gathered

six other halo metal-poor stars showing enhancement of the first peak of heavy elements, which have [Y/Ba] = $+0.58 \pm 0.18$ on the other extreme. The same is applied to Zr-to-Ba, having [Zr/Ba] = -0.18 ± 0.12 and $+0.95 \pm 0.15$ in the two extremes.

In the middle panel of Figure 2.8, we show the [Zr/Ba] vs [Y/Ba] diagram for Pal 6 and the other three reference bulge GCs. For diagnostics purposes, we highlighted the region of main r-process stars (red region) at $[Y/Ba]_r = -0.4 \pm 0.1$ (Sneden et al., 2008) and $[Zr/Ba]_r = -0.2 \pm 0.1$ (Siqueira-Mello et al., 2016). Only three of the six observed stars are plotted due to the absence of Ba abundance. The member stars 785 and 401 are consistent with r-rich stars, considering the errors. Besides that, star 401 is located at the highest star density and, consequently, compatible with the reference GCs.

The bottom panel of Figure 2.8 shows the further inspection of the r- and s-process to the r-rich stars selected by the [Eu/Ba] vs. [Fe/H], and [Zr/Ba] vs. [Y/Ba] diagrams. The two-member stars (785 and 401) classified as r-rich are compatible with the definition of r-I, in agreement with the observed for the reference GCs.

2.4.6 Two stellar populations?

The expected N-O anticorrelation (Carretta et al., 2010; Gratton et al., 2004, 2012) is given in the left panel of Figure 2.9. We also found two N-rich non-member stars, possible field members, with [N/Fe]$> +0.70$. These could be stars that were Pal 6 or other cluster members trapped by the Galactic bulge (Schiavon et al., 2017). Another indicator of MPs is the Na-O anticorrelation. Carretta et al. (2009) demonstrated that this anticorrelation is more probable to be seen in massive clusters. Since Pal 6 is a relatively low-mass cluster (with an absolute magnitude of $M_V = -6.79$; Harris, 1996, 2010), in Figure 2.9 (right panel) we can observe a slight Na-O anticorrelation.

To verify if our N-enhanced star 401 is a probable second-generation member, we investigated the Al-NaON relations (Figure 2.10). Meszaros et al. (2020) analyzed stars observed with the APOGEE for 31 GCs. They observed that the stars are split reasonably well into two populations at [Al/Fe]$= +0.30$. We investigated these patterns and observed that our N-enhanced star has [Al/Fe]$> +0.30$, while the other three member stars have [Al/Fe]$< +0.30$. Even though the phenomenon of MPs (Bastian and Lardo, 2018a) is a characteristic of the majority of GCs (Piotto et al., 2015), Lagioia et al. (2019) presented the first evidence of a GC consistent with hosting a simple stellar population (Terzan 7).

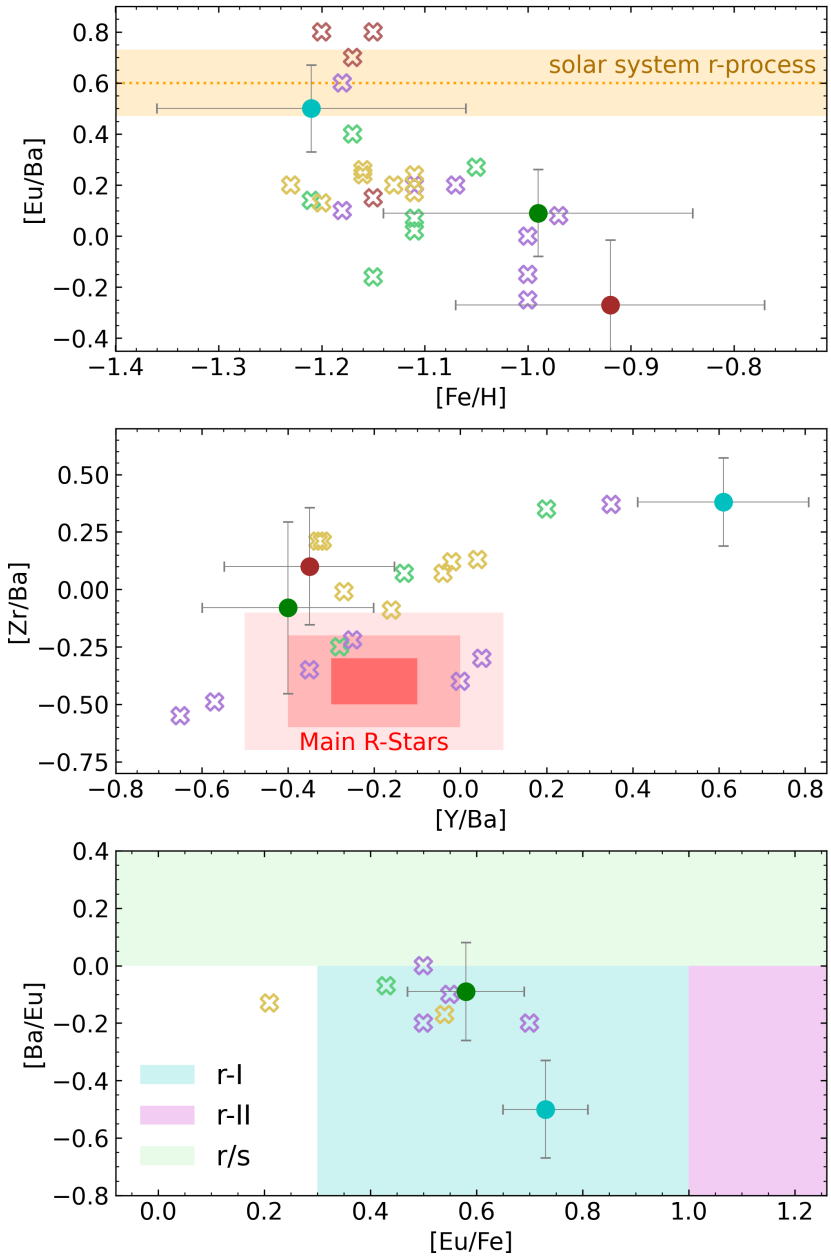

Figure 2.8: Heavy-elements enhancement diagnostic. *Top panel:* [Eu/Ba] vs. [Fe/H] diagram for the four reference GCs. The orange strip highlights the solar system r-process region for [Eu/Ba]$= +0.60 \pm 0.13$ (see text). *Middle panel:* [Zr/Ba] vs [Y/Ba] diagram for the three reference GCs which have Zr, Y, Ba abundances determinations. The region of main r-process stars domains with 3σ as red. *bottom panel:* [Ba/Eu] vs [Eu/Fe] diagram for the selected r-rich stars from the upper panel (see text). The light green region represents the enhancement regime by both the r- and s-process. The cyan and magenta regions show the domains of mainly r-process enhancement.

Therefore, the abundance pattern observed for Pal 6 is essential to check if it hosts at least two stellar populations.

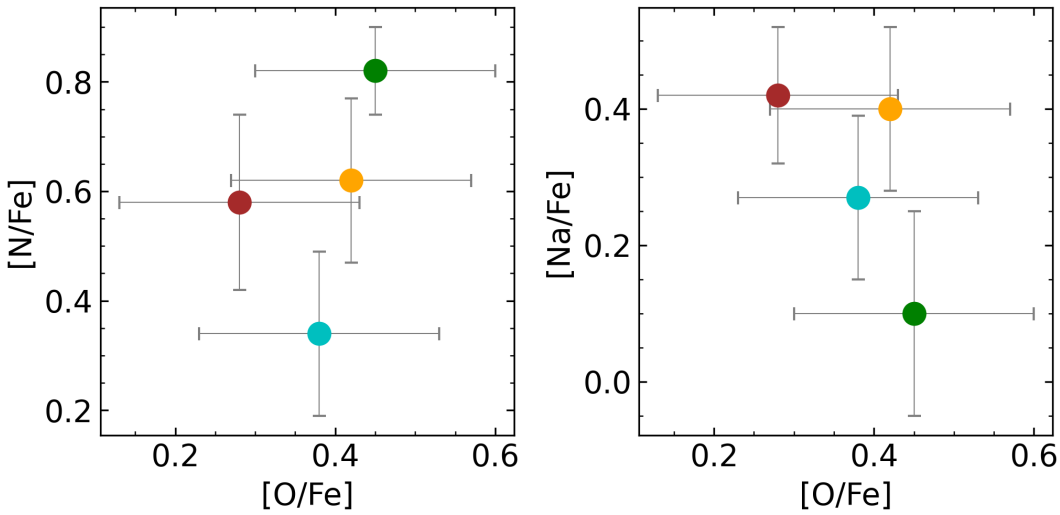

Figure 2.9: Anticorrelations N-O (left) and Na-O (right) for Pal 6 member stars.

2.5 Age and Distance

Previous photometric studies did not attempt to derive the age of Pal 6, and there are controversies about its distance in the literature. These are largely due to the absence of observed standard candle stars in Pal 6, and different values result from different methods. Ortolani et al. (1995) derived a distance of $\sim$ 8.9 kpc from the HB magnitude method with an extinction of $A_V = 4.12$. Lee and Carney (2002), comparing the Pal 6 HB magnitude to the 47 Tuc one, obtained a distance of $\sim$ 7.2 kpc with $A_V = 4.1$ mag. Harris (1996) gives a distance of 5.80 kpc, which was adopted by Baumgardt et al. (2019), and used in Massari et al. (2019) and Pérez-Villegas et al. (2020).

With the final corrected CMD, we used the `SIRIUS` code (Souza et al., 2020) to perform the statistical isochrone fitting to get the accurate probability distributions for the fundamental parameters of Pal 6. We employed isochrones from MESA Isochrones & Stellar Tracks database (MIST; Dotter, 2016; Choi et al., 2016) with metallicity [Fe/H] ranging from 0.0 to -2.0 dex in steps of 0.01 dex, ages from 10 Gyr to 15 Gyr with an interval of 0.1 Gyr, and the reddening and distance modulus can vary freely. To obtain a consistent analysis, we used a Gaussian prior for the metallicity with information from the high-resolution spectroscopic determination by this work.

We also obtained the temperature-dependent second-order extinction corrections ΔC_λ ($\Delta A_\lambda / A_V^{\rm reff}$) through comparing the MIST isochrones with $A_V = 0.00$ and 6.0 for each

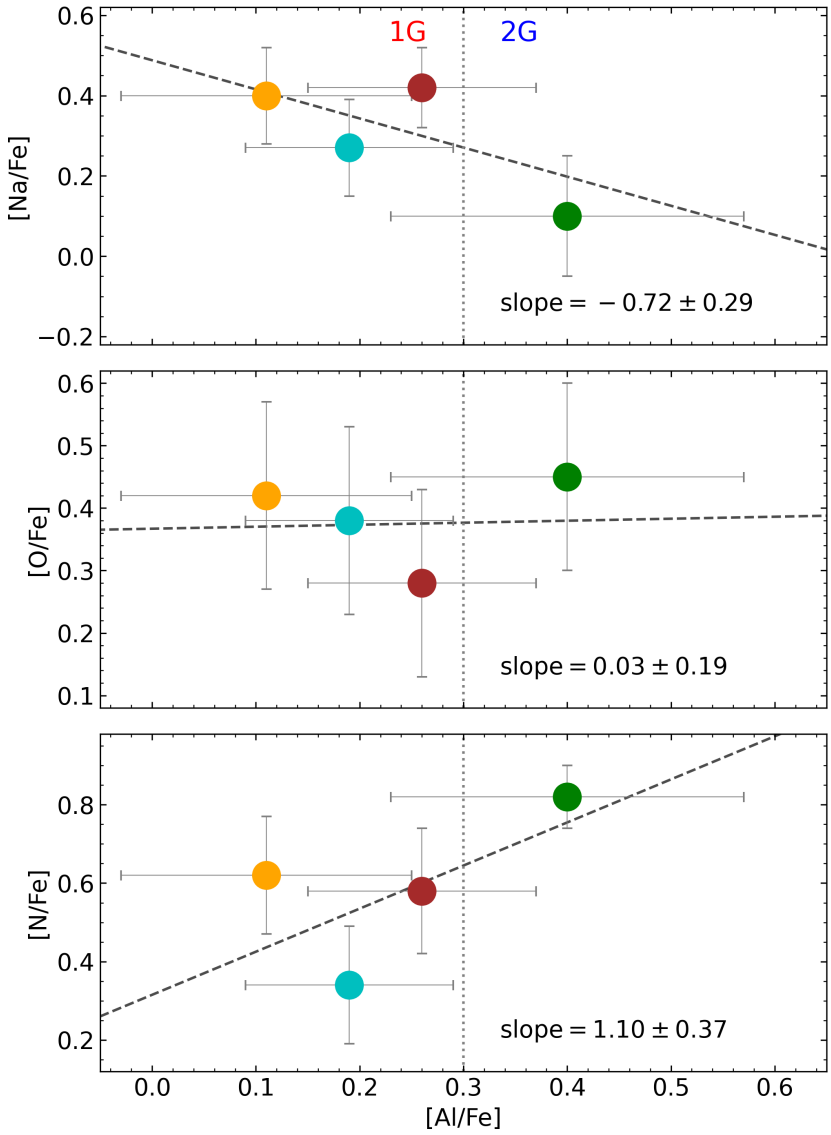

Figure 2.10: Al-NaON (anti)correlations. The dots are coloured with the same colour code as Figure 2.9. The dotted grey line represents the generation split around [Al/Fe] = +0.30 (Meszaros et al., 2020). The black dashed lines show the obtained linear regression.

value of $T_{\rm eff}$. The correction is given by the second order polynomial function $\Delta C_\lambda = a_0 \times (\log T_{\rm eff})^2 + a_1 \times \log T_{\rm eff} + a_2$, and the $A_V^{\rm reff} = 6.0$. As mentioned in Oliveira et al. (2020), the second-order correction is obtained by interpolation considering the desired A_V. The coefficients $a_{0,1,2}$ are listed in Table 2.9.

We adopted the $50^{\rm th}$ percentile as the best solution and $50^{\rm th} - 16^{\rm th}$ and $84^{\rm th} - 50^{\rm th}$ percentiles for the uncertainties. The red line in Figure 2.11 represents the best fit, while the red strip shows the region of 1σ solutions. We want to stress that the HB model fits well with the HB region in the CMD. Also, this technique allows us to get a better distance determination with low uncertainty. The best distance, reddening, and well-constrained

Table 2.9 - Coefficients for effective temperature second-order correction to different passbands. The coefficients order are given by the equation: $\Delta C_\lambda = a_0 \times (\log T_{\rm eff})^2 + a_1 \times \log T_{\rm eff} + a_2$.

ΔC_λ	a_0	a_1	a_2
F606W	-0.325	$+2.555$	-5.041
F110W	$+0.056$	-0.365	$+0.571$
F160W	$+0.012$	-0.078	$+0.127$
$V*$	-0.328	$+2.515$	-4.840
I	-0.056	$+0.442$	-0.878
G	-0.506	$+4.129$	-8.495
G_{BP}	-0.191	$+1.723$	-3.847
G_{RP}	-0.302	$+2.342$	-4.584

metallicity values gave us the first derivation of age for Pal 6 as 12.4 ± 0.9 Gyr, among the oldest GCs in the Galaxy.

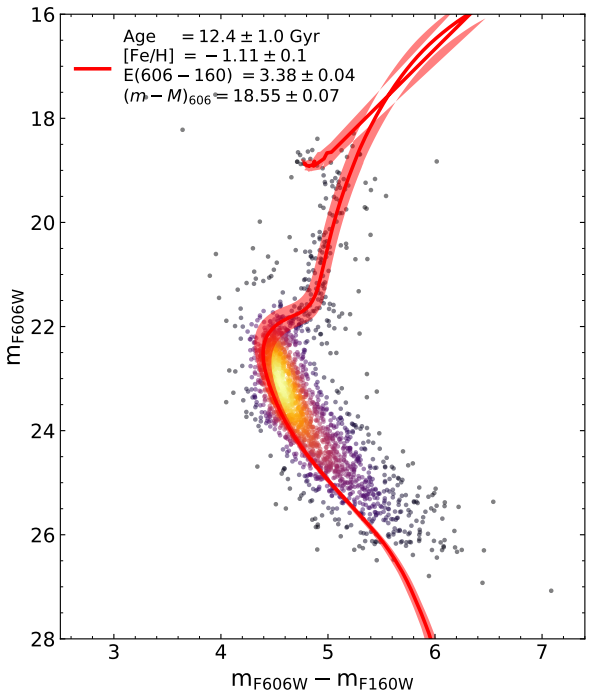

Figure 2.11: Best-fit from isochrone fitting (solid line) and results for $\pm 1\sigma$ (red region).

The reddening E(606−160)= 3.38±0.04 and distance modulus $(m-M)_{606}$ = 18.55±0.07 obtained from isochrone fitting can be converted in E(B−V) and $(m-M)_0$ by using the

relations:

$$E(606-160) = R_V \times E(B-V) \times (C_{606,R_V} - C_{160,R_V}) \tag{2.2}$$

$$(m-M)_{606} = (m-M)_0 + R_V \times C_{606,R_V} \times E(B-V) \tag{2.3}$$

where C_{λ,R_V} is the ratio of temperature- gravity-dependent coefficients at the λ for an extinction law with R_V (Pallanca et al., 2021, and references therein). Since the extinction is given by $A_\lambda = R_V \times C_{\lambda,R_V} \times E(B-V)$, the reddening is inversely proportional to R_V. Therefore, the assumption of R_V will affect the fundamental parameters of the cluster.

The isochrone fitting is expected to use the extinction law setting $R_V = 3.1$, which is the case for all the fundamental parameters calculated for Pal 6 in the literature. With this extinction law, our determination is $A_V = 4.56 \pm 0.06$ ($E(B-V) = 1.47 \pm 0.02$), compatible with the reddening used to derive the photometric temperatures. However, Nataf et al. (2016) argue that a lower value of R_V is more compatible with the Galactic bulge population where it could reach down to $R_V = 2.5$ at least for (absolute) Galactic latitudes between 2 and 7 degrees and $-10° < l < 10°$. Vasiliev and Baumgardt (2021) compared the distance from literature to the Gaia EDR3 parallaxes. They found a discrepancy between the photometric distances and the inverse of parallaxes for the bulge GCs, precisely those with high reddening values (E(B−V)>1.0). Also, Pallanca et al. (2021) shows that the $R_V = 3.1$ needs different values of reddening and distance moduli to fit the CMD with different colours well in the case of the bulge GC Liller 1. They demonstrated that to fit the three CMDs simultaneously with a unique set of reddening and distance values, adopting an extinction law with $R_V = 2.5$ is necessary. They also conclude that the variation in the extinction law results in variations in the reddening and distance modulus determinations (consequently in the distance).

To determine the value of R_V for Pal 6, we compare the optical (VI; Ortolani et al., 1995), Gaia $G_{BP} - G_{RP}$ vs. G, and NIR HST CMDs using the best-fit parameters of Figure 2.11. Since we varied the R_V, we rederived the extinction coefficients in the adopted bands (A_{F606W}/A_V, A_{F110W}/A_V, A_{F160W}/A_V, $A_{G_{BP}}/A_V$, $A_{G_{RP}}/A_V$, A_G/A_V, and A_I/A_V) using the extinction laws from Cardelli et al. (1989). The corresponding extinction law to a given R_V value has been done by interpolating the curves in a grid with the values $R_V = 2.1, 3.1, 4, 5$ (Figure 2.12). We derived $R_V = 2.6$ by maximising the χ^2 for the optical and Gaia CMDs (first and second panels of Figure 2.13). Finally, we determined

an extinction of $A_V = 4.21 \pm 0.05$ ($E(B-V) = 1.62 \pm 0.02$) and a distance of $d_\odot = 7.67 \pm 0.19$ kpc, a result within the range between 5.8 kpc (Harris, 1996, 2010) and 8.9 kpc (Ortolani et al., 1995) and very close to the Lee and Carney (2002) value of 7.2 kpc. We stress that the latter distance determination derived from near-IR JHK photometry is independent of the R_V optical value.

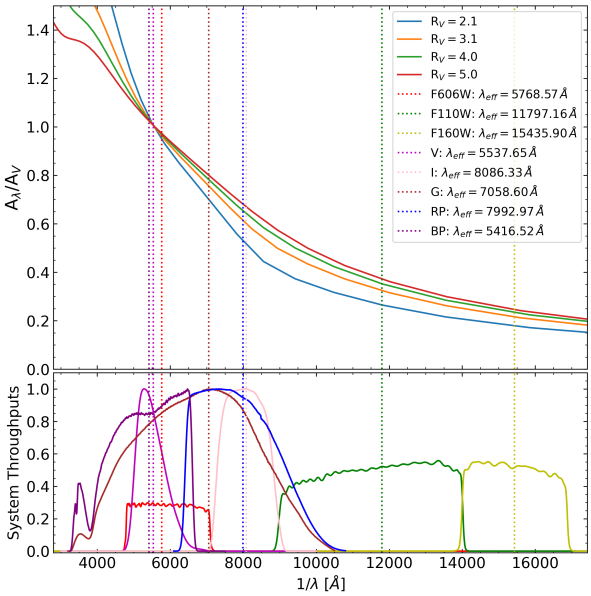

Figure 2.12: Extinction law curves derivation. The effective wavelengths are computed from $\lambda_{\rm eff} = \int \lambda^2 T_\lambda d\lambda / \int \lambda T_\lambda d\lambda$.

We performed the distance calculation using the other two methods to confirm our determination. From the relation Mv−[Fe/H] derived by Oliveira et al. (2022) for RR Lyrae stars, we can obtain the HB absolute magnitude of 0.758 ± 0.086 in the V band. Assuming the apparent V magnitude value of 19.70 ± 0.15 calculated for the HB of Pal 6 by Ortolani et al. (1995), we obtain the distance modulus of $(\mathrm{m}-\mathrm{M})_V = 18.94 \pm 0.18$. Finally, with the extinction value found in the present work ($A_V = 4.21 \pm 0.05$, compatible with the average calculated with dust map of the Galaxy using the DUST web tool[3]), we have a distance of $d_\odot^{(\mathrm{HB})} = 8.73 \pm 0.75$ kpc.

Using the Gaia EDR3 membership analysis (Section 2.2), we identified five stars with distances derived by the StarHorse calculations (with Gaia EDR3 and APOGEE DR16; Queiroz et al., 2020, 2021). Due to the low statistics, we expanded the sample with a bootstrapping method, considering the uncertainties. The mean distance derived from the expanded sample is $d_\odot^{(\mathrm{SH})} = 7.3 \pm 0.8$ kpc.

[3] https://irsa.ipac.caltech.edu/applications/DUST/

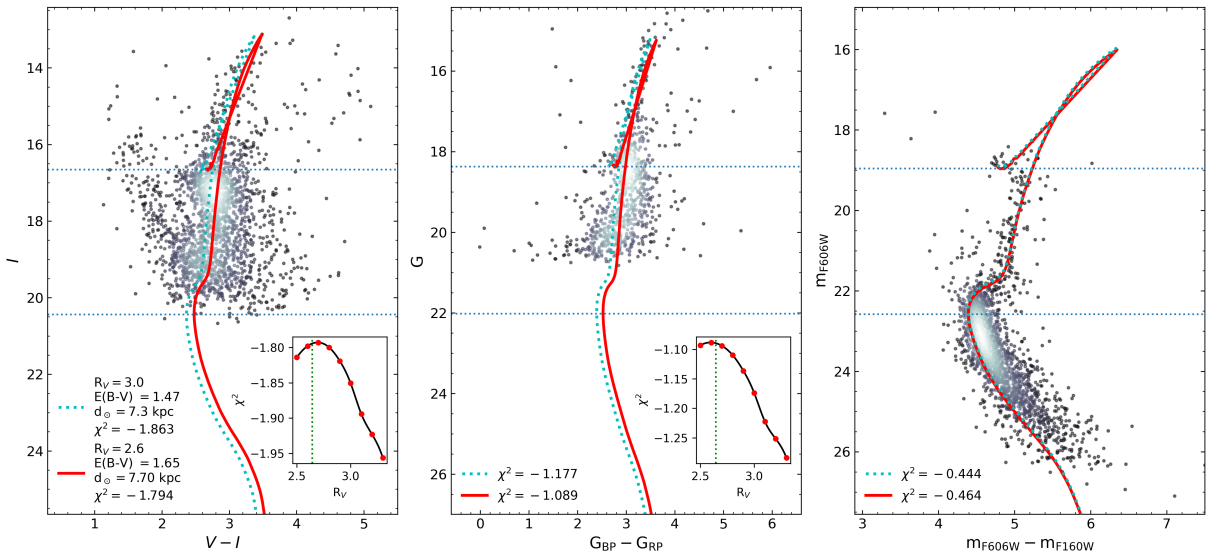

Figure 2.13: Posterior fitting to obtain the best value of R_V. First panel: optical CMD $V-I$ vs. I from Ortolani et al. (1995). Second panel: Gaia EDR3 $G_{BP}-G_{RP}$ vs. G CMD. Third panel: Corrected NIR HST CMD. The cyan dotted lines are the isochrones considering the best fit from the standard isochrone fitting and standard extinction coefficient ($R_V = 3.0$). The embedded plots show the χ^2 function to the variation of R_V. The solid red lines are the isochrones with the best R_V value. Finally, the blue horizontal lines denote the isochrone HB and Turn-off mean-locus.

The individual distance determinations through the HB and StarHorse are already compatible within 1.5σ with our determination from the isochrone fitting of 7.67 ± 0.19 kpc. In addition, the average of these determinations results in a distance of $< d_\odot >_{(\mathrm{HB,SH})}= 8.0 \pm 1.1$ kpc, compatible with the distance of the present work. Finally, we added the average of the literature of 7.05 ± 0.46 kpc given by Baumgardt and Vasiliev (2021)[4], resulting in $< d_\odot >_{(\mathrm{HB,SH,B\&V21})}= 7.5 \pm 1.0$kpc, which is in good agreement with our determination. Therefore, these results reinforce the one we found through the isochrone fitting of $d_\odot^{(\mathrm{Pal\ 6})} = 7.67 \pm 0.19$ kpc calculated with the derived extinction law ($R_V = 2.6$).

2.6 Dynamical properties

The chemical information, age, and distance obtained in the previous sections make it possible to infer a plausible origin of Pal 6.

Using the distance of (Harris, 1996) and adopted by Baumgardt et al. (2019), Pérez-Villegas et al. (2020) classified Pal 6 as belonging to the Galaxy thick disc with a probability

[4] They considered the distances from Ortolani et al. (1995), Barbuy et al. (1998), Lee and Carney (2002), and Lee et al. (2004). Because of the expected distance for Pal 6, they did not consider the inverse of the parallax given by Vasiliev and Baumgardt (2021).

of 98%. Caution was recommended, given other distance estimations in the literature. (e.g. Ortolani et al., 1995).

Given the much more reliable distance now derived in the present paper, we calculated orbits for the cluster. We employed the same Galactic model of Pérez-Villegas et al. (2020) that includes a triaxial Ferrers bar of 3.5 kpc (major axis). The total mass of the bar is 1.2×10^{10} $M_{\odot}$ with an angle of 25° with the Sun-major axis. We also assume three pattern speeds of the bar $\Omega_b = 40$, 45, and 50 km s^{-1} kpc^{-1}.

We generated a set of 1000 initial conditions employing a Monte Carlo approach. To do that, we considered the observational uncertainties of distance, heliocentric radial velocity, and absolute proper motion components to evaluate the errors in those observational parameters. Using the NIGO tool, we integrate the orbits forward for 10 Gyr (Rossi 2015). In Table 2.10, we give the new orbital parameters as the median value of the perigalactic distance $< r_{min} >$, apogalactic distance $< r_{max} >$, eccentricity $< e >= (r_{max} - r_{min})/(r_{max} + r_{min})$, and maximum vertical excursion from the Galactic plane $< |z|_{max} >$. The error of each orbital parameter is given as the standard deviation of the distribution.

Figure 2.14 shows the probability density map of the orbits of Pal 6 in the $x - y$ and $R - z$ projections co-rotating with the bar. The gold colour displays the space region where the orbits of Pal 6 cross more frequently, while the black curves are the orbits considering the central values of the observational parameters.

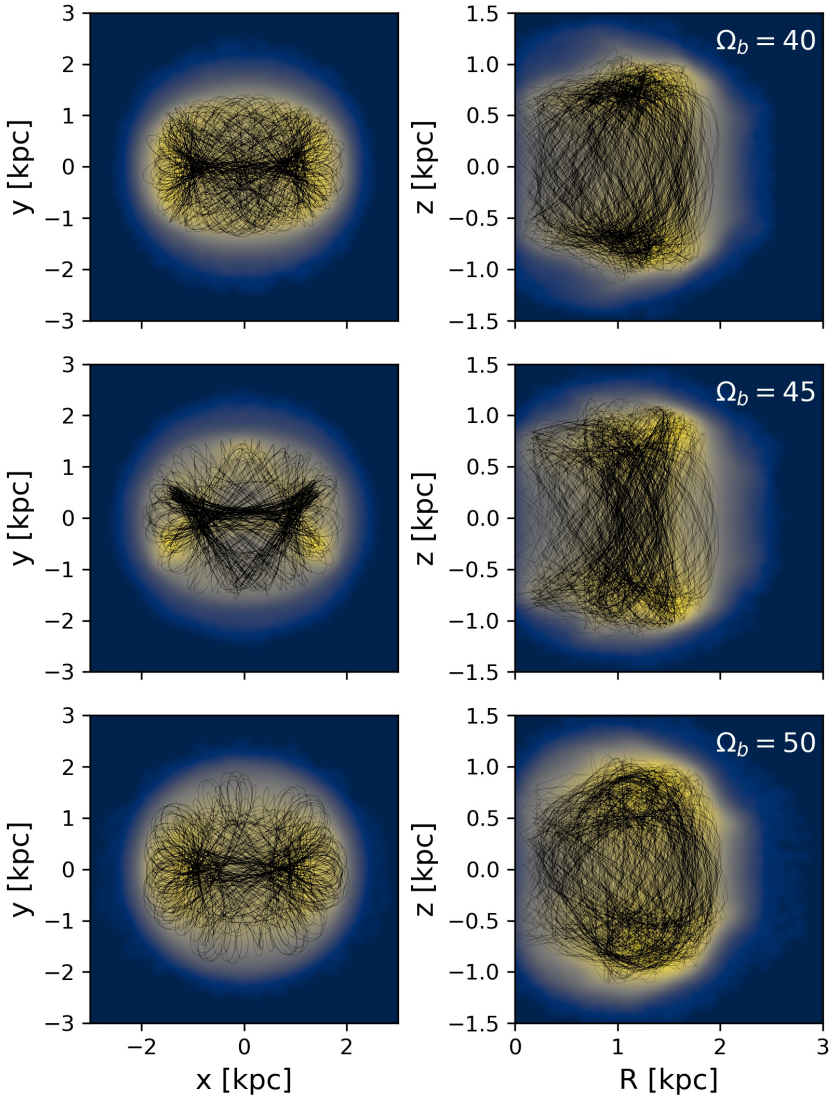

Figure 2.14: Probability density map for the $x - y$ and $R - z$ projections of the set of orbits for Pal 6 using three different values of $\Omega_b = 40, 45$, and 50 km s^{-1} kpc^{-1}. The orbits are co-rotating with the bar frame. The gold colour corresponds to the higher probabilities, while the black lines show the orbits using the central observational parameters.

Table 2.10 - Orbital parameters of Pal 6 for the McMillan (2017) potencial and the potential employed in Pérez-Villegas et al. (2020) assuming three different bar pattern speed values. The energy units are $[E]$=km^2 s^{-2} and angular momentum $[L]$=km s^{-1} kpc.

Parameter	PV $\Omega_b = 40$	PV $\Omega_b = 45$	PV $\Omega_b = 50$	McMillan17
$<r_{min}>$ [kpc]	0.08 ± 0.03	0.09 ± 0.04	0.10 ± 0.04	0.07 ± 0.04
$<r_{max}>$ [kpc]	2.06 ± 0.07	2.06 ± 0.07	2.10 ± 0.09	2.14 ± 0.19
$< \|z\|_{max} >$ [kpc]	1.07 ± 0.10	1.14 ± 0.05	1.16 ± 0.07	1.29 ± 0.04
<e>	0.92 ± 0.03	0.91 ± 0.03	0.90 ± 0.03	0.96 ± 0.05
<E> $[10^5 E]$	—	—	—	-2.40 ± 0.05
$<L_z>$ $[L]$	—	—	—	7.88 ± 13.2
$<L^{\dagger}_{perp}>$ $[10^2 L]$	—	—	—	1.67 ± 0.22
$<L_{z_c}>$ $[10^2 L]$	—	—	—	3.07 ± 0.19
$\mathcal{P}_{\rm Bulge}$ [%]	99.4	99.4	99.3	99.1
$\mathcal{P}_{\rm Disc}$ [%]	0.6	0.6	0.7	0.9

† The L_{perp} is not conserved for axisymmetric potentials. However, it is a good parameter to describe the origin of a group of stars (Helmi and de Zeeuw, 2000; Massari et al., 2019).

Chapter 3

The intriguing globular cluster NGC6355

The results presented in this chapter were published in Souza et al. (2023).[1]

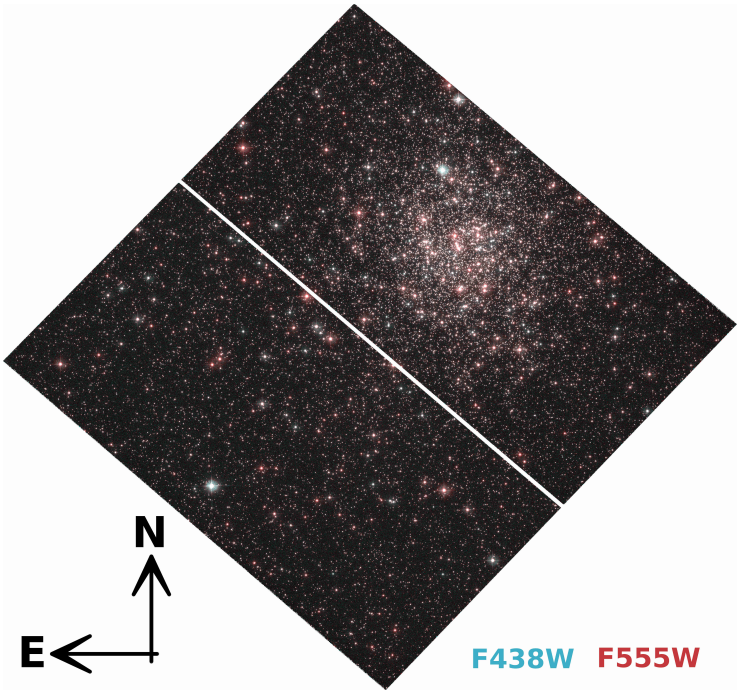

Figure 3.1: F438W/F555W combined colour image from the HST WFC3 camera for NGC 6355.

3.1 Introduction

Observing GCs within the Galactic bulge is difficult because the extinction tends to hide the objects. One example is NGC 6355 (also called GCl-63 and ESO 519-SC15), projected towards the direction of the Galactic bulge (l = 359.58°, b = +5.43°) with a

[1] https://ui.adsabs.harvard.edu/abs/2023A%26A...671A..45S/abstract

relatively high extinction ($E(B-V) = 0.79$; Harris, 1996). NGC 6355 is a well-known cluster that has been studied since the 1900s. It was classified as a probable open cluster (Shapley and Shapley, 1919). However, it did not take long before its globular nature was confirmed based on its relatively high mass, which according to Baumgardt and Hilker (2018) is 1.01×10^5 $M_\odot$. Djorgovski and King (1986) classified NGC 6355 as a core-collapse cluster. This result was recently confirmed by Cohen et al. (2021) using the Hubble Space Telescope (HST) filters F606W and F814W from the Advanced Camera for Survey (ACS).

Ortolani et al. (2003) analysed the horizontal branch (HB) and the red giant branch (RGB) of NGC 6355 using a $[V,V-I]$ colour-magnitude diagram (CMD). They obtained a reddening of $E(B-V) = 0.78$, a distance of $d_\odot = 8.8$ kpc, and a metallicity of [Fe/H]~ -1.3. This was deduced by comparing the cluster mean locus with the mean loci of the well-studied clusters NGC 6171 and M 5. Assuming their distance derivation, the authors concluded that the cluster is near the Galactic center (see also Bica et al., 2006). Valenti et al. (2007) analysed the RGB slope and the K magnitude of the RGB tip using the $[K,J-K]$ and $[H,\ J-H]$ CMDs. They found $E(B-V) = 0.82$, $d_\odot = 8.7$kpc, and [Fe/H]$= -1.42$. Both results agree with the metallicity scales of Carretta et al. (2009) and Zinn and West (1984) of [Fe/H]$= -1.33 \pm 0.14$ and [Fe/H]$= -1.50 \pm 0.15$, respectively. Subsequent metallicity derivation by Vásquez et al. (2015) and Dias et al. (2016) of [Fe/H]~ -1.49 and [Fe/H]~ -1.46, respectively, are also within the range of both metallicity scales.

Barbuy et al. (2009) identified NGC 6355 as a blue horizontal branch (BHB) metal-poor GC, located in the ring at $-6°$ – $-12°$ around the Galactic centre. This suggested that NGC 6355 belonged to the BHB moderately metal-poor clusters of the Galactic bulge, such as NGC 6558 (Barbuy et al., 2007, 2018b), HP 1 (Barbuy et al., 2006, 2016), AL 3 (Ortolani et al., 2006; Barbuy et al., 2021a), Terzan 9 (Ernandes et al., 2019), and UKS 1 (Fernández-Trincado et al., 2020). Nevertheless, when examined from the orbital viewpoint, it was suggested that NGC 6355 is more compatible with the Galactic thick disk with a probability of 93% (Rossi, 2015; Pérez-Villegas et al., 2018, 2020), assuming a distance of 8.70 ± 0.87 kpc. It also has a probability of 7% to be part of the Galactic bulge. Here we stress the importance of having a precise distance derivation.

Kharchenko et al. (2016, hereafter KC16) analysed 147 GCs including NGC 6355 using integrated JHK_s magnitudes. They derived its age as $\log t = 10.10$ (~ 12.5 Gyr). As-

suming this age derivation and the distances derived by Baumgardt and Hilker (2018), Massari et al. (2019) found that NGC 6355 may have been formed from the main-bulge progenitor and might therefore be an in-situ cluster. Their result for NGC 6355 was confirmed with a more realistic approach adopted in Moreno et al. (2022), who employed the formalism for dynamical friction. More recently, Cohen et al. (2021, hereafter C21) derived a relative age of 1.1 Gyr by comparing the CMDs of NGC 6355 and NGC 6205. The authors give an absolute age of $\sim$ 13.2 Gyr for NGC 6355 and assume an age of 12.1 Gyr for NGC 6205 (VandenBerg et al., 2013, hereafter VB13). This relatively older age compared to the previous one by KC16 was used by Callingham et al. (2022) to reclassify NGC 6355 as compatible with the main-bulge progenitor and also with the Kraken accreted structure as an alternative origin. It is worth noting that a possible accreted structure within the Galactic bulge was hypothesized also by Massari et al. (2019) (low-energy progenitor), Kruijssen et al. (2019) (Kraken), Forbes (2020) (Koala), and Horta et al. (2021) (Heracles).

3.2 Data

HST photometry processing

The photometric data for NGC 6355 were retrieved from the HST Project (GO-11628, PI:Noyola), which used the Wide Field Camera for Surveys 3 (WFC3) with the filters F438W and F555W. The observation consists of three F438W images with an exposure time of 440 s, and three F555W images with an exposure time of 80 s. Figure 3.1 shows the colour image composed of the combined HST images. We performed a further selection based on the pipeline described in Nardiello et al. (2018) using the quality-of-fit and photometric error parameters to select well-measured stars and reject poor measurements (top left panel of Figure 3.2). Additionally, we selected stars within a half-light radius of 0.88 arcmin (Harris, 1996) to avoid a substantial number of field stars. For the resulting sample, we computed a simple membership probability by combining the stars offset from the fiducial line on the CMD with the star distance to the cluster centre.

The extinction towards the cluster is relatively high, and it increases the CMD spread. To reduce the effect of differential reddening, we used the same method as was applied to Palomar 6 in Souza et al. (2021) (adapted from Milone et al., 2012; Bedin et al., 2017). The

differential reddening map (bottom left panel of Figure 3.2) shows that $\delta E(B-V) \sim -0.04$, which is approximately 5% of the expected reddening (E(B-V)= 0.79; Harris, 1996), and which we can convert into a magnitude difference of $\delta m_{F438W} = +0.17$ and $\delta m_{F555W} = +0.13$, and into a difference in colour $\delta\,(m_{F438W} - m_{F555W}) = +0.04$.

Finally, to scale the photometry to the same zero-point as in the evolutionary models, we converted the AB magnitudes into the Vega system. The final sample corrected for differential reddening shows a smaller spread and a clear morphology from the RGB and HB to the lower MS (top right panel of Figure 3.2).

The ACS F438W/F555W photometry is saturated for magnitudes brighter than F555W$\sim$ 17. Therefore, our spectroscopic targets were not observed for these filters. To estimate the position of our stars in the CMD, we derived an approximation of their F438W and F555W magnitudes. We fixed the reddening, metallicity, and distance modulus from Harris (1996). For each star, we fitted the magnitudes J, K_S, G, G_{BP}, and G_{RP} (green triangles in Figure 3.2). We also used this method for a sample of RGB stars of the Gaia EDR3 from the Vasiliev and Baumgardt (2021) catalogue (open red circles). It is worth noting that the F438W filter is affected by variations in C, N, and O abundances. Hence, this filter can better be estimated via spectral convolution and integration with the filter response curve.

Spectral data reduction

The UVES spectra were obtained using the FLAMES-UVES setup centred at 580 nm, covering the wavelength range 480 - 680 nm, from the ESO Programs 083.D-0063 (A) (PI: S. Ortolani) and 099.D-0136 (A) (PI: M. Valentini). The latter ESO program was coordinated with the program GO11126 (PI: M. Valentini) for campaign 11 of the K2 satellite: the goal was to obtain asteroseismology for the giants in the sample GCs. However, obtaining reliable light curves for these stars was not possible. The log of observations is given in Table 3.1.

We performed the FLAMES-UVES data reduction procedure using the ESO-Reflex software with the UVES-Fibre pipeline (Ballester et al., 2000; Modigliani et al., 2004). The corresponding spectra of each star were corrected for the radial velocity computed using the Python library `PyAstronomy`. The radial velocities were obtained by cross-correlating the stellar spectra with the Arcturus spectrum (Hinkle et al., 2000). The values of the

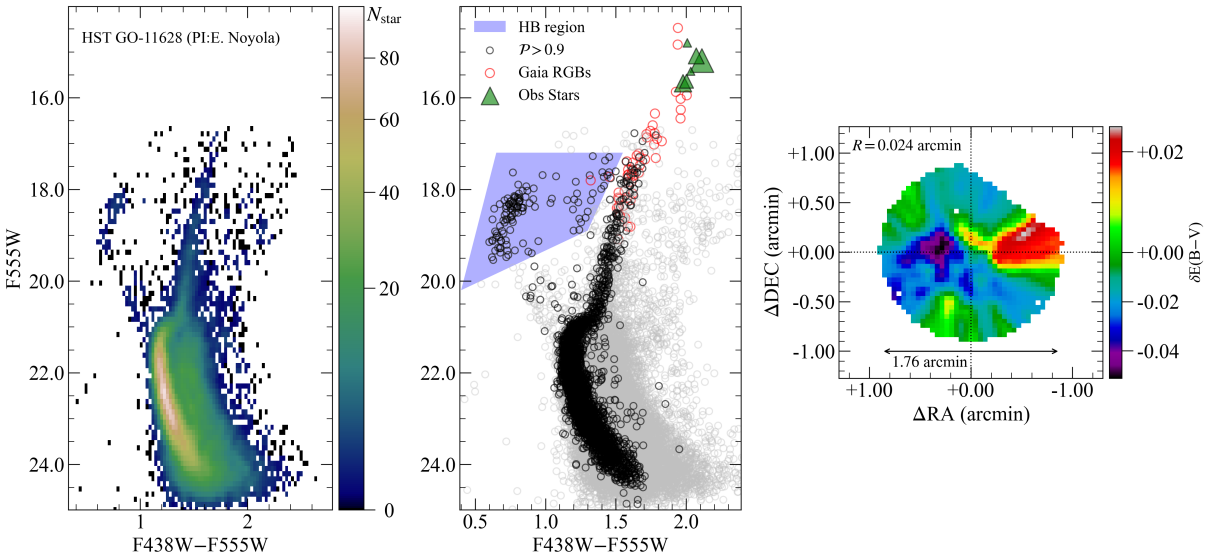

Figure 3.2: Photometric data processing. Left panel: All stars within the FOV obtained from the HST Project (GO-11628, PI: Noyola). Middle panel: Final differential-reddening-corrected CMD with selected stars (black) and discarded stars (grey). The Gaia EDR3 member stars from the Vasiliev and Baumgardt (2021) catalogue matched with 2MASS to obtain the HST are shown in red. The green triangles represent the spectroscopically observed stars with HST magnitudes obtained from the isochrone calibration, and the sizes are from the S/N. The HB region is plotted in blue. Right panel: Differential reddening map for stars within a half-light radius. The resolution of the map is 0.024 arcminutes (1.44 arcseconds).

Table 3.1 - Log of the spectroscopic FLAMES-UVES observations of programs 083.D-0063 (A) and 099.D-0136 (A), carried out in 2009 and 2017, respectively. The reported seeing and airmass are the mean values in the exposures. The last column contains the corresponding GIRAFFE setup, in which additional stars were observed.

Date	UT	exp (s)	Airmass	Seeing ($''$)	SETUP GIRAFFE
Program 083.D-0063 (A)					
2009-09-02	02:48:43	2700	1.455	1.88	H13-1
2009-09-01	01:03:00	2700	1.184	0.87	H13-2
2009-09-01	01:50:54	2700	1.191	0.72	H13-3
2009-09-13	23:32:32	2700	1.091	0.91	H13-4
2009-09-14	00:31:12	2700	1.182	0.82	H14-1
2009-09-14	01:17:51	2700	1.467	0.78	H14-2
2009-09-14	02:04:21	2700	1.848	0.75	H14-3
Program 099.D-0136 (A)					
2017-07-14	06:21:39	2400	1.751	0.75	H11-1
2017-07-14	04:34:44	2400	1.172	0.67	H11-2
2017-09-02	01:50:12	2400	1.279	0.61	H11-4
2017-09-07	02:53:12	2400	1.831	0.54	H13-1

heliocentric radial velocity of each spectrum and their mean values are presented in Table 3.2 for the member stars, selected from the membership analysis (see section 3.2).

The spectra of stars 1546 and 1239 from ESO Program 083.D-0063, have a low signal-to-noise ratio (S/N $<$ 15), which is significantly lower than those obtained from ESO

Program 099.D-0136. The spectra of these two stars are therefore strongly affected by noise, which makes it very difficult to distinguish strong lines and prevents a satisfactory radial velocity derivation from the cross-correlation method. For consistency, they can therefore not be confirmed as members of NGC 6355 given the uncertainties in their radial velocity values even though these stars are considered members from the proper-motion membership check. Consequently, the final observed star sample is composed of the four stars of ESO Program 099.D-0136.

Based on our final sample, we found a mean heliocentric radial velocity for NGC 6355 of -193.2 ± 1.1 km s^{-1}, which agrees well with the value of -194.6 ± 1.2 km s^{-1} obtained from the individual stars of Gaia DR2[2]. Finally, the normalized spectra were combined and were weighted by the median flux to obtain the final stellar spectra.

Table 3.2 - Heliocentric radial velocity obtained for each extracted spectrum and the average value for each star.

Target	V_r^{hel} km s^{-1}	σ_{V_r} km s^{-1}	**Target**	V_r^{hel} km s^{-1}	σ_{V_r} km s^{-1}
1546_1	−227.40	1.40	1239_1	−66.95	0.19
1546_2	−29.98	0.70	1239_2	−192.62	0.56
1546_3	−216.96	0.34	1239_3	−68.47	0.31
1546_4	−318.81	0.42	1239_4	−192.17	0.90
1546_5	−166.55	0.35	1239_5	−187.30	0.22
1546	−216.96	94.72	1239	−187.30	60.28
133_1	−192.92	0.47	1176_1	−196.35	0.56
133_2	−191.65	0.52	1176_2	−196.85	0.65
133_3	−192.80	0.48	1176_3	−193.25	0.69
133_4	−192.03	0.45	1176_4	−193.79	0.68
133	−192.41	0.53	1176	−195.07	1.56
1539_1	−192.25	0.41	1363_1	−193.93	0.41
1539_2	−192.36	0.40	1363_2	−194.01	0.40
1539_3	−192.30	0.41	1363_3	−192.44	0.40
1539_4	−191.90	0.41	1363_4	−192.34	0.39
1539	−192.27	0.18	1363	−193.18	0.79

Membership selection

The power of Gaia astrometry has been demonstrated in different ways, such as in the

[2] https://people.smp.uq.edu.au/HolgerBaumgardt/globular/appendix/ngc6355.txt

search for new open clusters and in the selection of the most probable members of a GC. In particular, regarding the latter, Gaia was not available until recent years, and now the membership probabilities should be verified in all samples preceding the Gaia era, and in particular for our sample stars.

To remove bias from our sample, we performed a membership analysis to determine which stars observed in both ESO programs are members of NGC 6355. Considering both programs, we have a total of nine stars. We selected the Gaia DR3 stars within 10′ from the cluster center, and we applied the Gaussian mixture models (GMM; Pedregosa et al., 2011) clustering method to separate the cluster members from the field stars. The derived mean proper-motion for NGC 6355 is $< \mu_\alpha^* >= -4.76 \pm 0.06$ mas yr^{-1} and $< \mu_\delta >= -0.58 \pm 0.05$ mas yr^{-1}. This agrees very well with the new values computed by Vasiliev and Baumgardt (2021).

The membership probabilities were computed considering cluster and field distributions, following the method presented in Bellini et al. (2009). When we had determined the membership probability, we cross-matched our sample stars with the Gaia data (Table 3.3.1), which are indicated with stars in Figure 3.3. We found that six of nine stars from both programs have membership probabilities above 80%. Combining the information of radial velocity and the proper-motion membership probability, we therefore disregard the non-member stars in the following analysis.

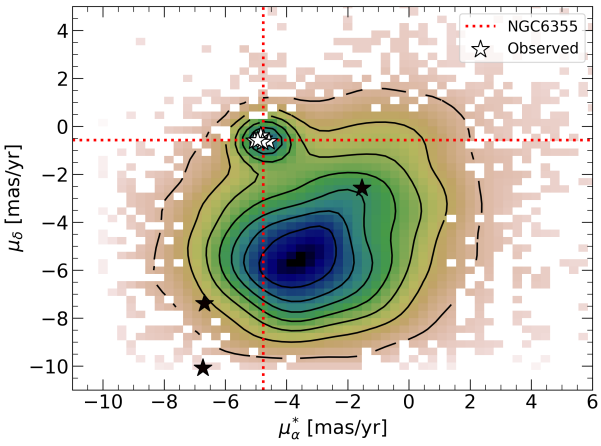

Figure 3.3: Proper-motion density map from Gaia DR3. The stars show all the observed stars in both programs (members are plotted in white, and non-members are given in black). The red lines show the position of the mean proper motion of NGC 6355.

3.3 Fundamental parameters

3.3.1 Atmospheric stellar parameters

Stellar magnitudes

The photometric effective temperature ($T_{\rm eff}$) and surface gravity ($\log g$) were derived from the $VIJHK_S$ magnitudes given in Table 3.3.1. For comparison purposes, we obtained the $T_{\rm eff}$ from the Transiting Exoplanet Survey Satellite (TESS) input catalogue (TIC; Stassun et al., 2018) for our sample. The 2MASS J, H, and K_S magnitudes were taken from Skrutskie et al. (2006). To obtain the $T_{\rm eff}$ from a wide wavelength range, we calculated the colour $V-I$ employing the photometric systems relations $G-V=f(G_{BP}-G_{RP})$ and $G-I=f(G_{BP}-G_{RP})$ from Gaia EDR3 (Riello et al., 2021).

Table 3.3 - Identifications, coordinates, magnitudes from JHK_s 2MASS survey, VI, HST/ACS, and matched Gaia DR3 information. The first two stars are from program 083.D-0063 (A), and the four last stars are from 099.D-0136 (A).

ID	ID	RA	DEC	V	$V-I$	J	H	K_S	F438W	F555W	$^{\dagger}\mu^*_\alpha$	μ_δ	G	BP−RP	S/N
	2MASS	(deg)	(deg)			2MASS			HST/WFC3		(mas yr^{-1})				
1546	17235883 − 2620183	260.996	−26.338	15.06	2.24	11.359	10.45	10.19	17.46	15.42	−4.747	−0.523	14.32	2.39	10.33
1239	17240227 − 2621267	261.010	−26.357	14.40	2.50	10.284	9.25	8.92	16.81	14.81	−4.839	−0.394	13.51	2.66	12.05
1539	17235356 − 2620223	260.973	−26.339	14.82	2.25	10.942	10.12	9.73	17.30	15.19	−4.780	−0.659	14.08	2.40	79.19
1363	17240101 − 2620597	261.004	−26.349	14.74	2.34	10.892	9.944	9.63	17.16	15.09	−4.942	−0.591	13.95	2.49	44.93
1176	17235712 − 2621441	260.988	−26.362	15.28	2.11	11.684	10.90	10.59	17.66	15.69	−5.041	−0.609	14.60	2.26	51.33
133	17235528 − 2621088	260.980	−26.352	15.30	2.24	11.435	10.62	10.21	17.64	15.64	−4.572	−0.635	14.56	2.39	36.36

$^{\dagger}\mu^*_\alpha = \mu_\alpha \cos\delta$.

Photometric effective temperatures $T_{\rm eff}$ and gravities $\log\ g$

The $T_{\rm eff}$ values were derived from $V-I$, $V-K_S$, and $J-K_S$ colour-temperature calibrations of Casagrande et al. (2010). To use the calibrations, we must perform the reddening corrections. For NGC 6355, we assumed the metallicity [Fe/H] = −1.33, $E(B-V)=0.77$, and $(m-M)_V=17.21$ from Harris (1996) . Table 3.4 lists the derived photometric effective temperatures. The $< T_{\rm eff} >$ value given in the fifth column is the mean effective temperature without the TESS values (which are too hot).

To derive the photometric $\log g$ value, we used the classical ratio $\log(g_*/g_\odot)$, where

Table 3.4 - Photometric parameters derived using calibrations by Casagrande et al. (2010) for $V-I$, $V-K$, $J-K$ colours are given in columns 2-8. In columns 9-14 are given the spectroscopic stellar parameters.

	Photometric parameters							Spectroscopic parameters					
ID	$T_{(V-I)}$ (K)	$T_{(V-Ks)}$ (K)	$T_{(J-Ks)}$ (K)	$<T_{eff}>$ (K)	BC_V	M_{bol}	$\log g$	T_{eff} (K)	$\log g$	[FeI/H]	[FeII/H]	[Fe/H]	v_t (km s^{-1})
1539	4359	4330	4297	4330	−0.615	−3.02	0.74	4300 ± 65	0.87 ± 0.23	−1.35 ± 0.11	−1.33 ± 0.18	−1.34 ± 0.15	1.0 ± 0.1
1363	4246	4315	4152	4246	−0.702	−3.19	0.64	4296 ± 76	0.84 ± 0.24	−1.36 ± 0.09	−1.35 ± 0.02	−1.36 ± 0.07	1.2 ± 0.1
1176	4573	4642	4660	4642	−0.481	−2.43	1.10	4580 ± 69	1.20 ± 0.26	−1.48 ± 0.08	−1.48 ± 0.23	−1.48 ± 0.17	1.0 ± 0.1
133	4373	4328	4250	4328	−0.606	−2.53	0.94	4378 ± 76	1.24 ± 0.19	−1.46 ± 0.07	−1.44 ± 0.17	−1.45 ± 0.13	0.9 ± 0.1

$\log g_\odot = 4.44$ is[3]:

$$\log g_* = 4.44 + 4\log\frac{T_{\rm eff}*}{T_\odot} + 0.4(M_{\rm bol} - M_{\rm bol\odot}) + \log\frac{M_*}{M_\odot}. \quad (3.1)$$

We adopted the values of $< T_{\rm eff} >$ from Table 3.4, $M_* = 0.85 M_\odot$ and $M_{\rm bol\odot} = 4.75$. The derived values of the photometric $T_{\rm eff}$ and $\log g$ are given in the left columns of Table 3.4.

Spectroscopic stellar parameters

The final spectroscopic stellar parameters $T_{\rm eff}$, $\log g$, and the microturbulence velocity v_t of NGC 6355 were derived together with [Fe/H] based on excitation and ionization equilibria. Equivalent widths (EW) for a list of lines of FeI and FeII lines were measured using DAOSPEC (Stetson and Pancino, 2008). Using a visual inspection of the stellar spectrum, we remeasured some lines with the IRAF routine to evaluate the impact of blending lines, mainly for FeII, and some lines that were poorly fitted with DAOSPEC. The employed lines are listed in the appendix (Table B.3) with the adopted oscillator strengths ($\log gf$) for FeI lines obtained from the VALD3 and NIST databases (Piskunov et al., 1995; Martín et al., 2002) and for FeII lines from Meléndez and Barbuy (2009).

We extracted 1D photospheric models for our sample using the MARCS grid of atmospheric models (Gustafsson et al., 2008). The adopted CN-mild models consider [α/Fe]= +0.20 for [Fe/H]= −0.50 and [α/Fe]= +0.40 for [Fe/H]≤ −1.00. For the solar Fe abundance, we adopted ϵ(Fe) = 7.50 (Grevesse and Sauval, 1998).

The mean photometric $< T_{\rm eff} >$ and $\log g$ values calculated in Section 3.3.1 were assumed as initial guesses to derive the spectroscopic parameters. The method consists of

[3] This equation is the same as Equation 2.1 in Chapter 2. It is repeated here because this chapter represents another paper (as mentioned before).

obtaining the excitation and ionization equilibrium of FeI and FeII lines. Figure 3.4 shows the excitation and ionization equilibrium for star 133. The derived spectroscopic parameters T_{eff}, $\log g$, [FeI/H], [FeII/H], [Fe/H], and v_t are presented in the right columns of Table 3.4.

To derive the final metallicity, we generated a Monte Carlo (MC) sample for each star to construct their [FeI/H] and [FeII/H] distributions[4]. The distributions composed of the individual MC sample of each star are shown in Figure 3.5 as grey and red for [FeI/H] and [FeII/H], respectively. Finally, the cluster metallicity distribution was obtained by combining the two distributions (grey and red). The best metallicity value, the corresponding standard deviation, and the error of the mean are [Fe/H]$= -1.39 \pm 0.15\,(0.08)$. This metallicity agrees well with the Carretta et al. (2009) metallicity scale, which gives a value of [Fe/H] $= -1.33 \pm 0.02$ for NGC 6355.

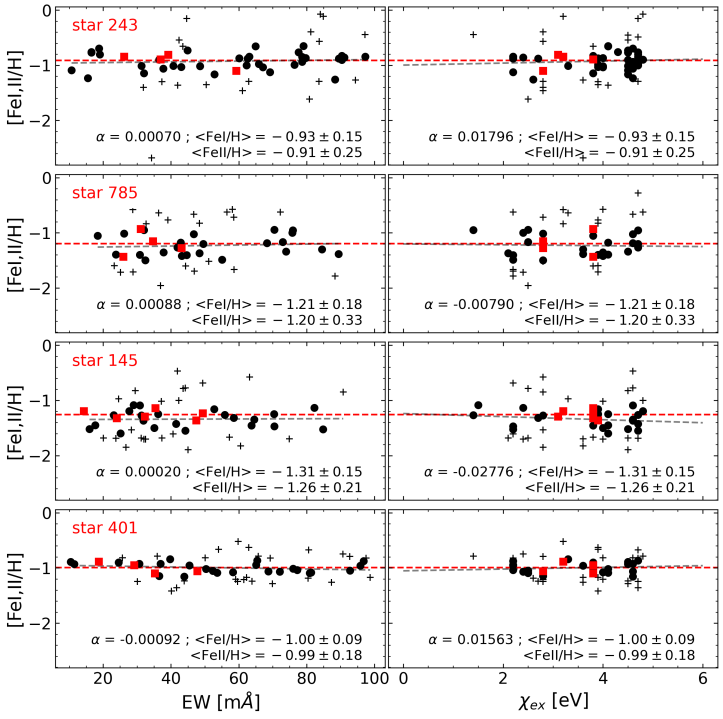

Figure 3.4: Ionization and excitation equilibria for NGC 6355 star 133. The black dots and red squares correspond to the [FeI/H] and [FeII/H] lines, respectively. The crosses are the FeI lines that were excluded through a 3σ clipping method.

[4] This method is an improvement of the procedure employed in Souza et al. (2021) and described in Chapter 2.

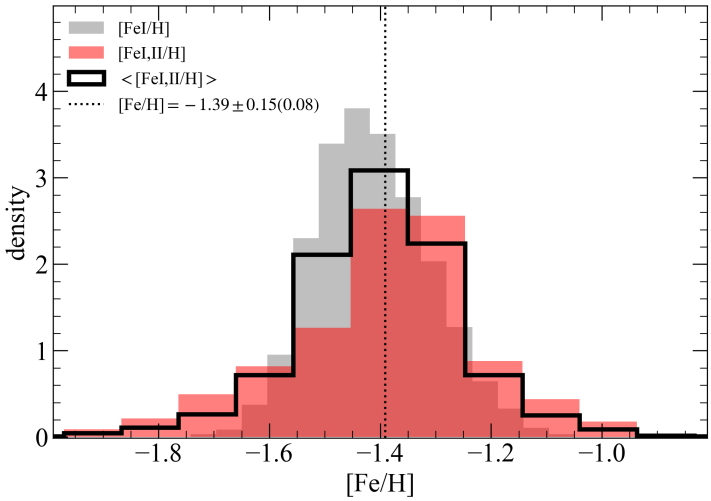

Figure 3.5: Metallicity distribution from sample stars of NGC 6355. The final distribution (black step histogram) considers both [FeI/H] (grey) and [FeII/H] (red) for all lines of our sample member stars.

3.3.2 Age and distance

We employed the `SIRIUS` code (Souza et al., 2020) to perform the isochrone fitting to the CMD [F555W, F438W-F555W] of NGC 6355. The code can provide a Bayesian view of the fundamental parameters age, reddening ($E(B-V)$), $d_{\odot}$, and metallicity ([Fe/H]). We adopted the isochrones from the Dartmouth Stellar Evolutionary Database (Dotter et al., 2008) with a further linear interpolation in age and [Fe/H] with the random values given by the algorithm. As a Gaussian prior for the metallicity, we employed the value derived in this work, while for the other parameters, we adopted uniform priors: 10 Gyr $\leq$ age $\leq$ 14 Gyr, E(B−V) $\geq$ 0.0, and $d_{\odot} \leq$ 20 kpc. We used the CMD structure constraints similar to the procedure described by VB13 to improve the code. Nevertheless, we kept the Bayesian nature of the code and used the structure pattern of the CMD as priors.

The direct comparison between observational data and isochrones cannot give an accurate physical interpretation of the cluster (D'Antona et al., 2018) because the likelihood in this case is purely geometrical. Therefore, the prior distributions are of great importance to improve the method. In that sense, we adopted a more robust prior to the magnitude of the horizontal branch (HB). This prior is crucial to give a more precise distance derivation when it is very close to the magnitude level of RR Lyrae stars. To constrain the HB magnitude, we employed the relation by Recio-Blanco et al. (2005):

$$M_{F555W}^{ZAHB} = 0.981 + 0.410 \times [M/H] + 0.061 \times [M/H]^2, \tag{3.2}$$

where $[M/H] = [Fe/H] + \log\left(0.638 \times 10^{[\alpha/Fe]} + 0.362\right)$. We assumed $[\alpha/Fe] = +0.4$ because this is the expected value for GCs with a similar metallicity (Barbuy et al., 2018b). Then, we recalculated the magnitude level for each iteration of the Markov chain Monte Carlo (McMC) sampling. For the apparent magnitude of the HB, we assumed $m_{F555W}^{ZAHB} = 17.9 \pm 0.1$ by a visual inspection, which is very close to the value derived by Ortolani et al. (2003) of $V_{HB} = 17.8 \pm 0.2$.

Another morphological parameter is the magnitude difference between zero-age HB (ZAHB) and the turn-off point (TO), also known as vertical parameter (Vandenberg et al., 1990; Rosenberg et al., 1999). However, this parameter is strongly dependent on the ZAHB level. Because of this, we decided to use the horizontal parameter (Vandenberg et al., 1990; Rosenberg et al., 1999). The horizontal parameter is the colour difference between the TO and the point at the RGB that is 2.5 magnitude brighter than the TO.

In order to implement the horizontal method in the observed CMD, we computed the fiducial or ridge line of NGC 6355 using the method described in Marín-Franch et al. (2009). The procedure is briefly described as follows. We first computed a simple fiducial line by binning the cluster magnitude and calculating the median colour for each bin. We applied a differential binning method to have more points around the TO. The second step was to derive the median colour perpendicular to each bin. This method is most important for the subgiant branch (SGB) because this sequence is almost horizontal for bluer filters. Finally, the algorithm computes the horizontal parameter for the cluster fiducial line and each McMC isochrone.

The posterior distributions of the parameters are given by the $50th$ percentile as the best value, and the $16th$ and $84th$ percentiles to provide the uncertainties (right corner plots of Figure 3.6). In Figure 3.6, the NGC 6355 CMD (left panel) is over-plotted by the best solution of the isochrone fitting composed of the median value (solid line) and the 1σ region (shaded region).

Because the expected extinction is relatively high, it is necessary to consider the $T_{\rm eff}$ correction to the isochrones. It is worth noting that the $T_{\rm eff}$ correction effect increases with the temperature and changes the isochrone morphology. The method is well described in

Oliveira et al. (2020) and Souza et al. (2020). We found the following equations:

$$A_{\rm F438W}/A_V = 7.688 - 86.606x + 325.254x^2 - 407.219x^3 \quad (3.3)$$

$$A_{\rm F555W}/A_V = 12.043 - 135.394x + 507.496x^2 - 634.233x^3 \quad (3.4)$$

$$A_{\rm J}/A_V = -0.128 + 1.428x - 5.309x^2 + 6.573x^3 \quad (3.5)$$

$$A_{\rm K_S}/A_V = 0.061 - 0.677x + 2.522x^2 - 3.134x^3 \quad (3.6)$$

$$A_{\rm G}/A_V = 4.346 - 48.867x + 183.277x^2 - 229.296x^3 \quad (3.7)$$

$$A_{\rm G_{BP}}/A_V = 6.899 - 77.627x + 291.243x^2 - 364.345x^3 \quad (3.8)$$

$$A_{\rm G_{RP}}/A_V = -0.154 - 1.695x - 6.175x^2 + 7.449x^3, \quad (3.9)$$

where x is $\log {\rm T_{eff}}$. The immediate effect on the isochrone is an offset in the direction of the CMD blue-brighter region. Therefore, the horizontal ($E(438-555)$) and vertical ($(m-M)_{\rm F555W}$) displacements should be different from those without a correction. In addition, the morphology is defined essentially by the age and metallicity when the helium mass fraction (Y) is fixed (see Souza et al., 2020). In our case, the metallicity was constrained to the value derived here from high-resolution spectroscopy. Therefore, only age changes the isochrone morphology. Because of this, the age considering the $T_{\rm eff}$ correction tends to be older than the simple isochrone fitting. The result is shown in Figure 3.6.

In this work, we derived the absolute age of 13.2 ± 1.1 Gyr for NGC 6355. The considerable uncertainty on the age derivation is due to the narrow colour baseline adopted in this work (F438W-F555W), which spread the TO region slightly more. Although we provide the first absolute age for NGC 6355 through isochrone fitting, KC16 derived an age of ~ 12.5 Gyr using integrated magnitudes, and C21 reported the age as 13.2 Gyr for NGC 6355 by comparing its CMD with that of NGC 6205. The age derived in this work assuming the $T_{\rm eff}$ correction agrees very well with the age in C21+VB13. This illustrates the importance of this correction for highly reddened clusters in the central part of the Galaxy.

Nataf et al. (2016) discussed the extinction towards GCs located in the Galactic bulge, where the R_V value can be as low as 2.5. Pallanca et al. (2021) reported a straightforward method for determining the best value of R_V for highly reddened clusters. The method was also applied by Souza et al. (2020), who derived a value of 2.6 for Pal 6. The method for deriving the R_V consists of simultaneously fitting CMDs with different colour baselines with the same set of reddening and distance. Here we fitted (in addition to the HST CMD)

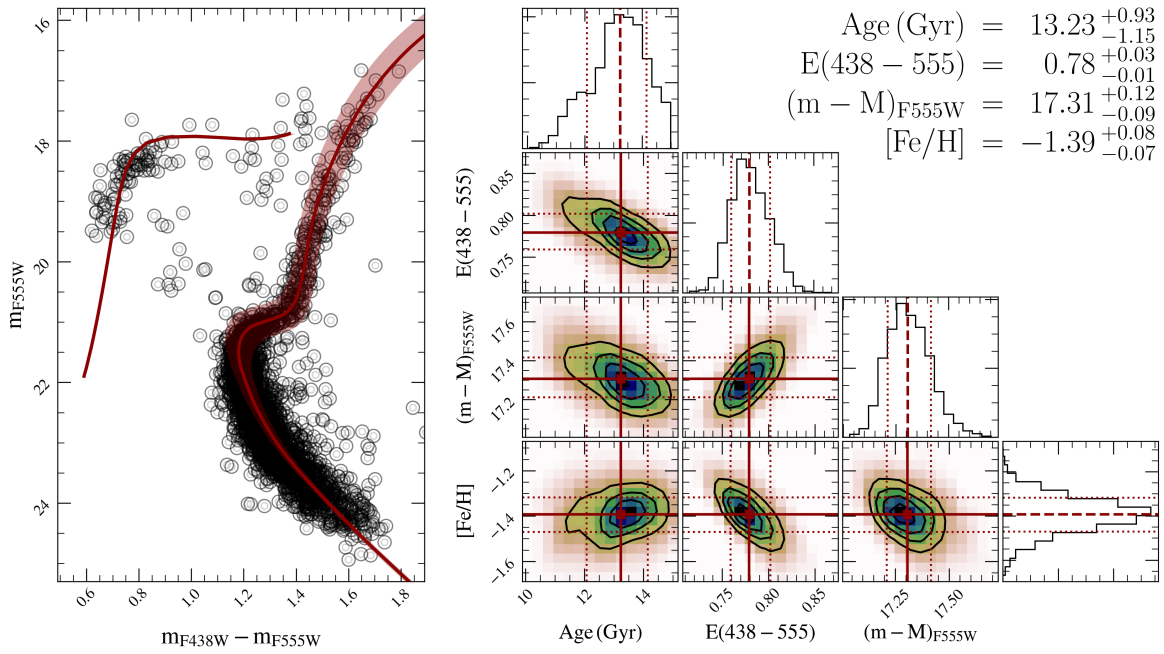

Figure 3.6: Isochrone fitting for NGC 6355. The best solution is composed of the median values of the posterior distributions (solid dark red line), and the 1σ extrapolation is constructed from the $16th$ and $84th$ percentiles (shaded dark red region). The corner plot shows the correlations among the parameters.

the CMDs $[J,\, J-K_S]$ from Valenti et al. (2007) and $[G,\, G_{\rm BP}-G_{\rm RP}]$ from Gaia DR3. From the HST CMD, we found $E(438-555) = 0.78 \pm 0.03$ and $(m-M)_{\rm F555W} = 17.31 \pm 0.12$. These values were converted into $E(B-V)$ and $(m-M)_0$ for different values of R_V, as shown in Figure 3.7. The best R_V is the mean between the best values for Valenti et al. (2007) and Gaia DR3 CMDs. We find $R_V = 2.84 \pm 0.02$. Hence, for NGC 6355 with the derived R_V, we find $E(B-V) = 0.89 \pm 0.03$ and $\mathrm{d}_\odot = 8.54 \pm 0.19$ kpc.

The distance value is crucial for deriving the orbital parameters of the clusters, as demonstrated by Pérez-Villegas et al. (2020) and illustrated by the case of Palomar 6, as discussed in Souza et al. (2021). To verify our distance derivation, we collected the RR Lyrae star members of NGC 6355 from the fourth data release of the Optical Gravitational Lensing Experiment (OGLE-IV; Soszyński et al., 2019). We adopted the calibrations from (Gaia Collaboration et al., 2017, G17) using the least-squares (LQS) and Bayesian (BA) methods (Muraveva et al. (2018, M18), and Oliveira et al. (2022, O22)). All distances are displayed in Figure 3.8, including the derivation by Baumgardt and Vasiliev (2021, B22) [5]. The value of 8.54 ± 0.19 kpc derived in this work agrees well with the others, particularly the B22 value of 8.65 ± 0.22 kpc, which is the most recent value.

[5] https://people.smp.uq.edu.au/HolgerBaumgardt/globular/fits/disfit/ngc6355_dist.pdf

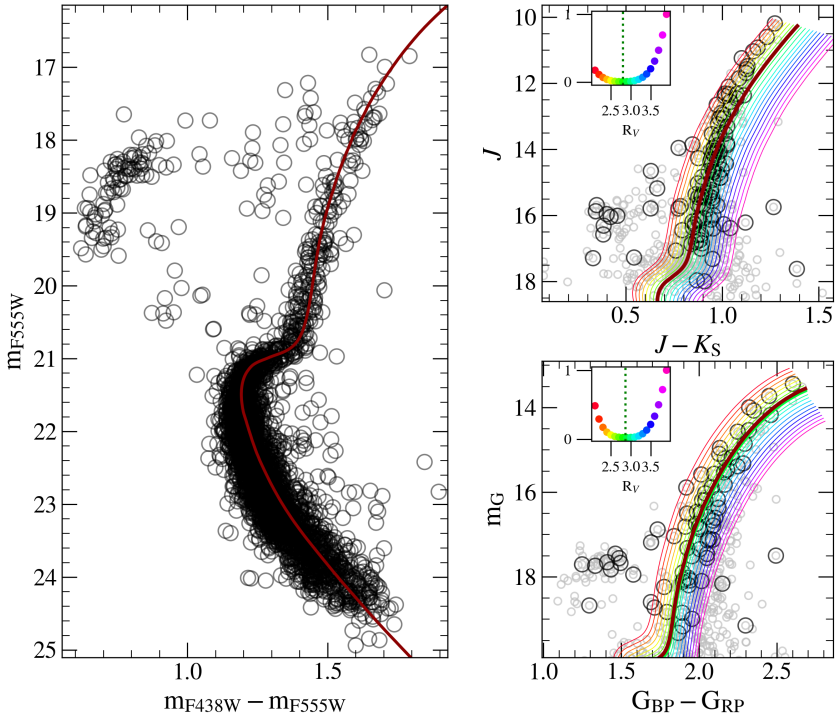

Figure 3.7: Simultaneous isochrone fitting to derive the cluster R_V using three CMDs: HST (left panel), 2MASS JK_S from Valenti et al. (2007) (top right panel), and Gaia DR3 (bottom right panel). The isochrones are coloured according to their R_V value. In each panel, the best solution is represented by the solid dark red isochrone. For the two right panels, the χ^2 analysis is plotted in the inset plot, and the dots are coloured by the same colour as the corresponding isochrone.

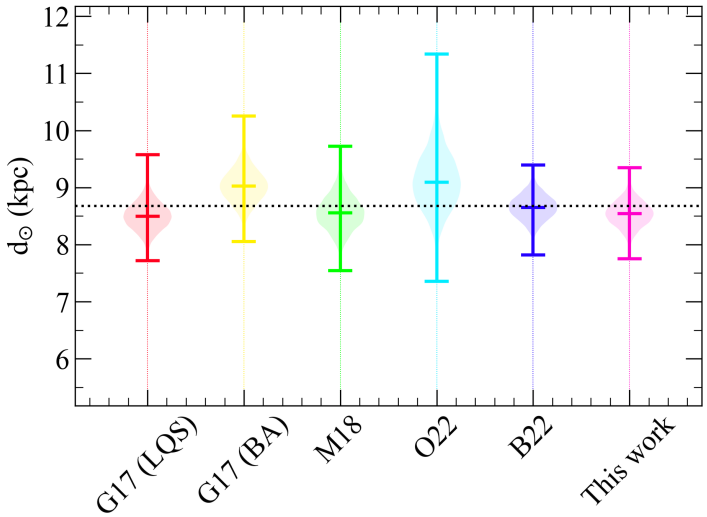

Figure 3.8: Our distance derivation compared with the literature. The violins show the distance distribution using RR Lyrae stars, the recent distance derivation by Baumgardt and Vasiliev (2021), and the distance found in this work through isochrone fitting. For the derived RR Lyrae distances, four calibrations were adopted that are represented by the first four violins (see the text).

3.4 Abundance analysis

We carried out a detailed abundance analysis employing line-by-line spectrum synthesis.

We employed the spectrum synthesis code PFANT (Barbuy et al., 2018a) to derive the abundances of the elements C, N, O, Na, Mg, Al, Si, Ca, Ti, V, Mn, Co, Cu, Zn, Y, Zr, Ba, La, Nd, and Eu. The line list with the abundance ratios for each line are given in the appendix (Table B.4). The code PFANT is an update of the Meudon code by M. Spite and adopts local thermodynamic equilibrium (LTE). The atomic line list is from VALD3 (Ryabchikova et al., 2015).

The abundance values were derived through the χ^2 minimization algorithm described in detail in Souza et al. (2021). Figure 3.9 gives a visual illustration of the method for star 1363, where the observed spectrum around the lines NaI 5682.633Å and AlI 6698.673Å is shown in black. The best-fit solution is the solid red line. For completeness, we also compare the spectrum without the abundance contribution of the current element (solid green line), the best fit plus 0.15 (solid magenta line), and the best fit minus 0.15 (solid cyan line). Finally, we adopted the solar abundances from Grevesse et al. (2015).

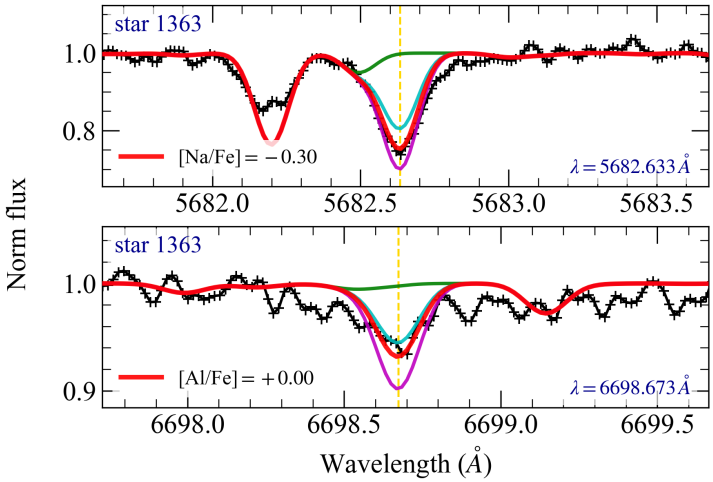

Figure 3.9: Example of line-profile fitting for star 1363. The upper panel shows the result for the NaI 5682.633Å, and the bottom panel shows the fit for the AlI 6698.673Å line. The black lines correspond to the observed spectra. The solid red line shows the best-fit solution as the median. For comparison purposes, we also plot the best-fit solution with a variation of ±0.15 (solid cyan and magenta lines) and the spectrum without the element abundance (green line).

C, N, and O abundances

The CNO abundances were derived through an iterative fitting of the C_2(1,0) Swan bandhead at 5635.3Å, and CN(6,2) at 6478.48Å of the $A^2\Pi X^2\Sigma$ system band heads and the forbidden oxygen line [OI] 6300.31Å. The algorithm fits the three lines simultaneously

and takes the interdependent continuum variation due to changes in C, O, and N values into account. Table 3.5 lists the derived abundances. Because the region of the C_2(1,0) bandhead is strongly affected by the S/N and the line is weak, we assumed the C abundances as upper limits. Finally, before fitting the [OI] line, we verified the contamination by telluric lines in this region and concluded that for our sample, none of the stars has telluric line contamination on the [OI] line. The spectral fitting for C, N, and O for star 1363 are shown in Figure 3.10.

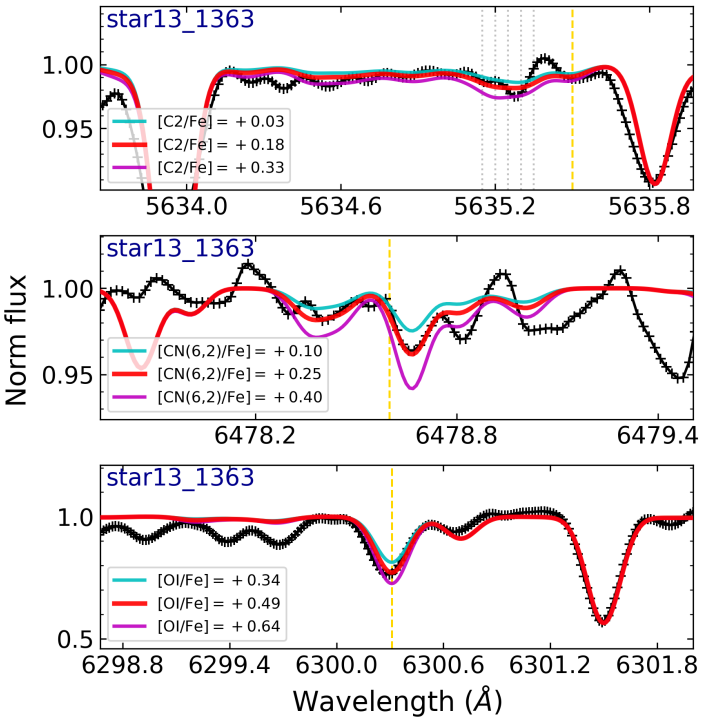

Figure 3.10: Spectral fitting of C, N, and O for star 1363. The observed spectrum is given in black. The solid red line is the best fit, and the cyan and magenta lines show the best fit ±0.15, respectively. The yellow line shows the line region. For C_2 (upper panel) we also show the bandhead lines in dotted silver lines.

As expected for most GCs (Piotto et al., 2015; Milone et al., 2017), NGC 6355 seems to host multiple stellar populations (MPs; see the reviews Gratton et al., 2004, 2012; Bastian and Lardo, 2018a; Milone and Marino, 2022). The relatively high nitrogen abundance of stars 1176 and 133 with relatively low values of carbon abundances indicates the presence of MPs in NGC 6355. The other two stars have a relatively low N abundance and relatively normal (solar) C. Because stellar evolution theory predicts an N-C anti-correlation, we must further investigate to confirm the presence of MPs in NGC 6355. This is further analysed below.

Table 3.5 - Carbon, nitrogen, and oxygen abundances from C_2, CN bandhead, and [OI], respectively.

	[C/Fe]	[N/Fe]	[O/Fe]
Star	C_2	CN(6,2)	[OI]
	5635.50Å	6478.60Å	6300.31Å
1539	$\leq +0.10$	+0.21	+0.43
1363	$\leq +0.18$	+0.25	+0.49
1176	$\leq +0.00$	+0.87	+0.37
133	≤ -0.09	+0.70	+0.24

alpha-elements

The α-elements O and Mg are the most reliable indicators of enrichment in α-elements from hydrostatic phases of massive stars (Woosley and Weaver, 1995). Together with the explosive α-elements Si and Ca, they are good indicators of a fast early enrichment of the proto-cluster gas by supernovae type II (SNII). Ti is classified as an iron-peak element (Woosley and Weaver, 1995), but shows a similar α-element behaviour and is often included as another α-element. The spectral fitting results for Mg, Si, Ca, and Ti of star 1363 are shown in Figure 3.11, and the results are presented in Table 3.6.

Odd-Z elements

The sodium abundances were derived from NaI 5682.633Å, 5688.194Å, 6154.23Å, and 6160.753Å lines. The Al abundances were derived from lines AlI 6696.185Å, 6698.673Å.

The (anti-)correlations indicating the effect of MPs are shown in Figure 3.12. We also calculated the Spearman correlation parameter for each combination. For N-Al, we found a strong correlation, and the anti-correlation for N-O, Na-O, and Al-O is high. Moreover, the main correlations come from the nitrogen abundances (Fernández-Trincado et al., 2022). However, [Al/Fe]= +0.30 is also a threshold for second-generation (2G) stars (Meszaros et al., 2020). The figure shows a visible separation of our sample into two groups: two stars are moderately rich in N and Al, and two stars have low values of [Al/Fe]. This affects their mean abundances (Table 3.6). This is further discussed below.

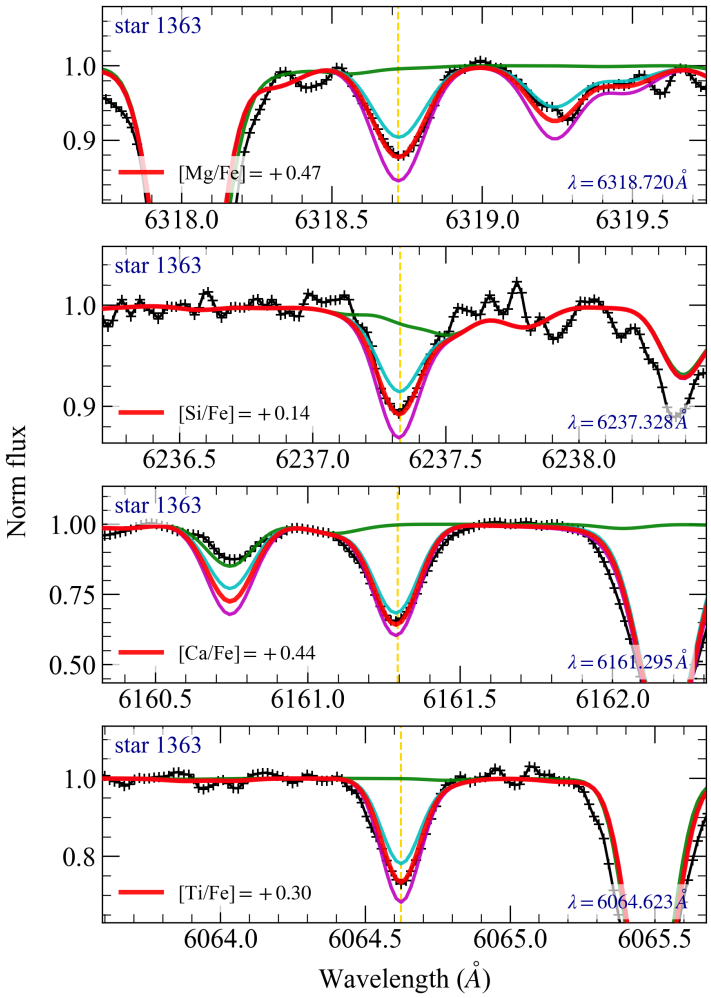

Figure 3.11: Same as figure 3.10 for Mg, Si, Ca, and Ti. The solid red line is the best fit, and the cyan and magenta lines show the best fit ±0.15, respectively.

Iron-peak elements

We derived the abundances of the iron-peak elements V, Mn, Co, Cu, and Zn. While V and Mn are members of the lower iron-peak element group, Co, Cu, and Zn are considered to belong to the upper iron-peak group (Woosley and Weaver, 1995). The first group is mainly produced in type Ia supernovae (SNIa) with a contribution from core-collapse supernovae (Nomoto et al., 2013, and refereces therein). In contrast, Co, Cu, and Zn are predominantly produced by core-collapse supernovae (Woosley et al., 2002, and references therein). The atomic lines were adopted from Ernandes et al. (2018) and Ernandes et al. (2020), together with their hyperfine structure. The spectral fitting results for V, Mn, and Co are shown in Figure 3.13 for star 1363, and Cu and Zn are given in Figure 3.14 for star 1539.

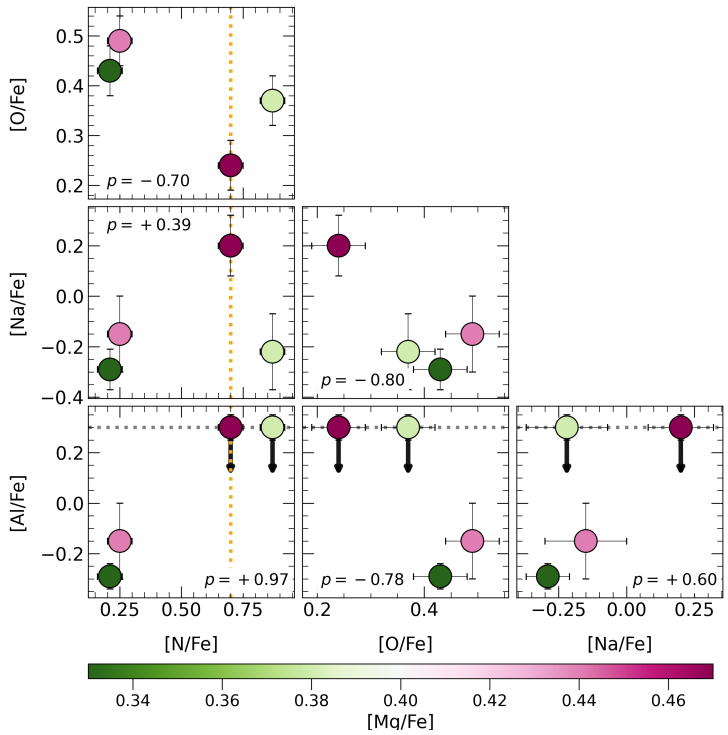

Figure 3.12: (Anti-)Correlations indicating effects of multiple stellar populations. The dotted orange line in both left panels represents the transition to the N-rich regime at [N/Fe]$\sim$ 0.7 for [Fe/H] around the NGC 6355 value (Fernández-Trincado et al., 2022). Additionally, the grey line in the two bottom panels shows the upper limit for first-generation stars (Meszaros et al., 2020). The colour bar shows the Mg abundances.

Heavy elements

The abundances of the heavy neutron-capture s-elements Y, Zr, Ba, La, and Nd, and the r-element Eu also were derived. For Y, we measured the YI 6435.004Å and the YII 6613.73Å lines, and we assumed for the mean that the ionized species of Y contributes with 99% to the abundance. For the barium abundance, we used the BaII lines 5853.675Å, 6141.713Å, and 6496.897Å, with hyperfine structure from Barbuy et al. (2014). The ZrI 6127.47Å, 6134.58Å, 6140.535.58Å, and 6143.25Å, LaII 6262.287Å, 6320.376Å, and 6390.477Å, NdII 6740.078Å, 6790.372Å, and 6549.525Å, and EuII 6437.6Å and 6645.1Å were used for Zr, La, Nd, and Eu. The spectral fitting results for Y, Zr, Ba, La, Eu, and Nd are shown in Figures 3.15 for star 1363.

Errors

The uncertainties in spectroscopic parameters are given in the last four columns of Table 3.6 for star 133. For each stellar parameter, we adopted the usual uncertainties

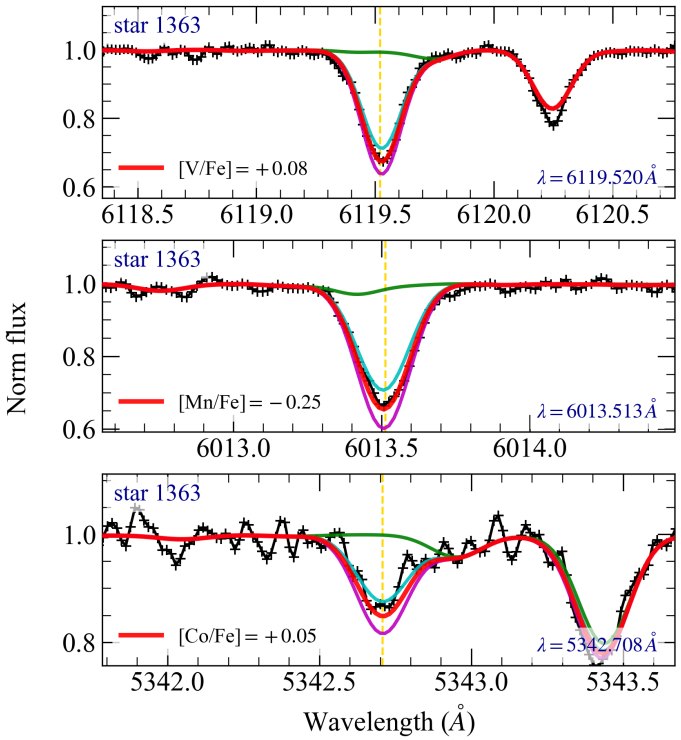

Figure 3.13: Same as figure 3.10 for V, Mn, and Co. The solid red line is the best fit, and the cyan and magenta lines show the best fit ±0.15, respectively.

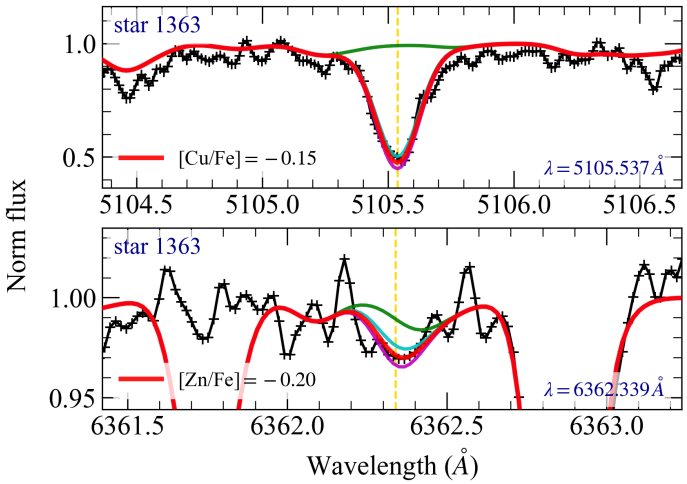

Figure 3.14: Same as figure 3.10 for Cu and Zn. The solid red line is the best fit, and the cyan and magenta lines show the best fit ±0.15, respectively.

for similar samples (Barbuy et al., 2014, 2016, 2018b). The sensitivities were computed by employing models with these modified parameters and recomputing lines of different elements considering changes of $\Delta T_{\rm eff}$ = +100 K, Δlog g= +0.2, Δv_t = 0.2 km s^{-1}. The given error is the difference between the new and the adopted abundance. The uncertainties due to non-LTE effects are negligible for these stellar parameters, as discussed in Ernandes

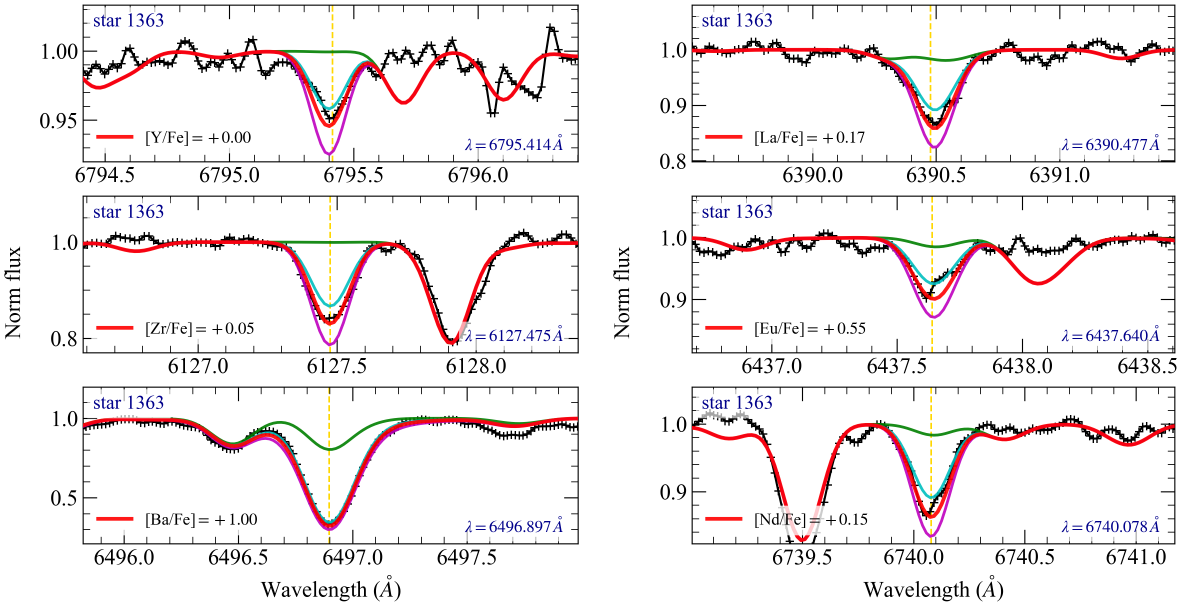

Figure 3.15: Same as figure 3.10 for Y, Zr, and Ba on the left, and for La, Eu, and Nd on the right. The solid red line is the best fit, and the cyan and magenta lines show the best fit ±0.15, respectively.

et al. (2018). The same error analysis and estimations can be applied to other stars in our sample. It is worth noting that star 133 has the lowest S/N of the four sample stars. The uncertainties given in Table 3.6 can therefore be considered as upper limits. The faint La lines appear to be more reliable than the strong Ba lines. Finally, it is important to note that the main uncertainties in stellar parameters are due to uncertainties in the $T_{\rm eff}$, as shown in Table 3.6.

3.5 Dynamical properties

In order to obtain the orbital parameters of NGC 6355, we employed an axisymmetric potential McMillan (2017) adopting the Python package `galpy` (Bovy, 2015). We integrated a set of 1000 initial conditions forward for 10 Gyr. The set was generated by using a MC algorithm adopting the observational uncertainties of the cluster data on proper motions μ_α^* and μ_δ, heliocentric radial velocity, and the heliocentric distance. The McMillan (2017) Galactic potential was adopted to compare our results with those of Massari et al. (2019) and to relate NGC 6355 with its plausible progenitor. A more realistic potential, including a contribution of the Galactic bar (Pérez-Villegas et al., 2018, 2020), could provide a farther inward orbit for the GC members of the Galactic bulge. The orbital parameters are listed in Table 3.7, including the values of the IOM.

Table 3.6 - Abundances in the four UVES member stars. The mean values were computed considering all four stars (< all >), considering only 1G stars (< 1G >), and only 2G stars (< 2G >). The last four columns show the abundance sensitivity due to variation in atmospheric parameters for star 15 (133) considering uncertainties of ΔT_{eff} = 100 K, Δlog g = 0.2, and Δv_t = 0.2 km s^{-1}, and the last column is the total error. These errors were taken into account when we composed the final reported abundances.

[X/Fe]	star 1539	star 1363	star 1176	star 133	< all >	< 1G >	< 2G >	ΔT	$\Delta \log g$	Δv_t	$(\frac{1}{3}\sum x^2)^{1/2}$
	1G		2G					K		kms^{-1}	
C	+0.10 ± 0.05	+0.18 ± 0.05	+0.00 ± 0.05	−0.09 ± 0.05	+0.05 ± 0.11	+0.14 ± 0.06	−0.04 ± 0.07	+0.02	+0.03	+0.00	+0.03
N	+0.21 ± 0.05	+0.25 ± 0.05	+0.87 ± 0.05	+0.70 ± 0.05	+0.51 ± 0.29	+0.23 ± 0.05	+0.78 ± 0.10	+0.12	+0.08	+0.00	+0.08
O	+0.43 ± 0.05	+0.49 ± 0.05	+0.37 ± 0.05	+0.24 ± 0.05	+0.38 ± 0.11	+0.46 ± 0.06	+0.30 ± 0.08	+0.00	+0.03	+0.00	+0.03
Mg	+0.33 ± 0.05	+0.44 ± 0.05	+0.38 ± 0.05	+0.47 ± 0.05	+0.41 ± 0.07	+0.39 ± 0.07	+0.42 ± 0.07	+0.02	−0.02	−0.03	+0.03
Si	+0.27 ± 0.10	+0.25 ± 0.12	+0.33 ± 0.15	+0.28 ± 0.27	+0.28 ± 0.16	+0.26 ± 0.11	+0.30 ± 0.21	−0.02	−0.02	−0.07	+0.04
Ca	+0.48 ± 0.16	+0.47 ± 0.10	+0.34 ± 0.26	+0.57 ± 0.12	+0.46 ± 0.18	+0.47 ± 0.13	+0.45 ± 0.22	+0.26	+0.04	−0.08	+0.16
Ti	+0.30 ± 0.12	+0.34 ± 0.12	+0.28 ± 0.12	+0.38 ± 0.10	+0.33 ± 0.12	+0.32 ± 0.12	+0.33 ± 0.12	−0.03	+0.09	−0.06	+0.06
Na	−0.29 ± 0.08	−0.15 ± 0.15	−0.22 ± 0.15	+0.20 ± 0.12	−0.11 ± 0.23	−0.22 ± 0.14	−0.01 ± 0.25	+0.10	−0.00	−0.05	+0.06
Al	−0.29 ± 0.05	−0.15 ± 0.15	< +0.30 ± 0.05	< +0.30 ± 0.05	< +0.04 ± 0.28	−0.22 ± 0.12	< +0.30 ± 0.06	+0.08	−0.00	−0.02	+0.05
Y	+0.20 ± 0.07	−0.00 ± 0.07	−0.00 ± 0.07	—	+0.06 ± 0.12	+0.10 ± 0.12	−0.00 ± 0.07	+0.24	+0.09	−0.14	+0.17
Zr	−0.06 ± 0.08	+0.09 ± 0.08	—	−0.11 ± 0.26	−0.02 ± 0.16	+0.02 ± 0.11	−0.11 ± 0.26	+0.20	+0.02	−0.01	+0.12
Ba	+0.84 ± 0.17	+0.93 ± 0.09	+0.92 ± 0.19	+1.02 ± 0.16	+0.93 ± 0.17	+0.89 ± 0.14	+0.97 ± 0.19	+0.02	+0.03	−0.13	+0.08
La	+0.08 ± 0.12	+0.06 ± 0.08	+0.10 ± 0.07	+0.27 ± 0.05	+0.13 ± 0.12	+0.07 ± 0.10	+0.19 ± 0.11	+0.03	+0.09	−0.02	+0.06
Eu	+0.53 ± 0.05	+0.55 ± 0.05	+0.57 ± 0.08	+0.60 ± 0.10	+0.56 ± 0.07	+0.54 ± 0.05	+0.59 ± 0.09	−0.03	+0.07	−0.02	+0.05
Nd	+0.47 ± 0.06	+0.28 ± 0.10	+0.06 ± 0.08	−0.30 ± 0.05	+0.13 ± 0.30	+0.38 ± 0.12	−0.12 ± 0.19	+0.03	+0.09	−0.03	+0.06
V	+0.03 ± 0.06	+0.19 ± 0.10	−0.33 ± 0.06	+0.00 ± 0.08	−0.03 ± 0.20	+0.11 ± 0.11	−0.17 ± 0.18	+0.20	+0.02	−0.07	+0.12
Mn	−0.34 ± 0.05	−0.42 ± 0.10	−0.39 ± 0.13	−0.43 ± 0.08	−0.39 ± 0.10	−0.38 ± 0.09	−0.41 ± 0.11	+0.11	−0.00	−0.02	+0.06
Co	+0.03 ± 0.05	+0.07 ± 0.05	+0.07 ± 0.09	+0.16 ± 0.11	+0.08 ± 0.09	+0.05 ± 0.06	+0.11 ± 0.11	+0.15	+0.04	−0.00	+0.09
Cu	−0.35 ± 0.05	−0.07 ± 0.07	−0.12 ± 0.17	−0.17 ± 0.17	−0.18 ± 0.16	−0.21 ± 0.15	−0.15 ± 0.18	+0.13	+0.04	−0.09	+0.09
Zn	−0.30 ± 0.05	−0.20 ± 0.05	−0.30 ± 0.05	−0.10 ± 0.05	−0.23 ± 0.10	−0.25 ± 0.07	−0.20 ± 0.11	+0.01	+0.03	−0.06	+0.04
[Fe/H]	−1.34 ± 0.15	−1.36 ± 0.07	−1.48 ± 0.17	−1.45 ± 0.13	−1.39 ± 0.08	−1.35 ± 0.09	−1.46 ± 0.13	+0.10	+0.10	+0.04	+0.08

Figure 3.16 shows the density probability map of the orbits of NGC 6355 in the $x - y$ and $R - z$ projections. The space region in which the orbits of NGC 6355 cross more frequently are shown in orange, and the black curves are the orbits considering the central values of the observational parameters. NGC 6355 is mostly confined within $\sim$ 2.6 kpc and therefore has a high probability of belonging to the bulge component ($> 95\%$) when we adopt the distance of 8.54 ± 0.22 kpc that we estimated in this work. Our new distance derivation indicates that the cluster NGC 6355 lies far inward based on its maximum height of $|z| < 2.1$ kpc and the high eccentric orbit > 0.8. It may well be that this perigalactic distance is one the closest distances to the Galactic center.

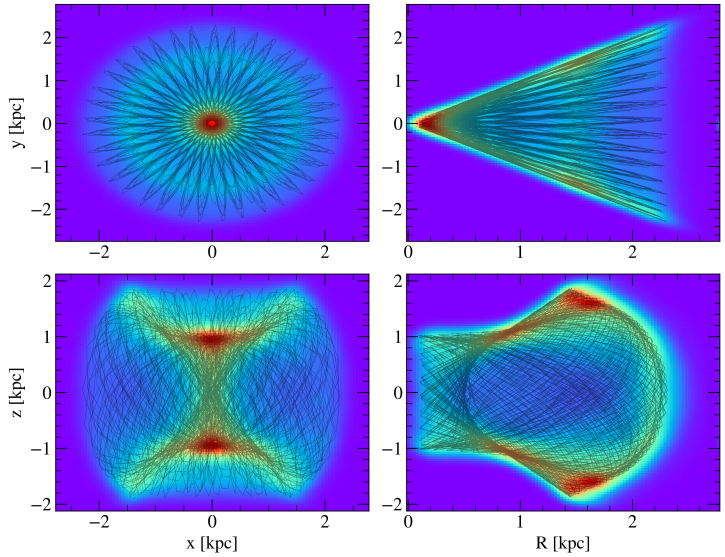

Figure 3.16: Density probability map for the $x-y$ and $R-z$ projections of the set of orbits for NGC 6355. Orange corresponds to higher probabilities, and the black lines show the orbits using the main observational parameters.

Table 3.7 - Orbital parameters, velocities, and membership probabilities.

Parameter	Mean	Unit
E	-2.31 ± 0.03	$\times 10^5 \mathrm{km^2\,s^{-2}}$
L_Z	-31.28 ± 24.42	$\mathrm{km\,s^{-1}kpc}$
r_{peri}	0.25 ± 0.08	kpc
r_{apo}	2.46 ± 0.14	kpc
$\lvert z\rvert_{max}$	1.91 ± 0.08	kpc
ecc	0.82 ± 0.05	—
v_R	-218.27 ± 66.25	$\mathrm{km\,s^{-1}}$
v_ϕ	-192.39 ± 34.54	$\mathrm{km\,s^{-1}}$
$\mathcal{P}_{\mathrm{bulge}}$	95.00	%
$\mathcal{P}_{\mathrm{disk}}$	5.00	%
$\mathcal{P}_{\mathrm{inner\,halo}}$	0.00	%
$\mathcal{P}_{\mathrm{outer\,halo}}$	0.00	%

Chapter 4

A GC like star lost in the Galactic bar

The results presented in this chapter were submitted to Nature (Souza et al. submitted) with some modifications due to the journal copyright rules.

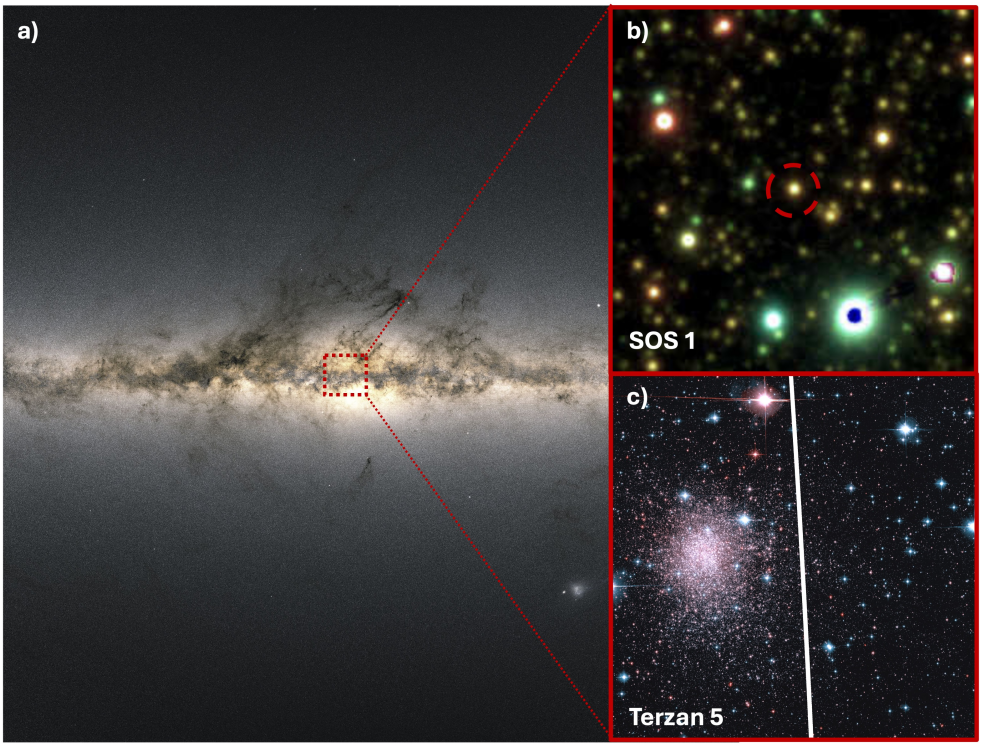

Figure 4.1: Colorful image presenting the SOS1 star and Terzan 5. Panel (a) shows the Gaia all-sky view of the Milky Way based on measurements of almost 1.7 billion stars. Panel (b) shows the PanSTARRS y/i/g combined image of SOS1 star, and panel (c) the F110W/F160W combined colour image from HST of Terzan 5. Credit:ESA/Gaia/DPAC, CC BY-SA 3.0 IGO

4.1 Introduction

The bar structure is the most prominent component in the inner Galaxy. It extends up to approximately 5 kpc from the Galactic centre and is tilted by around 25° with respect

to the Sun position Portail et al. (2017). Even though the Galactic bar formation happens through a gravitational instability of the disk, it is still under debate whether the bar formed earlier ($\sim$ 8 Gyr ago Bovy et al., 2019; Wylie et al., 2022; de Sá-Freitas et al., 2023) or more recently in the Galaxy evolution timeline ($\sim$ 3 Gyr ago Nepal et al., 2024). Due to the dynamical mechanisms that the bar induces in the Galaxy, it captures material over time. Nevertheless, obtaining observational evidence for this process is a complex task because almost all objects in the bar have already lost their origin signatures. Therefore, investigating the nature of the material that composes the bar needs additional information beyond dynamics (e.g., chemical composition and age).

To show the bar trapping effect, we analysed the star 2M17454705-2639109 (hereafter SOS1), which is part of the sample observed with the NASA-Kepler project K2GO4_2-0125 (PI: M. Valentini) in the K-2 Campaign 11, targeting the Galactic Bulge/thick disc region. We crossmatched the K2 sample with APOGEE DR17, obtaining chemical abundances and atmospheric parameters for all stars. After that, we crossmatched the resulting table with Gaia DR3. The information is listed in Table 4.1. This star is located within the innermost part of the MW ($l = 1.97°$ and $b = 1.16°$) in a heliocentric distance of $\sim$ 6.9 kpc. These values place SOS1 confined into the inner Galaxy with a bar-shape orbit (blue line in Figure 4.2).

We integrated the orbits 13 Gyr backwards using the newest Galactic potential constructed using the method made-to-measure and that fits very well the Galactic centre, the focus of the present work, including the bar and X-shape structures (Portail et al., 2017; Sormani et al., 2022). We used the analytic approximation implemented with the AGAMA code by Sormani et al. (2022). For each object, SOS1 and all MW GCs, we generated 500 initial conditions considering the errors in proper motion, radial velocity, and distance.Â The orbital parameters are listed in Table 4.1.

We employed the orbital criteria by Portail et al. (2015) to compute the probability of the object orbits to support the bar structure. To do that, for each orbit (corresponding to one initial condition), we computed the frequencies in the X, Z, and R directions through a Fourier transformation. With these frequencies, we can analyse the ratios fR/fx and fR/fx, which provide a numerical interpretation of how many radial or vertical excursions the orbits have for one loop. Orbits that support the bar structure must be confined no farther than the corotation radius (which is around 6 kpc for the Galactic Potential

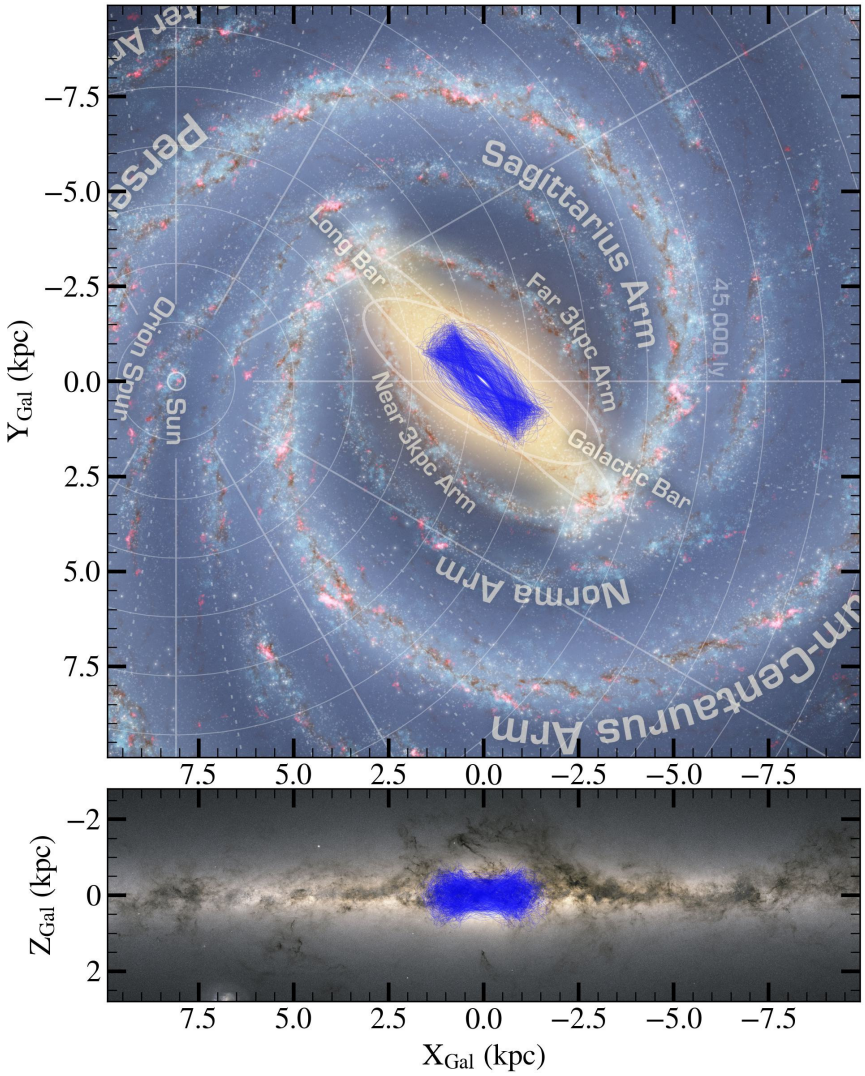

Figure 4.2: Proojections face-on X-Y (upper) and edge-on X-Z (bottom) of the Galaxy with the orbit of SOS1 star in blue line. The colorful face-on image of the Galaxy is from NASA/JPL-Caltech/R. Hurt (SSC/Caltech) while the edge-on picture is Gaia all-sky view of the Milky Way based on measurements of almost 1.7 billion stars created by ESA/Gaia/DPAC.

employed here) and also has fR/fx = 2.0±0.1 (Portail et al., 2015). Therefore, we compute the fR/fx ratio and the apogalactic distance for each orbit. After that, the final probability of following the bar ($\mathcal{P}_{\rm bar}$) for the object is the number of orbits with fR/fx = 2.0±0.1 and with apogalactic distance lower than 6kpc divided by the total of the initial conditions (in this case, 500).

Since we are working with a Galactic potential, which includes a non-axisymmetric bar component that rotates, the total energy (E_T) and the z component of the angular momentum (L_Z) are not conserved during the orbit. Nonetheless, the Jacobi energy (E_J) is conserved if we move in the bar rotating frame. The E_J, in units of mass, is calculated as follows:

$$E_J = \frac{1}{2}\mathbf{V}'^2 + \Phi(\mathbf{r}') - \frac{1}{2}\Omega^2\left(x'^2 + y'^2\right) \tag{4.1}$$

where Ω is the pattern speed of the bar, assumed to be -39 km/s/kpc (Portail et al., 2017).

SOS1 exhibits an abundance pattern of α-[1] and light-elements[2] (Figure 4.3) different than expected for the field stellar population of the bar (Queiroz et al., 2021). Even though the high N and Al abundances were already observed in many field stars (Fernández-Trincado et al., 2022), this abundance pattern cannot be explained by stellar evolution alone, indicating that this kind of star (therefore SOS1 as well) is more likely to come from another part of the Galaxy, being GCs the perfect environment to for these chemical anomalies (Bastian and Lardo, 2018a; Milone and Marino, 2022).

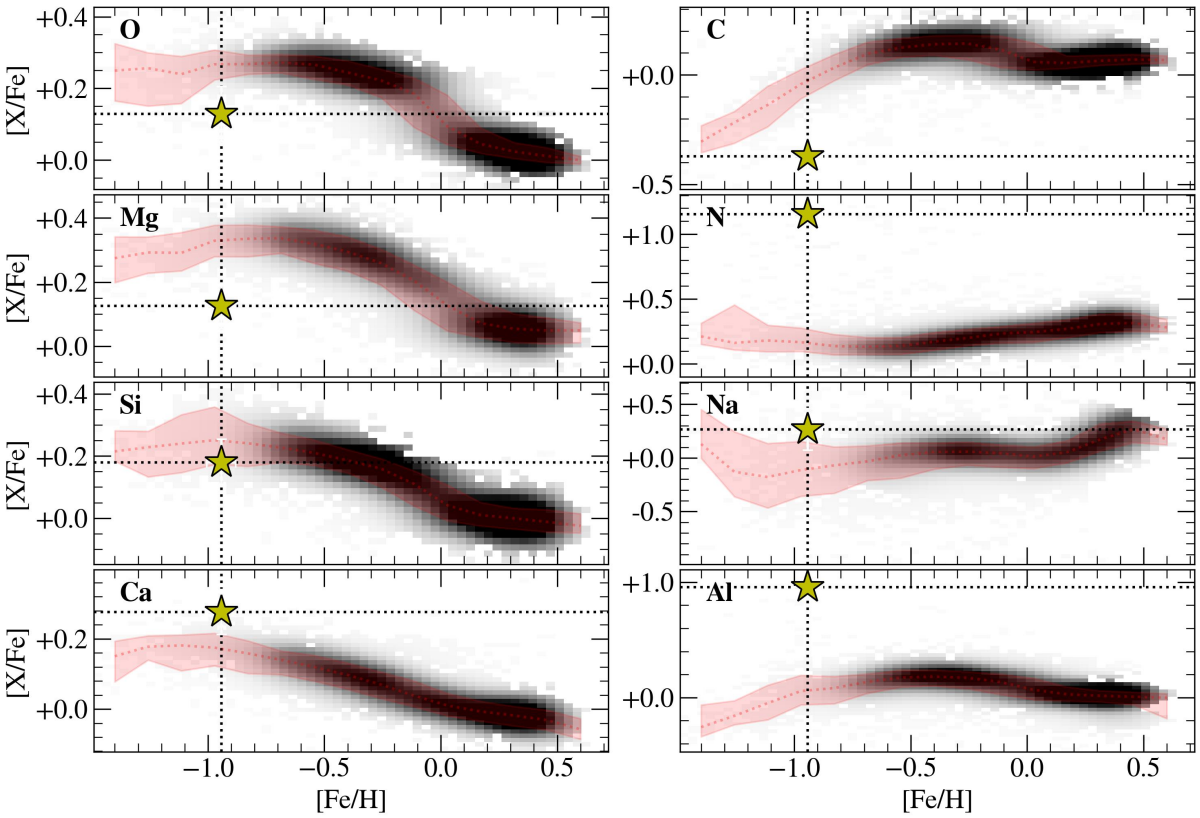

Figure 4.3: Abundances of α and light-elements for SOS1 (yellow star symbol) compared with field stars in the inner Galaxy (density plot). The red dotted line shows the mean locus of field stars, while the red shared region represents the 1σ interval.

[1] Elements created by summing up of He nuclei. Here: Oxygen, Magnesium, Silicon, and Calcium.

[2] Low atomic number elements. Here: Carbon, Nitrogen, and Aluminium.

Table 4.1 - Atmorspheric and chemical information of SOS1 and STARB stars. We added 50K to the temperature and 0.05 dex in the abundance errors.

	SOS1		STARB	
APOGEE ID	2M17454705-2639109		2M07273047-7511343	
μ^*_α	-1.45 ± 0.10		$+5.12 \pm 0.01$	
μ_δ	-6.20 ± 0.06		-4.72 ± 0.01	
T_{eff} (K)	4366 ± 61		4357 ± 62	
$\log g$	1.51 ± 0.04		1.51 ± 0.04	
SNR	129		117	
RUWE	1.008		1.078	
ASPCAPFLAG	0		0	
STARFLAG	0		0	
	Value	FLAG	Value	FLAG
[Fe/H]	-0.94 ± 0.06	0	-1.07 ± 0.06	0
[C/Fe]	-0.37 ± 0.08	0	-0.36 ± 0.08	0
[N/Fe]	$+1.15 \pm 0.08$	0	$+0.11 \pm 0.08$	0
[O/Fe]	$+0.13 \pm 0.08$	0	$+0.28 \pm 0.08$	0
[Mg/Fe]	$+0.13 \pm 0.07$	0	$+0.19 \pm 0.07$	0
[Ca/Fe]	$+0.35 \pm 0.08$	0	$+0.14 \pm 0.09$	0
[Si/Fe]	$+0.18 \pm 0.07$	0	$+0.17 \pm 0.08$	0
[Na/Fe]	$+0.27 \pm 0.14$	0	$+0.32 \pm 0.18$	0
[Al/Fe]	$+0.96 \pm 0.08$	0	-0.16 ± 0.09	0
[Mn/Fe]	-0.17 ± 0.08	0	-0.34 ± 0.09	0
[V/Fe]	$+0.14 \pm 0.13$	0	$+0.16 \pm 0.09$	0
[Ce/Fe]	$+0.43 \pm 0.08$	0	-0.18 ± 0.08	0
[Co/Fe]	$+0.23 \pm 0.11$	0	-0.78 ± 0.13	0

4.2 Chemical analysis

From the Apache Point Observatory Galactic Evolution Experiment (APOGEE; Allende Prieto et al., 2008)) data release 17 (DR17), SOS1 presents high nitrogen (N) and aluminium (Al) abundances ([N/Fe]$>$ 1.0, [Al/Fe]$>$ 1.0) and a carbon (C) depletion ([C/Fe]$<$ -0.2), being in good agreement with the Galactic ArchaeoLogIcaL Excavati-Ons (GALILEO; Fernández-Trincado et al., 2022). This chemical pattern is characteristic of the GC multiple stellar populations phenomenon, where GCs present a peculiar chemical pattern showing abundance variation star-by-star mainly regarding light elements sodium (Na) and Al, also for C, N, O, and metallicity [3] for more complex GCs (Carretta et al., 2009, 2012; Meszaros et al., 2020). The most significant variation is in N abundance, which can differ one dex star-by-star, followed by depletion in O and C. The well-known Na-O anticorrelation is also evidence of MPs (Carretta et al., 2012). The SOS1 O abundance (+0.13) is slightly lower than those observed in GCs ($\sim$ +0.40), and the Na abundance (+0.27) is higher than the solar value, indicating that SOS1 come from a Na-O anticorre-

[3] Here in the form of iron abundance [Fe/H].

lated population. These N-Al-enhanced stars are called the second stellar generation (2G) since they are supposed to be formed after the cluster formation by atmosphere pollution of first-generation stars (1G) or by a new star formation burst. However, the origin of MPs is still under debate (Bastian and Lardo, 2018a; Milone and Marino, 2022). Table 4.1 presents the APOGEE DR17 information for SOS1. Since the parameter errors are sometimes sub-estimated by the ASPCAP pipeline, we added 50 K to the final error in effective temperature and 0.05 dex in the abundance error of all elements. We also provide the ASPCAP flag for SOS1 and the flag in each abundance.

We verified the high N-Al abundances of SOS1 through a double-check. First, we selected a star with similar atmospheric parameters gravity log g, effective temperature T_{eff}, metallicity [Fe/H], and SNR as SOS1, but with solar N and Al. The selected star (hereafter STARB) has APOGEE ID 2M07273047-7511343 (the information of STARB star is in Table 4.1). Figure 4.4 shows the direct comparison between SOS1 and STARB spectra. The upper panels compare the Al abundance for the lines 16718.90Å (left) and 16763.30Å (right). The blue line represents the STARB, while the SOS1 is in red. The direct comparison for N abundances is in the bottom panels. This analysis clearly shows the difference between both spectra for Al and N.

For the second verification method, we remeasured Al, C, and N abundances through spectrum synthesis using the `MOOG2017` code with solar abundances adopted from Asplund et al. (2009). Figure 4.5 shows the spectral fitting for the Al lines 16718.90Å (upper left) and 16763.30Å (upper right), where the very high Al abundance is made clear from a comparison with the synthetic spectra for different [Al/Fe] values. For the C and N abundances (bottom panel), we overplotted synthetic spectra with different combinations of C, N, and O abundances between 15300.00Å and 15400.00Å. We can see that, on average, the SOS1 observed spectrum is well reproduced by the high N and low C, as provided by APOGEE DR17.

The validation experiments showed that the abundances provided by APOGEE DR17 for SOS1 are recovered, which is also expected due to the SNR$>$ 50, RUWE (renormalised unit weight error) below 1.4, and `APSCAPFLAGs`$=0$. These quality cuts are similar to the recent studies using APOGEE DR17 data (Hasselquist et al., 2021; Queiroz et al., 2021; Horta et al., 2021; Limberg et al., 2022; Horta et al., 2023, , among others). Therefore, we can rely on the hypothesis that SOS1 is a 2G star.

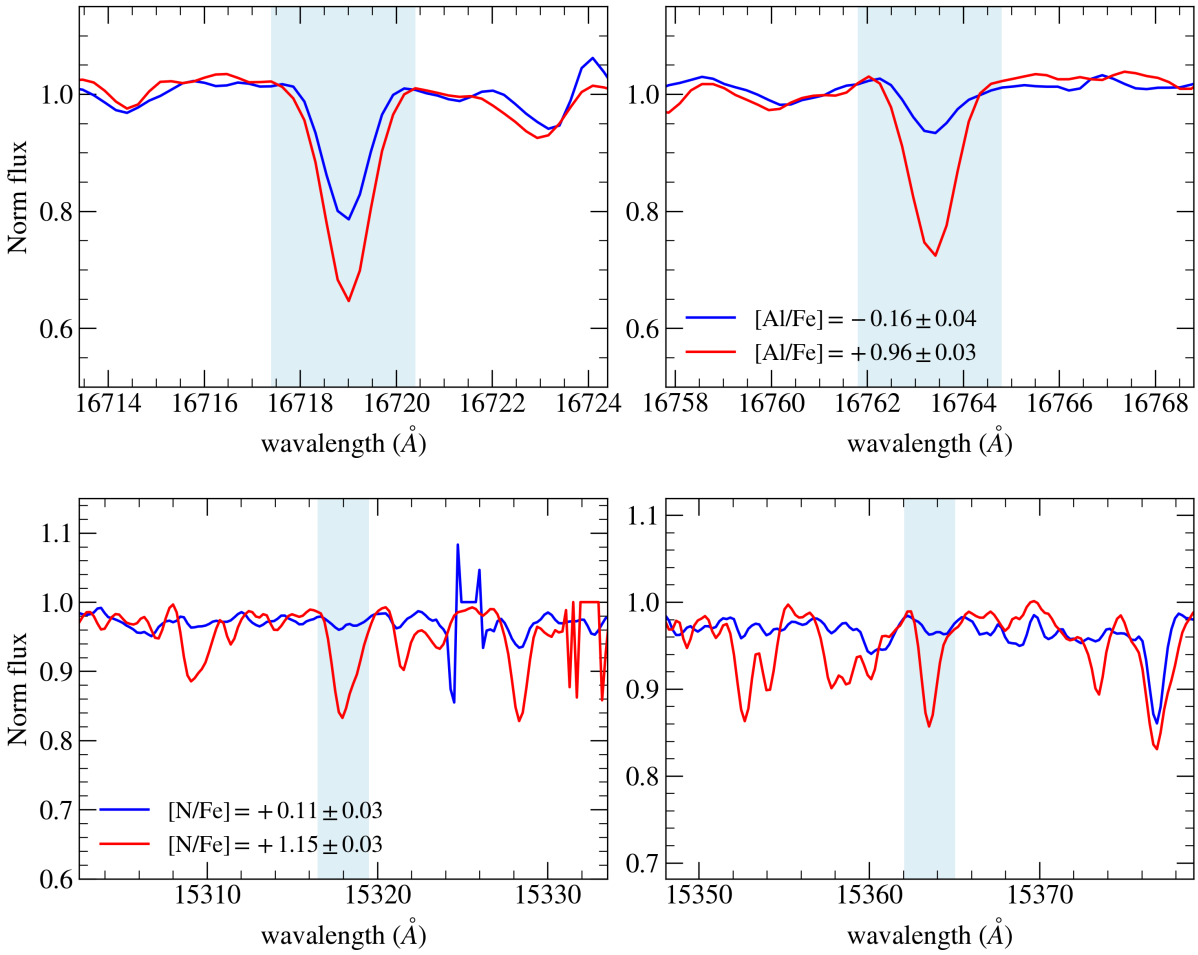

Figure 4.4: Verification of the APOGEE-ASPCAP abundances of Al (upper panels) and N (bottom panels): comparison of spectra of the sample star SOS1 (red line) with a reference star with similar stellar parameters and solar abundances (blue line). The dots are the observed spectrum.

4.3 Dynamical properties

The assumption of SOS1 coming from a GC has two main scenarios. For instance, the star could have been ejected from the cluster due to a strong encounter (e.g. star - binary interaction), resulting in a star with a velocity larger than 10^3 km s^{-1} (hypervelocity star Weatherford et al., 2023), the SOS1, however, presents a maximum velocity of $\sim$ 300 km s^{-1}. On the other hand, the GCs that are tidally interacting with the bar can lose stars to the Galaxy via tidal stripping, mainly those stars placed in the outer parts of the cluster (Moreno et al., 2022). The star is then captured slowly during several passages of the GC through the bar. In this case, the captured star might retain the original dynamical signature in the Jacobi energy (E_J) for more time. Assuming that the parent cluster of

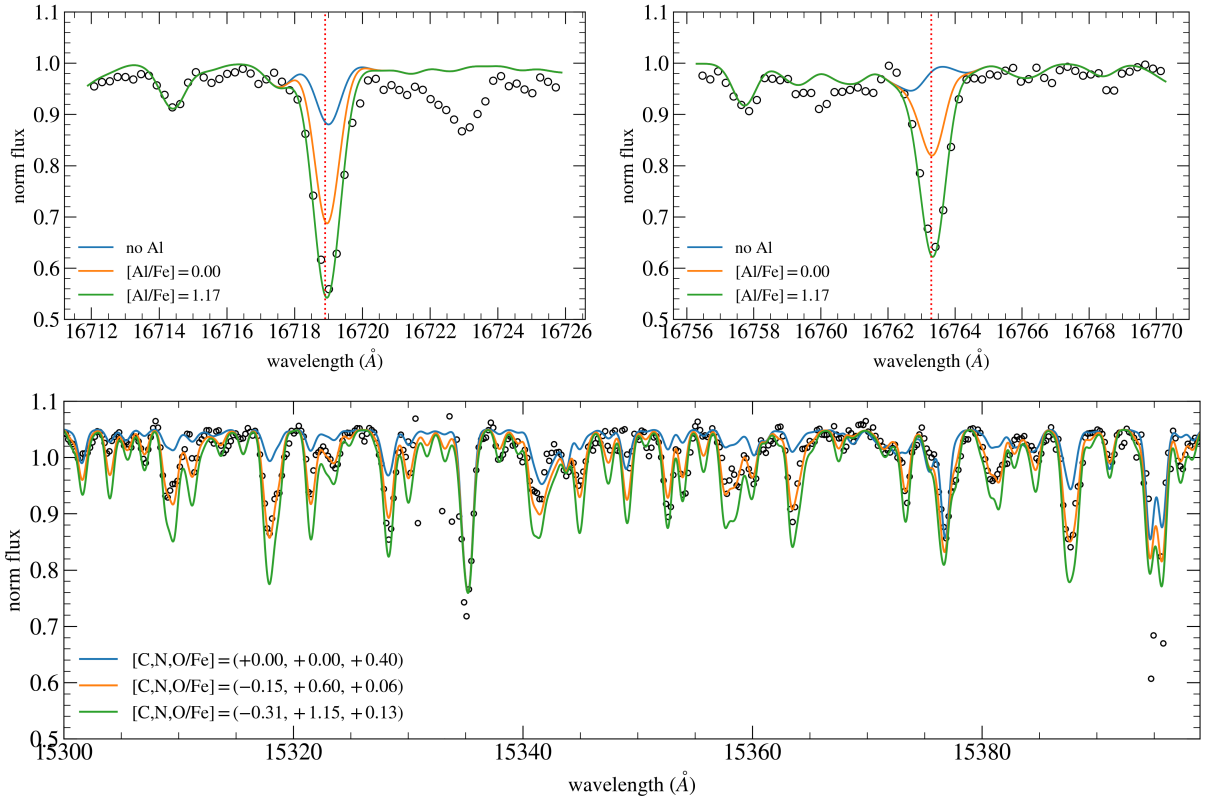

Figure 4.5: Verification of APOGEE-ASPCAP abundances. Upper panels: Spectrum synthesis of Al. The coloured lines represent synthetic spectra with no Al abundance (blue), solar Al abundance (orange), and [Al/Fe]= 1.17 (green, the value provided by APOGEE). Bottom panels: Spectrum synthesis of C, N, and O. The blue line is the normal CNO abundance set [C, N, O/Fe]= $(0.0, 0.0, +0.40)$, orange line [C, N, O/Fe]= $(-0.15, +0.60, +0.06)$, and green line [C, N, O/Fe]= $(-0.31, +1.15, +0.13)$ the set provided by APOGEE.

SOS1 is still orbiting the MW[4], we selected the GCs with E_J compatible within 1σ with the E_J of SOS1 (Figure 4.6, left panel), this sample is composed of the most probable SOS1's parent clusters. The closest GC to SOS1 with similar E_J is Terzan 5 (Figure 4.6, right panel). However, SOS1 is far from the cluster centre a distance equivalent to six tidal radii of Terzan 5, showing that it is no longer gravitationally bound to any cluster. The parameters for the selected clusters were taken from Baumgardt's compilation and are listed in Table 4.2.

[4] A third approach could be that the parent cluster was completely destroyed during the Galaxy evolution. However, we did not find any tracer of a remnant stellar population due to the dynamical mixing of the inner Galaxy. This lack of information is one caveat of this work.

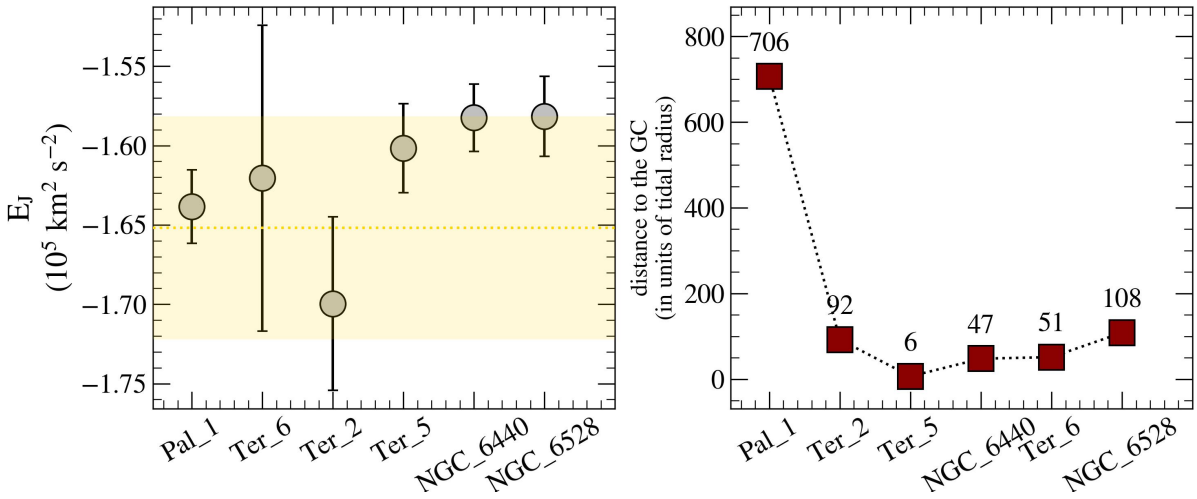

Figure 4.6: Dynamical selection of most propable parent clusters for SOS1. The left panel shows the Jacobi energy of the GCs compatible within 1σ with SOS1 Jacobi Energy (shaded yellow region), and the right panel shows the SOS1 distance to the centre of the selected clusters.

Table 4.2 - Orbital input and output parameters of SOS1 and its most likely parent cluster. The input values were taken from Baumgardt's compilation[1], and the output was obtained from orbital integration.

		SOS 1	Palomar 1	Terzan 2	Terzan 5	NGC 6440	Terzan 6	NGC 6528
		Input parameters						
RA	(deg)	266.446	+53.334	261.888	267.020	267.220	267.693	271.207
DEC	(deg)	−26.653	+79.581	−30.802	−24.779	−20.360	−31.275	−30.056
R_{sun}	(kpc)	6.9 ± 1.0	11.1 ± 0.3	7.8 ± 0.3	6.6 ± 0.2	8.3 ± 0.2	7.3 ± 0.4	7.8 ± 0.2
<RV>	(km s^{-1})	-75.4 ± 0.1	-75.7 ± 0.2	133.5 ± 0.7	-81.9 ± 0.9	-69.4 ± 0.9	137.2 ± 1.7	211.9 ± 0.4
μ^*_α	(mas yr^{-1})	-1.45 ± 0.02	-0.26 ± 0.03	-2.14 ± 0.03	-1.86 ± 0.03	-1.19 ± 0.02	-4.99 ± 0.05	-2.17 ± 0.02
μ_δ	(mas yr^{-1})	-6.20 ± 0.06	$+0.02 \pm 0.03$	-6.26 ± 0.03	-5.11 ± 0.03	-4.00 ± 0.02	-7.46 ± 0.05	-5.64 ± 0.02
Mass	($M_\odot$)	—	$(9.26 \pm 1.83) \times 10^2$	$(8.05 \pm 2.31) \times 10^4$	$(1.09 \pm 0.08) \times 10^6$	$(5.69 \pm 0.45) \times 10^5$	$(1.00 \pm 0.01) \times 10^5$	$(9.44 \pm 0.91) \times 10^4$
$Mass_{ini}$	($M_\odot$)	—	1.23×10^4	5.89×10^6	4.20×10^7	6.17×10^6	4.57×10^6	2.14×10^6
r_t	(pc)	—	22.84	12.45	51.26	33.88	13.89	10.98
Age	(Gyr)	> 10.0	7.3 ± 1.2	—	12.0 ± 1.0	13.0 ± 1.5	—	11.0 ± 1.0
		Output parameters						
r_{apo}	(kpc)	1.6 ± 0.3	21.6 ± 0.4	0.9 ± 0.1	1.9 ± 0.1	1.5 ± 0.2	1.5 ± 0.2	1.7 ± 0.2
r_{peri}	(kpc)	0.04 ± 0.02	15.81 ± 0.14	0.21 ± 0.06	0.10 ± 0.02	0.04 ± 0.02	0.03 ± 0.01	0.04 ± 0.02
$\|Z\|_{zm}$	(kpc)	0.71 ± 0.20	5.51 ± 0.14	0.49 ± 0.08	0.87 ± 0.06	1.23 ± 0.05	1.01 ± 0.09	1.11 ± 0.06
ecc		0.95 ± 0.02	0.16 ± 0.01	0.63 ± 0.12	0.89 ± 0.02	0.95 ± 0.03	0.96 ± 0.02	0.96 ± 0.02
E_J	(10^5km^2 s^{-1})	-1.652 ± 0.072	-1.635 ± 0.008	-1.699 ± 0.018	-1.602 ± 0.009	-1.582 ± 0.007	-1.620 ± 0.032	-1.582 ± 0.008
P_{bar}	%	84	0	0	94	0	9	27
N_{diss}	%	—	0	0	1	0	0	0

[1] https://people.smp.uq.edu.au/HolgerBaumgardt/globular/

4.4 Dissociation points and dissociation time

The SOS1's parent cluster can be found recovering its (and the GCs') entire orbit around the Galaxy. Since SOS1 and each GC have 500 initial conditions, for each pair SOS1-GC, we have 2.5×10^5 combinations of orbits and in each of them we searched for a crossing point. It is also important to consider that if the star has enough velocity, it

can pass through the cluster volume without being bound to it. Therefore, to consider the crossing point as a dissociation point (the probable point when and where SOS1 is captured from the cluster by the bar), the star should be inside the cluster volume defined as a tidal radius and gravitationally bound to the cluster (Figure 4.7).

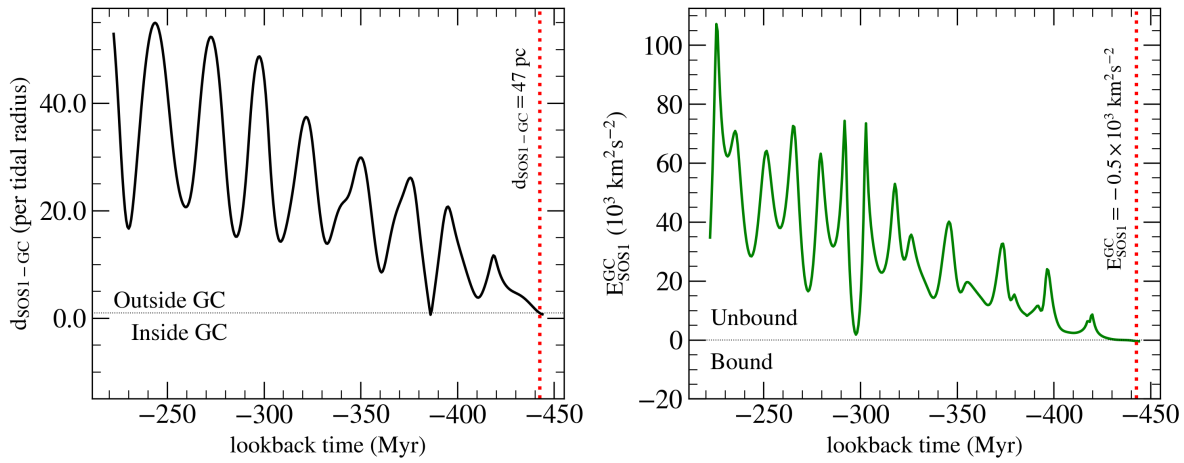

Figure 4.7: Dissociation point selection criterea. The left panel shows the SOS1 distance to GC's centre in tidal radius units as a time function. The black dotted line shows the one tidal radius region limiting the cluster volume. The right panel shows the SOS1 total energy concerning the GC as a function of time. The black dotted line represents the bound energy limit. The red dotted lines show the dissociation point with the corresponding distance to the cluster centre (top panel) and the bound energy (bottom panel).

We computed the dissociation points employing the values of tidal radius from Table 4.2. During the orbital time, SOS1 can pass through all the MW GCs during its orbits. Therefore, we only accepted the close encounter point where the star is also gravitationally bound to the cluster potential. We calculated the total energy of SOS1 for all close encounter points due to the cluster potential, where the points with negative energy were considered gravitationally bound. For the combinations with more than one close encounter gravitationally bound point, we considered only the first one (closest to the present day). We assume that SOS1 belongs to the cluster before the first point. The number of combinations with gravitationally bound close encounter points shows the probability of SOS1 being a cluster member. Performing the dissociation point analysis for each pair, Terzan 5 was the most probable parent cluster. In contrast, the other clusters did not present any dissociation point.

We then recovered the time at the dissociation point, called the dissociation time (τ_d). The result is a time distribution where we fitted the peak to obtain the time when the bar captured the star from the cluster. For Terzan 5, we found the dissociation time

approximately 300 Myr ago (Figure 4.8). Even though the time distribution presents values up to 13 Gyr ago, these points do not make physical sense because the Galaxy's potential evolves with time, and at that time, even the bar had not been formed yet. For the potential employed here (Portail et al., 2017), we can trust the results until approximately −1 Gyr (Moreno et al., 2022). Therefore, the result for SOS1-Terzan 5 is inside the time range for physical meaning.

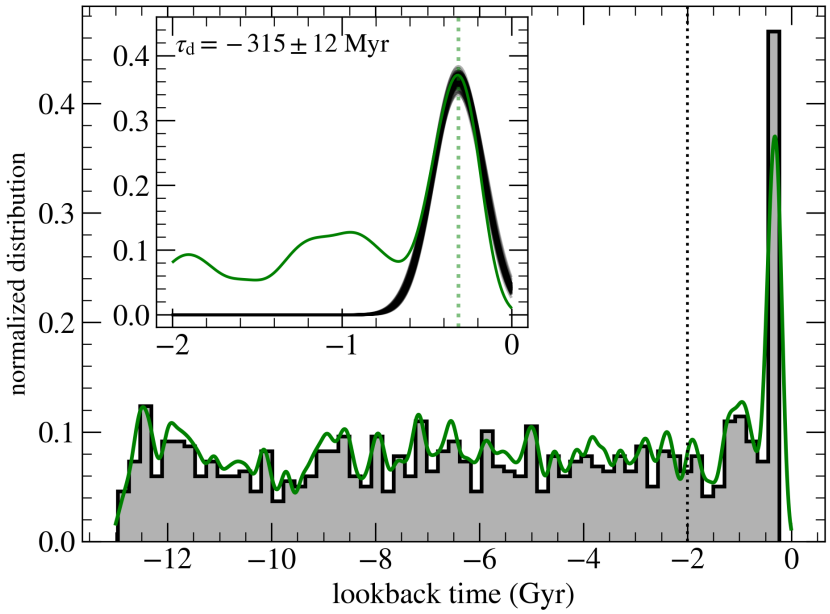

Figure 4.8: Dissociation time distribution fitting. The figure shows the distribution of lookback time obtained from the dissociation points. The dissociation time is adopted as the distribution peak (insert plot).

A more detailed analysis of the link between SOS1 and Terzan 5 will be provided in Chapter 6.

Chapter 5

Dating other GCs using SIRIUS code

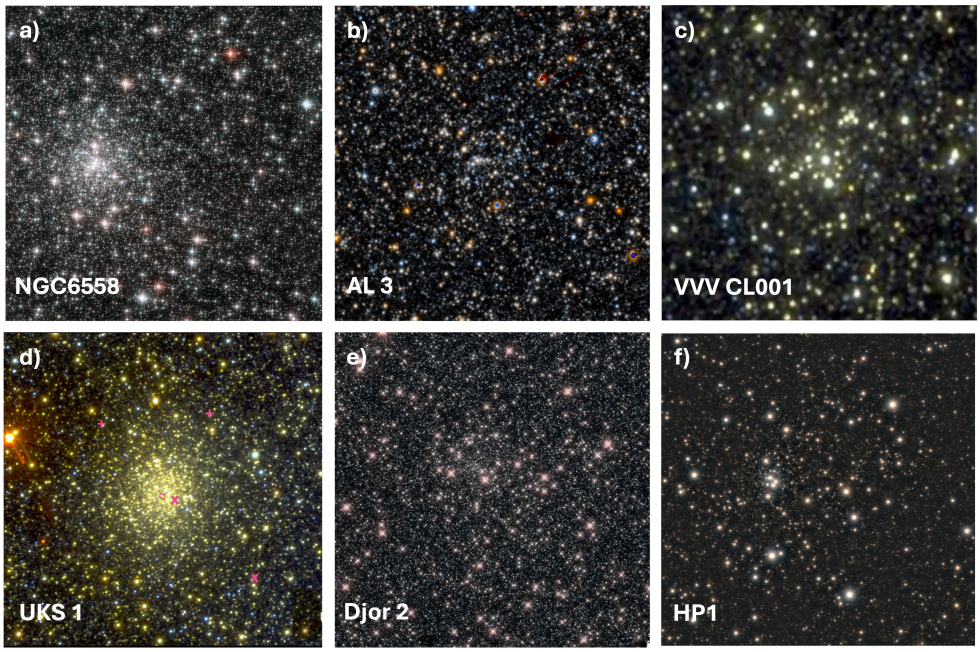

Figure 5.1: Colorful images of the GCs studied in parallel with the thesis. Panel (a) shows the combined F606W/F814W HST image of NGC6558. Panel (b) is the PanSTARRS image taken from Baumgardt's website database. Panel (c) is the VVV image of VVV CL001 taken from Minniti et al. (2011). Panel (d) is also the VVV image, but for the GC UKS1 taken from Fernández-Trincado et al. (2021). Panel (e) shows the combined F110W/F160W HST image for Djor2. Finally, panel (f) represents the colour composite GSAOI+GeMS image of HP 1 (Credit: Gemini Observatory/AURA/NSF; a composite image produced by Mattia Libralato of Space Telescope Science Institute).

In this Chapter, I present my other contributions to the field through different collaborations. The SIRIUS code (Section 1.2.1) was designed in collaboration with Dr. Leandro Kerber. Since we published the paper presenting the code, although it is not public for the community, several works have been done using it. We present some studies where SIRIUS had an important contribution and whose results were used in this thesis.

The GC NGC6558

NGC 6558 is a low Galactic latitude globular cluster projected in the direction of the Galactic bulge along its minor axis. We obtained GSAOI/Gemini high-resolution JHK_S images and optical HST/ACS F606W/F814W photometries in two epoches which allows a proper motion and field stars cleaned CMD reaching almost six magnitudes below the main sequence turnoff. These data allowed us to provide a more precise age determination for NGC 6558. We applied the method to compare the observed and synthetic CMDs, employing a Bayesian isochrone fitting using the Markov chain Monte Carlo algorithm, using the SIRIUS code. The isochrone fitting using the method of synthetic CMDs gives a distance of $8.41^{+0.11}_{-0.10}$ kpc, age of 13.0 ± 0.9 Gyr with a reddening of E(B-V)$= 0.34 \pm 0.02$, adopting as a prior the RR Lyrae apparent magnitude level and the metallicity from the literature. We also derived a total-to-selective coefficient $R_V = 3.2 \pm 0.2$ thanks to the simultaneous NIR-Optical synthetic CMD fitting. Figure 5.2 shows the NIR and Optical CMDs overplotted by the results from the isochrone fitting.

This work is titled as *GSAOI/Gemini and ACS/HST photometry of the globular cluster NGC 6558: A steep age-metallicity relation of the metal-poor bulge* submitted to the A&A, which author list is:

S. O. Souza, M. Libralato, D. Nardiello, L. O. Kerber, S. Ortolani, A. Pérez-Villegas, R. A. P. Oliveira, B. Barbuy, E. Bica, and M. Griggio.

The GC AL 3

We here carried out the isochrone fitting using the SIRIUS code to the B, V, and Cousins I images of AL 3, observed on 2000 March 6, using the 1.54m Danish telescope at the European Southern Observatory (ESO) at La Silla. The data is the same as presented in Ortolani et al. (2006). The metallicity was limited by using a Gaussian prior with the value of Ortolani et al. (2006). We adopted the DSED isochrone database, with $[\alpha/\mathrm{Fe}]$=0.4 and primordial helium. The AGB is also shown, based on BaSTI isochrones, since they are not available in DSED. We obtain a reddening of $E(B-V) = 0.38 \pm 0.04$, a distance of $d_\odot = 6.0 \pm 0.6$ kpc, and a metallicity of [Fe/H]$= -1.34 \pm 0.18$. Our age determination indicates an old age of $13.4^{+1.0}_{-1.2}$ Gyr, indicating that AL 3 is another relic fossil. Figure 5.3 shows the solution of isochrone fitting. In the right panel, the solid blue line represents the

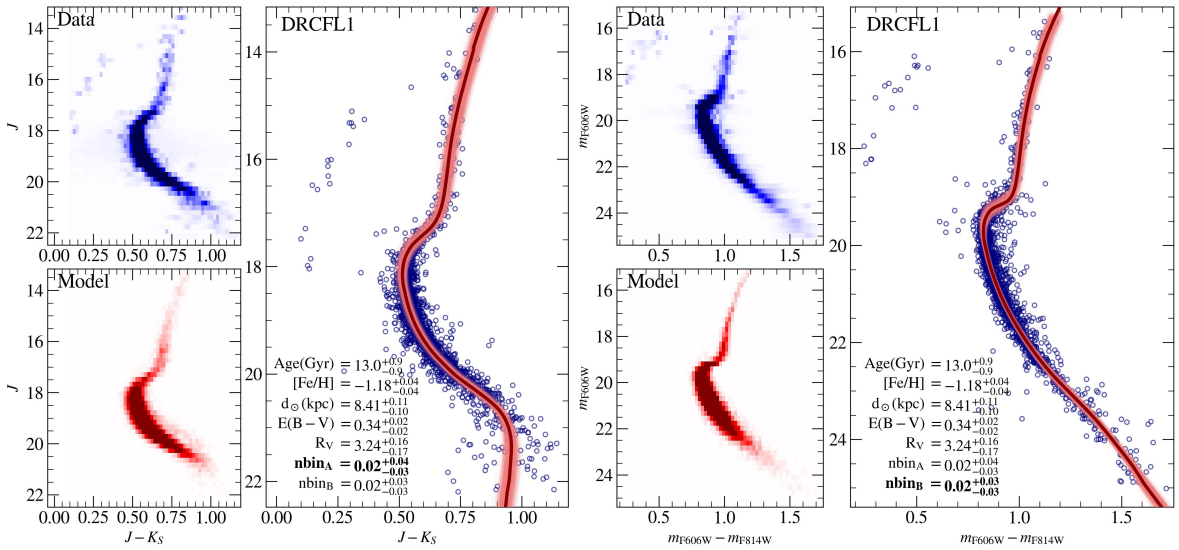

Figure 5.2: Simultaneous isochrone fitting for NGC 6558 using the differential reddening correction from fiducial line 1 (DRCFL1). The left panels show the NIR GSAOI CMD, and the right panels show the optical F606W/F814W HST CMD. The small panels show the Hess diagram of the data (upper) and model (best-fit synthetic CMD, lower). In the bigger panel, the blue dots are the cluster member stars, the red line represents the isochrone of the best synthetic CMD fit, and the thin lines are solutions within the errors. The values obtained from the simultaneous fitting are in the bottom left corner of the bigger panels, with the respective binary fraction value highlighted.

median solution, while the shaded regions indicate the solutions within 1σ. The red stars are the three sample stars analysed in this paper using spectroscopy. Finally, the right panel exhibits the corner plots showing the (anti)correlations between the parameters.

This paper was published in the Astronomy & Astrophysical journal as *Gemini/Phoenix H-band analysis of the globular cluster AL 3*, and the author list is:

Barbuy, B., H. Ernandes, **S. O. Souza**, R. Razera, T. Moura, J. Meléndez, A. Pérez-Villegas, M. Zoccali, D. Minniti, B. Dias, S. Ortolani, & E. Bica A&A, 648, A16 (2021)

The GC VVVCL001

The paper focused on VVV CL001, a GC discovered by the VVV survey (Minniti et al., 2011). This GC lies in the direction of the Galactic bulge and is strongly dominated by large foreground extinction, E(B−V)$\sim$ 2.0, hampering the observations of this object in the optical bands. In order to have a self-consistent age derivation via statistical isochrone fitting, we use the `SIRIUS` code and the most probable cluster members in the VVV catalogue located inside 1.5 arcmin from the cluster centre that have proper motions compatible with that of VVV CL001, as well as those sources with radial velocities information. Due to the quality of our data, we applied some assumptions to obtain an age distribution: a

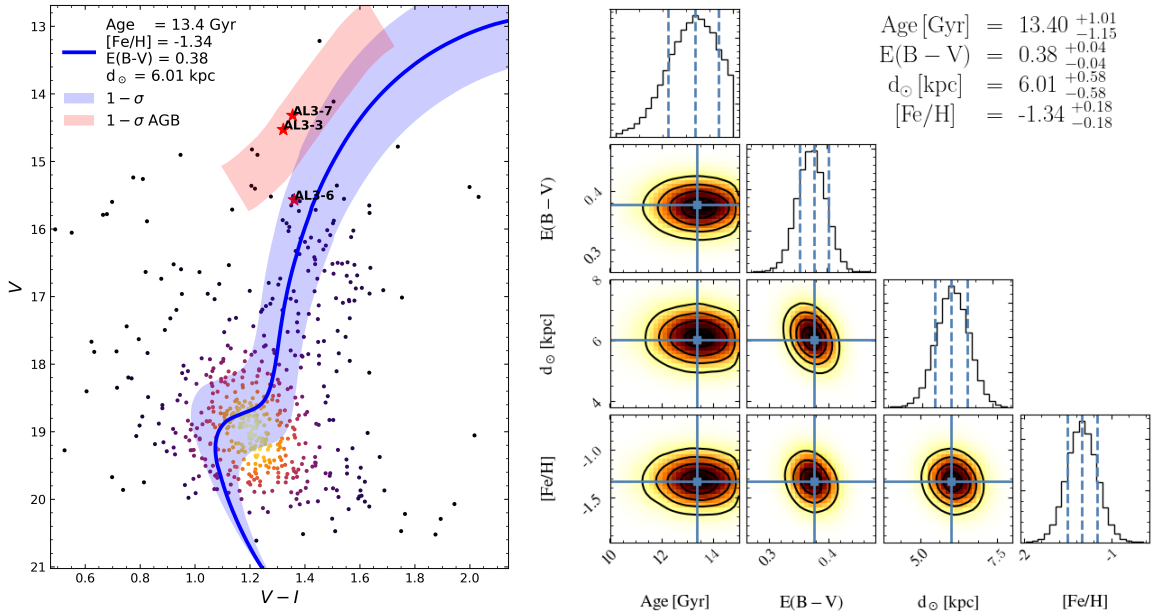

Figure 5.3: Left panel: AL 3 V vs. $V-I$ CMD. The black dots are the stars within 120 pixels of the cluster centre (see Ortolani et al. 2006). The red stars are the observed stars of the present work. The solid blue line represents the median solution of the isochrone fitting, while the blue region reveals the solutions within 1σ. Right panel: The corner plot represents the N-D parameter space of the Markov-Chain constructed by Monte-Carlo during the isochrone fitting. To represent the solutions, we adopt the mode of the distribution as the best value, and the uncertainties are computed by the 16^{th} and 84^{th} percentiles.

uniform prior in age between 1 and 15 Gyr combined with a slow drop above the age of the universe; the metallicity was varied around the value determined with high-resolution spectroscopy in this work; the isochrone is limited to $\log g < 4.5$ representing the RGB region. We dereddened and extinction-corrected the VVV+2MASS Kss and $J-K_S$ colours with the bulge-specific reddening maps from Gonzalez et al. (2011, 2012) assuming the reddening law of Cardelli et al. (1989). Finally, we adopted the DSED isochrones with [α/Fe]= +0.4 and canonical helium. Figure 5.4 presents the best isochrone fits in the [Ks, $J-K_S$] CMD. Our fit provides a reasonable solution in the overplotted isochrone (left panel) and the posterior distributions of the corner plot (right panel). We adopt the median as the most probable value and the uncertainties calculated from the 16th and 84th percentiles to represent the distributions. We found an age of 11.9 ± 3.12Gyr and a probable distance of $\sim 8.22 \pm 1.84$ kpc. Our probable solutions, within 1σ, fit the central part of the CMD, providing confidence that the age estimate is reasonable for VVV CL001.

This paper was published as a letter to the editor in the Astrophysical Journal with the title *VVV CL001: Likely the Most Metal-poor Surviving Globular Cluster in the Inner Galaxy*, which the author list is:

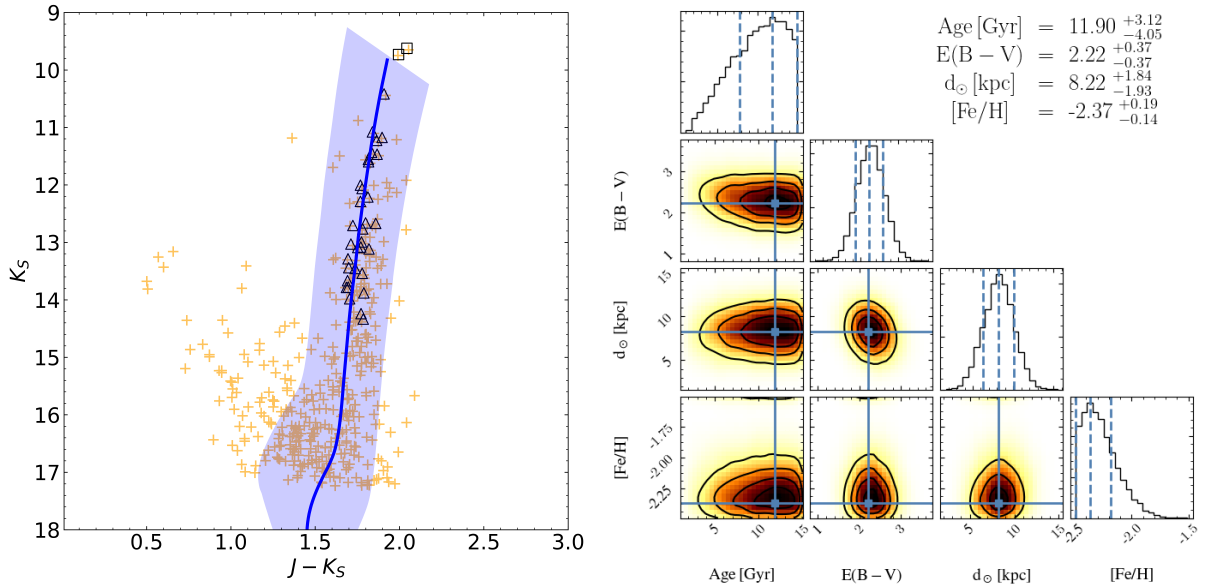

Figure 5.4: Isochrone fitting results for VVV CL001. Left panel: the best isochrone fit in the $[K_S, J-K_S]$ CMD using DSED models, where the blue line shows the most probable solution and the blue shadowed region indicates the solutions within 1σ. The orange symbols mark the potential candidates from the VVV survey, while the black open squares and triangles refer to stars with radial velocities information from APOGEE-2 and Baumgardt's compilation, respectively. Right panel: the posterior distributions of the indicated quantities.

Fernández-Trincado, J. G., D. Minniti, **S. O. Souza**, T. C. Beers, D. Geisler, C. Moni Bidin, S. Villanova, S. R. Majewski, B. Barbuy, A. Pérez-Villegas, L. Henao, M. Romero-Colmenares, A. Roman-Lopes, & R. R. Lane ApJL, 908, L42 (2021)

The GC UKS1

In this work, we employ the VVV Infrared Astrometric Catalogue (VIRAC) to study the bulge globular cluster UKS 1. Deriving the age of the UKS 1 GC is not easy because, as mentioned before, it is in a region with very high extinction (Minniti et al., 2011). Through isochrone fitting, we tried to estimate the age using the `SIRIUS` code. We adopted the DSED with an $\alpha-$enhancement of +0.4 and canonical helium ($Y \sim 0.25$) models. The DSED isochrones are available in the 2MASS photometry system and were converted to the VVV photometry system. Since we do not have the entire CMD available, in particular, the TO region, we imposed Gaussian distribution priors for the metallicity of [Fe/H]$= -0.98$, determined within this work, with a standard deviation of 0.11 dex, and for the distance of 7.8 kpc (Baumgardt et al., 2019) with a standard deviation of 0.78 kpc. Figure 5.5 presents the best isochrone fitting in the $[K_S, J-K_S]$ CMD. Our fit provides a reasonable solution in the overplotted isochrone (left panel) and the posterior distributions of the corner plot

(right panel). As the best determination to represent the distributions, we adopted the median as the most probable value and the uncertainties calculated from the 16th and 84th percentiles. Based on the DSED isochrones, we found an age of 13.10 ± 0.90 Gyr. The 1σ region (the red stripe in Figure 5.5) is mostly affected by age uncertainties. It is relevant to mention that in the RGB region of the CMD, an age variation could be seen as a colour displacement (see Figure 1.13). Also, we want to highlight that our probable solutions within 1σ fit the central part of the CMD, reinforcing that the age estimation is a reasonable determination for UKS 1.

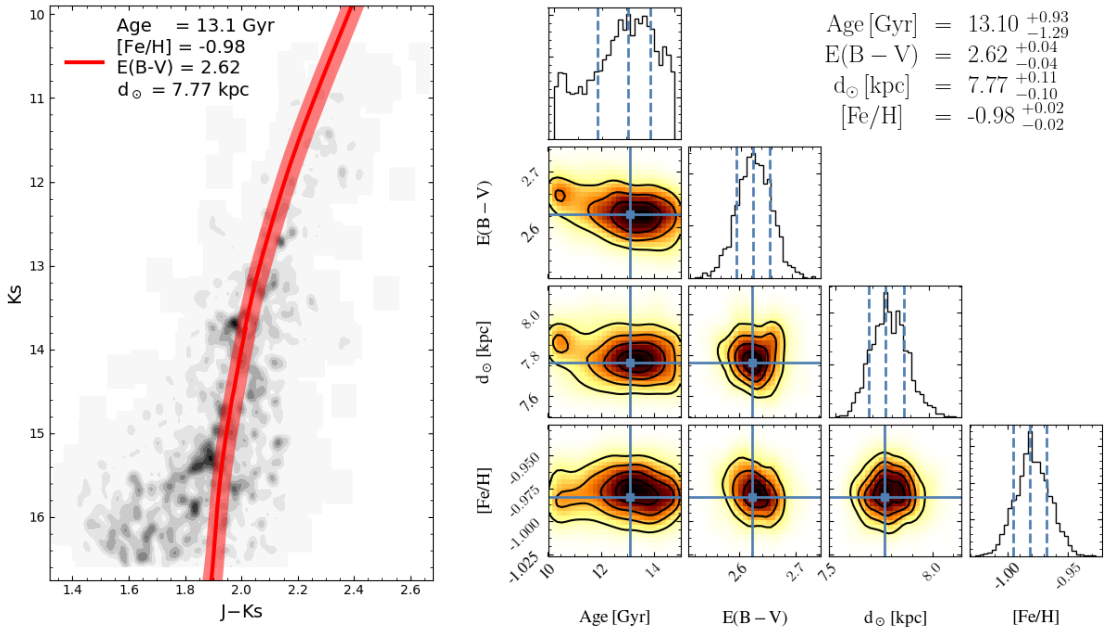

Figure 5.5: Best isochrone fit for UKS1 in the $[K_S, J-K_S]$ CMD using DSED models. Left panel: CMD with the results from the fitting. The red line is the most probable solution, and the red stripe is the solution within 1σ. Right panel: posterior distributions.

This paper was published in the Astronomy & Astrophysical journal with the title *The enigmatic globular cluster UKS 1 obscured by the bulge: H-band discovery of nitrogen-enhanced stars*. The author list is as follows:

Fernández-Trincado, J. G., D. Minniti, T. C. Beers, S. Villanova, D. Geisler, **S. O. Souza**, L. C. Smith, V. M. Placco, K. Vieira, A. Pérez-Villegas, B. Barbuy, A. Alves-Brito, C. M. Bidin, J. Alonso-García, B. Tang, & T. Palma A&A, 643, A145 (2020)

ESO 456-SC38 (Djorgovski 2)

The GC ESO 456-SC38 (also known as Djorgovski 2, hereafter Djor2) is one of the GCs closest to the Galactic centre. It is on the blue horizontal branch and has a moderate metallicity of [Fe/H]= −1.0, similar to the very old inner bulge globular clusters NGC 6522, NGC 6558, and HP 1, and therefore appears to be part of the early formation stages of the Milky Way. We analysed ESO 456-SC38 based on HST photometry, with the filters F606W from ACS, F110W and F160W from WFC3. We selected a subsample of stars within a radius of 1.7 mas yr^{-1} around the mean proper motion to increase the cluster membership probability and reduce the contamination by the Galactic disk and bulge. In Figure 5.6, we plot the inner region of the CMD (within 0.15 arcmin of the cluster centre) from the HST. The subsample of probable cluster members from the Gaia DR2 match is plotted as red dots. The BaSTI alpha-enhanced isochrones were adopted for the isochrone fitting. The isochrones were corrected for reddening dependency on effective temperatures, as discussed in Ortolani et al. (2017). We used the star-by-star reddening provided for the PARSEC. This correction mainly shrinks the CMDs in colour, and the fit quality greatly improves for very reddened clusters. In Figure 5.6, the HST [$F606W$, $F606W - F110W$] CMD of Djor2 is fit `SIRIUS` code. In the middle and right panels, we superimpose the same parameters as are adopted in the left panel for the CMDs [$F606W$, $F606W - F160W$] (middle) and [$F110W$, $F110W - F160W$] (right). The panels show very good compatibility. This Figure shows that the isochrone fitting is near the MS blue edge due to a combined effect of field contamination (prevailing on the red side), binarity, and loss of completeness in the cluster sequence at the faint end. We derive an accurate distance of $d_\odot = 8.75 \pm 0.12$ kpc and a reddening of E(B−V)= 0.81 ± 0.02. The best-fitting corresponds to an age of 12.7 ± 0.7 Gyr and a metallicity of [Fe/H]= -1.11 ± 0.03. Our findings on Djor2 have led to its inclusion in the list of the oldest moderately metal-poor globular clusters in the inner bulge.

This paper was published in the Astronomy & Astrophysical journal with the title *Another relic bulge globular cluster: ESO 456-SC38 (Djorgovski 2).* The author list is:

Ortolani, S., E. V. Held, D. Nardiello, **S. O. Souza**, B. Barbuy, A. Pérez-Villegas, S. Cassisi, E. Bica, Y. Momany, & I. Saviane A&A, 627, A145 (2019)

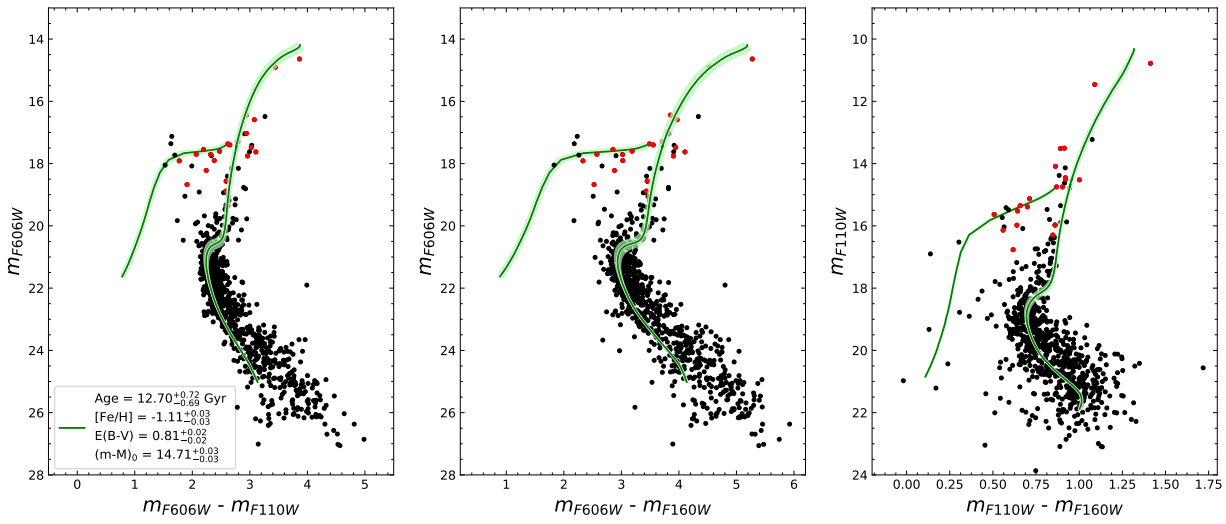

Figure 5.6: Results for Djor2 using the $[F606W,\ F606W - F110W]$ CMD from HST/ACS and WFC3 observations fitted with BaSTI isochrones. The green solid lines are the most probable solution, and the green region represents the solutions inside 1σ from the posterior distributions. Large red dots are stars identified in Gaia within 25 arcsec of the cluster centre. The middle and right panels show the solution computed in the left panel projected over the $[F606W,\ F606W - F160W]$ (middle) and $[F110W,\ F110W - F160W]$ (right) CMDs. Stars within 0.15 arcmin of the cluster centre are selected.

HP 1

HP 1 is an α-enhanced ($[\alpha/\mathrm{Fe}]\sim +0.3$) and moderately metal-poor bulge globular cluster ($[\mathrm{Fe/H}]= -1.06 \pm 0.15$) with a blue horizontal branch. These combined characteristics make it a probable relic of the early star formation in the innermost Galactic regions. In this paper, we presented a detailed analysis of a deep near-infrared (NIR) photometry of HP 1 obtained with the NIR GSAOI+GeMS camera at the Gemini-South telescope. We combine our GSAOI data with archival F606W-filter *HST* ACS/WFC images to compute relative proper motions and select bonafide cluster members. Figure 5.7 presents the best isochrone fits in the $[K_\mathrm{s},\ J{-}\mathrm{K_s}]$ (left panel) and $[F606W,\ F606W - K_S]$ (right panel) CMDs, using DSED isochrones with $[\mathrm{Fe/H}]= -1.06$. Each panel shows an overview of the best solution, a zoom-in panel with the stars that were effectively used in the fit. The best fits provide excellent solutions, as attested by the overplotted isochrone. According to the analysis using DSED isochrones and the $[K_\mathrm{s},\ J{-}\mathrm{K_s}]$ CMD, the age of HP 1 is $12.9^{+0.8}_{-0.5}$ Gyr, without any significant uncertainties from metallicity. The results from the optical-NIR $[F606W,\ F606W - K_S]$ CMD indicate an age of 12.7±0.5 Gyr, in excellent agreement with the NIR one. Taking the average results from statistical isochrone fits in the NIR and optical-NIR CMDs, an age of $12.8^{+0.8}_{-0.7}$ Gyr is obtained, confirming that HP 1 is one of the oldest clusters in the Milky Way.

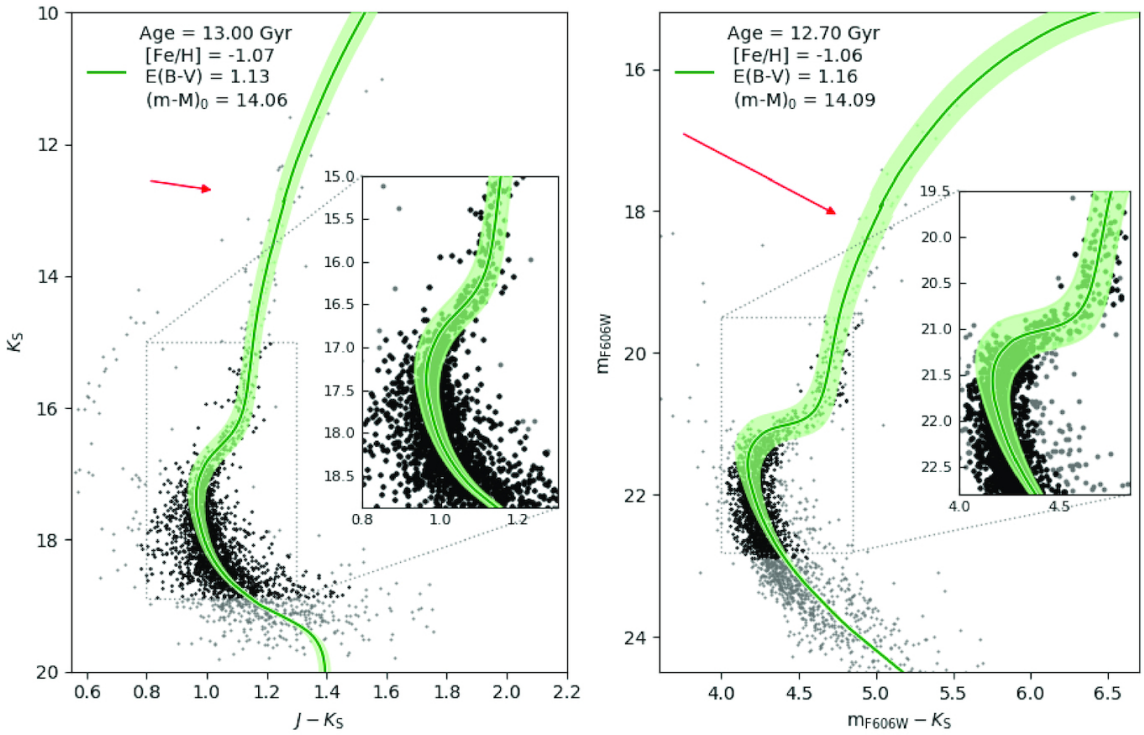

Figure 5.7: Best isochrone fit in the [K_s, $J-K_s$] (left panel) and [$F606W$, $F606W - K_S$] (right panel) CMDs using DSED models. The CMD shows all observed stars (grey) and those used in the fit (black). The red arrow is the reddening vector corresponding to $\delta E(B-V) = 0.10$. The zoom-in panel in the CMD shows the region more sensitive to the age variation. A thick line highlights the best fit. The green area shows the region between the two isochrones using the values within 1σ for all the parameters.

This paper was published in the MNRAS with the title *A deep view of a fossil relic in the Galactic bulge: the Globular Cluster HP 1*, and the author list:

Kerber, L. O., M. Libralato, **S. O. Souza**, R. A. P. Oliveira, S. Ortolani, A. Pérez-Villegas, B. Barbuy, B. Dias, E. Bica, & D. Nardiello MNRAS, 484, 5530 (2019)

Chapter 6

Discussion: The fossils of the Galactic Bar/Bulge formation

This chapter discusses the fossil relics of the Galactic bulge and bar formation and evolution using the GCs as tracers. The discussion comprises four previous chapters and is based on the discussions of the paper about Pal6 (Souza et al., 2021) and NGC6355 (Souza et al., 2023), the submitted paper about NGC6558 (Souza et al.) and SOS1 (Souza et al.).

6.1 The fundamental bricks of the Galactic Bulge

The orbital analysis shows that the orbits of Palomar 6 and NGC 6355 are compatible with a location at the Galactic bulge volume according to the classification of Pérez-Villegas et al. (2020), which presents the probability distribution of belonging to each Galactic component through the values of r_{apo} and $|z|_{max}$. Table 6.1 summarises the orbital parameters and other fundamental parameters used in this section. It is essential to mention that their classification is based on a Galactic potential that includes the contribution of the Galactic bar. Another robust Galactic potential, considering the dynamical friction, was applied by Moreno et al. (2022). Their orbital parameters are essentially compatible with our results. The values of E are precisely the same. The L_Z and r_{peri} are compatible within 1σ. In contrast, our value of r_{apo} for NGC 6355 is higher than that of Moreno et al. (2022), indicating that a more realistic Galactic potential confines NGC 6355 even more within the Galactic bulge volume. With the results using the McMillan (2017) Galactic potential, Palomar 6 and NGC 6355 are Galactic bulge GCs with a probability above 99%. The other clusters in Table 6.1 were also classified as bulge members by Pérez-Villegas et al. (2020) or in their respective papers as mentioned in Chapter 5.

Table 6.1 - Age, metallicity, and orbital parameters for the GCs used in the final discussion of this thesis. The clusters are divided into three groups: those analysed in this thesis, where I am the first author; those analysed in parallel; and the GCs analysed by our group.* The total energy and angular momentum in the Z direction were derived from the orbital integration employing the McMillan (2017) mass model because it does not have a non-asymmetric component. Therefore, these quantities are conserved in the entire orbit. References: S21 Souza et al. (2021); S23 Souza et al. (2023); SIP Souza et al. submitted; B21 Barbuy et al. (2021a); O19 Ortolani et al. (2019); K19 Kerber et al. (2019); F20 Fernández-Trincado et al. (2020); F21 Fernández-Trincado et al. (2021); B21 Barbuy et al. (2021); O20 Oliveira et al. (2020).

Cluster	Age (Gyr)	[Fe/H]	REF	r_{peri} (kpc)	r_{apo} (kpc)	$\|Z\|_{max}$ (kpc)	*ecc*	E_T $(10^5 km^2 s^{-2})^*$	L_Z $(10^2 km\,s^{-1}\,kpc)^*$
Main objects of the thesis									
Palomar 6	12.4 ± 1.0	-1.10 ± 0.09	S21	0.08 ± 0.03	2.06 ± 0.07	1.07 ± 0.10	0.92 ± 0.03	-2.40 ± 0.05	$+0.07 \pm 0.13$
NGC 6355	13.2 ± 1.0	-1.39 ± 0.08	S23	0.25 ± 0.08	2.46 ± 0.14	1.91 ± 0.08	0.82 ± 0.05	-2.31 ± 0.03	-0.31 ± 0.24
NGC 6558	13.0 ± 0.9	-1.18 ± 0.05	SIP	0.05 ± 0.04	1.83 ± 0.28	1.51 ± 0.04	0.95 ± 0.04	-2.45 ± 0.02	$+0.30 \pm 0.17$
Secondary objects									
AL 3	13.4 ± 1.0	-1.34 ± 0.18	B21	0.42 ± 0.26	4.32 ± 0.30	1.59 ± 0.24	0.83 ± 0.10	-2.12 ± 0.03	$+4.29 \pm 0.55$
Djor 2	12.7 ± 0.7	-1.11 ± 0.03	O19	0.25 ± 0.17	1.46 ± 0.24	1.38 ± 0.09	0.71 ± 0.19	-2.53 ± 0.03	-1.36 ± 0.29
HP 1	12.8 ± 0.8	-1.06 ± 0.15	K19	0.07 ± 0.11	3.04 ± 0.52	2.12 ± 0.06	0.95 ± 0.09	-2.34 ± 0.02	$+0.03 \pm 0.08$
UKS 1	13.1 ± 1.1	-0.98 ± 0.02	F20	0.09 ± 0.10	9.76 ± 0.63	5.65 ± 1.10	0.98 ± 0.02	-1.83 ± 0.04	-1.29 ± 0.91
VVVCL001	11.9 ± 3.5	-2.37 ± 0.16	F21	0.09 ± 0.15	4.71 ± 0.74	3.10 ± 0.34	0.96 ± 0.07	-2.12 ± 0.12	-2.34 ± 1.63
Analysed by our group									
NGC 6522	12.8 ± 1.0	-1.05 ± 0.11	B21	0.06 ± 0.08	1.54 ± 0.11	1.18 ± 0.04	0.92 ± 0.08	-2.47 ± 0.03	$+0.88 \pm 0.25$
NGC 6723	12.6 ± 0.6	-1.01 ± 0.05	O20	1.26 ± 0.05	4.08 ± 0.33	3.72 ± 0.03	0.54 ± 0.03	-2.06 ± 0.02	$+0.53 \pm 0.19$
NGC 6717	13.5 ± 0.8	-1.26 ± 0.07	O20	0.05 ± 0.02	3.09 ± 0.10	1.88 ± 0.10	0.96 ± 0.01	-2.28 ± 0.02	$+2.06 \pm 0.07$

After establishing that Palomar 6 and NGC 6355 currently are members of the Galactic bulge, we investigated whether these clusters originated from the primordial material of the Galaxy or if they are a remnant of the first mergers of the MW. For this task, we must analyse the chemodynamical and photometric information derived previously in this thesis.

6.1.1 Comparison with bulge field stars

To study Palomar 6 and NGC 6355 in the context of the Galactic bulge, we compared the orbital parameters derived in this thesis with the field star population composed by the reduced proper motion (RPM) sample from Queiroz et al. (2021) and the bulge RR Lyrae from the OGLE Galaxy Variability Survey (Soszyński et al., 2019). We also selected the globular clusters analysed and classified as bulge members by our group. They are NGC6558 (with our recent age determination; Barbuy et al., 2018b), Djorg 2 (Ortolani et al., 2019), HP1 (Kerber et al., 2019), NGC6717 (Oliveira et al., 2020), NGC6723 (Oliveira et al., 2020), UKS1 (Fernández-Trincado et al., 2020), AL3 (Barbuy et al., 2021b),

NGC6522 (Barbuy et al., 2021), and VVV CL001 (Fernández-Trincado et al., 2021). We reintegrate their orbits to obtain their orbital parameters. For NGC6717, NGC6723, and Djor2, we obtained the chemical abundances from APOGEE DR17 by selecting the members for each cluster via proper motion membership probability. In the case of Pal6, we also obtained chemical abundances from APOGEE DR17 for the iron-peak elements to complement the abundances derived in Souza et al. (2021). The sample of GCs of Table 6.1 will be called hereafter as moderately metal-poor GCs (MMPGCs).

We matched the OGLE sample with APOGEE DR17, which already provides the abundances, radial velocities, and proper motions (previously obtained from Gaia EDR3). After that, we matched the sample with Starhorse (Queiroz et al., 2020) to obtain the distance values. The final OGLE sample is composed of 4132 stars.

Pal 6 and NGC 6355, have a relatively high $|Z|_{max}$ and *ecc*, placing them in the cell **F** of Figure 20 in Queiroz et al. (2021). The same figure is reproduced here in the upper left panel of Figure 6.1 for the RPM sample and in the upper right panel for the RR Lyrae sample. It is worth noting that the cell **F** is populated by all the reference bulge GCs, making it the so-called old-bulge region. The 58 stars of the spheroidal bulge defined by Razera et al. (2022) are also confined in the region of high *ecc* (yellow squares), indicating that the cells C, F, and I are pressure-supported (spheroidal). The normalised population densities as a function of [Fe/H] (MDF), R_{mean} (mean between r_{apo} and r_{peri}), and v_ϕ are shown in the three bottom panels of Figure 6.1, respectively. Based on the MDF (lower left panel), the RPM sample comprises the moderately metal-rich bulge MDF, while the RR Lyrae sample is the metal-poor tail one. As expected, Pal 6 and NGC 6355, both old GCs, match the peak of the RR Lyrae MDF and R_{mean} distribution.

The comparison with the bulge field populations shows that Palomar 6 and NGC 6355 are likely in-situ GCs compatible with the Galactic bulge's old and metal-poor RR Lyrae component.

6.1.2 Comparison with chemodynamical models

To investigate the chemical abundances in the context of nucleosynthesis, we compared our results with chemical evolution models. The models for O, Mg, Si, Ca, V, Mn, Co, Cu, and Zn were computed with the code described in Friaça and Barbuy (2017) (see also Barbuy et al., 2015; Ernandes et al., 2020, 2022, for V, Mn, Co, Cu, and Zn). The star

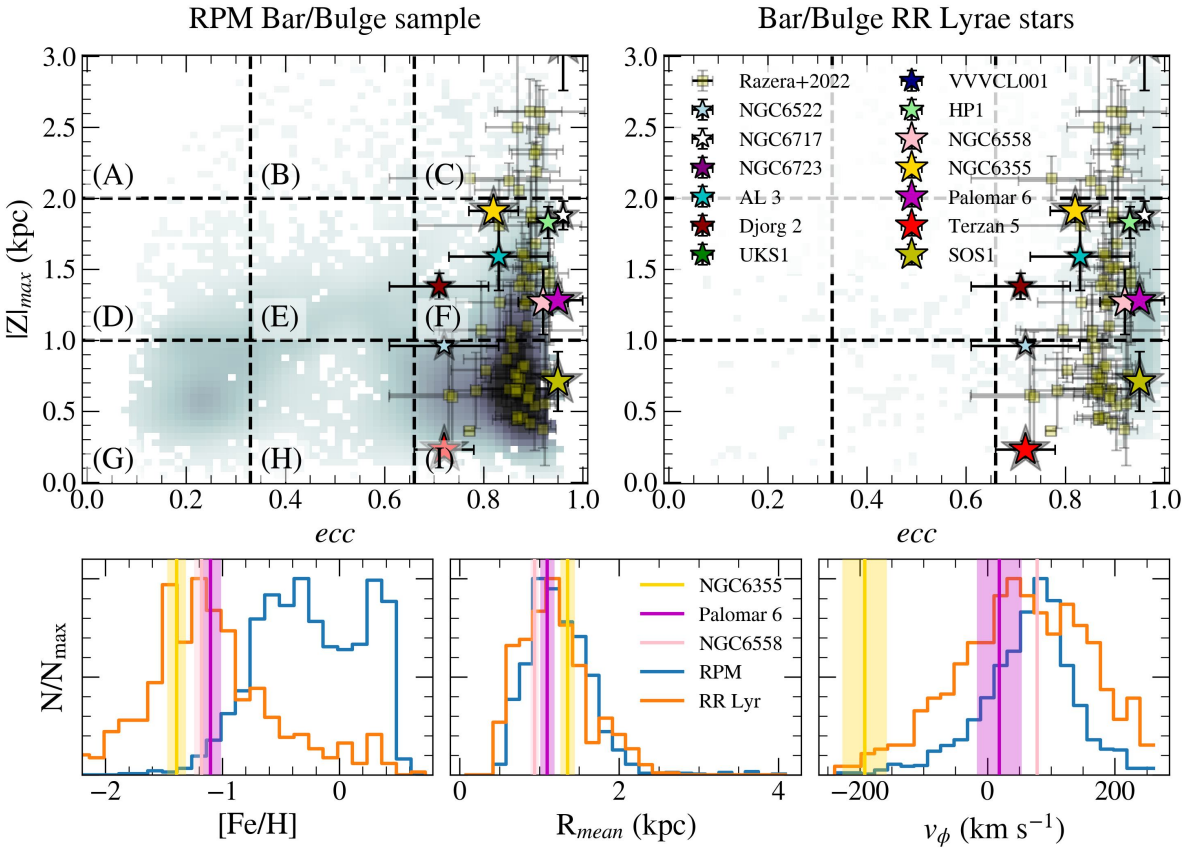

Figure 6.1: Pal 6 and NGC6355 compared with the RPM bulge sample of Queiroz et al. (2021) (left panel) and Galactic bulge RR Lyrae population (right panel). Upper panels: $|Z|_{max}$ as a function of the eccentricity plane divided into nine frames defined by the letter close to the horizontal lines. The magenta star represents Pal 6, and the golden one represents the locus of NGC 6355. The bottom panels show the population density of [Fe/H], R_{mean}, and v_ϕ for cell F. The magenta and gold lines represent the position of Palomar 6 and NGC 6355, respectively, in each panel, and the shaded gold region shows the 1σ distribution.

formation rate (SFR) was found to be best suited with $\nu = 1$ Gyr^{-1} to fit the abundances of a selected sample of bulge stars in Razera et al. (2022). Therefore, we adopted this SFR for all elements. The SFR is the rate at which the available gas mass is turned into stars. Consequently, it measures the inverse of the system formation timescale: Our adopted $\nu = 1.0$ Gyr^{-1} represents a relatively fast star formation of 1.0 Gyr. The chemical evolution models assume a baryonic mass of 2×10^9 M$_\odot$, a dark halo mass 1.3×10^{10} M$_\odot$, and the cosmological parameters from Planck Collaboration et al. (2016). The bulge is considered a classical spheroidal component. Finally, the models project the chemical abundance distribution at different radius ranges r$<$ 0.5 kpc (dash-dotted line in Figure 6.2), 0.5 $<$ r $<$ 1 kpc (dashed line), 1 $<$ r $<$ 2 kpc (dotted line), and 2 $<$ r $<$ 3 kpc (solid line). For Na and Al, we used the Kobayashi et al. (2020) models for the Galactic bulge. These models also assume an SFR $\nu \sim 1.0$ Gyr^{-1}.

In addition to the chemodynamical models, in the following analysis, we also compare the abundance ratios obtained in this work with the reference clusters. To compare with the RPM and RR Lyrae samples, we selected only stars within the cell **F** of Figure 6.1.

Figure 6.2 shows the abundances of O, Mg, Si, and Ca as a function of [Fe/H]. To better illustrate the comparison, the mean locus of the RPM sample is shown as a solid black line. We derived [α/Fe] considering the α elements O, Mg, Si, and Ca. Our means [α/Fe] are compatible within 1σ with the assumed value for the isochrone fitting for Pal6 and BGC6355, reinforcing the analysis's consistency. Pal 6 and NGC 6355 are compatible with the RR Lyr locus in all cases. Moreover, they are also compatible with the other GCs, except for Ca, in which NGC6355 is relatively richer than the others.

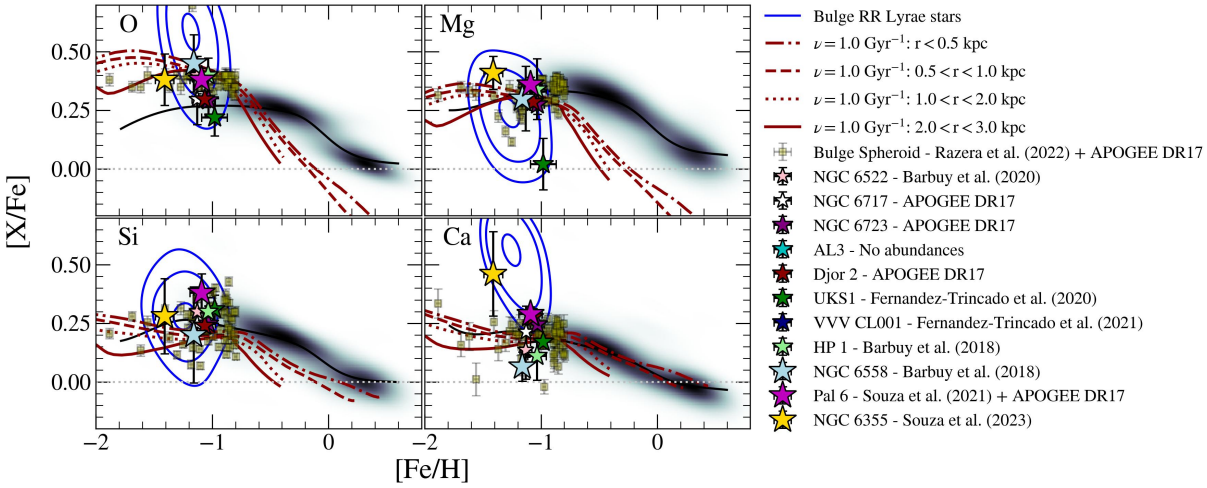

Figure 6.2: O, Mg, Si, and Ca abundance as a function of [Fe/H]. The KDE plot represents the RPM bulge selection from cell F, and the blue contours represent the RR Lyrae sample. The magenta and golden stars represent the mean abundance of Palomar 6 and NGC 6355, respectively. The spheroidal bulge 58 stars are the yellow squares. The chemodynamical evolution models are shown in different radii ranges: r< 0.5 kpc (dash-dotted line), 0.5 < r < 1 kpc (dashed line), 1 < r < 2 kpc (dotted line), and 2 < r < 3 kpc (solid line).

Due to the presence of MPs, the spread in [Na/Fe] is higher than for the other elements. This effect can be observed in the top panel of Figure 6.3 with the discrepancy between the two models and the mean locus for the case of low metallicities. Palomar 6 is not compatible with a bulge [Na/Fe]. The reason is due to the presence of a 2G star in their sample. The same effect is expected for [Al/Fe] because the Al abundance is a good indicator of 2G stars (Meszaros et al., 2020). The lower panel of the same figure shows the high error bars of [Al/Fe] for NGC 6355 due to the presence of two moderately Al-rich stars.

We investigate the iron-peak elements V, Mn, Co, and Cu (Figure 6.4). We also

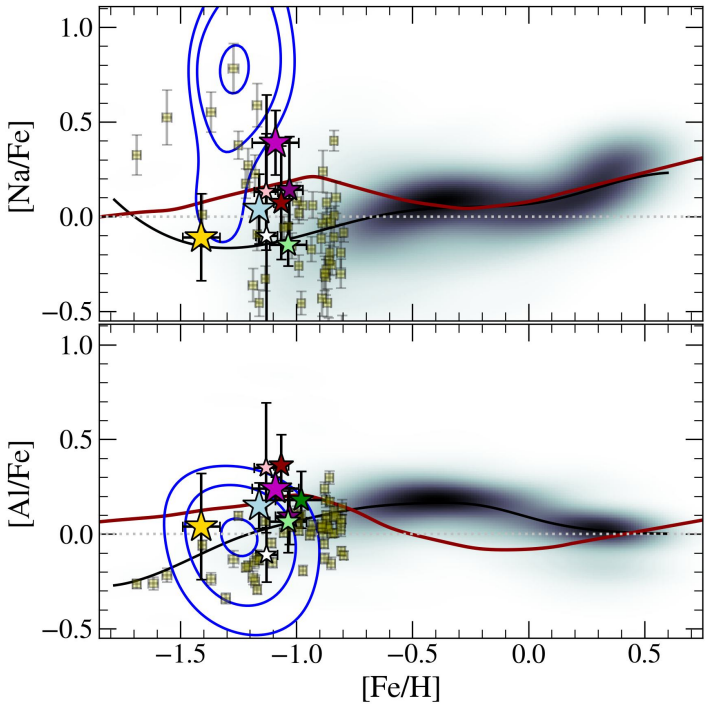

Figure 6.3: Same as Figure 6.2 for odd-Z elements Na (upper) and (bottom). The solid red line is the chemical evolution model from Kobayashi et al. (2020).

compared our results with bulge GC stars from Ernandes et al. (2018) and bulge field stars from Ernandes et al. (2020) to increase the bulge sample. The chemical evolution model fits Pal 6 and NGC 6355 perfectly. For Cu abundances, the selected bulge clusters have relatively lower values than NGC 6355, indicating a different possible scenario for its early evolution. In the case of V (top left panel), the evolution model is shifted to lower abundances for all metallicities than the mean locus. The models suitably fit Palomar 6 and NGC 6355 abundances, the selected clusters, and the bulge GC stars for Mn, Co, and Cu.

The Zn abundances derived are based only on the line ZnI 6362.339 Å. In Figure 6.5, NGC 6355 is perfectly fitted by the models and is compatible with all reference clusters. Here, it is worth noting that the models predict supersolar zinc abundances for metallicities above −1.0 and subsolar abundances for values below −1.0. The low Zn as an indicator of an ex-situ origin was suggested only for the case of near-solar metal-rich stars (Minelli et al., 2021). Palomar 6 is not presented in this analysis because there is no Zn abundance for this cluster, even from APOGEE.

The comparison of heavy-element abundances of Palomar 6 and NGC 6355 with literature GCs is shown in Figure 6.6. NGC 6355 abundances are compatible with HP 1 in

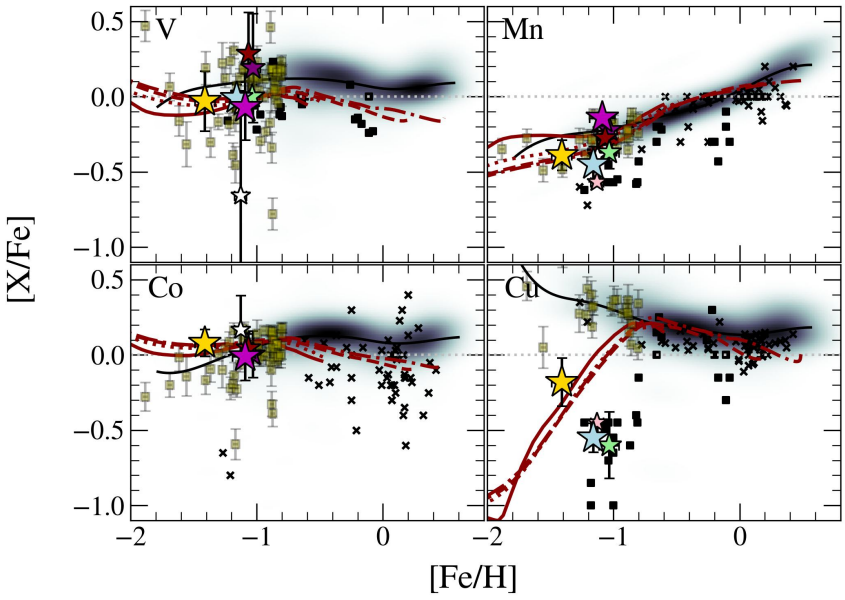

Figure 6.4: Same as Figure 6.2 for V, Mn, Co, and Cu. The black squares are bulge GC stars from Ernandes et al. (2018), and black crosses show bulge field stars from Ernandes et al. (2020). The chemodynamical evolution models are shown in different radius ranges: r< 0.5 kpc (dash-dotted line), 0.5 < r < 1 kpc (dashed line), 1 < r < 2 kpc (dotted line), and 2 < r < 3 kpc (solid line).

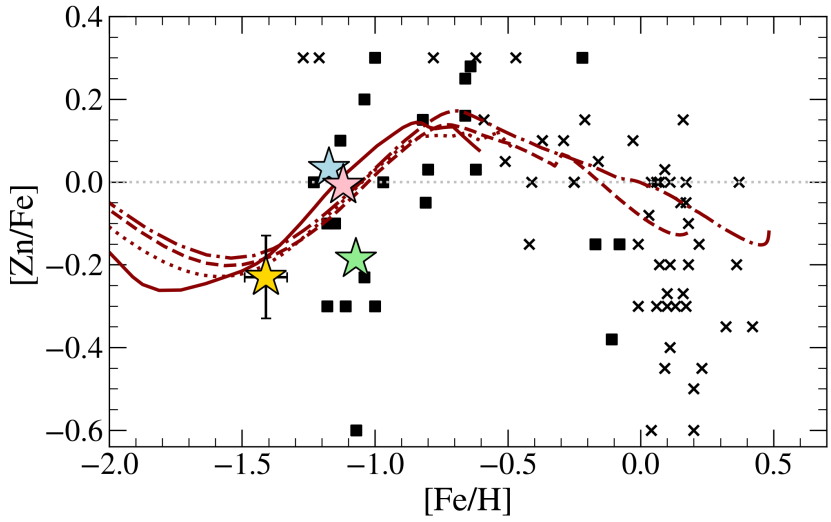

Figure 6.5: Same as Figure 6.2 for Zn. The Friaça and Barbuy (2017) evolution models are shown in different radius ranges: r< 0.5 kpc (dash-dotted line), 0.5 < r < 1 kpc (dashed line), 1 < r < 2 kpc (dotted line), and 2 < r < 3 kpc (solid line).

almost all heavy elements except for Ba, which NGC 6355 has higher values. Palomar 6, for its part, agrees only regarding Ba and Eu abundances with HP1. There is a rather large scatter in the abundance of n-capture elements, especially Y, Zr, and Ba. This pattern is better explained in Chiappini et al. (2011), Cescutti and Chiappini (2014), and Barbuy et al. (2018b).

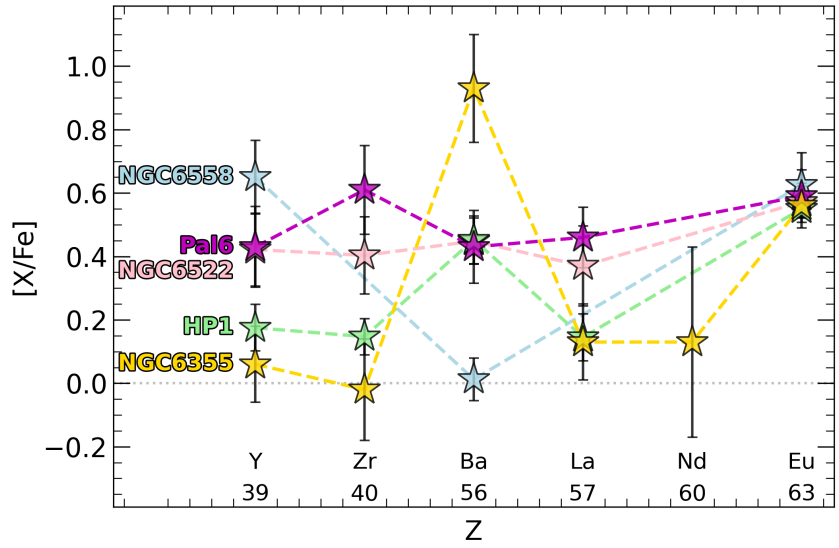

Figure 6.6: Abundance pattern [X/Fe] vs atomic number (Z) for heavy elements Y, Zr, Ba, La, Nd, and Eu. The colours are the same as in Figure 6.2.

6.1.3 Analysis of abundance discriminators

The [Mg/Mn]-[Al/Fe] plane is often used in the context of the Galactic halo to split the original MW population from merger remnants (Hawkins et al., 2015; Limberg et al., 2022) because the accreted population shows lower [Al/Fe] abundances and high α abundances due to the abrupt evolution interruptions of the merger progenitor. Horta et al. (2021) applied the same idea for a star sample located in the Galactic centre to find debris stars within the Galactic bulge. They called *Heracles* this inner Galaxy structure placed in the ex-situ portion of the [Mg/Mn]-[Al/Fe] plane and defined it as follows (Horta et al., 2021):

$$\text{Heracles} = \begin{cases} -2.60 \leq E/10^5 \leq -2.00\,\mathrm{km^2\,s^{-2}} \\ ecc \geq 0.60 \\ r^{\dagger} \leq 4kpc \longrightarrow {}^{\dagger}\ \text{Galactic centre distance} \\ [\mathrm{Mg/Mn}] > +0.25, [\mathrm{Al/Fe}] < -0.07 \\ [\mathrm{Mg/Mn}] > 5 \times [\mathrm{Al/Fe}] + 0.5 \\ [\mathrm{Fe/H}] > -1.7 \end{cases} \tag{6.1}$$

In the context of the [Mg/Mn]−[Al/Fe] plane (right panel of Figure 6.7), the reference bulge GCs have no preferential position. However, Palomar 6 and NGC 6355 show interesting behaviours. Palomar 6 is an in-situ member confirmed through the [Mg/Mn]−[Al/Fe] plane, with APOGEE abundances, because this cluster is located perfectly in the high-α

in-situ region as well as Djor2, NGC6723, and NGC6558. In contrast, NGC 6355, HP1, and NGC6717 are located at the border between Heracles and the *in-situ high-α* region. Two of our four stars of NGC6355 present a maximum Al abundance of +0.30, which could be 2G stars (2G; Meszaros et al., 2020; Fernández-Trincado et al., 2022). Figure 3.12 shows the (anti-)correlations that indicate the presence of MPs. We do not find a Mg-Al anticorrelation, although this is expected mainly for massive clusters because of the metallicity multimodality (Meszaros et al., 2020). We can also observe a slight difference between the 1G and 2G [La/Fe] mean abundances. Marino et al. (2021) showed that separating the MPs using La abundances is impossible. However, the mean abundance value is higher for anomalous stars than for normal stars. For the case of NGC6522, although the high error bars, the mean value is clearly in the high-α in-situ region.

The mean on the [Mg/Mn]-[Al/Fe] plane changes in the diagonal direction going to the left or right when only the 1G or 2G stars are considered for computing the cluster mean abundance, respectively. Then, assuming the mean abundance of the 1G stars, NGC 6355 is placed inside the Heracles region on the [Mg/Mn]-[Al/Fe] plane. It is worth pointing out that Queiroz et al. (2021) showed that a sample of counter-rotating stars in the RPM sample presents no preferential location in the [Mg/Mn]-[Al/Fe] plane, suggesting that this region may not be entirely composed of accreted objects as can be seen by the contours of the spheroidal bulge stars. Therefore, even though NGC 6355, HP1, and NGC6717 are placed in the accreted region, this does not signify an ex-situ origin.

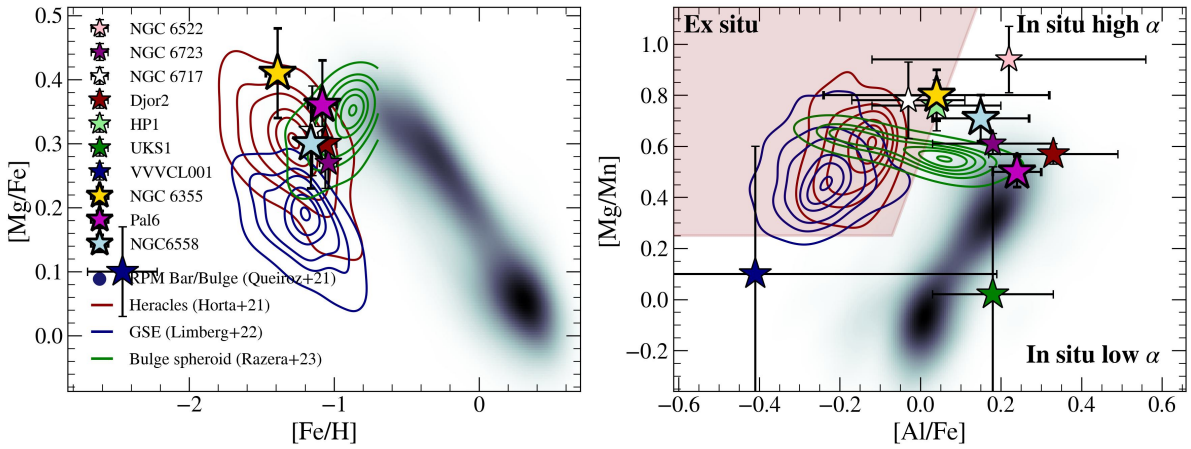

Figure 6.7: [Mg/Mn]-[Al/Fe] plane with the identification of Heracles in red contours. The colours and density map are the same as Figure 6.1. The circles represent the mean considering only 1G (left) and 2G (right) stars in NGC 6355.

6.1.4 Age-metallicity relation and integral-of-motion space

Figure 6.1 shows that most bulge GCs are located in F, representing high eccentric orbits supported by pressure, indicating a spheroidal structure. Razera et al. (2022) analysed a sample of 58 stars from the RPM sample of the inner Galaxy (Queiroz et al., 2021) with metallicity values around the peak of the bulge metallicity distribution function (~ -1.1; Bica et al., 2016). After meticulous chemical analysis, the authors concluded that this star sample is a genuine member of a spheroidal structure in the inner Galaxy, also placed in the high eccentricity region. The fact that all MMPGCs are located in cells C and F indicates that they are also possible members of a pressure supported structure more consistent with a spheroidal bulge. Moreover, since all MMPGCs are in cell F, this cell probably represents the oldest population of the inner Galaxy.

In principle, the AMR of the Galactic bulge MMP GCs shows they are almost coeval among them (Figure 6.8, left panel). The grey dots in the right panel of Figure 6.8 compose the sample of 96 Galactic GCs collected by Kruijssen et al. (2019). The authors provide an average age for all GCs using the three by Forbes and Bridges (2010), Dotter et al. (2010, 2011), and VandenBerg et al. (2013). In order to investigate the old and spheroidal structure of the inner Galaxy (cell F), we fitted the AMR for the MMP GCs using the leaky-box formalism often used in the literature (e.g. Massari et al., 2019; Forbes, 2020; Limberg et al., 2022; Callingham et al., 2022) with some modifications:

$$Z = -\rho \cdot \ln\left(\frac{t}{t_f}\right) = Z_{\odot} \cdot 10^{[\mathrm{M/H}]} \tag{6.2}$$

where t_f is the lookback time when the stellar population starts to form stars, $Z_{\odot} = 0.019$ for the solar total metallicity, and ρ is the effective yield of the stellar population. The ρ represents the mass ratio of the new stars formed from the enriched gas expelled from supernovae, being, therefore, a measure of chemical enrichment efficiency of the stellar population and is in units of solar total metallicity ($Z_{\odot}$). We are considering the relation $[\mathrm{M/H}] = [\mathrm{Fe/H}] + \log_{10}\left(0.694 \cdot 10^{[\alpha/\mathrm{Fe}]} + 0.306\right)$. For the MMP GCs of the Galactic bulge we assumed $[\alpha/\mathrm{Fe}] = +0.4$ (Barbuy et al., 2018b) and $[\alpha/\mathrm{Fe}] = +0.0$ for the ex-situ GCs (Helmi et al., 2018). Therefore:

$$t = t_f \cdot \exp\left(-\frac{Z_{\odot}}{\rho} \cdot 10^{[\mathrm{Fe/H}]+\Delta}\right) \begin{cases} \Delta = 0.312 & \text{for MMPGCs} \\ \Delta = 0.0 & \text{for ex-situ GCs} \end{cases} \tag{6.3}$$

For the MMP GCs Galactic bulge population (Table ref family), we obtained a yield $\rho = 0.061 \pm 0.013\ Z_{\odot}$ and $t_f = 13.679 \pm 0.135$ Gyr. The derived t_f value indicates that this population is among the oldest ones in the Galaxy since their formation time is close to the age of the Universe of 13.799 ± 0.021 Gyr (Planck Collaboration et al., 2016). This finding raises intriguing questions about the early formation of the Galactic bulge population. To investigate the derived effective yield, we also fitted the ex-situ branch of the AMR. The result is the cyan solid line in the right panel of Figure 6.8 with $\rho = 0.007 \pm 0.009\ Z_{\odot}$ and $t_f = 13.083 \pm 0.124$ Gyr. The effective yield is approximately 8 times smaller than the value derived for the MMP GCs. In the right panel of Figure 6.8, we also present as a red dashed line the AMR with an effective yield 10 times smaller than the MMP GCs and with the same t_f. It indicates that the spheroidal structure of the inner Galaxy represented by cell F was formed at the beginning of the Galaxy at 13.679 ± 0.135 Gyr ago and has been chemically enriched approximately ten times faster than the rest of the Galaxy (Barbuy et al., 2018b). These implications of rapid chemical enrichment in the spheroidal structure of the inner Galaxy open up new avenues for further research and exploration.

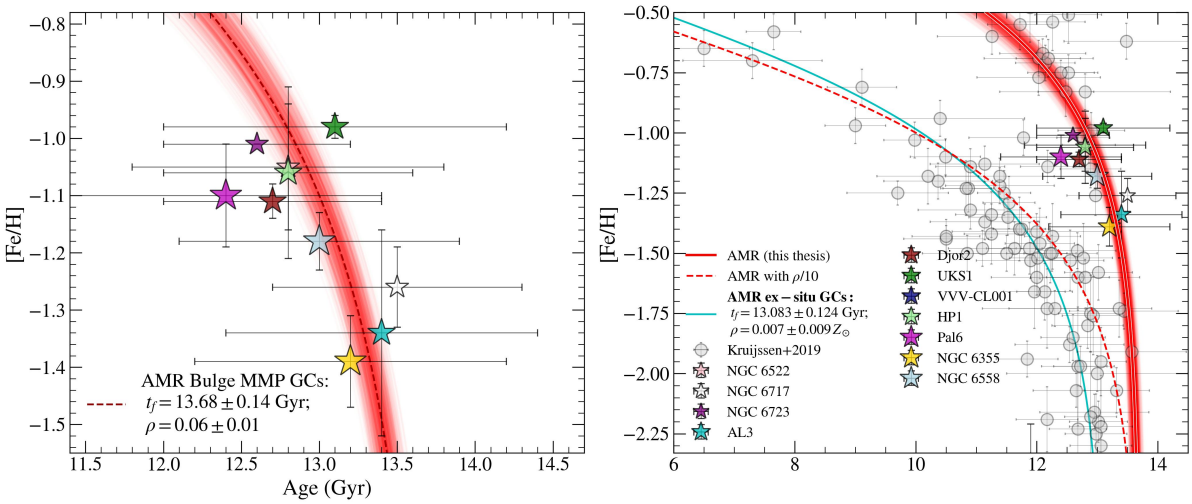

Figure 6.8: AMR for the Galactic GCs system. The left panel shows the AMR fitting for the GCs from Table 6.1. The red line shows the best fit with the parameters in the legend, and the thin red lines are the results of the errors. The right panel shows the complete AMR for all GCs of the Galaxy from Kruijssen et al. (2019) (grey dots). The red dashed line represents the locus of ex-situ GCs considering a chemical enrichment efficiency ten times lower than the bulge, as represented by the effective yields (ρ). The cyan line is the best-fit for the ex-situ branch.

In Figure 6.8, we show Palomar 6 and NGC 6355 as magenta and gold star symbols, respectively, together with the bulge GCs. Age is hugely crucial for the progenitor of a GC classification. For the case of NGC 6355, the isochrone fitting considering the $T_{\rm eff}$

correction indicates an in-situ candidate. Nevertheless, the uncertainty on age still gives NGC 6355 a low probability of having an ex-situ origin. The same hypothesis could be said for the Palomar 6 case. Nevertheless, since the chemical analysis indicates an in-situ origin, the age error bar for Palomar 6 does not enable another origin.

The dynamics based on the orbital parameters of Table 6.1 place the MMPGCs in the low-energy and low absolute L_Z region. Horta et al. (2021) also analysed the IOM space in the context of the inner Galaxy separating Heracles (as defined above) from the bulge selection (Figure 6.9). The main-bulge progenitor is in the left panel, and the Heracles (supposedly ex-situ) progenitor is in the right. While Palomar 6 and the MMPGCs are placed almost in the same prograde region in the IOM space ($L_Z > 0$, Figure 6.9), NGC 6355 presents a retrograde motion ($L_Z < 0 = -31.28 \pm 24.42$ km s^{-1}kpc). Even though it is not possible to distinguish a specific region for the main bulge and Heracles progenitors, the retrograde motion of NGC6355 strongly indicates an external origin.

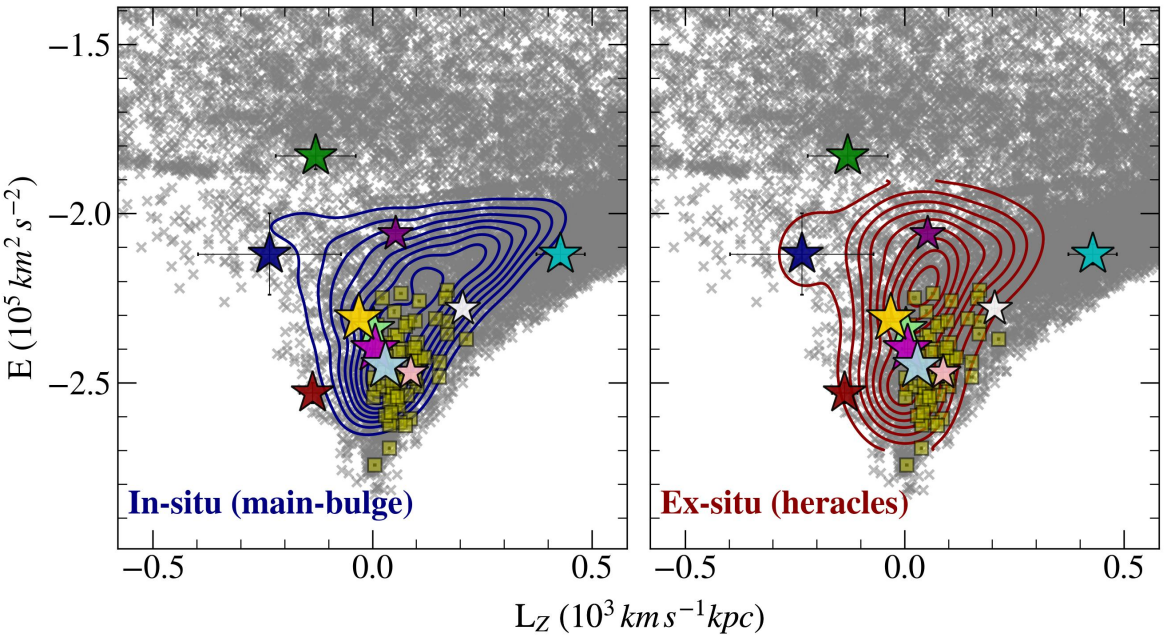

Figure 6.9: IOM space for the bulge stars selected by Horta et al. (2021). The left panel shows the contours of the main-bulge progenitor stars. The right panel shows the contours of the Heracles progenitor. The stars are coloured as in Figure 6.1.

Although NGC 6355 has properties of ex-situ GCs such as the [Mg/Mn] and [Al/Fe] abundances, which are compatible with Heracles, we cannot confirm that it is in-situ GC only because it is confined to the volume of the Galactic bulge. From the point of view of chemical abundances, most of its element abundances follow the in-situ clusters and bulge

RR Lyrae population, including its low Zn abundance, which appears to be compatible with the chemodynamical evolution models. The old age of NGC 6355 completes a possible in-situ scenario for the cluster because its age fits the predictions for the early evolution of the Galactic bulge. Therefore, NGC6355 may be one member of the primordial building blocks of the Galaxy that formed even before the Galaxy formation.

6.2 The GC Terzan 5 versus the Galactic bar.

Terzan 5 is a massive cluster (2×10^6 $M_\odot$; Lanzoni et al., 2010) located in the inner Galaxy ($d_\odot$ = 6.62 kpc; Baumgardt and Vasiliev, 2021) obscured by a high reddening ($E(B-V) = 2.38$; Valenti et al., 2007). Some studies (Origlia et al., 2011, 2013) have demonstrated that Terzan 5 possesses a three-peak metallicity distribution function (MDF): [Fe/H]= +0.30 (popA), [Fe/H]= −0.30 (popB), and [Fe/H]= −0.87 (popC). SOS1 has a metallicity value that agrees with Terzan 5's popC. Figure 6.10 shows SOS1 abundances of O, Mg, Ca, Si, C, and Al compared with Terzan 5 (Origlia et al., 2011, 2013). Even though popC comprises only three stars, it is possible to observe good compatibility between SOS1 and popC for the *alpha* elements. We show the expected variation from 1G stars with similar metallicity values as SOS1 (arrows) to form the 2G stars for the O, Mg, C, and Al cases. To construct the arrows, we took the abundance differences between the extreme stellar generations for all GCs of the HST UV Legacy Survey in Milone et al. (2018). We applied different methods to calculate the differences. These expected variations can explain the SOS1 abundances, chemically making its GC 2G origin more evident. Moreover, the chemical evolution model that better fits Terzan 5 comprises a double-burst of a primordial cloud with a mass of 4×10^7 $M_\odot$ with a delay of 5 Gyr between both bursts, gas loss, and $\sim 60\%$ of stars stripped (Romano et al., 2023). Also, the metal-poor population of Terzan 5 is located mainly in the outer part of the cluster (Romano et al., 2023), being easier to be trapped by the Galactic bar than most internal stars, a scheme consistent with SOS1 properties.

Another important link we can provide between SOS1 and Terzan 5 is the stellar age. We employed the abundance ratio [C/N] and age relation to date SOS1. The [C/N] abundances of red giants can be used as a proxy for ages because they change their [C/N] atmospheric abundance ratio after experiencing their first dredge-up. This process synthe-

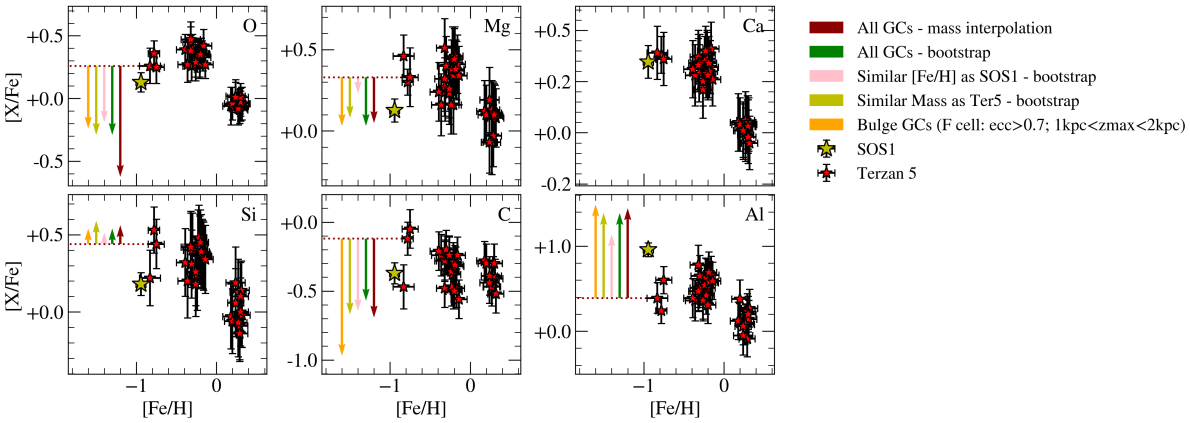

Figure 6.10: Chemical abundances comparison between SOS1 and Terzan 5. The abundances of α elements, C, and Al vs. the iron content [Fe/H] for Terzan 5 (Origlia et al., 2011, 2013) (blue) and the SOS1 (yellow). The arrows show the abundance difference due to the phenomenon of MPs for the most metal-poor population of Terzan 5 derived following different methods. The arrow's length in each panel shows the average maximum difference from Milone et al. (2018) between 1G (dotted line) and 2G for metallicity around [Fe/H]$= -1.0$ (the arrows are shifted in the x-axis to make the plot clearer).

sises new material in their cores through the CNO cycle toward the atmosphere. Since the maximum penetration during the first dredge-up depends on the stellar mass, the mixture brought up to the stellar surface also depends on the mass, consequently related to the stellar age (Masseron and Gilmore, 2015; Salaris et al., 2015; Lagarde et al., 2017). The [C/N]$-$age relation is widely used in the literature. Before applying the calibrations for SOS1, we remove the effect of MPs from the C and N abundances of SOS1. This correction is necessary because the calibrations derived in the literature (e.g. Martig et al., 2016; Casali et al., 2019; Spoo et al., 2022) are based on stellar evolution. The corrections are as follows:

$$[C/N]_{\rm SOS1} = [C/N]_{\rm 1G} + [C/N]_{\rm MPs} \tag{6.4}$$

the abundances derived from APOGEE for 2G stars are the abundance of 1G stars added by a contribution from MPs: enhancement for N and depletion for C. The variations due to MPs were derived using the values provided for the GCs inside the HST UV Legacy Survey (Piotto et al., 2015; Milone et al., 2018) and from different approaches:

1. Considering all GCs and doing a linear regression for logMass (Baumgardt and Vasiliev, 2021) vs. abundance variations (Milone et al., 2018). The differences are then obtained by interpolating for the Terzan 5's mass.

2. Considering all GCs and doing a bootstrap to get the median values.

3. Taking only the GCs with [Fe/H] (Kruijssen et al., 2019) around the SOS1 value (within a range of 0.20 dex). Then, the median differences are computed through a bootstrap.

4. Taking only the GCs with Mass round the Terzan 5 value within a range of 0.5 in logMass.

5. Considering only the GCs inside the cell F (old bulge, Queiroz et al., 2021), $ecc > 0.7$ and 1kpc$< |z|_{\max} <$ 2kpc.

The values are represented in Figure 6.10 as arrows coloured according to the above-mentioned approach. We placed the arrows starting from the median value of the Terzan 5's popC since there is no evidence of 2G stars in the reference sample taken from Origlia et al. (2013). It is also important to note that the N abundance is not presented in Figure 6.10 because there are no calculations for this element. The variations due to MPs are then removed (or added) from the values derived by APOGEE, resulting in the possible 1G values. The distributions are also displayed in Figure 6.11. The best approach is obtaining the abundance variations interpolating by cluster mass due to the narrow distributions compared with the other approaches.

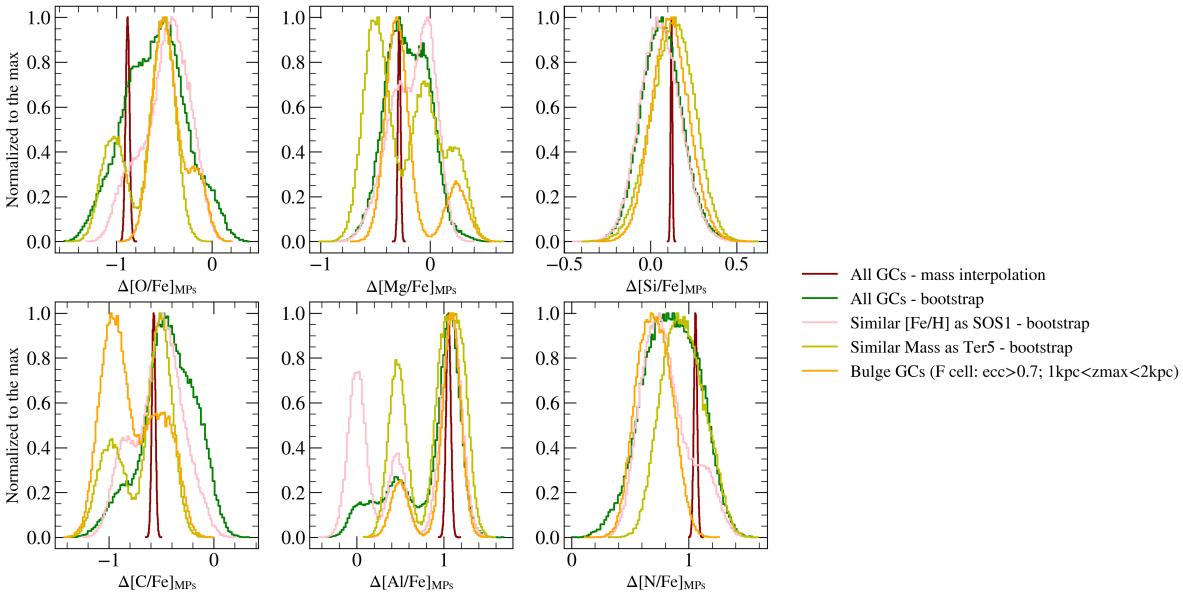

Figure 6.11: Derivation of the abundance contribution due to the MPs. The coloured lines represent different methods to determine the variations to SOS1, as listed on the right side of the figure. The method 1 interpolates the variations as a function of cluster mass. Since Terzan 5 is the most probable host of SOS1, we adopted its mass value. This method is the most reliable, evidenced by the narrow variation distributions. See the text for a detailed explanation of the methods employed.

In possession of the corrected [C/N] abundance, we applied the [C/N]−age relation using four different calibrations:

1. Spoo et al. 2022 for APOGEE DR16.
2. Spoo et al. 2022 for APOGEE DR17.
3. Casali et al. 2019 derived using Gaia-ESO Survey.
4. The generalised calibration using Kepler data by Martig et al. 2016.

Figure 6.12 shows the resulting age distributions using mass interpolation in the best variation derivation method, case 1. We also plotted the age distribution for Terzan 5 (Ferraro et al., 2016) for comparison purposes. In the left panel is the abundance distribution for [C/N] corrected by the variations due to MPs. On the right are the age distributions derived using the abovementioned calibrations. The age distributions are essentially old for the case of interpolating the variations by cluster mass. However, concluding anything about the SOS1 age is impossible for the other cases. Moreover, the calibrations employed in this work were derived for higher metallicities than the SOS1 value. Therefore, the discussion about the SOS1 age is only quantitative, aiming to say if SOS1 is as old as the Terzan 5's popC.

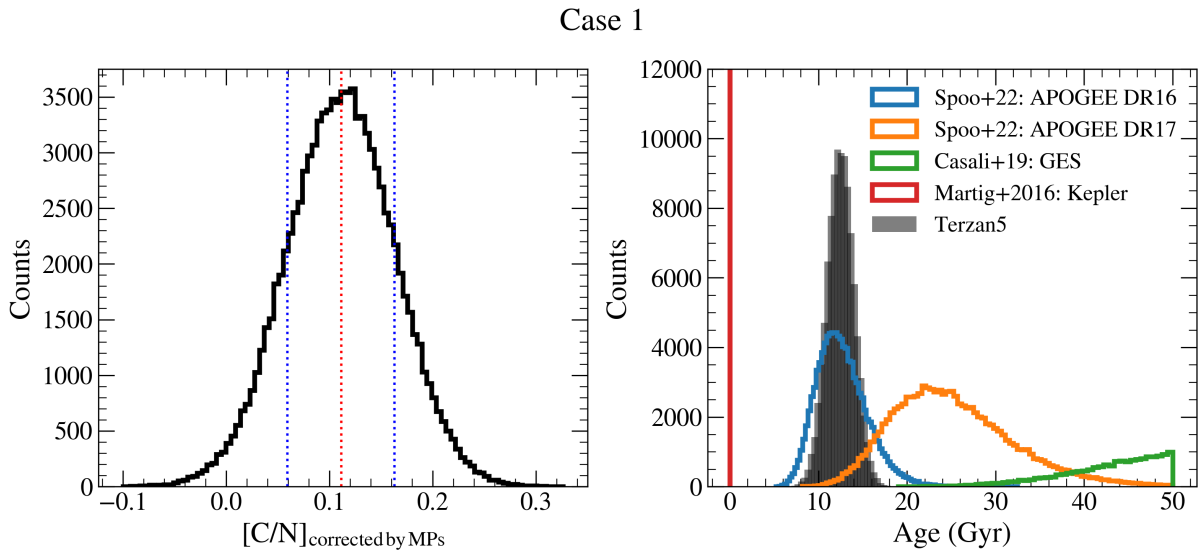

Figure 6.12: Age derivation for SOS1 using the variation derivation method 1. We derived the age distribution of SOS1. On the left is the corrected [C/N] abundance. On the right is the age distribution according to different calibrations (coloured lines). The shaded grey distributions show the expected age for Terzan 5.

Part II

What drives the origin of multiple stellar populations in star clusters?

Chapter 7

Multiple stellar populations in the halo globular cluster NGC6752

This chapter presents the description of the globular cluster NGC6752 concerning single and multiple stellar populations. These results were published in Souza et al. (2020).[1]

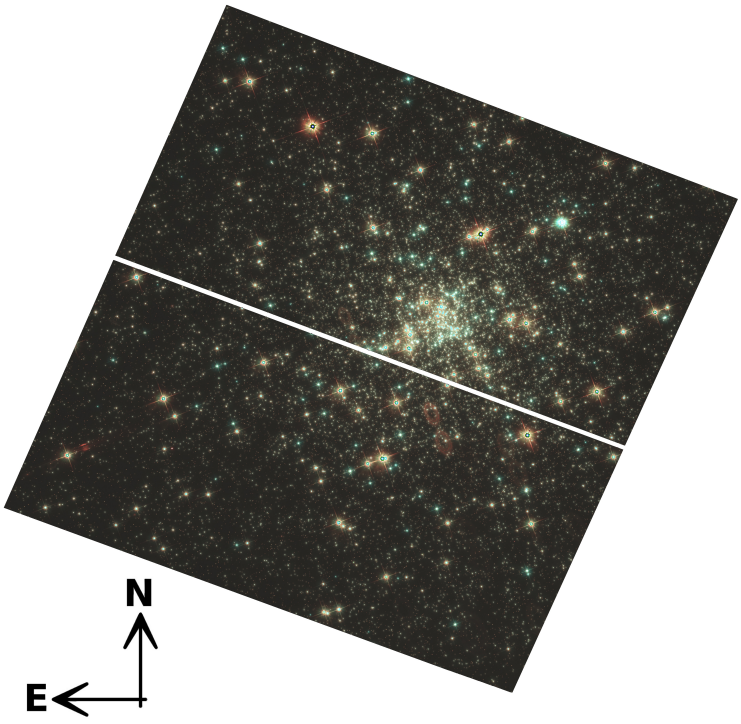

Figure 7.1: F390W/F555W/F814W combined colour image from the HST WFC3 camera for NGC 6752.

[1] https://ui.adsabs.harvard.edu/abs/2020ApJ...890...38S/abstract

7.1 Introduction

NGC 6752 is a halo globular cluster, located at l = 336°49, b = -25°63, with a distance from the Sun of $d_{\odot}$ = 4.0 kpc (Harris, 1996, edition 2010)[2]. Gratton et al. (2005) derived a metallicity of [Fe/H]= -1.48 ± 0.07 using high-resolution spectroscopy ($R = 40,000$) of seven stars near the RGB bump. Gratton et al. (2003) and VandenBerg et al. (2013) obtained an age of 12.50±0.25 Gyr and 13.4±1.1 Gyr, respectivaly. Additionally, Carretta et al. (2012) identified three stellar populations based on three values of abundances of O, Na, Mg, Al, and Si elements that are sensitive to stellar populations in GCs, denominated as first (P), intermediate (I), and extreme (E) populations. Milone et al. (2013) gave the first photometric evidence of three stellar populations by using *HST* data. Nardiello et al. (2015), using FORS2/VLT data, have observed the split of the MS of NGC 6752 using UBI filters and calculated the radial distribution of the populations and the difference in helium between the 1G and 2G stars. Milone et al. (2019) confirmed the existence of three stellar populations from NIR photometric data on MS stars. Finally, Cordoni et al. (2020) analysed the kinematics of the P and E populations of NGC 6752, and they found no difference in rotation between the two stellar populations.

7.2 Data

We used the *HST* photometric data for NGC 6752 in the ultraviolet (UV) filters within the UV-Legacy Survey GO-13297 (PI. G. Piotto) and the optical within GO-10775 (PI. A. Sarajedini). These programs made available data in the UV filters F275W, F336W, and F438W from the Wide Field Camera 3 (WFC3) and the optical filters F606W and F814W from the Wide Field Camera of the Advanced Camera for Survey (WFC/ACS). The reduced catalogues are presented in Nardiello et al. (2018). The combined colourful image of NGC 6752 is in Figure 7.1.

7.3 Controlled Experiment

In this Section, we test the reliability of our analysis that will be employed to NGC6752, by using synthetic CMDs. First, we constructed a synthetic CMD using an error function

[2] www.physics.mcmaster.ca/ harris/mwgc.dat

obtained from the atlas extracted by Nardiello et al. (2018) from the data of the *HST* UV-Legacy Survey of Galactic Globular Clusters (Piotto et al., 2015), allowing us to simulate MPs with the synthetic data. The stellar evolutionary model adopted was the DSED isochrone with Z $\sim$ 0.002 with [α/Fe] = +0.4, and age of 13.0 Gyr, as reported in Table 7.1, corresponding to typical values of moderately metal-poor bulge GCs (e.g. Kerber et al., 2018, 2019). We simulated the CMD of a cluster with a total number of 10,000 stars (N_{total}) that host 36% of 1G stars with an age of 13.0 Gyr and 64% of 2G stars 0.1, 0.5, 1.5 Gyr younger than 1G stars (12.90, 12.5, 11.5 Gyr). We considered a fraction of binaries (f_{bin}) of 30% and a minimum mass ratio (q_{min}) of 0.60. The resulting CMDs combining the different available filters are shown in Figure 7.2.

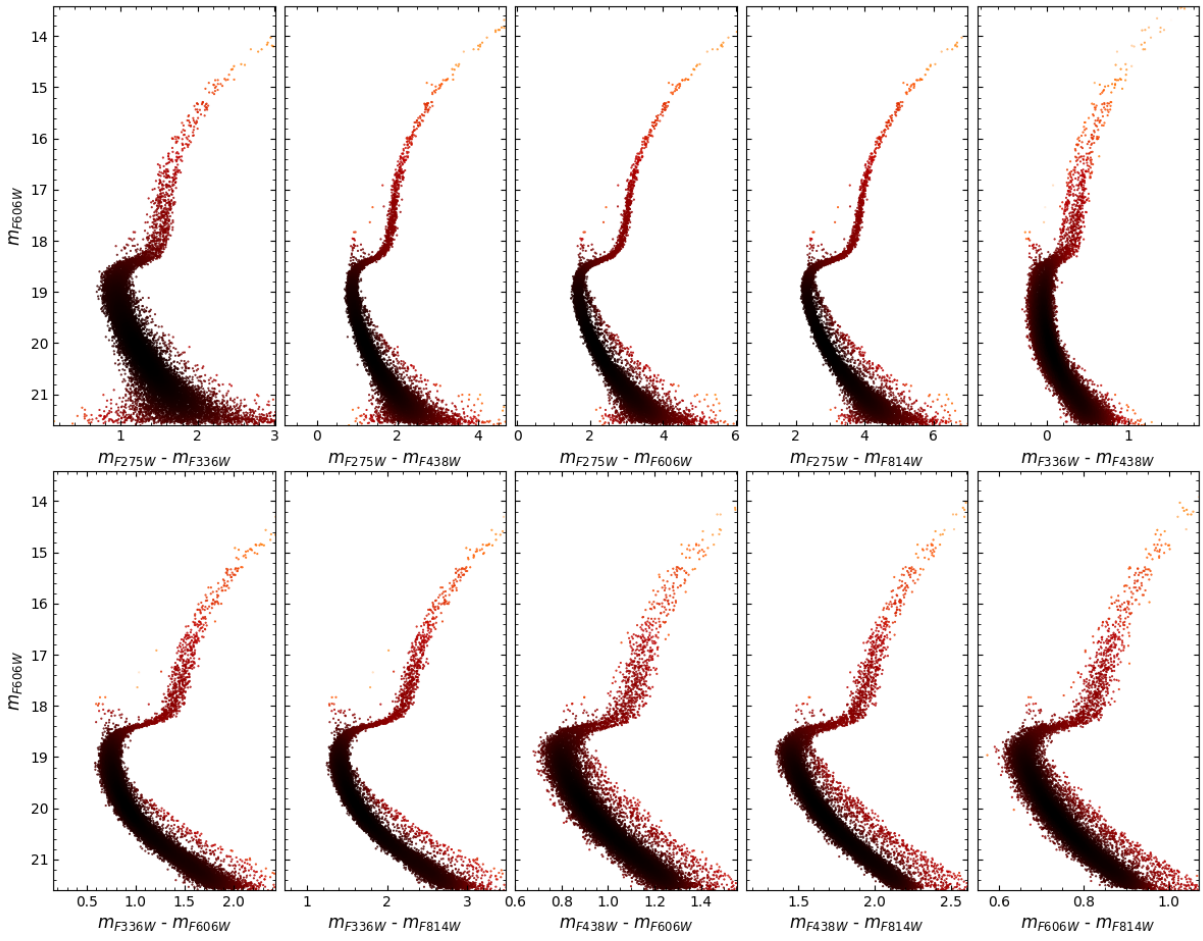

Figure 7.2: CMDs for the Synthetic Data using a DSED isochrone with age = 13.0 Gyr, [Fe/H]= −1.26, $E(B-V) = 0.18$, $(m-M)_0 = 14.38$, $\Delta\tau = 0.50$ Gyr and fraction of 1G stars (N_{1G}/N_{total})= 0.360, generated from *HST* filters. All available combinations of filters are shown.

Table 7.1 - Input parameters for the construction of the synthetic catalogues.

Parameter	No-Spread	Spread
Evolutionary Model	DSED	DSED
N_{total}	260	10,000
τ_{SSP} (Gyr)	13.0	13.0
$\Delta\tau$ (Gyr)	–	0.1, 0.5, 1.5
[Fe/H] (dex)	−1.26	−1.26
$E(B-V)$	0.18	0.18
$(m\text{-}M)_0$	14.38	14.38
f_{bin}	–	0.30
q_{min}	–	0.60
N_{1G}/N_{total}	1.000	0.360

7.3.1 Sources of uncertainty

In our method, we compute the likelihood star-by-star during the isochrone fitting. To keep the high performance of MCMC, we imposed a range in magnitudes based on stellar evolutionary models. The third panel of Figure 1.13 shows no significant difference in age for the ~ 3 magnitudes brighter than the TO. For this reason, we do not take stars above this limit into account in the likelihood calculation.

The faintest stars are limited to the completeness limit, meaning that the number of faint stars depends on the photometric depth. There are no differences between the isochrones in the databases employed in `SIRIUS` for the faintest stars (~ 2 magnitudes below the TO). Therefore, the fit does not depend on the faintest stars. Ramírez-Siordia et al. (2019) presented an analysis considering the faintest stars. They concluded that the effect of the faintest stars only increases the uncertainties without changing the distribution mode since the isochrones do not seem different for the faintest stars, as shown in Figure 1.13 (third panel).

Binary stars' magnitudes represent the combination of the fluxes from the two companion stars. Since the magnitude is the logarithm of the stellar flux, for a binary system with two stars of the same mass, the magnitude of this system corresponds to the magnitude of one star subtracted by $2.5 \times \log(2) \sim 0.75$ (Kerber et al., 2002, 2007). The decrement

in magnitude tends to cause the binary stars to be brighter and redder on the CMD.

The standard BaSTI isochrones overestimate ages by $\sim$ 0.80 Gyr concerning DSED isochrones. The main reason for this discrepancy is that BaSTI isochrones do not include atomic diffusion in the calculations, among other differences in basic physics. Whereas the solar alpha-to-iron, more complete models, including atomic diffusion, are already available in Hidalgo et al. (2018), the available alpha-enhanced models taking this effect into account have yet to be available.

7.3.2 Stellar population tagging

The stellar population tagging allows us to distinguish the first (1G) and second (2G) generation stars (and subsequent ones) from a given CMD. Figure 7.3 shows the procedure to separate the stellar populations in each region of the created synthetic CMD generated using `SIRIUS` code recipes. Milone et al. (2013) defined the HST pseudo-colour C to maximise the separation among MPs on the CMD. Piotto et al. (2015) have shown the power of *HST* UV filters F275W, F336W, and F438W to separate the MPs. F275W is sensitive to OH and F438W to CN and CH. For these filters, the 1G stars are fainter than the 2G because the latter are oxygen- and carbon-poorer than the 1G ones. For the filter F336W, which is sensitive to NH, the 1G stars are brighter than the 2G stars, given that the 2G stars are nitrogen-richer (see Figure 1.7). Note that stronger lines lead to larger opacity and lower brightness. For these reasons, the colour (F275W-F438W) inverts the stellar populations on the CMD concerning the colour (F336W-F438W). The 2G stars in that colour seem redder than the 1G stars. Therefore, combining both colours, the resulting pseudo-colour increases the effect on N abundance through the filter F336W, which is considered twice: $C_{F275W,F336W,F438W} = (F275W - F336W) - (F336W - F438W)$.

Chromosome maps (RGB and MS): Milone et al. (2017) describe the method to separating the stars likely to belong to each stellar population using the so-called chromosome maps based on combinations of UV HST filters. Lee (2019) used UBV data to distinguish MPs and reviewed methods discussed earlier. To construct the chromosome map diagrams, we adopted the method presented in Milone et al. (2017) that is briefly described below. For the CMDs [m_{F814W}, $C_{F275W,F336W,F438W}$] and [m_{F814W}, ($m_{F275W} - m_{F814W}$)], the red and blue fiducial lines are defined as 96^{th} (C_r) and 4^{th} (C_b) percentiles for bins of magnitudes,

respectively. The top- and bottom-middle panels of Figure 7.3 show the red and blue fiducial lines enclosing the RGB and MS stars, respectively. The chromosome map axes are the relative distance between each star and the fiducial lines, defined by:

$$\Delta_{C_{F275W,F336W,F438W}} = \frac{C_{\rm r} - C}{C_{\rm r} - C_{\rm b}} \tag{7.1}$$

$$\Delta_{F275W,F814W} = \frac{G - G_{\rm r}}{G_{\rm r} - G_{\rm b}} \tag{7.2}$$

where the indices r and b refer to the red and blue fiducial lines, respectively, and G represents the colour $\rm m_{F275W} - m_{F814W}$, which is more sensitive to helium mass fraction Y abundance (Milone et al., 2017).

The diagram $[\Delta_{C_{F275W,F336W,F438W}}, \Delta_{F275W,F814W}]$ quantifies the colour distance of each star to the blue and red envelopes so that the Δ-value is closer to zero as the star is closer to the red envelope. The right panels of Figure 7.3 show the final chromosome maps for the RGB (top) and MS (bottom), respectively, for the synthetic CMD.

Some modifications to the identification of the MPs were implemented in the original method from Milone et al. (2017) to preserve uniformity in the MPs separation for the three evolutionary stages (MS, SGB, RGB). The MPs are identified using the Gaussian Mixture Models (GMM), a non-supervised machine learning algorithm that searches to fit K Gaussian distributions to a sample of N data. The fit comes from the basic equation of the Bayes' theorem:

$$G(x) = \sum_{i=1}^{K} \phi_i \times \mathcal{N}\left(x \,|\, \mu_i, \sigma_i\right) \tag{7.3}$$

where $\mathcal{N}(x \,|\, \mu_i, \sigma_i)$ represents the ith Gaussian distribution with mean of μ_i and standard deviation of σ_i. This algorithm was adopted from the `Python` library `Scikit-learn` (Pedregosa et al., 2011).

Here, we assume two subclasses for GMM on a two-dimensional plane. Then, each star is classified as 1G or 2G according to the strength of the two Gaussian distributions on that point of the chromosome map. The separation between the two populations includes clear members of both and stars in the limiting intersection, which can contaminate each other samples. This analysis can be improved by increasing the number of subdivisions in GMM to select the bona-fide stars of each stellar population, as in Milone et al. (2018).

Two-color diagrams (SGB): The slope of the SGB sequence depends on the adopted filter and the cluster's metallicity and age, which are sometimes nearly horizontal. The MPs could appear mixed in this phase, making applying the chromosome map method ineffective. Therefore, we applied a conventional two-color diagram [$m_{\rm F336W} - m_{\rm F438W}$, $m_{\rm F275W} - m_{\rm F336W}$], as described in Nardiello et al. (2015). In order to apply the GMM procedure (same as described in the previous Section), Δ_1 and Δ_2 are the axes that were normalised and then rotated counterclockwise by an angle of 45° to align the stellar distribution with the x-axis. The method is graphically represented in Figure 7.3 (middle panels).

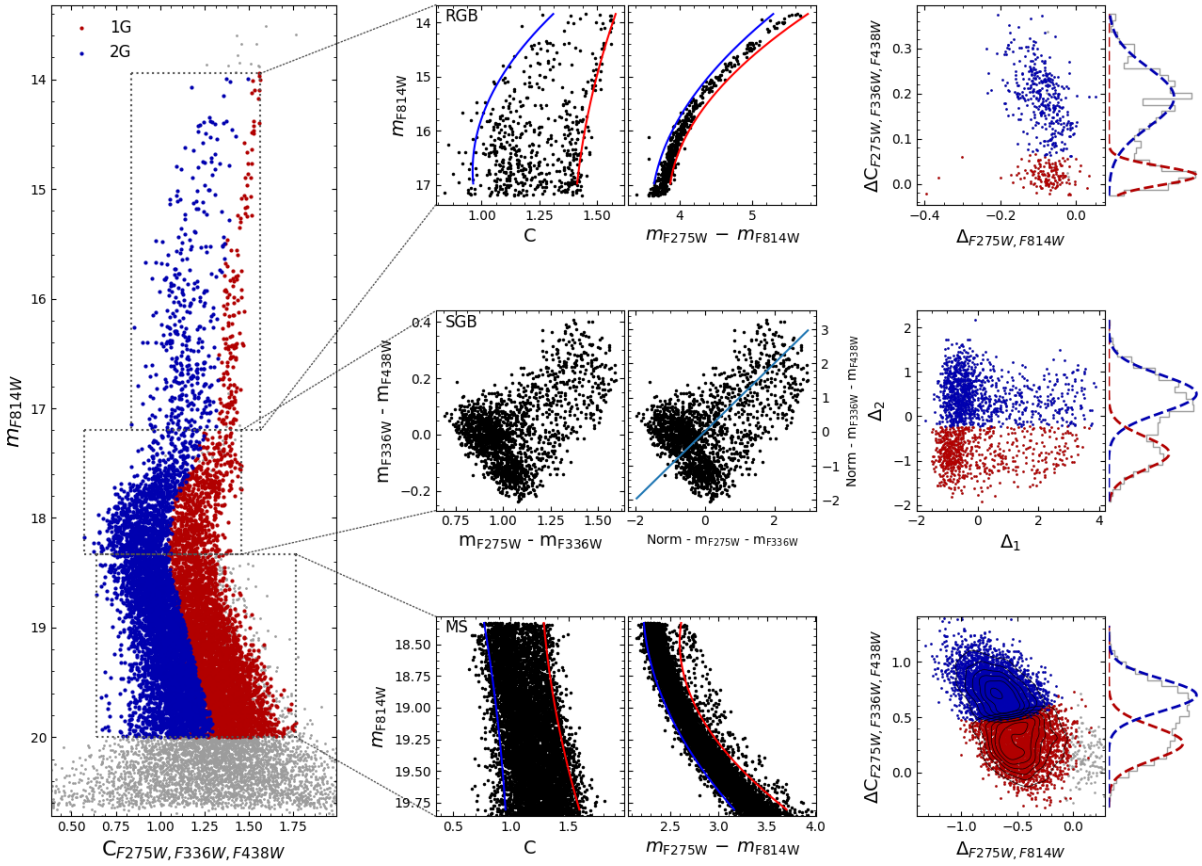

Figure 7.3: MP separation and population tagging applyed to synthetic data with $\Delta\tau = 0.5$ Gyr. The left panel shows the pseudo-colour C, which gives a pronounced MP separation. The middle panels show the procedure we apply to separate the stellar populations. The RGB, SGB, and MS stars are shown from top to bottom. The right panels show the stars identified to belong to 1G and 2G.

7.3.3 Sanity Check

For the NIR filters, the effect of interstellar medium extinction is considerably lower than that of the UV filters. Also, colour-combining filters with a small bandwidth are more suitable for observing the structures on the CMD. Therefore, the combination of magnitudes and colours on the CMD is very important in terms of the information expected to be obtained from isochrone fitting. In order to estimate the effect of the choice of colour, we performed the isochrone fitting using ten different colours, without spreading the stars, combining the five *HST* filters available in the UV Legacy survey of globular clusters (Piotto et al., 2015).

Firstly, we perform the fit considering the SSP without the photometric spread of stars. The DSED isochrones are here fitted to the synthetic No-Spread catalogue data (Table 7.1) to check if we can recover the synthetic CMD's input parameters. For this test, we adopted uniform distribution priors for all parameters. The range of values we used are: for age, between 10 to 15 Gyr; for the metallicity, between 0.00 to −2.00 in [Fe/H]; for reddening, between 0.0 to 1.0 mag; and for the distance modulus, between 12.0 to 16.0 mag. Figure 7.4 shows the behaviour of the parameter space as a function of colour. Age is the most sensitive parameter to the filters, whereas the other parameters vary only slightly with the choice of filters. For colour 8 (third lower panel in Fig. 7.2), which is equivalent to B-V, there is a strong effect on the age, whereas for colour 6 (first lower panel in Fig. 7.2) the parameters are closer to the original ones. Colour 10 ($m_{F606W} - m_{F814W}$, last lower panel in Fig. 7.2), is also close to the input values and has small uncertainties due to its lowest reddening-dependency. Therefore, for our analysis, we chose colour 10.

Secondly, to verify the sensitivity of the method, we simulate real data through synthetic CMDs to perform the isochrone fitting, taking into account a spread of stars and assuming Gaussian priors centred on the parameters given in Table 7.1 (Spread). In Figure 7.5, we show the isochrone fitting for the synthetic CMD with $\Delta\tau = 0.50$ Gyr, assuming that it is SSP (left panel) and MPs (right panel).

We employ the corner plots to present the posterior distributions. (Figure 7.6). They show the N parameter space in a 2D representation, where it is possible to see the correlations between the parameters. As the best value for each parameter, we adopted the distribution mode. For the confidence interval, we selected the 16^{th} and 84^{th} percentile of

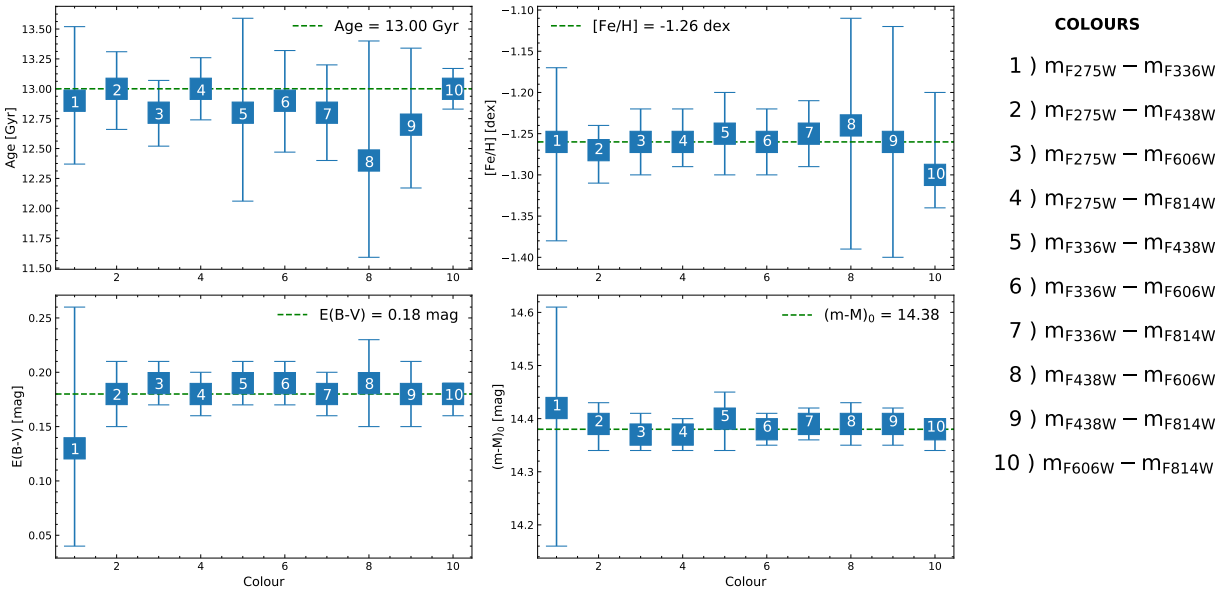

Figure 7.4: Sanity checks with no-spread data, the parameter space as a function of colour. The posterior distributions of each parameter for the ten combinations of *HST* filters of the UV Legacy survey of globular clusters (Piotto et al., 2015). DSED isochrones are adopted. The numbers represent each colour.

the distributions that give us the values inside 1σ from the mode. The top-left panel in Figure 7.6 shows the corner plot for the DSED SSP isochrone fitting. Figure 7.6, in the top-right, bottom-left, and bottom-right panels, show the results for the age derivation in the context of MPs using DSED.

Table 7.2 - Sanity check with spread data, results summarized for synthetic-data in SSP context and MPs.

Sanity Check	N_{1G}/N_{Tot}	Model	τ_{SSP} (Gyr)	$\Delta\tau_{1G,2G}$ (Gyr)	[Fe/H] (dex)	$E(B-V)$ (mag)	$(m-M)_0$ (mag)
SSP	–	DSED	$12.70^{+0.36}_{-0.37}$	–	$-1.26^{+0.03}_{-0.03}$	$0.18^{+0.01}_{-0.01}$	$14.35^{+0.03}_{-0.03}$
		BaSTI	$13.80^{+0.61}_{-0.61}$	–	$-1.26^{+0.03}_{-0.03}$	$0.18^{+0.01}_{-0.01}$	$14.30^{+0.04}_{-0.03}$
MPs $\Delta\tau = 0.10$ Gyr	0.377 ± 0.011	DSED	–	$0.11^{+0.36}_{-0.38}$	$-1.26^{+0.02}_{-0.03}$	$0.18^{+0.01}_{-0.01}$	$14.38^{+0.03}_{-0.03}$
		BaSTI	–	$0.19^{+0.49}_{-0.49}$	$-1.26^{+0.03}_{-0.03}$	$0.18^{+0.01}_{-0.01}$	$14.33^{+0.03}_{-0.03}$
MPs $\Delta\tau = 0.50$ Gyr	0.370 ± 0.012	DSED	–	$0.41^{+0.43}_{-0.37}$	$-1.26^{+0.03}_{-0.02}$	$0.18^{+0.01}_{-0.01}$	$14.38^{+0.03}_{-0.03}$
		BaSTI	–	$0.51^{+0.54}_{-0.54}$	$-1.26^{+0.02}_{-0.02}$	$0.18^{+0.01}_{-0.01}$	$14.33^{+0.03}_{-0.03}$
MPs $\Delta\tau = 1.50$ Gyr	0.339 ± 0.008	DSED	–	$1.20^{+0.44}_{-0.38}$	$-1.26^{+0.02}_{-0.03}$	$0.18^{+0.01}_{-0.01}$	$14.37^{+0.03}_{-0.03}$
		BaSTI	–	$1.47^{+0.53}_{-0.46}$	$-1.26^{+0.03}_{-0.02}$	$0.18^{+0.01}_{-0.01}$	$14.35^{+0.03}_{-0.03}$

Even though the spread of stars changes the visual aspect of the CMD, the parameters

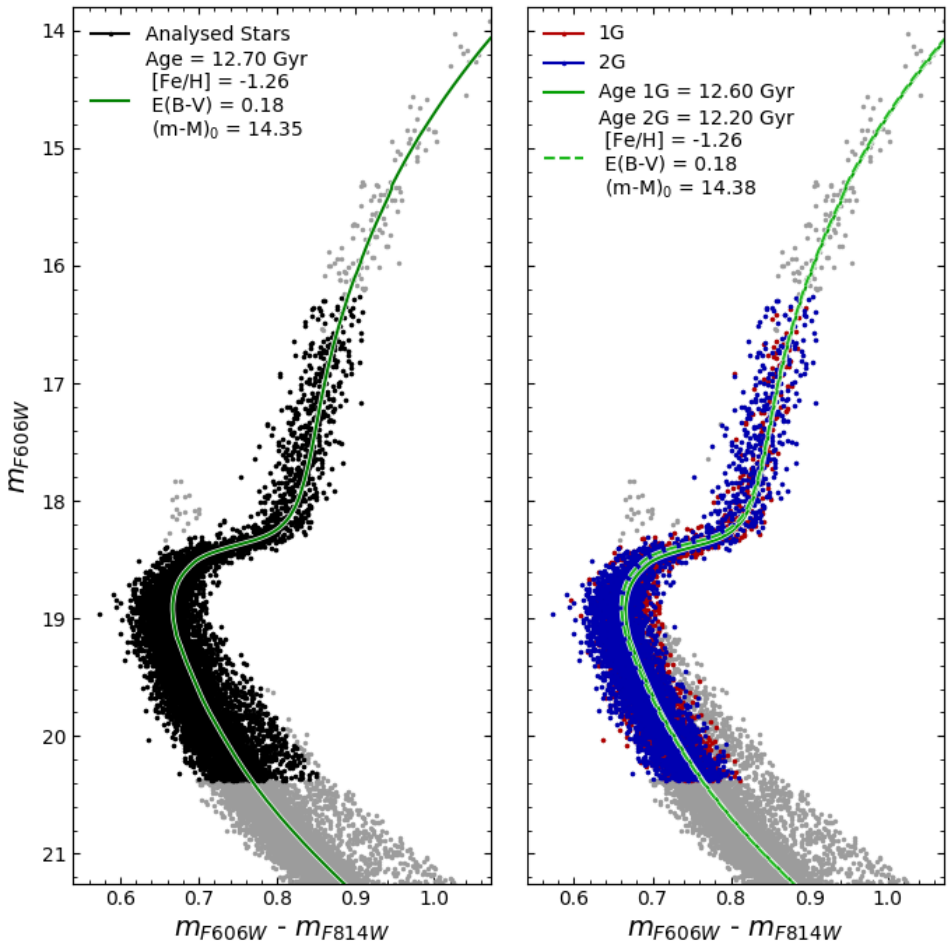

Figure 7.5: Sanity check with spread data, isochrone fitting for the synthetic CMD considering SSP (left) and MPs (right) for DSED isochrones. The grey dots are discarded for the fit.

obtained from the isochrone fitting given in Table 7.2 for SSP and MPs are both in good agreement with the input values from Table 7.1. In conclusion, in this Section, we could describe the approach and check the validity of `SIRIUS` in the context of MPs.

7.4 Analysis of NGC 6752

In order to separate the populations P, I, and E (hereafter 1G, 2G, and 3G), the number of components on GMM were increased to three for the RGB and SGB, and to four for the MS. The classification of 1G, 2G, and 3G stars is in agreement with Milone et al. (2013) since a clear distinction of three stellar populations can be verified in Figure 7.7. Milone et al. (2013) derived the mass fraction of each population to be of ~ 25, ~ 45, and ~ 30 per cent, respectively. We found a fraction of stars of 25 ± 5, 46 ± 7, and 29 ± 5 per cent for the 1G, 2G, and 3G, respectively, in excellent agreement with Milone et al. (2013).

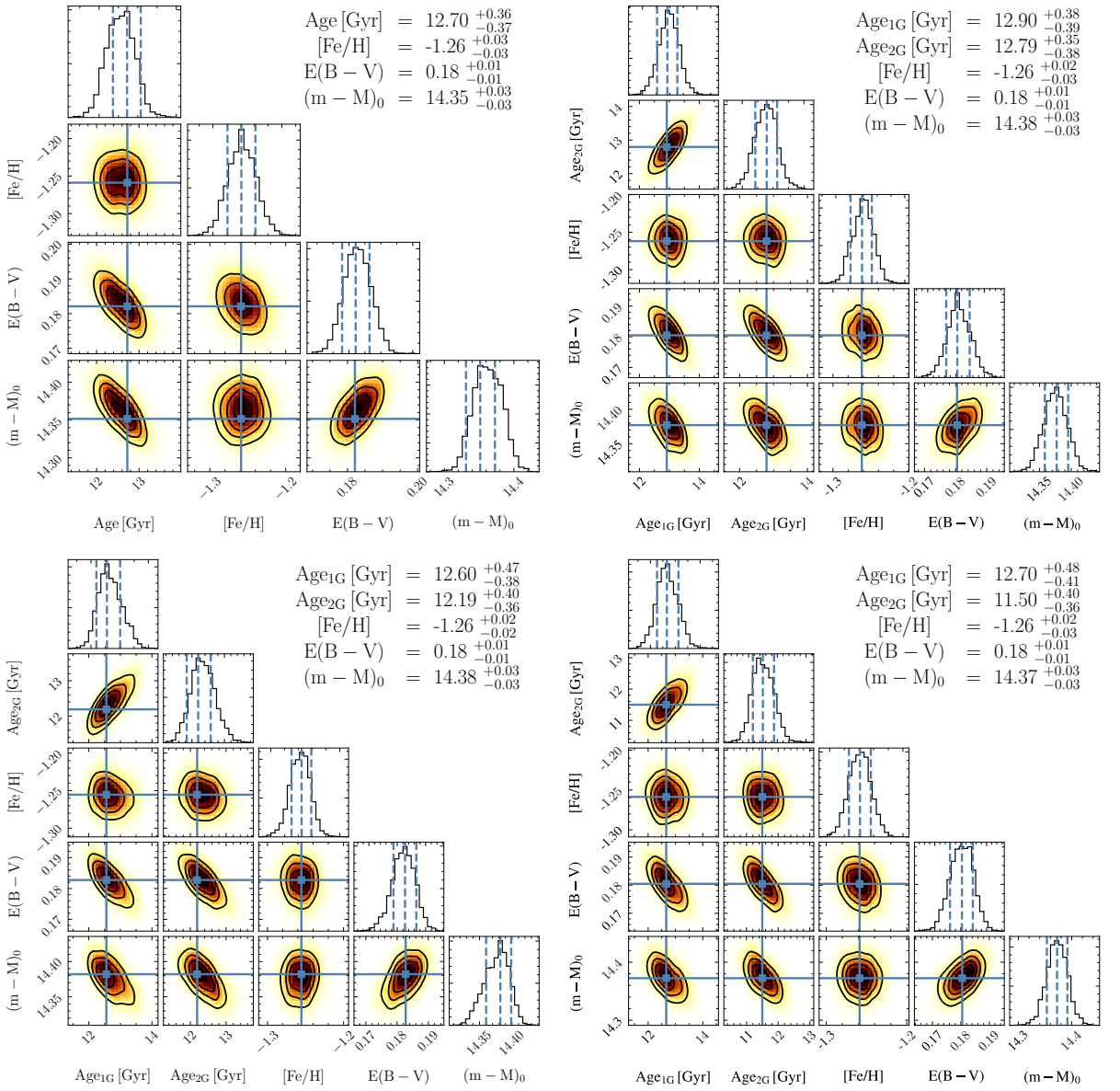

Figure 7.6: Sanity check 2, corner plots using DSED isochrones, relating physical parameters. Top left panel: results of the sanity check applied to a synthetic SSP CMD where Monte Carlo spread of data is implemented, with a $\Delta\tau = 0.50$ Gyr. Other panels: 1G and 2G combined for $\Delta\tau = 0.10$ Gyr (top right), $\Delta\tau = 0.50$ Gyr (bottom left), and $\Delta\tau = 1.50$ Gyr (bottom right).

In the following, the analysis of NGC 6752 is restricted to DSED isochrones. The procedure starts with the isochrone fitting assuming the CMD to consist of an SSP and the method is subsequently applied to the MPs. In order to carry out the isochrone fitting, we employed the same CMD m_{F606W} vs $(m_{F606W} - m_{F814W})$ used for the synthetic data. In the left panel of Figure 7.7 is shown the CMD of NGC 6752, including all-stars as an SSP. The value of [Fe/H] $= -1.48$ dex was used as prior through Gaussian distribution with a standard deviation of 0.07. A prior in distance was applied with the value of apparent distance modulus $(m - M)_V = 13.26 \pm 0.08$ taken from Gratton et al. (2003).

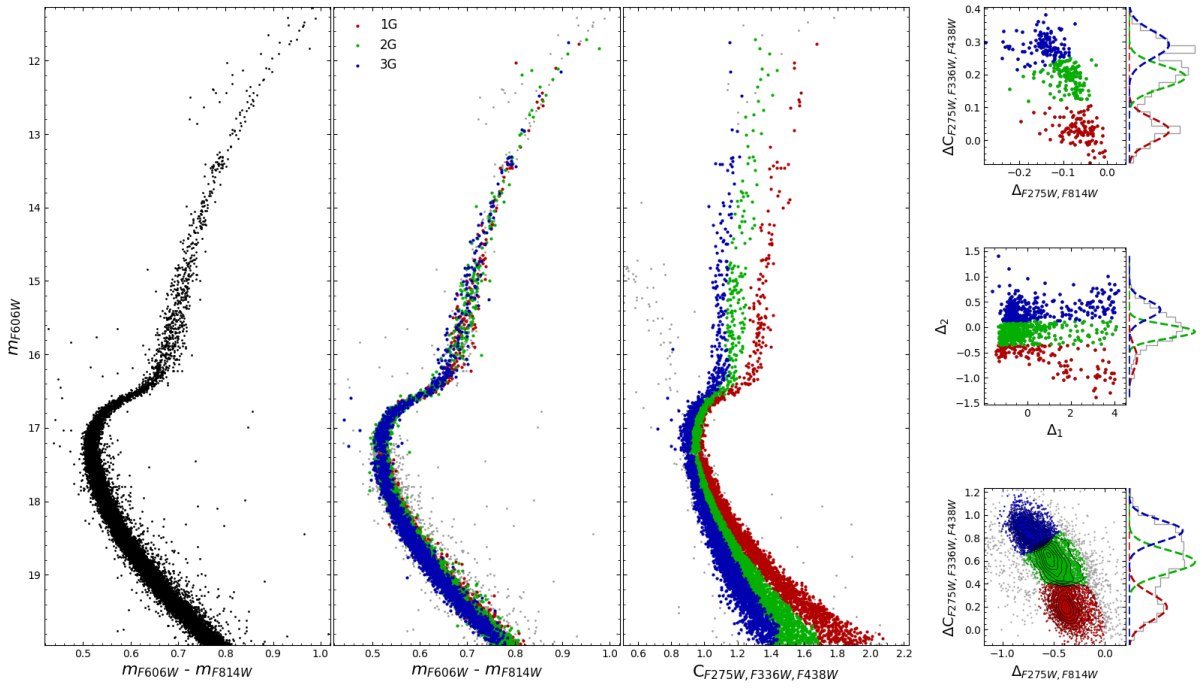

Figure 7.7: Multiple stellar populations in NGC 6752. Left panel: SSP; Middle panel: same as left panel, but color-identified stars; Right panel: pseudo-color showing the clear separation of three stellar populations.

The results of SSP isochrone fitting are shown in Table 7.3 and Figures 7.8 and 7.9. The SSP age derivation of 13.7 ± 0.5 Gyr is in good agreement with Gratton et al. (2003), which obtained 13.4 ± 1.1 Gyr, and with the Bayesian technique from Wagner-Kaiser et al. (2017) that resulted in an age of $13.202^{+0.174}_{-0.152}$ Gyr. The parallax from Gaia DR2 (Gaia Collaboration et al., 2018) for the NGC 6752, $\bar{\omega} = 0.2610 \pm 0.0011$ mas, corrected by the zero point of -0.03 mas given by Lindegren et al. (2018), gives a heliocentric distance of 3.85 ± 0.02 kpc. Considering NGC 6752 as an SSP, the derived distance is 4.11 ± 0.08 kpc, in agreement with 3σ with Gaia DR2.

The metallicity estimated from SSP isochrone fitting, [Fe/H] $= -1.49^{+0.05}_{-0.05}$, was fixed for the MPs approach. The metallicity can be fixed because no [Fe/H] variation is detected in this cluster.

The fit is carried out simultaneously to 1G, 2G, and 3G. Firstly, we consider the primordial helium content value for all populations. In a second run, we assume a helium enhancement by a type of polluter star, changing the amount of helium for each generation, according to values computed by Milone et al. (2019): $\delta Y_{1G,2G} = 0.010$ and $\delta Y_{1G,3G} = 0.042$ for the 2G, and 3G, respectively (Figures 7.7, 7.9, and Table 7.3). We assumed the helium enhancement values from Milone et al. (2019) since they were derived using the same

DSED stellar evolutionary models employed here, therefore there is compatibility. For the metallicity of NGC 6752, the corresponding canonical helium content in the DSED isochrones is 0.247, which was associated to 1G. The 2G and 3G helium contents were assumed to be of 0.257 and 0.289, adopting the δY values from Milone et al. (2019).

Table 7.3 - Results of isochrone fitting for NGC 6752 in SSP context and MPs.

	Y	τ (Gyr)	$\Delta\tau_{1G,2G}$ (Gyr)	$\Delta\tau_{2G,3G}$ (Gyr)	$\Delta\tau_{1G,3G}$ (Gyr)	[Fe/H] (dex)	$E(B-V)$	$(m-M)_0$	$(m-M)_V$	$d_\odot$ (kpc)
SSP	Y(Z)†	$13.70^{+0.61}_{-0.38}$	–	–	–	$-1.49^{+0.05}_{-0.05}$	$0.03^{+0.02}_{-0.02}$	$13.07^{+0.03}_{-0.03}$	$13.16^{+0.07}_{-0.07}$	4.11 ± 0.08
MPs with Y canonical										
1G	0.247	$13.80^{+0.45}_{-0.40}$								
2G	0.247	$13.50^{+0.39}_{-0.38}$	$0.30^{+0.42}_{-0.39}$	$0.20^{+0.39}_{-0.38}$	$0.50^{+0.43}_{-0.39}$	-1.49††	$0.04^{+0.01}_{-0.01}$	$13.08^{+0.02}_{-0.02}$	$13.20^{+0.03}_{-0.03}$	4.13 ± 0.06
3G	0.247	$13.30^{+0.39}_{-0.38}$								
MPs with Y enhancement										
1G	0.247	$13.50^{+0.39}_{-0.42}$								
2G	0.257	$13.20^{+0.39}_{-0.41}$	$0.20^{+0.38}_{-0.41}$	$0.30^{+0.37}_{-0.41}$	$0.50^{+0.38}_{-0.42}$	-1.49††	$0.04^{+0.01}_{-0.01}$	$13.07^{+0.03}_{-0.03}$	$13.19^{+0.03}_{-0.03}$	4.11 ± 0.08
3G	0.289	$13.00^{+0.41}_{-0.41}$								

† Y as function of Z, defined by: $0.245 + 1.5 \times$ Z.

†† Fixed value from the SSP isochrone fitting.

Table 7.3 and Figure 7.10 provide the results of isochrone fitting to the MPs. The derived distances using canonical helium and helium enhanced are 4.13±0.06 and 4.11±0.08 kpc, respectively. The latter distance determination is in agreement with the distance from the inverse Gaia DR2 parallax (Gaia Collaboration et al., 2018) (see above). We derive age differences of $\Delta\tau_{1G,2G} = 300 \pm 400$ Myr, and $\Delta\tau_{1G,3G} = 500 \pm 400$ Myr, relative to the age of 1G stars, considering that there is no helium enhancement within the GC. However, taking into account the GC helium enhancement cf. Milone et al. (2019), and noting that the method fits the three stellar populations simultaneously, the 1G is less old (even if its He is still canonical), and the age differences are of $\Delta\tau_{1G,2G} = 200 \pm 400$ Myr, and $\Delta\tau_{1G,3G} = 500 \pm 400$ Myr. These results could give hints on the possible mechanism of GC internal pollution.

It is interesting to note that, for the He enhanced populations, the result is similar to those with no He enhancement. Assuming the primordial helium for the 1G, 2G, and 3G stars, the χ^2 values are 0.10, 0.13, and 0.12, respectively, resulting in a total value of 0.35.

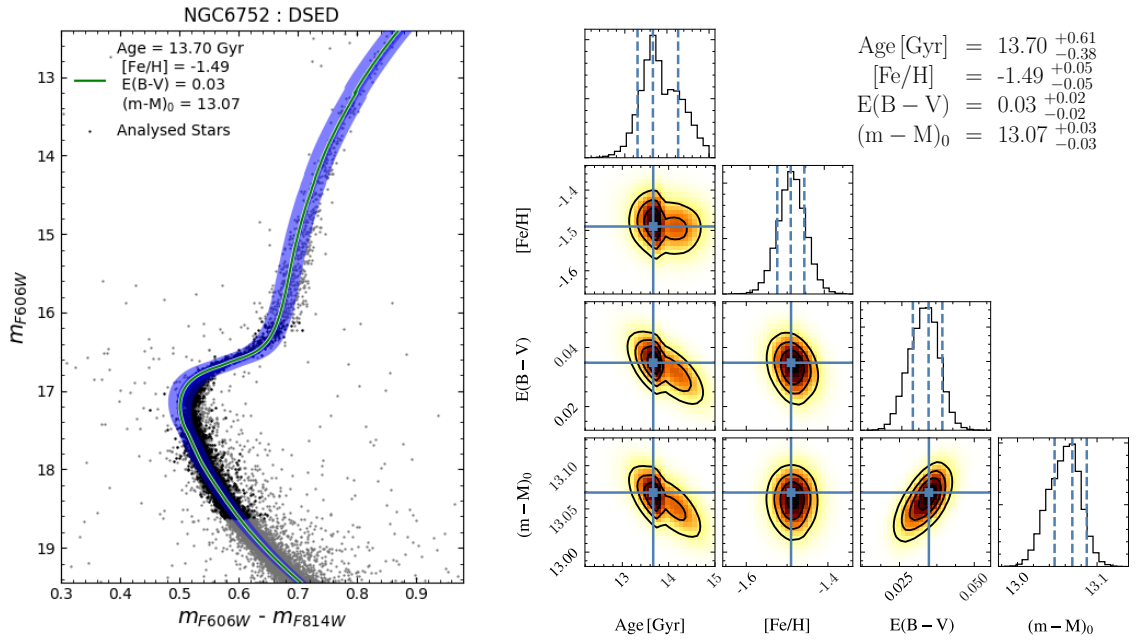

Figure 7.8: Results for the SSP analysis of NGC 6752. Left panel: CMD with the result from isochrone fitting, green line is the most probable solution, and the blue strip is the solutions within 1σ. Right panel: The posterior distributions.

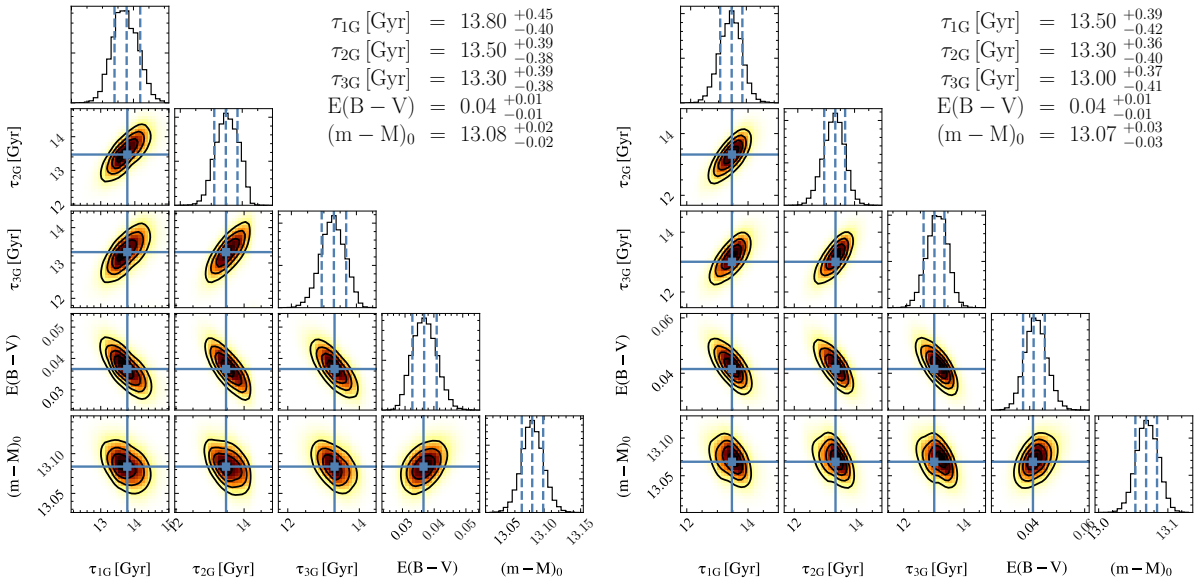

Figure 7.9: Corner plots for NGC 6752. Left panel: simultaneous fitting of the three stellar populations, adopting canonical helium abundance; Right panel: same as in left panel, but taking into account helium abundance differences.

For He enhanced isochrones, the values of χ^2 are 0.09, 0.14, and 0.11, for the 1G, 2G, and 3G stars, respectively and with a total of 0.34. Therefore, the fitting using He enhanced isochrones are similarly well-fit.

Even though the uncertainties on the age derivation do not take into account the differences between the stellar evolutionary models, our uncertainty determinations are

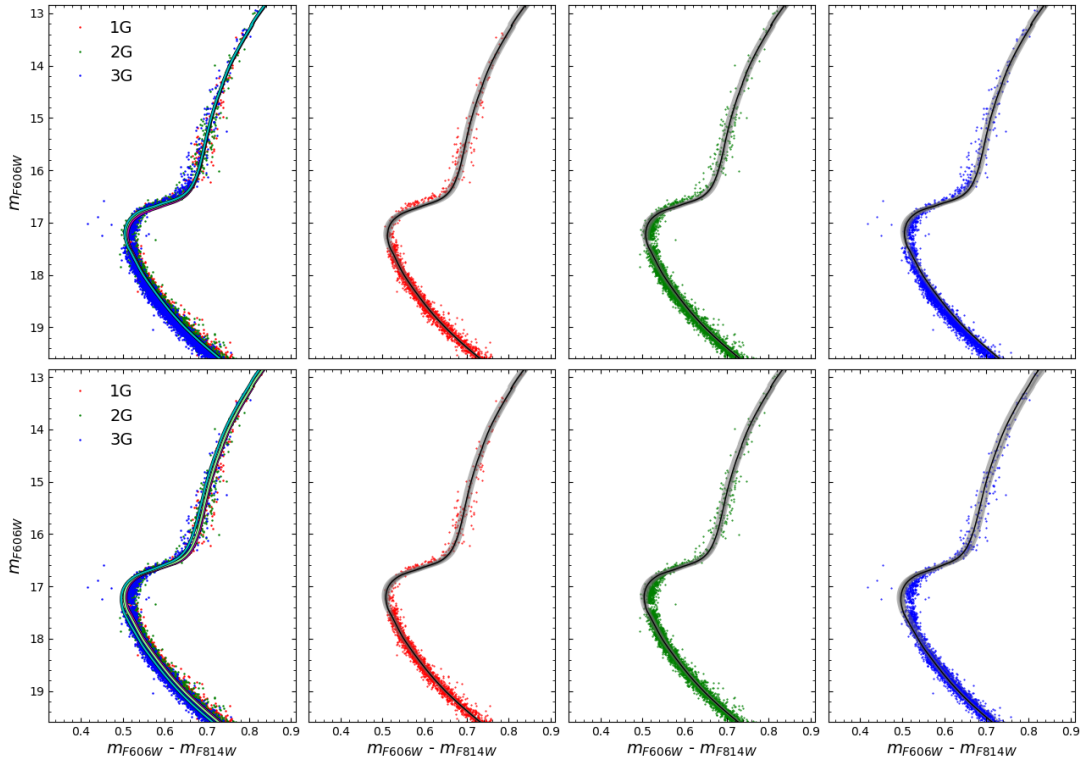

Figure 7.10: Isochrone fitting for NGC 6752. Left panel: MPs all together. Second to fourth panels: isochrone fitting to 1G, 2G, and 3G. Upper panels: Canonical helium. Lower panels: Enhanced helium. The strips are the solutions within 1σ.

of the same order of magnitude as those by Monty et al. (2018). Given that we did not propagate the uncertainties from the grid size of the parameter space, the uncertainties given here are the formal errors from MCMC algorithm and they are larger than the ones reported by Wagner-Kaiser et al. (2017).

7.5 Conclusions

The `SIRIUS` code is applied to analyse the halo globular cluster NGC 6752 of metallicity [Fe/H]≈-1.49. Three stellar populations are identified, confirming previous findings by Carretta et al. (2012) from spectroscopy, and Milone et al. (2019) from photometry. The age derivation of the three stellar populations, taking into account He abundance differences from Milone et al. (2019), results to be of $200/300 \pm 400$ Myr between 1G and 2G and between 2G and 3G. This points to a possible interpretation of having the same mechanism producing 2G, and later the 3G.

Many authors have extensively discussed the probable candidates to produce the chemical abundance patterns of second (and subsequent) stellar populations from self-enrichment

of the cluster. The main candidates are the AGB stars, and SMS, in both cases through their winds, as well as FRMSs (Decressin et al., 2007; Krause et al., 2013). All of them predict an age difference between the stellar populations.

In conclusion, given the uncertainties in the models of pollution, and the uncertainties in the age difference derived from the CMDs, it is not possible to firmly indicate a scenario for the formation of a second stellar population. The age differences derived for NGC 6752 could be compatible with the AGB scenario if only the best value determinations are taken into account. However, considering the uncertainties, the results could be compatible with all scenarios regarding the origin of MPs (SMS and FRMS), even those with no age difference. Further analyses of age differences of multiple stellar populations are of great interest. In particular, within the *HST* Legacy survey collaboration, Nardiello et al. (2015) derived the relative age of NGC 6352 MPs from χ^2 minimization isochrone fitting, assuming each of them as SSPs, and Oliveira et al. (2020) applied the methods described here to derive the ages for seven bulge globular clusters and their MPs.

Chapter 8

The extended Main Sequence Turn-Off in low mass star clusters

This chapter presents the results submitted to A&A as a Letter to the Editor titled *The VISCACHA survey X. Deciphering the eMSTO in intermediate-age MC star clusters* (Souza et al. submitted).

8.1 Introduction

Some studies have found some peculiarities in the colour-magnitude diagram (CMD) of the Magellanic Clouds (MCs) star clusters obtained with the *Hubble Space Telescope* (HST, e.g. Goudfrooij et al., 2009; Milone et al., 2009). They found that intermediate-age (1-3Gyr) clusters host an extended main-sequence turn-off (eMSTO). More recently, Martocchia et al. (2017, 2018) have analysed a wider age range of MC clusters. They found that some clusters older than $\sim$ 2 Gyr show a spread the red-giant branch (RGB) as in the Milky Way globular clusters (Bastian and Lardo, 2018b; Milone and Marino, 2022) when using HST ultra-violet filters, which indicates chemical abundance variations star-by-star. For the clusters younger than $\sim$ 2 Gyr, the eMSTO takes place. In addition to that, the eMSTO phenomenon was also observed in open clusters of the Galaxy (e.g. Cordoni et al., 2018; Bastian et al., 2018; Cordoni et al., 2022).

The eMSTO was first associated with a prolonged star formation (e.g. Mackey et al., 2008; Milone et al., 2009). Nevertheless, it is well-known that stellar rotation can mimic the age variation (gyrochronology, Vidotto et al., 2014; Niederhofer et al., 2015). That effect occurs because the rotation carries the hydrogen (H) from the outer layers to the nucleus, keeping the star in the main-sequence (MS) phase and, consequently, extending the MSTO. Therefore, a rotation velocity spread of MSTO stars can explain the eMSTO (Bastian and

de Mink, 2009). Indeed, Milone et al. (2018) found a population of fast rotator stars spread along the MSTO. However, some works have demonstrated that stellar rotation is essential but not unique in explaining the eMSTO (e.g. Goudfrooij et al., 2014; Salinas et al., 2016).

Stellar rotation also produces gravity darkening, making the star brighter and hotter when seen in pole-on (Rivinius et al., 2013). Usually, one can detect this effect when the rotation velocity is close to the critical value ($v/v_{critic} = \omega$ ~80-90%), as in the case of Be stars ($\omega \geq 0.75$ Rivinius et al., 2013). On the other hand, a distribution of spin orientation can spread the MSTO uniformly, contributing to the eMSTO, even though a preferred direction of the rotation angle to the observer is expected (e.g. Healy et al., 2023).

The binary fraction anticorrelates with cluster luminosity (Milone et al., 2016) because unresolved binary stars, which appear as a single, typically brighter and redder star along the main sequence (MS) in the CMDs, are a purely observational effect caused by the spatial resolution limits.

Recently, Cordoni et al. (2022) analysed the 40 Myr old cluster NGC 1818 of the Large Magellanic Cloud (LMC) with HST photometry. Their method concluded that NGC 1818 has no extended star formation, and stellar rotation explains the eMSTO almost wholly.

In this work, we analyse the effects on the MSTO caused by an extended star formation or multiple bursts, stellar rotation and spin orientation angle, and unresolved binaries in explaining the presence of eMSTO. We selected for a first analysis seven intermediate-age stellar clusters in the Small Magellanic Cloud (SMC).

This letter is organized as follows. Section 2 presents the star clusters selection, the VISCACHA data, and the decontamination method. In Section 3, we discuss the parametrisation of the eMSTO in terms of the physical ingredients we employ and the selection of MSTO stars. Section 4 shows the results and discussion. Finally, the conclusions are drawn in Section 5.

8.2 VISCACHA data

We based our sample selection on the SMC clusters: NGC152, Kron 37, Lindsay 106, Kron 6, HW20, HW67, and Lindsay 116. All clusters are within the age range classified as intermediate-age, $\sim 1 - 3$ Gyr, which predicts the presence of a more evident eMSTO (e.g. Goudfrooij et al., 2014).

We exploit the SAMI/SOAR (Tokovinin et al., 2016) instrument, which delivers high quality images in V and I-bands due to its adaptive optics module excellent performance. The observations are part of the VISCACHA survey (Maia et al., 2019). The data reduction is based on Diolaiti et al. (2000) - more details can be found in Maia et al. (2019). The photometric completeness level reaches $V \sim 23$ mag within the clusters' core radius, allowing us to analyse their low-mass MS stars.

Following the decontamination recipes given by Maia et al. (2010), we estimated the star membership probability for each cluster. Briefly, the method compares the density of field and cluster stars. Finally, we concluded the photometric treatment of the sample CMDs with a differential reddening correction following the method presented by Milone et al. (2012). The method consists essentially of computing the star distance to the cluster fiducial line, substantially reducing the spread of the eMSTO (Platais et al., 2012). The final clusters CMD have enough stars to populate them well, with small photometric errors, which are conditions that help the analysis of CMDs morphology and density (see Figure 8.1).

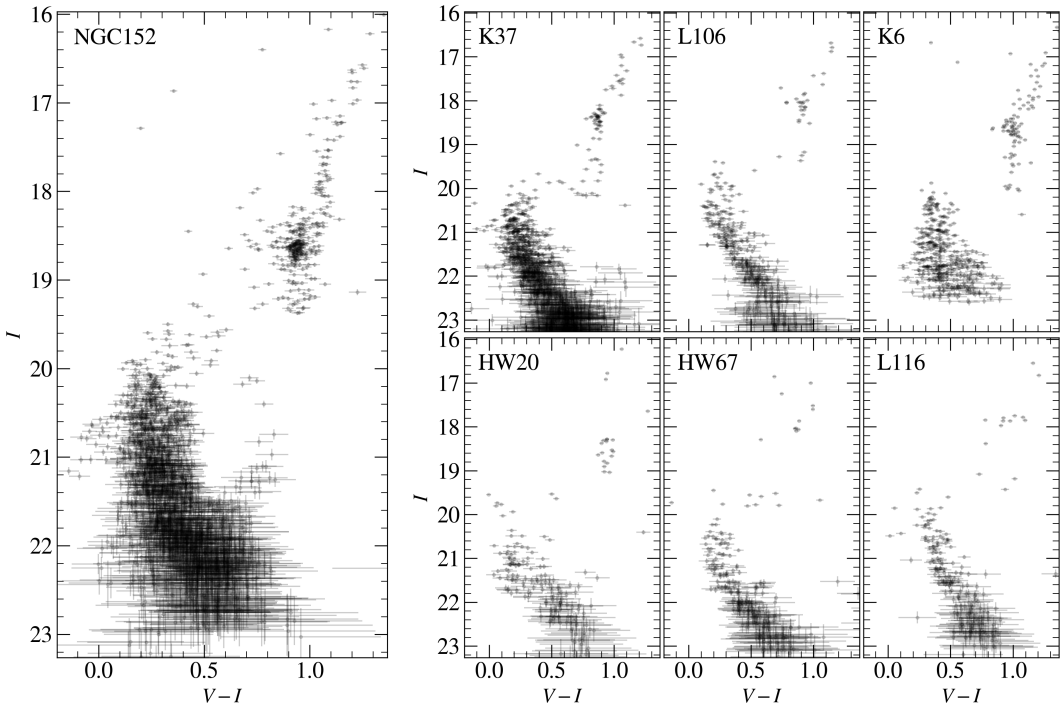

Figure 8.1: CMDs for our star cluster sample. The bars are the photometric errors. All panels show the CMD after the differential reddening correction.

8.3 eMSTO Parametrization

For this work, we use the newly released PARSEC isochrones, which include stellar rotation (Nguyen et al., 2022). The novelty of those isochrones is the inclination angle, which is the angle between the symmetry axis of the system and the observer (Carciofi et al., 2010). With that, we can consider angles between 0° (pole-on) and 90° (equator-on), which changes considerable the CMD morphology. We adopted the maximum rotation value of $\omega = 0.99$ for our analysis, varying the inclination angle. Therefore, the conclusions regarding the rotation phenomenon is in the limit case.

When preparing this work, only isochrones with metallicities higher than -0.6 dex were available. Most of our sample has a metallicity around $0.1 - 0.2$ dex lower than this limit. Therefore, we make an approximation in our analysis using the isochrones with [Fe/H] $= -0.6$ dex. In order to estimate the impact of that assumption in our analysis, we fixed the age as 1.5 Gyr (mean age of our sample) and varied the metallicity values. Left panels of Figure 8.2 shows different values of metallicity. The solid lines consider the pole-on view (0°) while the dashed lines are equator-on view (90°). Since our analysis in terms of rotation is based on the inclination angle, we estimate the width of the MSTO between pole-on and equator-on for different metallicities. We found that, for a variation of 0.6 dex in metallicity, the width decreased by 20%. Therefore, assuming a linear trend, we can expect that for a metallicity variation of 0.2 dex the spread increment will be of $\sim$ 6%, which is imperceptible for the eMSTO spread. For the models with rotation, we are taking the degeneracy age-metallicity to find the corresponding age which, together with [Fe/H]$= -0.58$, mimics the morphology of the isochrone with the metallicity value provided by the literature (see Table 8.1).

Another effect to be considered is the isochrone age. We are fixing an age value when analyzing the rotation effect. However, the width of the MSTO increases with age until 1.5 Gyr and decreases up to $\sim$ 3 Gyr (Martocchia et al., 2017, 2018). In Figure 8.2 (right panels), we estimate the effect of the mean age on the MSTO width between pole-on and equator-on for maximum rotation value. The expected behaviour is observed here, and we can estimate that the width is maximum for an age around 1.5 Gyr.

To consider the unresolved binaries in the CMD, we follow the method proposed by Milone et al. (2012). The main parameter to construct the binary sequence is the mass

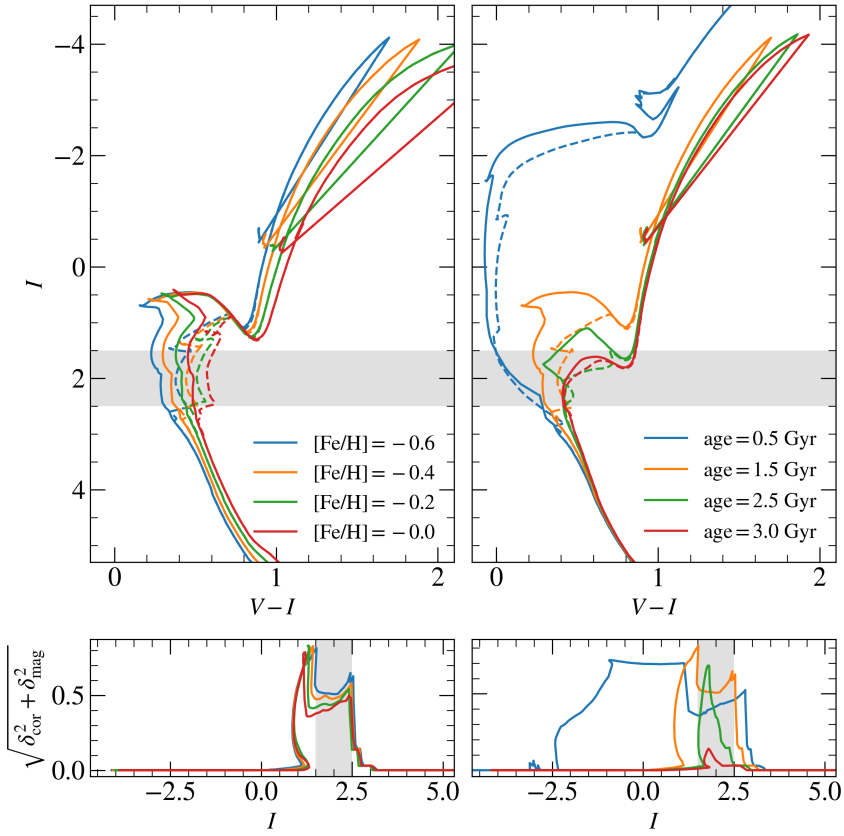

Figure 8.2: Effect due to the inclination angle. The left panels show the variation in the metallicity value, fixing an age of 1.5 Gyr. The right panels show the variation in the age value, fixing the metallicity at −0.60 dex. In the bottom panels, the Euclidian distance between a star with the same mass value in pole-on (solid lines) and equator-on (dashed lines) views are shown as a function of magnitude I.

ratio q, defined as $q = M_2/M_1$ assuming values from 0 to 1, being $q = 0$ for the no binaries case and $q = 1$ for equal mass binaries. For the latter, the difference in magnitude is equal to -0.75 what means that the star appears 0.75 magnitude brighter in the CMD. We defined several binary sequences with different mass ratios. In panel c of Figure 8.3, we highlighted the $q = 0.7$ isochrone in solid-black line.

Following the assumption in Cordoni et al. (2022), we negleted the effect of metallicity in our analysis. This simplification is based on the fact that we do not expect a large metallicity dispersion. In addition, the narrow metallicity distribution can be inferred by a well-defined RGB.

We follow the method applied by Goudfrooij et al. (2014) and Correnti et al. (2021) to define the eMSTO region. Briefly, the eMSTO region, represented by the blue box in Figure 8.3, is defined by two lines. The X' axis is the line crossing the different age isochrones in the region where their difference is higher. While the Y' axis is the line nearly parallel to the isochrones and perpendicular to the first line. We adapted the method for

the context of our data because some clusters have low statistics. The changes are: the X' is parallel to the top of the MS, and the box size is adapted to contain approximately 10% of stars without going much fainter in the MS. Note that, for a cluster with a large number of stars, one can construct a box as thin as possible so that Y' goes to zero. This method is particularly useful because it maximizes the effect of an age variation in the eMSTO. The X' and Y' axes are represented in Figure 8.3 with black arrows.

To convert the spread in X' into the parameters age, inclination angle, and mass ratio, we calculate the distance of each star inside the MSTO box to the X' and Y' axes. After that, we applied the same for the isochrone points inside the same box. Then, we have each parameter as a function of X' and Y'.

8.4 Discussion

It is relatively well established that, neither an age variation nor a stellar rotation spread can explain by itself the effect observed in the MSTO of intermediate-age clusters (e.g. Girardi et al., 2011; Goudfrooij et al., 2014; Brandt and Huang, 2015; Niederhofer et al., 2015; Cordoni et al., 2018; Sun et al., 2019). Some studies have devoted efforts to finding a combination of regions of the CMD that would enable to explain the phenomenon thoroughly. Cordoni et al. (2022) combined the eMSTO with the turn-on point. The latter was adopted because stellar rotation does not affect it due to its low mass regime. We cannot analyse this region because the turn-on point gets fainter with increasing age, and the magnitude of VISCACHA photometry only reaches turn-on of clusters younger than about 10-20 Myr. Nevertheless, we can analyse the MSTO with the red clump (RC), as in Girardi et al. (2009, 2013). Similar to the turn-on point, the stellar rotation does not affect the RC also because this region is outside the mass limit to rotation. The authors found that the spread in the RC can be explained by different overshooting efficiency and an age spread. Therefore, we employed the RC as a constraint for the parameters variation range in the following discussion.

In Figure 8.3, we show the result of our analysis for the case of NGC152. In the literature, many studies have dedicated to analyse this cluster, making it a perfect benchmark for our analysis. Rich et al. (2000) found that NGC152 is compatible with two different age values. Dias et al. (2016) performed synthetic CMD fitting and converged to a good fit.

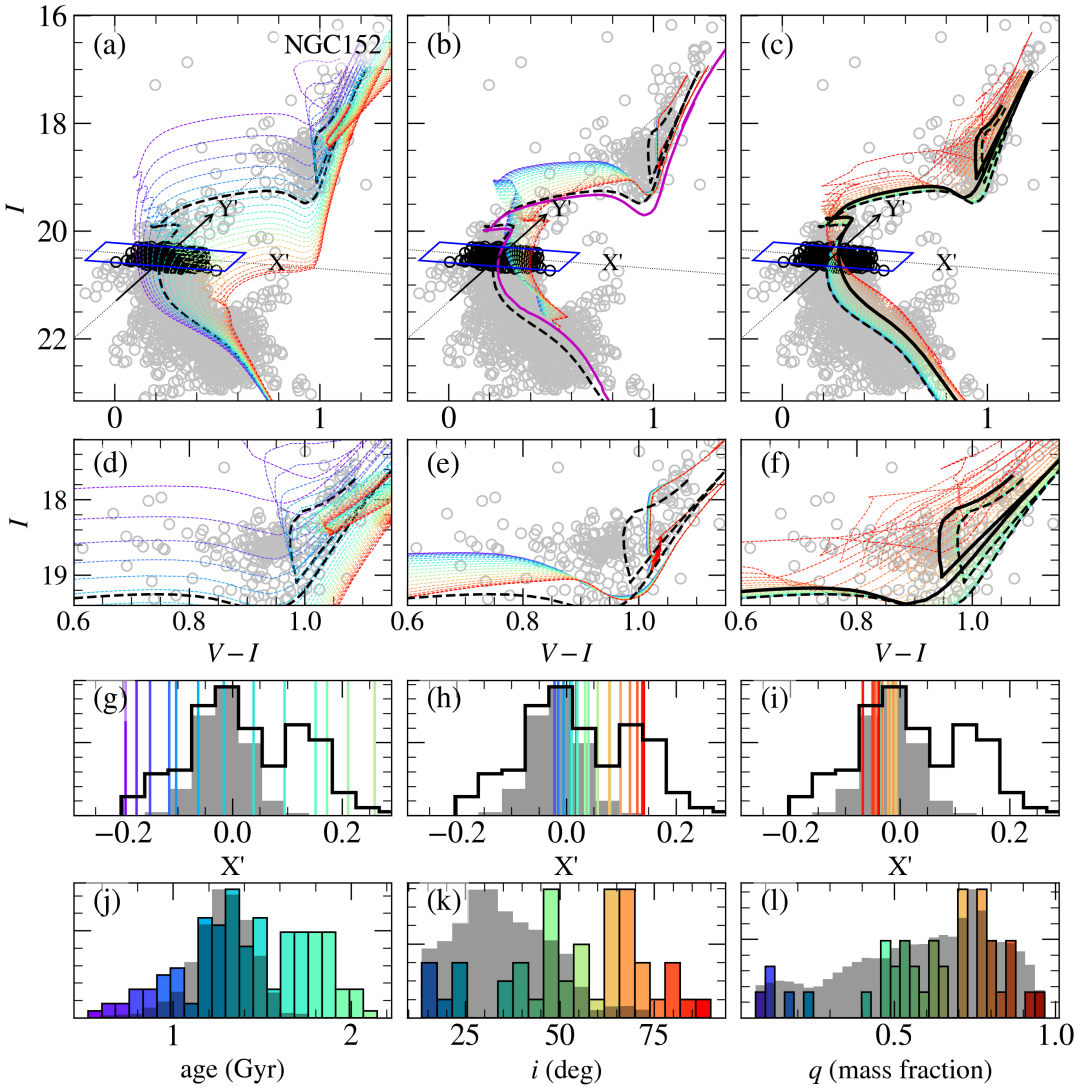

Figure 8.3: Simultaneous analysis of the eMSTO and RC for the NGC152 template cluster. The age variation analysis is illustrated in the left column (panels a, d, g, and j), the i inclination view angle variation in the middle column (panels b, e, h, and k), and the q binary mass ratio variation in the right column (panels c, f, i, and l). The top panels a, b, and c show the [I, V-I] CMDs with the set of isochrones varying the correspondent parameter. The black dashed line is the best fit of age and [Fe/H] provided by the literature. In the middle CMD, the solid magenta line shows the isochrone of the new dataset limited to [Fe/H]≥ -0.58 with age 250 Myr younger than the best fit to mimic the black-dashed line. The coloured lines in the middle CMD are also 250 Myr rejuvenated, with a rotation rate of $\omega = 0.99$. The black-solid line in the right CMD is the mean locus for $q = 0.70$. Inside the blue box are the selected MSTO stars. Panels d, e, and f show the zoomed RC regions. The histogram in the X' axis with vertical lines representing the identification of different values of the corresponding parameter is plotted in the panels g, h, and i. The colours are the same as in the bottom row panels (j, k, and l), that display the histograms of the X' converted to age (left), i (middle), and q (right). The grey-shaded histogram is the synthetic distribution of SSP computed from the best-fit and photometric errors.

However, the best synthetic CMD exhibited a much narrow MSTO, suggesting the need of a more detailed analysis. Even though they considered binaries, that effect combined to a single age value does not explain the eMSTO (see their Figure 8). Dias et al. (2022) determined another isochrone-fitting age using the SIRIUS code (Souza et al., 2020). Their

Figure B.1 shows that the age posterior distribution possesses two peaks, at 1.3 and 1.5 Gyr.

In the left panels of Figure 8.3, we show the effect of age spread. Ages are identified by the colour line following the colour code of the bottom panels histograms. The black dashed line is the best fit provided by the literature. We found for NGC152 a double peak distribution along the X' axis (panels g, h, and i). Converting that to age, we also found a double peak distribution in age (panels j, k, l), which is expected. For comparison, we show the expected distribution for a single stellar population (SSP) without binaries as grey-shaded regions in the histograms constructed using the photometric errors and a Monte Carlo resample. For that age regime, the mass of the eMSTO is around 1.4 $M_{\odot}$. The age spread can explain the eMSTO assuming a scenario where a second star formation burst happened around 500 Myr after the cluster formation. However, it is known that there are some fast rotator stars in this region (e.g. Milone et al., 2018). Therefore, the age spread is not the unique physical effect.

The fast rotator effect is represented in the panels of the middle column in Figure 8.3. We assumed a rotation rate of $\omega = 0.99$, close to the breakout limit in order to intensify the effect of stellar rotation. For the present analysis, we are mainly interested in the effect of the inclination angle (i). As explained, the fast rotating isochrones are limited to [Fe/H]> -0.58 dex. Therefore, we assume a different age (magenta solid line, Table 7.1) in other to mimic the position and morphology of the black dashed isochrone. We can observe in the centre histogram that the inclination angle variation can explain the spread, but only if combined with an adittional age spread. However, even if both effects act together, they explain a magnitude spread but cannot explain the colour spread on the RC.

With the similar argument by Cordoni et al. (2022), we can use the RC to constrain the age range inside the first peak with age $1.0 - 1.6$ Gyr, which limits the isochrones in the first panel to the cyan one. This means that an age spread does not explain the red half of the eMSTO. On the other hand, the red half of the eMSTO is inside the inclination angle variation region (for a fixed age). However, as mentioned before, the stellar rotation, and consequently the inclination angle, do not affect the spread in the RC region (Nguyen et al., 2022). Therefore, the binarity effect becomes more important. In the right panel, we show the effect of binaries with different mass ratio values. We can observe that the

binaries effect causes a spread that is much smaller than that caused by photometric errors in the eMSTO, but has an essential role in the colour spread of the RC. The black solid line in this panel is the binary boundary for which $q = 0.7$. The red lines on the left side of the black line show the contribution of binaries with $q > 0.7$ to the colour spread of the RC (Milone et al., 2012).

The same analysis has been done for the other clusters in our sample. For the most massive ones that include Kron 37 (Figure 8.4), Lindsay 106 (Figure 8.5), Kron 6 (Figure 8.6), and HW20 (Figure 8.7), we have reasonable statistics in the RC region, which allows to constrain the age spread around the expected age distribution for an SSP without binaries. For the less massive clusters (figs 8.8 and 8.9), we point out a similar conclusion having the low statistics of the RC as a caveat. Therefore, the RC region can be used to constrain the age spread and the binary population in order to find their contributions to the eMSTO morphology.

8.5 Conclusions

In this letter, using VISCACHA data, we tested the hypothesis that neither age, rotation, nor binaries can explain the full extent of the eMSTO alone. We also used the shape of the RC simultaneously to constrain the range of the parameters.

We found that the RC is an excellent region to analyse in combination with the eMSTO. As observed in previous works, the age spread alone easily explains the extent of the MSTO. However, when we look at the RC, we see that only a few age values fit that region well. The measured age range limits the isochrones to the blue region of the MSTO, explaining the red region by the spread in the inclination angle of fast rotator stars.

Results found in this work revealed that eMSTO phenomenon is not mainly caused by an age spread. It is consistent with previous findings (e.g. Bastian and Lardo, 2018b; Cordoni et al., 2018, 2022) concerning several star clusters with eMSTO feature and located in the Milky Way and the Large Magellanic Cloud.

In this work, we also show the importance of the inclination angle apart from the rotation rate since the inclination angle is not equal for each cluster. Even though the inclination angle seems to be isotropic (e.g. Healy et al., 2023), a distribution of angles is observed. Therefore, the spin angle and the rotation velocity must be taken into account

together. Future works should analyse the contribution of each parameter, looking for the convolved effects.

8.6 Appendix

8.6.1 eMSTO analysis for the other clusters

In this Apendix, we show the analysis for the other clusters in our sample: Kron 37 (Figure 8.4), Lindsay 106 (Figure 8.5), Kron 6 (Figure 8.6), HW20 (Figure 8.7), HW67 (Figure 8.8), and Lindsay 116 (Figure 8.9).

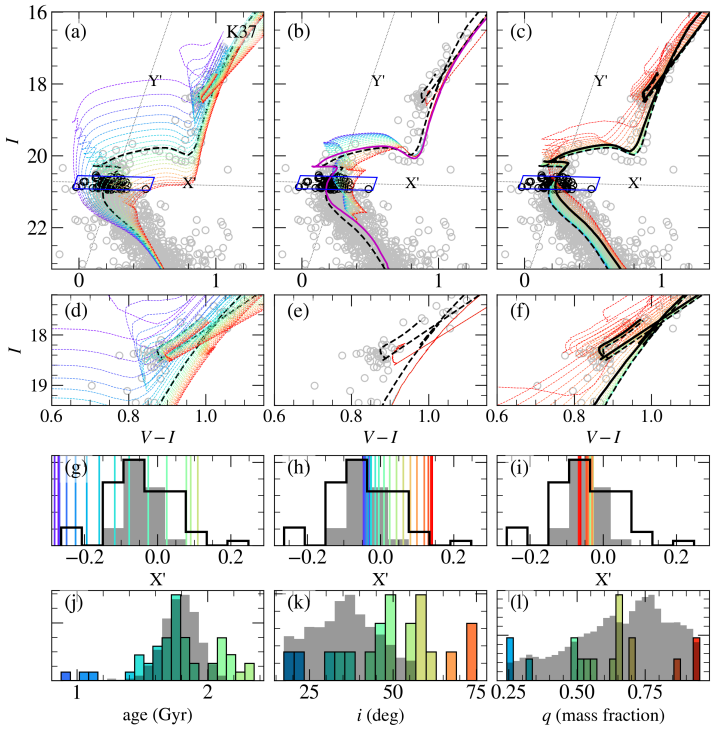

Figure 8.4: Same as Figure 8.3 for Kron 37.

8.6.2 Literature parameters

In this Appendix we list the fundamental parameters age, metallicity, distance, and reddening from the literature. In the case of metallicity, we also provide, when available, the value derived from spectroscopy. The references are listed in the last column.

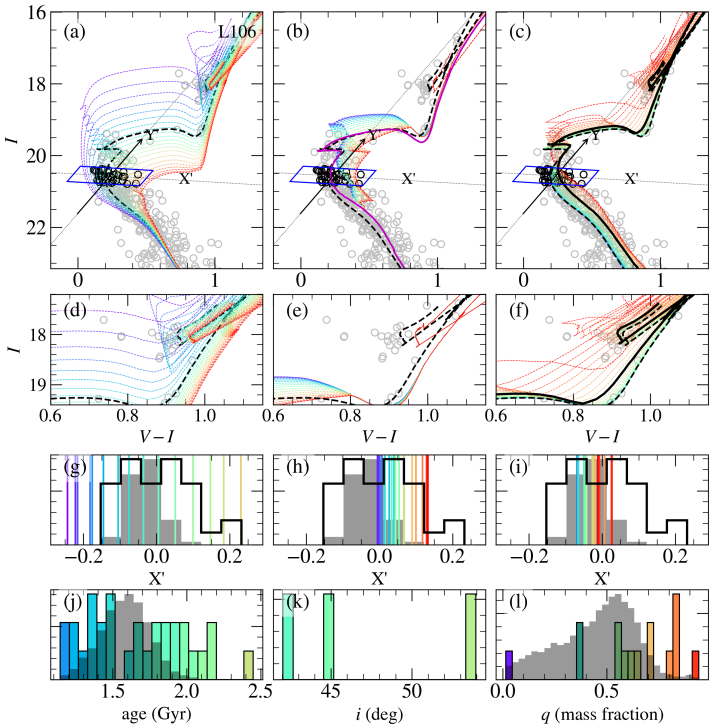

Figure 8.5: Same as Figure 8.3 for Lindsay 106.

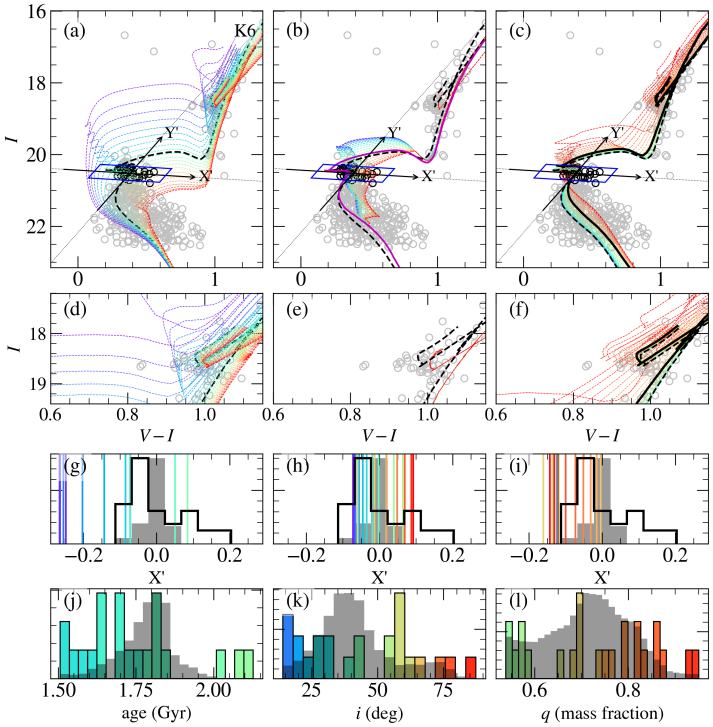

Figure 8.6: Same as Figure 8.3 for Kron 6.

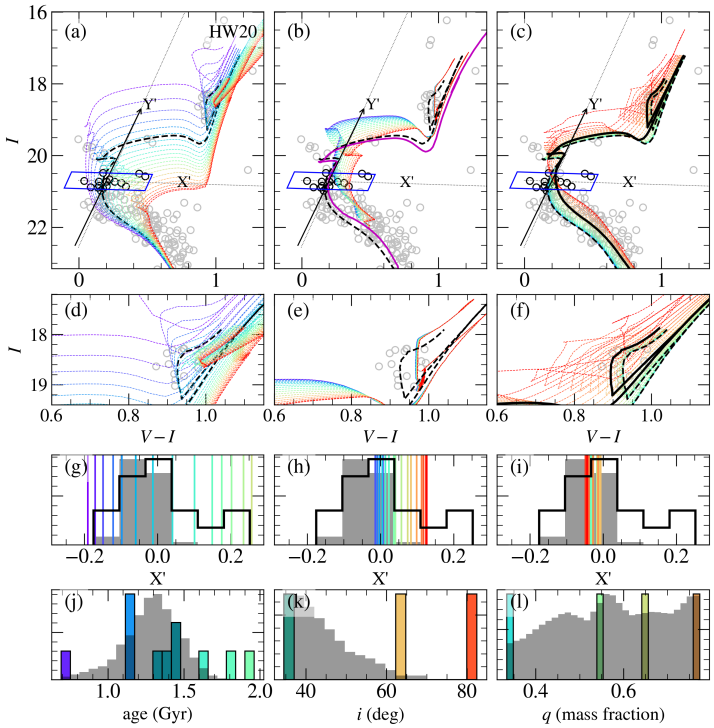

Figure 8.7: Same as Figure 8.3 for HW20.

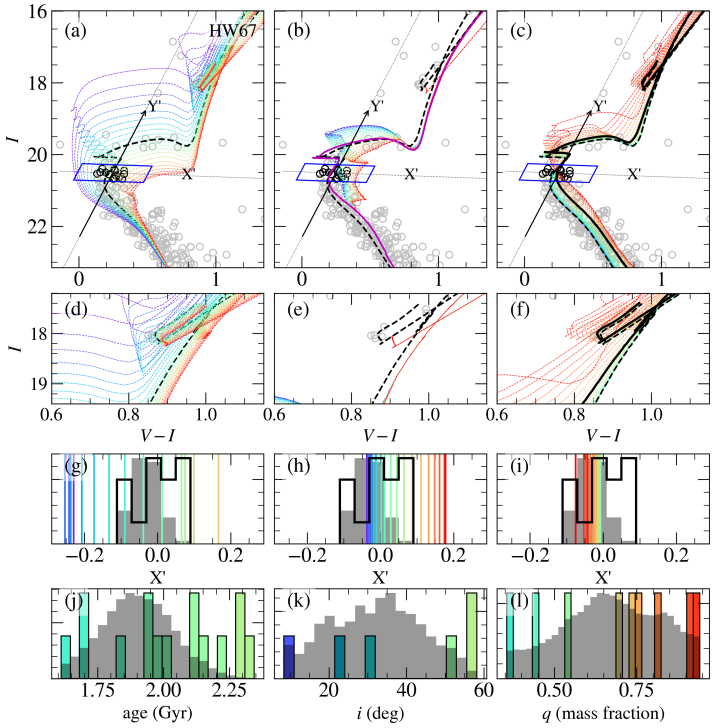

Figure 8.8: Same as Figure 8.3 for HW67.

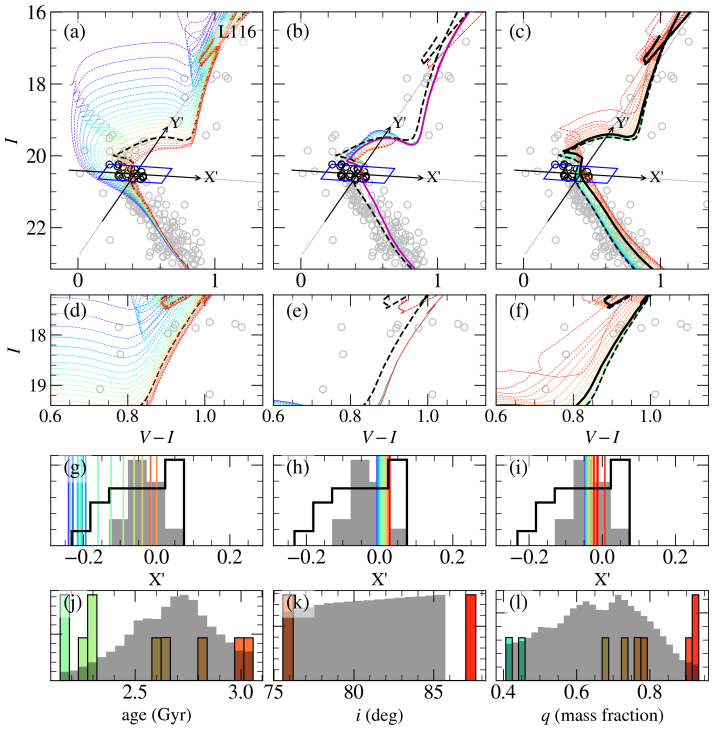

Figure 8.9: Same as Figure 8.3 for Lindsay 116.

Table 8.1 - Previous clusters parameters age, metallicity, distance, and extinction derived from other works. In the case of absence of distance and extinction values, we fitted visually the CMD with the fixed age and metallicity. The $\mathrm{Age_{rot}}$ is the derived age which, together with metallicity of -0.58, mimics the isochrone morphology with the literature metalicity value. N_T and N_{eMSTO} are the total number of stars and the number of stars inside the eMSTO box, respectively.

Age (Gyr)	$[Fe/H]_{phot}$	$[Fe/H]_{spec}$	d (kpc)	A_V	$\mathrm{Age_{rot}}$ (Gyr)	N_{eMSTO}	N_T	ref.
			NGC 152					
$1.40^{+0.20}_{-0.20}$	$-0.94^{+0.15}_{-0.15}$	—	$60.7^{+1.9}_{-1.9}$	$0.10^{+0.01}_{-0.01}$	—	—	—	Crowl et al. (2001)
$1.23^{+0.07}_{-0.07}$	$-0.87^{+0.07}_{-0.07}$	—	$60.0^{+2.9}_{-2.9}$	$0.09^{+0.03}_{-0.03}$	—	—	—	Dias et al. (2016)
$1.27^{+0.20}_{-0.08}$	$-0.77^{+0.07}_{-0.21}$	$-0.75^{+0.08}_{-0.08}$	$55.2^{+1.8}_{-1.5}$	$0.34^{+0.21}_{-0.12}$	—	—	—	Dias et al. (2022)
—	—	—	—	—	1.10	180	1963	This work
			Kron 37					
—	—	$-0.79^{+0.11}_{-0.11}$	—	—	—	—	—	Parisi et al. (2015)
$1.81^{+0.24}_{-0.21}$	$-0.81^{+0.13}_{-0.14}$	—	$62.4^{+2.3}_{-1.8}$	$0.15^{+0.03}_{-0.06}$	—	—	—	Maia et al. (2019)
—	—	—	—	—	1.40	65	1002	This work
			Lindsay 106					
—	—	$-0.88^{+0.06}_{-0.06}$	—	—	—	—	—	Parisi et al. (2009)
$2.00^{+0.30}_{-0.30}$	—	—	—	—	—	—	—	Parisi et al. (2014)
$1.58^{+0.41}_{-0.33}$	$-0.70^{+0.43}_{-0.43}$	—	$59.7^{+1.7}_{-1.6}$	$0.00^{+0.03}_{-0.03}$	—	—	—	Perren et al. (2017)
—	—	—	—	—	1.10	16	181	This work
			Kron 6					
—	—	$-0.63^{+0.02}_{-0.02}$	—	—	—	—	—	Parisi et al. (2015)
$1.81^{+0.24}_{-0.21}$	$-0.81^{+0.13}_{-0.14}$	—	$62.4^{+2.3}_{-1.8}$	$0.15^{+0.03}_{-0.06}$	—	—	—	Maia et al. (2019)
—	—	—	—	—	1.40	36	452	This work
			HW 20					
$1.10^{+0.08}_{-0.14}$	$-0.55^{+0.13}_{-0.10}$	—	$62.2^{+2.5}_{-1.2}$	$0.22^{+0.03}_{-0.06}$	—	—	—	Maia et al. (2019)
$1.26^{+0.05}_{-0.05}$	$-0.87^{+0.14}_{-0.14}$	—	—	—	—	—	—	Parisi et al. in prep
—	—	—	—	—	1.10	16	181	This work
			HW 67					
—	—	$-0.72^{+0.04}_{-0.04}$	—	—	—	—	—	Parisi et al. (2015)
$1.89^{+0.22}_{-0.18}$	—	—	$55.18^{+3.33}_{-3.13}$	$0.14^{+0.04}_{-0.04}$	—	—	—	Piatti (2022)
—	—	—	—	—	1.50	15	237	This work
			Lindsay 116					
$2.80^{+1.00}_{-1.00}$	$-1.10^{+0.20}_{-0.20}$	—	—	—	—	—	—	Piatti et al. (2001)
—	—	$-0.89^{+0.02}_{-0.02}$	—	—	—	—	—	Parisi et al. (2022)
—	—	—	—	—	2.6	22	206	This work

Chapter 9

Conclusions and Outlook

In this thesis, we further analysed the GCs Palomar 6 and NGC 6355 from a chrono-chemodynamical point of view (Souza et al., 2021, 2023). We gathered high-resolution spectroscopy from FLAMES-UVES, photometry from the HST F438W/F555W/F606W/F110W filters, and Galactic dynamics calculations. Other six clusters HP1 (Kerber et al., 2019), Djor 2 (Ortolani et al., 2019), UKS1 (Fernández-Trincado et al., 2020), VVVCL001 (Fernández-Trincado et al., 2021), AL3 (Barbuy et al., 2021), and NGC6558 (Souza et al. submitted) had their age determined using the `SIRIUS` code (Souza et al., 2020) in their respective work. We also include three GCs previously analysed by our group: NGC6522 (Barbuy et al., 2021b); NGC6717 and NGC6723 (Oliveira et al., 2020). We collected their chemical abundances, and when they were not available in the literature, we obtained them from APOGEE DR17.

Which GCs have formed in-situ?

- Our studies show that the metallicity of in-situ globular clusters typically is around [Fe/H]~ -1.0, which we call moderately metal-poor (MMP). The ages are estimated to be between 12 and 13.6 billion years. For example, the age of NGC6355 ([Fe/H]$= -1.39 \pm 0.08$) we estimated as 13.2 ± 0.9 Gyr, while Pal6 ([Fe/H]$= -1.10 \pm 0.09$) is 12.4 ± 1.0 Gyr old. The in-situ GCs often exhibit enhanced α-element abundances, with [α/Fe] ratios around +0.4. Also, since the in-situ GCs are essentially old, their dynamics and cinematics are mixed with the bulge field population. Therefore, in-situ bulge GCs are strongly bound to the Galaxy and rotate in the same direction as the Galaxy, which means very low values of total energy E_T and present prograde motion ($L_Z > 0$). Palomar 6 satisfies all these characteristics, making it a genuine

in-situ bulge GC. In contrast, NGC 6355 do not satisfy the prograde motion and some chemical patterns (such as [Mg/Mn] vs [Al/Fe]). This cluster has a retrograde motion with $L_Z = -31 \pm 24$ km s^{-1} kpc. With the low value of L_Z and its high uncertainty, NGC 6355 has a probability of flipping its rotation and starting to present a prograde motion. Therefore, more analysis is necessary for this cluster to exclude this ambiguity.

Where and when were formed the early bulge clusters?

- The MMP GCs were shown to form the oldest population of the in-situ bulge GCs. Employing the AMR for the MMP GCs, we found that the bulge population started to form 13.69 ± 0.12 Gyr ago. This forming age is consistent with the age of the universe (13.799 ± 0.021 Gyr; Planck Collaboration et al., 2016) and the predictions by the *two-infall* and *three-infall* models (Chiappini et al., 1997; Spitoni et al., 2023) where the bulge forms between 200 to 500 Myr after the major mergers of the building blocks. Therefore, the in-situ bulge GCs form before and after the bulge itself. The oldest GCs, like NGC 6355, come from the building blocks, and the GCs younger than 13.0 Gyr, like Palomar 6, form from the material of the proto bulge. Also, the AMR result evidenced the rapid enrichment experienced by the bulge during its early evolution. We found an effective yield of $\rho = 0.03 \pm 0.01\, Z_\odot$, which is ten times larger than the obtained fitting the ex-situ population.

Can we recover the building blocks using GCs?

- The study of the MMP GCs offers a unique opportunity to recover the building blocks of the Milky Way and unravel its formation history. By analysing the chemical abundances and kinematic properties, NGC 6355 was shown to be a likely representative example of a cluster originating within a building block. Therefore, GCs with low metallicities and old ages, like NGC 6355, compose the sample of GCs that can reconstruct the building blocks of the Galaxy.

How old is the Galactic Bulge?

- As mentioned before, using the AMR for the bulge MMP GCs, we found an age for the bulge population of 13.69 ± 0.12 Gyr. It is important to mention that this

age is when the bulge population starts forming stars (and, therefore, GCs). Also, the AMR equation used in this thesis is a leak-box formalism under the assumption of *instantaneous recycling approximation* (IRA) often used in the literature (e.g. Massari et al., 2019; Forbes, 2020; Limberg et al., 2022). This approximation means that all the SNe yields are instantaneously used to form new stars, which is close to the prediction of rapid enrichment for the bulge population.

In this thesis, we also investigated the role of GCs in the formation and evolution of the galactic bar. To do that, we analysed an N-Al-rich star trapped in the Galactic bar today.

Is there observational evidence of GCs in the bar formation?

- The presence of N-rich stars composing the sample of field stars is well-known in the literature (e.g. Fernández-Trincado et al., 2022). The chemical pattern of these stars is undoubtedly of 2G stars of GCs. Nevertheless, finding evidence of this interaction between the Galactic bar and GCs is difficult. We successfully managed to link the SOS1 star, an N-Al-rich star trapped in the bar, with a GC: Terzan 5. We derived that the SOS1 star was completely captured by the Galactic bar from Terzan 5 at 315 ± 12 Myr ago. This finding is incredible because we provide, at the same time, observational evidence for the predicted huge destruction which Terzan 5 has experienced to reach its present mass. Therefore, Terzan 5 may have contributed to forming most of the N-rich stars that compose the inner Galaxy today.

The results concerning the multiple stellar populations in GCs allow us to conclude the following points in this thesis.

Is there an age difference among the different stellar populations? Is there a more probable formation scenario, or can it be a combination of different scenarios?

- We found for NGC 6752 (Souza et al., 2020) three stellar populations differing from each other 500 Myr. This result agrees with the predictions for intracluster pollution

via stellar winds from AGB stars. Our studies of the MCs' star clusters show that the stellar rotation is not the unique effect that explains the eMSTO in intermediate-age clusters. Moreover, some studies have found different results (Oliveira et al., 2020; Lucertini et al., 2021). Therefore, the phenomenon may happen differently depending on the environment, or multiple events can occur within the same GC.

Perspective for a future work

While significant progress has been made in identifying GCs formed in-situ, further investigations are crucial to determine the exact mechanisms and conditions under which they formed. A Galaxy mass model that takes into account different astrophysical processes, like dynamical friction, can provide profound insights into the in-situ formation of GCs and their evaporation process, potentially revolutionizing our understanding of galactic dynamics and stellar populations.

Despite efforts to constrain the age of the Galactic bulge, uncertainties persist due to observational limitations and complex stellar populations. However, the advent of next-generation telescopes, combined with refined stellar models and statistical methods, holds great promise in narrowing down the age range of the Galactic bulge more accurately. High-resolution observations targeting the inner regions, like 4MOST (PI: R. de Jong; de Jong et al., 2019), and asteroseismology surveys like HADYN (PI: A. Miglio; Miglio et al., 2021), are poised to provide precise ages for individual stars located in the inner Galaxy and also within GCs, ushering in a new era of precision in galactic research.

While observational evidence suggests the presence of GC-like stars in the Galactic bar, the exact mechanisms driving their formation and evolution within it remain elusive. Future observational campaigns targeting regions with prominent bar features, coupled with numerical simulations, can provide deeper insights into the role of GCs in bar formation and dynamics. We also had observation time approved to observe stars members of the most metal-poor population of Terzan 5. With these data, we will be able to improve our finding regarding SOS1 and provide more insights on the formation and evolution of Terzan 5.

Understanding the origin and nature of multiple stellar populations in old clusters requires a multi-faceted approach. We already have ongoing work to implement new stellar evolutionary tracks, taking into account the chemical pattern observed in 2G stars. With

this study, it will be possible to determine the age difference among the stellar populations within a GC with a more precise method. Besides that, we are progressing within the VISCACHA collaboration on studying the secular evolution of MPs in star clusters.

Bibliography

Allende Prieto C., Majewski S. R., Schiavon R., Cunha K., Frinchaboy P., Holtzman J., Johnston K., Shetrone M., Skrutskie M., Smith V., Wilson J., APOGEE: The Apache Point Observatory Galactic Evolution Experiment, Astronomische Nachrichten, 2008, vol. 329, p. 1018

Alonso A., Arribas S., Martínez-Roger C., The effective temperature scale of giant stars (F0-K5). II. Empirical calibration of T_{eff} versus colours and [Fe/H], A&AS, 1999, vol. 140, p. 261

Asplund M., Grevesse N., Sauval A. J., Scott P., The Chemical Composition of the Sun, ARA&A, 2009, vol. 47, p. 481

Auer L. H., Demarque P., Possible Large Carbon and Nitrogen Abundance Variations on the Horizontal Branch of M92. In CNO Isotopes in Astrophysics , vol. 67 of Astrophysics and Space Science Library, 1977, p. 25

Baade W., A Search For the Nucleus of Our Galaxy, PASP, 1946, vol. 58, p. 249

Ballester P., Modigliani A., Boitquin O., Cristiani S., Hanuschik R., Kaufer A., Wolf S., The UVES Data Reduction Pipeline, The Messenger, 2000, vol. 101, p. 31

Barbuy B., Bica E., Ortolani S., Globular clusters within 5(deg) of the Galactic center, A&A, 1998, vol. 333, p. 117

Barbuy B., Cantelli E., Muniz L., Souza S. O., Chiappini C., Hirschi R., Cescutti G., Pignatari M., Ortolani S., Kerber L., Maia F. F. S., Bica E., Depagne E., UVES analysis of red giants in the bulge globular cluster NGC 6522, A&A, 2021a, vol. 654, p. A29

Barbuy B., Cantelli E., Muniz L., Souza S. O., Chiappini C., Hirschi R., Cescutti G., Pignatari M., Ortolani S., Kerber L., Maia F. F. S., Bica E., Depagne E., UVES analysis of red giants in the bulge globular cluster NGC 6522, A&A, 2021b, vol. 654, p. A29

Barbuy B., Cantelli E., Vemado A., Ernandes H., Ortolani S., Saviane I., Bica E., Minniti D., Dias B., Momany Y., Hill V., Zoccali M., Siqueira-Mello C., High-resolution abundance analysis of red giants in the metal-poor bulge globular cluster HP 1, A&A, 2016, vol. 591, p. A53

Barbuy B., Chiappini C., Cantelli E., Depagne E., Pignatari M., Hirschi R., Cescutti G., Ortolani S., Hill V., Zoccali M., Minniti D., Trevisan M., Bica E., Gómez A., High-resolution abundance analysis of red giants in the globular cluster NGC 6522, A&A, 2014, vol. 570, p. A76

Barbuy B., Chiappini C., Gerhard O., Chemodynamical History of the Galactic Bulge, ARA&A, 2018a, vol. 56, p. 223

Barbuy B., Chiappini C., Gerhard O., Chemodynamical History of the Galactic Bulge, ARA&A, 2018b, vol. 56, p. 223

Barbuy B., Ernandes H., Souza S. O., Razera R., Moura T., Meléndez J., Pérez-Villegas A., Zoccali M., Minniti D., Dias B., Ortolani S., Bica E., Gemini/Phoenix H-band analysis of the globular cluster AL 3, A&A, 2021, vol. 648, p. A16

Barbuy B., Friaça A. C. S., da Silveira C. R., Hill V., Zoccali M., Minniti D., Renzini A., Ortolani S., Gómez A., Zinc abundances in Galactic bulge field red giants: Implications for damped Lyman-α systems, A&A, 2015, vol. 580, p. A40

Barbuy B., Friaça A. C. S., Ernandes H., Moura T., Masseron T., Cunha K., Smith V. V., Souto D., Pérez-Villegas A., Souza S. O., Chiappini C., Queiroz A. B. A., Fernández-Trincado J. G., da Silva P., Santiago B. X., Anders F., Schiavon R. P., Valentini M., Minniti D., Geisler D., Placco V. M., Zoccali M., Schultheis M., Nitschelm C., Beers T. C., Razera R., Light elements Na and Al in 58 bulge spheroid stars from APOGEE, MNRAS, 2023, vol. 526, p. 2365

Barbuy B., Muniz L., Ortolani S., Ernandes H., Dias B., Saviane I., Kerber L., Bica E., Pérez-Villegas A., Rossi L., Held E. V., High-resolution abundance analysis of four red giants in the globular cluster NGC 6558â, A&A, 2018a, vol. 619, p. A178

Barbuy B., Muniz L., Ortolani S., Ernandes H., Dias B., Saviane I., Kerber L., Bica E., Pérez-Villegas A., Rossi L., Held E. V., High-resolution abundance analysis of four red giants in the globular cluster NGC 6558â, A&A, 2018b, vol. 619, p. A178

Barbuy B., Perrin M. N., Katz D., Coelho P., Cayrel R., Spite M., Van't Veer-Menneret C., A grid of synthetic spectra and indices Fe5270, Fe5335, Mgb and Mg_2 as a function of stellar parameters and [alpha/Fe], A&A, 2003, vol. 404, p. 661

Barbuy B., Zoccali M., Ortolani S., Hill V., Minniti D., Bica E., Renzini A., Gómez A., VLT-FLAMES analysis of 8 giants in the bulge metal-poor globular cluster NGC 6522: oldest cluster in the Galaxy?. Analysis of 8 giants in NGC 6522, A&A, 2009, vol. 507, p. 405

Barbuy B., Zoccali M., Ortolani S., Minniti D., Hill V., Renzini A., Bica E., Gómez A., NGC 6558: A Blue Horizontal Branch Moderately Metal-Poor Globular Cluster in the Bulge, AJ, 2007, vol. 134, p. 1613

Barbuy B., Zoccali M., Ortolani S., Momany Y., Minniti D., Hill V., Renzini A., Rich R. M., Bica E., Pasquini L., Yadav R. K. S., VLT-UVES analysis of two giants in the bulge metal-poor globular cluster HP-1. Analysis of two giants in HP-1, A&A, 2006, vol. 449, p. 349

Barbuy B. L. S., CNO dans les etoiles du halo : Methode de la synthese spectrale de bandes moleculairesCNO dans les etoiles du halo : Methode de la synthese spectrale de bandes moleculaires, Universite de Paris Diderot (Paris VII), France, 1982, Ph.D. Thesis

Bastian N., de Mink S. E., The effect of stellar rotation on colour-magnitude diagrams: on the apparent presence of multiple populations in intermediate age stellar clusters, MNRAS, 2009, vol. 398, p. L11

Bastian N., Kamann S., Cabrera-Ziri I., Georgy C., Ekström S., Charbonnel C., de Juan Ovelar M., Usher C., Extended main sequence turnoffs in open clusters as seen by Gaia - I. NGC 2818 and the role of stellar rotation, MNRAS, 2018, vol. 480, p. 3739

Bastian N., Lamers H. J. G. L. M., de Mink S. E., Longmore S. N., Goodwin S. P., Gieles M., Early disc accretion as the origin of abundance anomalies in globular clusters, MNRAS, 2013, vol. 436, p. 2398

Bastian N., Lardo C., Multiple Stellar Populations in Globular Clusters, ARA&A, 2018a, vol. 56, p. 83

Bastian N., Lardo C., Multiple Stellar Populations in Globular Clusters, ARA&A, 2018b, vol. 56, p. 83

Baumgardt H., Hilker M., A catalogue of masses, structural parameters, and velocity dispersion profiles of 112 Milky Way globular clusters, MNRAS, 2018, vol. 478, p. 1520

Baumgardt H., Hilker M., Sollima A., Bellini A., Mean proper motions, space orbits, and velocity dispersion profiles of Galactic globular clusters derived from Gaia DR2 data, MNRAS, 2019, vol. 482, p. 5138

Baumgardt H., Makino J., Dynamical evolution of star clusters in tidal fields, MNRAS, 2003, vol. 340, p. 227

Baumgardt H., Vasiliev E., Accurate distances to Galactic globular clusters through a combination of Gaia EDR3, HST, and literature data, MNRAS, 2021, vol. 505, p. 5957

Bedin L. R., Piotto G., Anderson J., King I. R., Cassisi S., Momany Y., The double main sequence of Omega Centauri, Memorie della Societa Astronomica Italiana Supplementi, 2004, vol. 5, p. 105

Bedin L. R., Pourbaix D., Apai D., Burgasser A. J., Buenzli E., Boffin H. M. J., Libralato M., Hubble Space Telescope astrometry of the closest brown dwarf binary system - I. Overview and improved orbit$^{\hat{a}}$, MNRAS, 2017, vol. 470, p. 1140

Beers T. C., Christlieb N., The Discovery and Analysis of Very Metal-Poor Stars in the Galaxy, ARA&A, 2005, vol. 43, p. 531

Bekki K., Freeman K. C., Formation of ω Centauri from an ancient nucleated dwarf galaxy in the young Galactic disc, MNRAS, 2003, vol. 346, p. L11

Bellini A., Milone A. P., Anderson J., Marino A. F., Piotto G., van der Marel R. P., Bedin L. R., King I. R., The State-of-the-art HST Astro-photometric Analysis of the Core of ω Centauri. III. The Main Sequence's Multiple Populations Galore, ApJ, 2017, vol. 844, p. 164

Bellini A., Piotto G., Bedin L. R., Anderson J., Platais I., Momany Y., Moretti A., Milone A. P., Ortolani S., Ground-based CCD astrometry with wide field imagers. III. WFI@2.2m proper-motion catalog of the globular cluster ω Centauri, A&A, 2009, vol. 493, p. 959

Belokurov V., Erkal D., Evans N. W., Koposov S. E., Deason A. J., Co-formation of the disc and the stellar halo, MNRAS, 2018, vol. 478, p. 611

Belokurov V., Kravtsov A., In-situ versus accreted Milky Way globular clusters: a new classification method and implications for cluster formation, MNRAS, 2024, vol. 528, p. 3198

Bica E., Bonatto C., Barbuy B., Ortolani S., Globular cluster system and Milky Way properties revisited, A&A, 2006, vol. 450, p. 105

Bica E., Maia F. F. S., Oliveira R. A. P., Dias B., Santos J. F. C., Rocha J. P., Kerber L., Gardin J. F., Armond T., Parisi M. C., Souza S. O., Barbuy B., The VISCACHA survey - V. Rejuvenating three faint SMC clusters, MNRAS, 2022, vol. 517, p. L41

Bica E., Ortolani S., Barbuy B., Globular Clusters in the Galactic Bulge, PASA, 2016, vol. 33, p. e028

Bica E., Pavani D. B., Bonatto C. J., Lima E. F., A Multi-band Catalog of 10978 Star Clusters, Associations, and Candidates in the Milky Way, AJ, 2019, vol. 157, p. 12

Bissantz N., Gerhard O., Spiral arms, bar shape and bulge microlensing in the Milky Way, MNRAS, 2002, vol. 330, p. 591

Bonanno A., Schlattl H., Paternò L., The age of the Sun and the relativistic corrections in the EOS, A&A, 2002, vol. 390, p. 1115

Bovy J., galpy: A python Library for Galactic Dynamics, ApJS, 2015, vol. 216, p. 29

Bovy J., Leung H. W., Hunt J. A. S., Mackereth J. T., García-Hernández D. A., Roman-Lopes A., Life in the fast lane: a direct view of the dynamics, formation, and evolution of the Milky Way's bar, MNRAS, 2019, vol. 490, p. 4740

Brandt T. D., Huang C. X., Rotating Stellar Models Can Account for the Extended Main-sequence Turnoffs in Intermediate-age Clusters, ApJ, 2015, vol. 807, p. 25

Callingham T. M., Cautun M., Deason A. J., Frenk C. S., Grand R. J. J., Marinacci F., The chemo-dynamical groups of Galactic globular clusters, MNRAS, 2022, vol. 513, p. 4107

Carciofi A. C., Miroshnichenko A. S., Bjorkman J. E., Toward Understanding the B[e] Phenomenon. IV. Modeling of IRAS 00470+6429, ApJ, 2010, vol. 721, p. 1079

Cardelli J. A., Clayton G. C., Mathis J. S., The Relationship between Infrared, Optical, and Ultraviolet Extinction, ApJ, 1989, vol. 345, p. 245

Carini R., Sollima A., Brocato E., Biazzo K., He abundance in NGC 1850 A and B: Are we observing the early stage of the formation of multiple populations in a stellar cluster?, MNRAS, 2024, vol. 528, p. 909

Carretta E., Bragaglia A., Gratton R., D'Orazi V., Lucatello S., Intrinsic iron spread and a new metallicity scale for globular clusters, A&A, 2009, vol. 508, p. 695

Carretta E., Bragaglia A., Gratton R., Lucatello S., Na-O anticorrelation and HB. VIII. Proton-capture elements and metallicities in 17 globular clusters from UVES spectra, A&A, 2009, vol. 505, p. 139

Carretta E., Bragaglia A., Gratton R. G., Lucatello S., Catanzaro G., Leone F., Bellazzini M., Claudi R., D'Orazi V., Momany Y., Ortolani S., Pancino E., Piotto G., Recio-Blanco A., Sabbi E., Na-O anticorrelation and HB. VII. The chemical composition of first and second-generation stars in 15 globular clusters from GIRAFFE spectra, A&A, 2009, vol. 505, p. 117

Carretta E., Bragaglia A., Gratton R. G., Lucatello S., D'Orazi V., Chemical Tagging of Three Distinct Populations of Red Giants in the Globular Cluster NGC 6752, ApJ, 2012, vol. 750, p. L14

Carretta E., Bragaglia A., Gratton R. G., Recio-Blanco A., Lucatello S., D'Orazi V., Cassisi S., Properties of stellar generations in globular clusters and relations with global parameters, A&A, 2010, vol. 516, p. A55

Casagrande L., Ramírez I., Meléndez J., Bessell M., Asplund M., An absolutely calibrated T_{eff} scale from the infrared flux method. Dwarfs and subgiants, A&A, 2010, vol. 512, p. A54

Casali G., Magrini L., Tognelli E., Jackson R., Jeffries R. D., Lagarde N., Tautvaišienė G., Masseron T., Degl'Innocenti S., Prada Moroni P. G., Kordopatis G., Pancino E., Randich S., Feltzing e. a., The Gaia-ESO survey: Calibrating a relationship between age and the [C/N] abundance ratio with open clusters, A&A, 2019, vol. 629, p. A62

Cayrel R., ed., 1988 The impact of very high S/N spectroscopy on stellar physics: proceedings of the 132nd Symposium of the International Astronomical Union held in Paris, France, June 29-July 3, 1987. vol. 132

Cayrel R., Perrin M. N., Barbuy B., Buser R., A grid of synthetic spectra for the determination of effective temperature, gravity and metallicity of F,G and K stars.I. Description of the method., A&A, 1991, vol. 247, p. 108

Cescutti G., Chiappini C., Explaining the Ba, Y, Sr, and Eu abundance scatter in metal-poor halo stars: constraints to the r-process, A&A, 2014, vol. 565, p. A51

Cescutti G., Chiappini C., Hirschi R., Meynet G., Frischknecht U., The s-process in the Galactic halo: the fifth signature of spinstars in the early Universe?, A&A, 2013, vol. 553, p. A51

Cescutti G., Romano D., Matteucci F., Chiappini C., Hirschi R., The role of neutron star mergers in the chemical evolution of the Galactic halo, A&A, 2015, vol. 577, p. A139

Chabrier G., Galactic Stellar and Substellar Initial Mass Function, PASP, 2003, vol. 115, p. 763

Chiappini C., Frischknecht U., Meynet G., Hirschi R., Barbuy B., Pignatari M., Decressin T., Maeder A., Imprints of fast-rotating massive stars in the Galactic Bulge, Nature, 2011, vol. 472, p. 454

Chiappini C., Matteucci F., Gratton R., The Chemical Evolution of the Galaxy: The Two-Infall Model, ApJ, 1997, vol. 477, p. 765

Choi J., Dotter A., Conroy C., Cantiello M., Paxton B., Johnson B. D., Mesa Isochrones and Stellar Tracks (MIST). I. Solar-scaled Models, ApJ, 2016, vol. 823, p. 102

Choplin A., Hirschi R., Meynet G., Ekström S., Chiappini C., Laird A., Non-standard s-process in massive rotating stars. Yields of 10-150 $M_{\odot}$ models at Z = 10^{-3}, A&A, 2018, vol. 618, p. A133

Coelho P., Barbuy B., Meléndez J., Schiavon R. P., Castilho B. V., A library of high resolution synthetic stellar spectra from 300 nm to 1.8 μm with solar and α-enhanced composition, A&A, 2005, vol. 443, p. 735

Cohen J. G., Abundances in globular cluster red giants. I. M3 and M13., ApJ, 1978, vol. 223, p. 487

Cohen R. E., Bellini A., Casagrande L., Brown T. M., Correnti M., Kalirai J. S., Relative Ages of Nine Inner Milky Way Globular Clusters from Proper-motion-cleaned Color-Magnitude Diagrams, AJ, 2021, vol. 162, p. 228

Cohen R. E., Bellini A., Libralato M., Correnti M., Brown T. M., Kalirai J. S., Structure and Internal Kinematics of Nine Inner Milky Way Globular Clusters, AJ, 2021, vol. 161, p. 41

Cohen R. E., Mauro F., Alonso-García J., Hempel M., Sarajedini A., Ordoñez A. J., Geisler D., Kalirai J. S., Deep Hubble Space Telescope Imaging of Globular Clusters toward the Galactic Bulge: Observations, Data Reduction, and Color-magnitude Diagrams, AJ, 2018, vol. 156, p. 41

Cordoni G., Milone A. P., Marino A. F., Cignoni M., Lagioia E. P., Tailo M., Carlos M., Dondoglio E., Jang S., Mohandasan A., Legnardi M. V., NGC1818 unveils the origin of the extended main-sequence turn-off in young Magellanic Clouds clusters, Nature Communications, 2022, vol. 13, p. 4325

Cordoni G., Milone A. P., Marino A. F., Di Criscienzo M., D'Antona F., Dotter A., Lagioia E. P., Tailo M., Extended Main-sequence Turnoff as a Common Feature of Milky Way Open Clusters, ApJ, 2018, vol. 869, p. 139

Cordoni G., Milone A. P., Mastrobuono-Battisti A., Marino A. F., Lagioia E. P., Tailo M., Baumgardt H., Hilker M., Three-component Kinematics of Multiple Stellar Populations in Globular Clusters with Gaia and VLT, ApJ, 2020, vol. 889, p. 18

Correnti M., Goudfrooij P., Bellini A., Girardi L., The wide upper main sequence and main-sequence turnoff of the $\sim$ 800 Myr old star cluster NGC 1831, MNRAS, 2021, vol. 504, p. 155

Crain R. A., Schaye J., Bower R. G., Furlong M., Schaller M., Theuns T., Dalla Vecchia C., Frenk C. S., McCarthy I. G., Helly J. C., Jenkins A., Rosas-Guevara Y. M., White S. D. M., Trayford J. W., The EAGLE simulations of galaxy formation: calibration of subgrid physics and model variations, MNRAS, 2015, vol. 450, p. 1937

Crowl H. H., Sarajedini A., Piatti A. E., Geisler D., Bica E., Clariá J. J., Santos João F. C. J., The Line-of-Sight Depth of Populous Clusters in the Small Magellanic Cloud, AJ, 2001, vol. 122, p. 220

D'Antona F., Caloi V., The Early Evolution of Globular Clusters: The Case of NGC 2808, ApJ, 2004, vol. 611, p. 871

D'Antona F., Caloi V., Tailo M., On the blind use of statistical tools in the analysis of globular cluster stars, Nature Astronomy, 2018, vol. 2, p. 270

D'Antona F., Vesperini E., D'Ercole A., Ventura P., Milone A. P., Marino A. F., Tailo M., A single model for the variety of multiple-population formation(s) in globular clusters: a temporal sequence, MNRAS, 2016, vol. 458, p. 2122

de Jong R. S., Agertz O., Berbel A. A., Aird J., Alexander D. A., Amarsi A., Anders F., Andrae R., Ansarinejad B., Ansorge W., Antilogus P., Anwand-Heerwart H., Arentsen A., Arnadottir A., Asplund M., Auger M., Azais N., Baade D., Baker G., Baker S., Balbinot E., Baldry I. K., Banerji M., Barden S., Barklem P., Barthélémy-Mazot e. a., 4MOST: Project overview and information for the First Call for Proposals, The Messenger, 2019, vol. 175, p. 3

de Sá-Freitas C., Fragkoudi F., Gadotti D. A., Falcón-Barroso J., Bittner A., Sánchez-Blázquez P., van de Ven G., Bieri R., Coccato L., Coelho P., Fahrion K., Gonçalves

G., Kim T., de Lorenzo-Cáceres A., Martig M., Martín-Navarro I., Mendez-Abreu J., Neumann J., Querejeta M., A new method for age-dating the formation of bars in disc galaxies. The TIMER view on NGC1433's old bar and the inside-out growth of its nuclear disc, A&A, 2023, vol. 671, p. A8

Decressin T., Meynet G., Charbonnel C., Prantzos N., Ekström S., Fast rotating massive stars and the origin of the abundance patterns in galactic globular clusters, A&A, 2007, vol. 464, p. 1029

Dehnen W., A Family of Potential-Density Pairs for Spherical Galaxies and Bulges, MNRAS, 1993, vol. 265, p. 250

Dehnen W., Binney J., Mass models of the Milky Way, MNRAS, 1998, vol. 294, p. 429

Dias B., Angelo M. S., Oliveira R. A. P., Maia F., Parisi M. C., De Bortoli B., Souza S. O., Katime Santrich O. J., Bassino L. P., Barbuy B., Bica E., Geisler D., Kerber L., Pérez-Villegas A., Quint B., Sanmartim D., Santos J. F. C., Westera P., The VISCACHA survey. III. Star clusters counterpart of the Magellanic Bridge and Counter-Bridge in 8D, A&A, 2021, vol. 647, p. L9

Dias B., Barbuy B., Saviane I., Held E. V., Da Costa G. S., Ortolani S., Gullieuszik M., Vásquez S., FORS2/VLT survey of Milky Way globular clusters. II. Fe and Mg abundances of 51 Milky Way globular clusters on a homogeneous scale, A&A, 2016, vol. 590, p. A9

Dias B., Palma T., Minniti D., Fernández-Trincado J. G., Alonso-García J., Barbuy B., Clariá J. J., Gomez M., Saito R. K., FSR 1776: A new globular cluster in the Galactic bulge?, A&A, 2022, vol. 657, p. A67

Dias B., Parisi M. C., Angelo M., Maia F., Oliveira R. A. P., Souza S. O., Kerber L. O., Santos J. F. C., Pérez-Villegas A., Sanmartim D., Quint B., Fraga L., Barbuy B., Bica E., Santrich O. J. K., Hernandez-Jimenez J. A., Geisler D., Minniti D., De Bórtoli B. J., Bassino L. P., Rocha J. P., The VISCACHA survey - IV. The SMC West Halo in 8D, MNRAS, 2022, vol. 512, p. 4334

Diolaiti E., Bendinelli O., Bonaccini D., Close L., Currie D., Parmeggiani G., Analysis of isoplanatic high resolution stellar fields by the StarFinder code, A&AS, 2000, vol. 147, p. 335

Djorgovski S., King I. R., A Preliminary Survey of Collapsed Cores in Globular Clusters, ApJ, 1986, vol. 305, p. L61

Dotter A., MESA Isochrones and Stellar Tracks (MIST) 0: Methods for the Construction of Stellar Isochrones, ApJS, 2016, vol. 222, p. 8

Dotter A., Chaboyer B., Jevremović D., Kostov V., Baron E., Ferguson J. W., The Dartmouth Stellar Evolution Database, ApJS, 2008, vol. 178, p. 89

Dotter A., Sarajedini A., Anderson J., Globular Clusters in the Outer Galactic Halo: New Hubble Space Telescope/Advanced Camera for Surveys Imaging of Six Globular Clusters and the Galactic Globular Cluster Age-metallicity Relation, ApJ, 2011, vol. 738, p. 74

Dotter A., Sarajedini A., Anderson J., Aparicio A., Bedin L. R., Chaboyer B., Majewski S., Marín-Franch A., Milone A., Paust N., Piotto G., Reid I. N., Rosenberg A., Siegel M., The ACS Survey of Galactic Globular Clusters. IX. Horizontal Branch Morphology and the Second Parameter Phenomenon, ApJ, 2010, vol. 708, p. 698

Einasto J., On Galactic Descriptive Functions, Astronomische Nachrichten, 1969, vol. 291, p. 97

Ernandes H., Barbuy B., Alves-Brito A., Friaça A., Siqueira-Mello C., Allen D. M., Iron-peak elements Sc, V, Mn, Cu, and Zn in Galactic bulge globular clusters, A&A, 2018, vol. 616, p. A18

Ernandes H., Barbuy B., Friaça A., Hill V., Spite M., Spite F., Castilho B. V., Evans C. J., Be, V, and Cu in the halo star CS 31082-001 from near-UV spectroscopy, MNRAS, 2022, vol. 510, p. 5362

Ernandes H., Barbuy B., Friaça A. C. S., Hill V., Zoccali M., Minniti D., Renzini A., Ortolani S., Cobalt and copper abundances in 56 Galactic bulge red giants, A&A, 2020, vol. 640, p. A89

Ernandes H., Dias B., Barbuy B., Kamann S., Ortolani S., Cantelli E., Bica E., Rossi L., A MUSE study of the inner bulge globular cluster Terzan 9: a fossil record in the Galaxy, A&A, 2019, vol. 632, p. A103

Fernández-Trincado J. G., Beers T. C., Barbuy B., Minniti D., Chiappini C., Garro E. R., Tang B., Alves-Brito A., Villanova S., Geisler D., Lane R. R., Diaz D. G., Galactic ArchaeoLogIcaL ExcavatiOns (GALILEO). I. An updated census of APOGEE N-rich giants across the Milky Way, A&A, 2022, vol. 663, p. A126

Fernández-Trincado J. G., Minniti D., Beers T. C., Villanova S., Geisler D., Souza S. O., Smith L. C., Placco V. M., Vieira K., Pérez-Villegas A., Barbuy B., Alves-Brito A., Bidin C. M., Alonso-García J., Tang B., Palma T., The enigmatic globular cluster UKS 1 obscured by the bulge: H-band discovery of nitrogen-enhanced stars, A&A, 2020, vol. 643, p. A145

Fernández-Trincado J. G., Minniti D., Souza S. O., Beers T. C., Geisler D., Moni Bidin C., Villanova S., Majewski S. R., Barbuy B., Pérez-Villegas A., Henao L., Romero-Colmenares M., Roman-Lopes A., Lane R. R., VVV CL001: Likely the Most Metal-poor Surviving Globular Cluster in the Inner Galaxy, ApJ, 2021, vol. 908, p. L42

Ferraro F. R., Massari D., Dalessandro E., Lanzoni B., Origlia L., Rich R. M., Mucciarelli A., The Age of the Young Bulge-like Population in the Stellar System Terzan 5: Linking the Galactic Bulge to the High-z Universe, ApJ, 2016, vol. 828, p. 75

Forbes D. A., Reverse engineering the Milky Way, MNRAS, 2020, vol. 493, p. 847

Forbes D. A., Bridges T., Accreted versus in situ Milky Way globular clusters, MNRAS, 2010, vol. 404, p. 1203

Foreman-Mackey D., Hogg D. W., Lang D., Goodman J., emcee: The MCMC Hammer, PASP, 2013, vol. 125, p. 306

Friaça A. C. S., Barbuy B., Tracing the evolution of the Galactic bulge with chemodynamical modelling of alpha-elements, A&A, 2017, vol. 598, p. A121

Frischknecht U., Hirschi R., Pignatari M., Maeder A., Meynet G., Chiappini C., Thielemann F.-K., Rauscher T., Georgy C., Ekström S., s-process production in rotating massive stars at solar and low metallicities, MNRAS, 2016, vol. 456, p. 1803

Gaia Collaboration Clementini G., Eyer L., Ripepi V., Marconi M., Muraveva T., Garofalo A., Sarro L. M., Palmer M., Luri X., Molinaro R., Rimoldini L., Szabados L., Musella I., Anderson R. I., Prusti T., de Bruijne J. H. J., Brown A. G. A., Vallenari A., Babusiaux C., Bailer-Jones C. A. L., Bastian e. a., Gaia Data Release 1. Testing parallaxes with local Cepheids and RR Lyrae stars, A&A, 2017, vol. 605, p. A79

Gaia Collaboration Helmi A., van Leeuwen F., McMillan P. J., Massari D., Antoja T., Robin A. C., Lindegren L., Bastian U., Arenou F., Babusiaux C., Biermann M., Breddels M. A., Hobbs D., Jordi C., Pancino E., Reylé C., Veljanoski J., Brown e. a., Gaia Data Release 2. Kinematics of globular clusters and dwarf galaxies around the Milky Way, A&A, 2018, vol. 616, p. A12

Gaia Collaboration Klioner S. A., Lindegren L., Mignard F., Hernández J., Ramos-Lerate M., Bastian U., Biermann M., Bombrun A., de Torres A., et al. Gaia Early Data Release 3. The celestial reference frame (Gaia-CRF3), A&A, 2022, vol. 667, p. A148

Gallart C., Bernard E. J., Brook C. B., Ruiz-Lara T., Cassisi S., Hill V., Monelli M., Uncovering the birth of the Milky Way through accurate stellar ages with Gaia, Nature Astronomy, 2019, vol. 3, p. 932

Garro E. R., Minniti D., Gómez M., Alonso-García J., Palma T., Smith L. C., Ripepi V., Confirmation and physical characterization of the new bulge globular cluster Patchick 99 from the VVV and Gaia surveys, A&A, 2021, vol. 649, p. A86

Garro E. R., Minniti D., Gómez M., Alonso-García J., Ripepi V., Fernández-Trincado J. G., Vivanco Cádiz F., Inspection of 19 globular cluster candidates in the Galactic bulge with the VVV survey, A&A, 2022, vol. 658, p. A120

Gerhard O., Wegg C., Portail M., Photometric Surveys of the Galactic Bulge and Long Bar. In The Universe of Digital Sky Surveys , vol. 42 of Astrophysics and Space Science Proceedings, 2016, p. 41

Gieles M., Charbonnel C., Krause M. G. H., Hénault-Brunet V., Agertz O., Lamers H. J. G. L. M., Bastian N., Gualand ris A., Zocchi A., Petts J. A., Concurrent formation of supermassive stars and globular clusters: implications for early self-enrichment, MNRAS, 2018, vol. 478, p. 2461

Girardi L., Eggenberger P., Miglio A., Can rotation explain the multiple main-sequence turn-offs of Magellanic Cloud star clusters?, MNRAS, 2011, vol. 412, p. L103

Girardi L., Goudfrooij P., Kalirai J. S., Kerber L., Kozhurina-Platais V., Rubele S., Bressan A., Chandar R., Marigo P., Platais I., Puzia T. H., An extended main-sequence turn-off in the Small Magellanic Cloud star cluster NGC 411, MNRAS, 2013, vol. 431, p. 3501

Girardi L., Rubele S., Kerber L., Discovery of two distinct red clumps in NGC 419: a rare snapshot of a cluster at the onset of degeneracy, MNRAS, 2009, vol. 394, p. L74

Gonzalez O. A., Rejkuba M., Zoccali M., Valenti E., Minniti D., Reddening and metallicity maps of the Milky Way bulge from VVV and 2MASS. I. The method and minor axis maps, A&A, 2011, vol. 534, p. A3

Gonzalez O. A., Rejkuba M., Zoccali M., Valenti E., Minniti D., Schultheis M., Tobar R., Chen B., Reddening and metallicity maps of the Milky Way bulge from VVV and 2MASS. II. The complete high resolution extinction map and implications for Galactic bulge studies, A&A, 2012, vol. 543, p. A13

Goudfrooij P., Girardi L., Kozhurina-Platais V., Kalirai J. S., Platais I., Puzia T. H., Correnti M., Bressan A., Chandar R., Kerber L., Marigo P., Rubele S., Extended Main Sequence Turnoffs in Intermediate-age Star Clusters: A Correlation between Turnoff Width and Early Escape Velocity, ApJ, 2014, vol. 797, p. 35

Goudfrooij P., Puzia T. H., Kozhurina-Platais V., Chandar R., Population Parameters of Intermediate-Age Star Clusters in the Large Magellanic Cloud. I. NGC 1846 and its Wide Main-Sequence Turnoff, AJ, 2009, vol. 137, p. 4988

Gratton R., Sneden C., Carretta E., Abundance Variations Within Globular Clusters, ARA&A, 2004, vol. 42, p. 385

Gratton R. G., Bragaglia A., Carretta E., Clementini G., Desidera S., Grundahl F., Lucatello S., Distances and ages of NGC 6397, NGC 6752 and 47 Tuc, A&A, 2003, vol. 408, p. 529

Gratton R. G., Bragaglia A., Carretta E., de Angeli F., Lucatello S., Momany Y., Piotto G., Recio Blanco A., Precise reddening and metallicity of NGC 6752 from FLAMES spectra, A&A, 2005, vol. 440, p. 901

Gratton R. G., Carretta E., Bragaglia A., Multiple populations in globular clusters. Lessons learned from the Milky Way globular clusters, A&A Rev., 2012, vol. 20, p. 50

Grevesse N., Sauval A. J., Standard Solar Composition, Space Sci. Rev., 1998, vol. 85, p. 161

Grevesse N., Scott P., Asplund M., Sauval A. J., The elemental composition of the Sun. III. The heavy elements Cu to Th, A&A, 2015, vol. 573, p. A27

Guedes J., Callegari S., Madau P., Mayer L., Forming Realistic Late-type Spirals in a ΛCDM Universe: The Eris Simulation, ApJ, 2011, vol. 742, p. 76

Gustafsson B., Edvardsson B., Eriksson K., Jørgensen U. G., Nordlund Å., Plez B., A grid of MARCS model atmospheres for late-type stars. I. Methods and general properties, A&A, 2008, vol. 486, p. 951

Harding G. A., A CH star in omega Centauri, The Observatory, 1962, vol. 82, p. 205

Harris W. E., A Catalog of Parameters for Globular Clusters in the Milky Way, AJ, 1996, vol. 112, p. 1487

Hartwick F. D. A., McClure R. D., Variation of the Nitrogen Abundance among Population II Objects, ApJ, 1972, vol. 176, p. L57

Hasselquist S., Hayes C. R., Lian J., Weinberg D. H., Zasowski G., Horta D., Beaton R., Feuillet D. K., Garro E. R., Gallart C., Smith V. V., Holtzman J. A., Minniti D., Lacerna I., Shetrone M., Jönsson H., Cioni M.-R. L., Fillingham S. P., Cunha K., O'Connell R., Fernández-Trincado J. G. e. a., APOGEE Chemical Abundance Patterns of the Massive Milky Way Satellites, ApJ, 2021, vol. 923, p. 172

Hawkins K., Jofré P., Masseron T., Gilmore G., Using chemical tagging to redefine the interface of the Galactic disc and halo, MNRAS, 2015, vol. 453, p. 758

Healy B. F., McCullough P. R., Schlaufman K. C., Kovacs G., A Study of Stellar Spins in 15 Open Clusters, ApJ, 2023, vol. 944, p. 39

Helmi A., Streams, Substructures, and the Early History of the Milky Way, ARA&A, 2020, vol. 58, p. 205

Helmi A., Babusiaux C., Koppelman H. H., Massari D., Veljanoski J., Brown A. G. A., The merger that led to the formation of the Milky Way's inner stellar halo and thick disk, Nature, 2018, vol. 563, p. 85

Helmi A., de Zeeuw P. T., Mapping the substructure in the Galactic halo with the next generation of astrometric satellites, MNRAS, 2000, vol. 319, p. 657

Hidalgo S. L., Pietrinferni A., Cassisi S., Salaris M., Mucciarelli A., Savino A., Aparicio A., Silva Aguirre V., Verma K., The Updated BaSTI Stellar Evolution Models and Isochrones. I. Solar-scaled Calculations, ApJ, 2018, vol. 856, p. 125

Hinkle K., Wallace L., Valenti J., Harmer D., Visible and Near Infrared Atlas of the Arcturus Spectrum 3727-9300 A, 2000

Horta D., Schiavon R. P., Mackereth J. T., Pfeffer J., Mason A. C., Kisku S., Fragkoudi F., Allende Prieto C., Cunha K., Hasselquist S., Holtzman J., Majewski S. R., Nataf D., O'Connell R. W., Schultheis M., Smith V. V., Evidence from APOGEE for the presence of a major building block of the halo buried in the inner Galaxy, MNRAS, 2021, vol. 500, p. 1385

Horta D., Schiavon R. P., Mackereth J. T., Weinberg D. H., Hasselquist S., Feuillet D., O'Connell R. W., Anguiano B., Allende-Prieto C., Beaton R. L., Bizyaev D., Cunha K., Geisler D., García-Hernández D. A., Holtzman J., Jönsson H., Lane R. R., Majewski S. R., Mészáros S., Minniti D., Nitschelm C., Shetrone M., Smith V. V., Zasowski G., The chemical characterization of halo substructure in the Milky Way based on APOGEE, MNRAS, 2023, vol. 520, p. 5671

Howell S. B., Sobeck C., Haas M., Still M., Barclay T., Mullally F., Troeltzsch J., Aigrain S., Bryson S. T., Caldwell D., Chaplin W. J., Cochran W. D., Huber D., Marcy G. W., Miglio A., Najita J. R., Smith M., Twicken J. D., Fortney J. J., The K2 Mission: Characterization and Early Results, PASP, 2014, vol. 126, p. 398

Hunter G. H., Sormani M. C., Beckmann J. P., Vasiliev E., Glover S. C. O., Klessen R. S., Soler J. D., Brucy N., Girichidis P., Göller J., Ohlin L., Tress R., Molinari S., Gerhard O., Benedettini M., Smith R., Hennebelle P., Testi L., Testing kinematic distances under a realistic Galactic potential, arXiv e-prints, 2024, p. arXiv:2403.18000

Johnson C. I., Calamida A., Kader J. A., Ferraro I., Pilachowski C. A., Bono G., Mastrobuono-Battisti A., Rest A., Zenteno A., Zocchi A., A Wide View of the Galactic Globular Cluster NGC 2808: Red Giant and Horizontal Branch Star Spatial Distributions, AJ, 2023, vol. 166, p. 3

Kauffmann G., White S. D. M., Guiderdoni B., The formation and evolution of galaxies within merging dark matter haloes., MNRAS, 1993, vol. 264, p. 201

Kerber L. O., Libralato M., Souza S. O., Oliveira R. A. P., Ortolani S., Pérez-Villegas A., Barbuy B., Dias B., Bica E., Nardiello D., A deep view of a fossil relic in the Galactic bulge: the Globular Cluster HP 1, MNRAS, 2019, vol. 484, p. 5530

Kerber L. O., Nardiello D., Ortolani S., Barbuy B., Bica E., Cassisi S., Libralato M., Vieira R. G., Ages of the Bulge Globular Clusters NGC 6522 and NGC 6626 (M28) from HST Proper-motion-cleaned Color-Magnitude Diagrams, ApJ, 2018, vol. 853, p. 15

Kerber L. O., Santiago B. X., Brocato E., Physical parameters of 15 intermediate-age LMC clusters from modelling of HST colour-magnitude diagrams, A&A, 2007, vol. 462, p. 139

Kerber L. O., Santiago B. X., Castro R., Valls-Gabaud D., Analysis of colour-magnitude diagrams of rich LMC clusters: NGC 1831, A&A, 2002, vol. 390, p. 121

Kharchenko N. V., Piskunov A. E., Schilbach E., Röser S., Scholz R. D., Global survey of star clusters in the Milky Way. V. Integrated JHK$_S$ magnitudes and luminosity functions, A&A, 2016, vol. 585, p. A101

Kobayashi C., Karakas A. I., Lugaro M., The Origin of Elements from Carbon to Uranium, ApJ, 2020, vol. 900, p. 179

Kraft R. P., Abundance Differences among Globular Cluster Giants: Primordial vs. Evolutionary Scenarios, PASP, 1994, vol. 106, p. 553

Kraft R. P., Sneden C., Langer G. E., Prosser C. F., Oxygen Abundances in Halo Giants. II. Giants in the Globular Clusters M13 and M3 and The Intermediately Metal-Poor Halo Field, AJ, 1992, vol. 104, p. 645

Kraft R. P., Sneden C., Smith G. H., Shetrone M. D., Fulbright J., Proton Capture Chains in Globular Cluster Stars. III. Abundances of Giants in the Second-Parameter Globular Cluster NGC 7006, AJ, 1998, vol. 115, p. 1500

Kraft R. P., Sneden C., Smith G. H., Shetrone M. D., Langer G. E., Pilachowski C. A., Proton Capture Chains in Globular Cluster Stars.II.Oxygen, Sodium, Magnesium, and Aluminum Abundances in M13 Giants Brighter Than the Horizontal Branch, AJ, 1997, vol. 113, p. 279

Kraft R. P., Suntzeff N. B., Langer G. E., Carbon D. F., Trefzger C. F., Friel E., Stone R. P. S., Carbon and nitrogen abundances in extremely metal-deficient red giants., PASP, 1982, vol. 94, p. 55

Krause M., Charbonnel C., Decressin T., Meynet G., Prantzos N., Superbubble dynamics in globular cluster infancy. II. Consequences for secondary star formation in the context of self-enrichment via fast-rotating massive stars, A&A, 2013, vol. 552, p. A121

Kroupa P., Tout C. A., Gilmore G., The Distribution of Low-Mass Stars in the Galactic Disc, MNRAS, 1993, vol. 262, p. 545

Kruijssen J. M. D., Pelupessy F. I., Lamers H. J. G. L. M., Portegies Zwart S. F., Bastian N., Icke V., Formation versus destruction: the evolution of the star cluster population in galaxy mergers, MNRAS, 2012, vol. 421, p. 1927

Kruijssen J. M. D., Pelupessy F. I., Lamers H. J. G. L. M., Portegies Zwart S. F., Icke V., Modelling the formation and evolution of star cluster populations in galaxy simulations, MNRAS, 2011, vol. 414, p. 1339

Kruijssen J. M. D., Pfeffer J. L., Chevance M., Bonaca A., Trujillo-Gomez S., Bastian N., Reina-Campos M., Crain R. A., Hughes M. E., Kraken reveals itself - the merger history of the Milky Way reconstructed with the E-MOSAICS simulations, MNRAS, 2020, vol. 498, p. 2472

Kruijssen J. M. D., Pfeffer J. L., Reina-Campos M., Crain R. A., Bastian N., The formation and assembly history of the Milky Way revealed by its globular cluster population, MNRAS, 2019, vol. 486, p. 3180

Kunder A., Crabb R. E., Debattista V. P., Koch-Hansen A. J., Huhmann B. M., Spectroscopic Observations of Obscured Populations in the Inner Galaxy: 2MASS-GC02, Terzan 4, and the 200 km s^{-1} stellar peak, AJ, 2021, vol. 162, p. 86

Kunder A., Rich R. M., Koch A., Storm J., Nataf D. M., De Propris R., Walker A. R., Bono G., Johnson C. I., Shen J., Li Z. Y., Before the Bar: Kinematic Detection of a Spheroidal Metal-poor Bulge Component, ApJ, 2016, vol. 821, p. L25

Lagarde N., Robin A. C., Reylé C., Nasello G., Population synthesis to constrain Galactic and stellar physics. I. Determining age and mass of thin-disc red-giant stars, A&A, 2017, vol. 601, p. A27

Lagioia E. P., Milone A. P., Marino A. F., Cordoni G., Tailo M., The Role of Cluster Mass in the Multiple Populations of Galactic and Extragalactic Globular Clusters, AJ, 2019, vol. 158, p. 202

Lanzoni B., Ferraro F. R., Dalessandro E., Mucciarelli A., Beccari G., Miocchi P., Bellazzini M., Rich R. M., Origlia L., Valenti E., Rood R. T., Ransom S. M., New Density Profile and Structural Parameters of the Complex Stellar System Terzan 5, ApJ, 2010, vol. 717, p. 653

Lardo C., Bellazzini M., Pancino E., Carretta E., Bragaglia A., Dalessandro E., Mining SDSS in search of multiple populations in globular clusters, A&A, 2011, vol. 525, p. A114

Latour M., Calamida A., Husser T. O., Kamann S., Dreizler S., Brinchmann J., A stellar census in globular clusters with MUSE. A new perspective on the multiple main sequences of ω Centauri, A&A, 2021, vol. 653, p. L8

Leaman R., VandenBerg D. A., Mendel J. T., The bifurcated age-metallicity relation of Milky Way globular clusters and its implications for the accretion history of the galaxy, MNRAS, 2013, vol. 436, p. 122

Lee J.-W., Multiple Stellar Populations of Globular Clusters from Homogeneous Ca-CN Photometry. II. M5 (NGC 5904) and a New Filter System, ApJ, 2017, vol. 844, p. 77

Lee J.-W., Multiple Stellar Populations of Globular Clusters from Homogeneous Ca–CN–CH Photometry. V. $cn'_{\rm JWL}$ as a Surrogate $cn_{\rm JWL}$ Index and NGC 6723, arXiv e-prints, 2019, p. arXiv:1908.06670

Lee J.-W., Five Stellar Populations in M22 (NGC 6656), ApJ, 2020, vol. 888, p. L6

Lee J.-W., Carney B. W., Near-Infrared Photometry of the Globular Cluster Palomar 6, AJ, 2002, vol. 123, p. 3305

Lee J.-W., Carney B. W., Balachandran S. C., Infrared Echelle Spectroscopy of Palomar 6 and M71, AJ, 2004, vol. 128, p. 2388

Lee Y. W., Joo J. M., Sohn Y. J., Rey S. C., Lee H. C., Walker A. R., Multiple stellar populations in the globular cluster ω Centauri as tracers of a merger event, Nature, 1999, vol. 402, p. 55

Legnardi M. V., Milone A. P., Armillotta L., Marino A. F., Cordoni G., Renzini A., Vesperini E., D'Antona F., McKenzie M., Yong D., Dondoglio E., Lagioia E. P., Carlos M., Tailo M., Jang S., Mohandasan A., Constraining the original composition of the gas forming first-generation stars in globular clusters, MNRAS, 2022, vol. 513, p. 735

Limberg G., Souza S. O., Pérez-Villegas A., Rossi S., Perottoni H. D., Santucci R. M., Reconstructing the Disrupted Dwarf Galaxy Gaia-Sausage/Enceladus Using Its Stars and Globular Clusters, ApJ, 2022, vol. 935, p. 109

Lindegren L., Hernández J., Bombrun A., Klioner S., Bastian U., Ramos-Lerate M., de Torres A., Steidelmüller H., Stephenson C., Hobbs D., Lammers U., Biermann M., Geyer R., Hilger T., Michalik D., Stampa U., McMillan P. J., Castañeda e. a., Gaia Data Release 2. The astrometric solution, A&A, 2018, vol. 616, p. A2

Lucertini F., Nardiello D., Piotto G., The Hubble Space Telescope UV Legacy Survey of Galactic Globular Clusters. XXII. Relative ages of multiple populations in five globular clusters, A&A, 2021, vol. 646, p. A125

Mackey A. D., Broby Nielsen P., Ferguson A. M. N., Richardson J. C., Multiple Stellar Populations in Three Rich Large Magellanic Cloud Star Clusters, ApJ, 2008, vol. 681, p. L17

Maia F. F. S., Corradi W. J. B., Santos J. F. C. J., Characterization and photometric membership of the open cluster NGC1981, MNRAS, 2010, vol. 407, p. 1875

Maia F. F. S., Dias B., Santos J. F. C., Kerber L. d. O., Bica E., Piatti A. E., Barbuy B., Quint B., Fraga L., Sanmartim D., Angelo M. S., Hernandez-Jimenez J. A., Katime Santrich O. J., Oliveira R. A. P., Pérez-Villegas A., Souza S. O., Vieira R. G., Westera P., The VISCACHA survey - I. Overview and first results, MNRAS, 2019, vol. 484, p. 5702

Malkan M. A., Near Infrared Photometry of Globular Clusters Near the Galactic Center. In IAU Colloq. 68: Astrophysical Parameters for Globular Clusters , 1981, p. 533

Marín-Franch A., Aparicio A., Piotto G., Rosenberg A., Chaboyer B., Sarajedini A., Siegel M., Anderson J., Bedin L. R., Dotter A., Hempel M., King I., Majewski S., Milone A. P., Paust N., Reid I. N., The ACS Survey of Galactic Globular Clusters. VII. Relative Ages, ApJ, 2009, vol. 694, p. 1498

Marino A. F., Milone A. P., Renzini A., Yong D., Asplund M., Da Costa G. S., Jerjen H., Cordoni G., Carlos M., Dondoglio E., Lagioia E. P., Jang S., Tailo M., Spectroscopy and Photometry of the Least Massive Type II Globular Clusters: NGC 1261 and NGC 6934, ApJ, 2021, vol. 923, p. 22

Martig M., Fouesneau M., Rix H.-W., Ness M., Mészáros S., García-Hernández D. A., Pinsonneault M., Serenelli A., Silva Aguirre V., Zamora O., Red giant masses and ages derived from carbon and nitrogen abundances, MNRAS, 2016, vol. 456, p. 3655

Martín E. L., Basri G., Pavlenko Y., Lyubchik Y., Lithium Abundances in Wide Binaries with Solar-Type Twin Components, ApJ, 2002, vol. 579, p. 437

Martocchia S., Bastian N., Usher C., Kozhurina-Platais V., Niederhofer F., Cabrera-Ziri I., Dalessandro E., Hollyhead K., Kacharov N., Lardo C., Larsen S., Mucciarelli A., Platais I., Salaris M., Cordero M., Geisler D., Hilker M., Li C., Mackey D., The search for multiple populations in Magellanic Cloud Clusters - III. No evidence for multiple populations in the SMC cluster NGC 419, MNRAS, 2017, vol. 468, p. 3150

Martocchia S., Cabrera-Ziri I., Lardo C., Dalessand ro E., Bastian N., Kozhurina-Platais V., Usher C., Niederhofer F., Cordero M., Geisler D., Hollyhead K., Kacharov N., Larsen

S., Li C., Mackey D., Hilker M., Mucciarelli A., Platais I., Salaris M., Age as a major factor in the onset of multiple populations in stellar clusters, MNRAS, 2018, vol. 473, p. 2688

Massari D., Koppelman H. H., Helmi A., Origin of the system of globular clusters in the Milky Way, A&A, 2019, vol. 630, p. L4

Masseron T., Gilmore G., Carbon, nitrogen and α-element abundances determine the formation sequence of the Galactic thick and thin discs, MNRAS, 2015, vol. 453, p. 1855

McLaughlin D. E., van der Marel R. P., Resolved Massive Star Clusters in the Milky Way and Its Satellites: Brightness Profiles and a Catalog of Fundamental Parameters, ApJS, 2005, vol. 161, p. 304

McMillan P. J., The mass distribution and gravitational potential of the Milky Way, MNRAS, 2017, vol. 465, p. 76

Meléndez J., Barbuy B., Both accurate and precise gf-values for Fe II lines, A&A, 2009, vol. 497, p. 611

Meszaros S., Masseron T., García-Hernández D. A., Allende Prieto C., Beers T. C., Bizyaev D., Chojnowski D., Cohen R. E., Cunha K., Dell'Agli F., Ebelke G., Fernández-Trincado J. G., Frinchaboy P., Geisler D., Hasselquist S., Hearty F., Holtzman J., Johnson J., Lane R. R., Lacerna I., Longa-Peña P., Majewski S. R., Martell S. L., Minniti D., Nataf D., Nidever D. L., Pan K., Schiavon R. P., Shetrone M., Smith V. V., Sobeck J. S., Stringfellow G. S., Szigeti L., Tang B., Wilson J. C., Zamora O., Homogeneous analysis of globular clusters from the APOGEE survey with the BACCHUS code - II. The Southern clusters and overview, MNRAS, 2020, vol. 492, p. 1641

Miglio A., Girardi L., Grundahl F., Mosser B., Bastian N., Bragaglia A., Brogaard K., Buldgen G., Chantereau W., Chaplin W., Chiappini C., Dupret M.-A., Eggenberger P., Gieles M., Izzard R., Kawata D., Karoff C., Lagarde N., Mackereth T., Magrin D., Meynet G., Michel E., Montalbán J., Nascimbeni V., Noels A., Piotto G., Ragazzoni R., Soszyński I., Tolstoy E., Toonen S., Triaud A., Vincenzo F., Haydn, Experimental Astronomy, 2021, vol. 51, p. 963

Milone A. P., Bedin L. R., Piotto G., Anderson J., Multiple stellar populations in Magellanic Cloud clusters. I. An ordinary feature for intermediate age globulars in the LMC?, A&A, 2009, vol. 497, p. 755

Milone A. P., Cordoni G., Marino A. F., D'Antona F., Bellini A., Di Criscienzo M., Dondoglio E., Lagioia E. P., Langer N., Legnardi M. V., Libralato M., Baumgardt H., Bettinelli M., Cavecchi Y., de Grijs R., Deng L., Hastings B., Li C., Mohandasan A., Renzini A., Vesperini E., Wang C., Ziliotto T., Carlos M., Costa G., Dell'Agli F., Di Stefano S., Jang S., Martorano M., Simioni M., Tailo M., Ventura P., Hubble Space Telescope survey of Magellanic Cloud star clusters. Photometry and astrometry of 113 clusters and early results, A&A, 2023, vol. 672, p. A161

Milone A. P., Marino A. F., Multiple Populations in Star Clusters, Universe, 2022, vol. 8, p. 359

Milone A. P., Marino A. F., Bedin L. R., Anderson J., Apai D., Bellini A., Dieball A., Salaris M., Libralato M., Nardiello D., Bergeron P., Burgasser A. J., Rees J. M., Rich R. M., Richer H. B., The HST Large Programme on NGC 6752 - II. Multiple populations at the bottom of the main sequence probed in NIR, MNRAS, 2019, vol. 484, p. 4046

Milone A. P., Marino A. F., Bedin L. R., Dotter A., Jerjen H., Kim D., Nardiello D., Piotto G., Cong J., The binary populations of eight globular clusters in the outer halo of the Milky Way, MNRAS, 2016, vol. 455, p. 3009

Milone A. P., Marino A. F., Di Criscienzo M., D'Antona F., Bedin L. R., Da Costa G., Piotto G., Tailo M., Dotter A., Angeloni R., Anderson J., Jerjen H., Li C., Dupree A., Granata V., Lagioia E. P., Mackey A. D., Nardiello D., Vesperini E., Multiple stellar populations in Magellanic Cloud clusters - VI. A survey of multiple sequences and Be stars in young clusters, MNRAS, 2018, vol. 477, p. 2640

Milone A. P., Marino A. F., Piotto G., Bedin L. R., Anderson J., Aparicio A., Bellini A., Cassisi S., D'Antona F., Grundahl F., Monelli M., Yong D., A WFC3/HST View of the Three Stellar Populations in the Globular Cluster NGC 6752, ApJ, 2013, vol. 767, p. 120

Milone A. P., Piotto G., Bedin L. R., Aparicio A., Anderson J., Sarajedini A., Marino A. F., Moretti A., Davies M. B., Chaboyer B., Dotter A., Hempel M., Marín-Franch A., Majewski S., Paust N. E. Q., Reid I. N., Rosenberg A., Siegel M., The ACS survey of Galactic globular clusters. XII. Photometric binaries along the main sequence, A&A, 2012, vol. 540, p. A16

Milone A. P., Piotto G., Renzini A., Marino A. F., Bedin L. R., Vesperini E., D'Antona F., Nardiello D., Anderson J., King I. R., Yong D., Bellini A., Aparicio A., Barbuy B., Brown T. M., Cassisi S., Ortolani S., Salaris M., Sarajedini A., van der Marel R. P., The Hubble Space Telescope UV Legacy Survey of Galactic globular clusters - IX. The Atlas of multiple stellar populations, MNRAS, 2017, vol. 464, p. 3636

Minelli A., Mucciarelli A., Massari D., Bellazzini M., Romano D., Ferraro F. R., A New Set of Chisels for Galactic Archeology: Sc, V, and Zn as Taggers of Accreted Globular Clusters, ApJ, 2021, vol. 918, p. L32

Minniti D., Geisler D., Alonso-García J., Palma T., Beamín J. C., Borissova J., Catelan M., Clariá J. J., Cohen R. E., Contreras Ramos R., Dias B., Fernández-Trincado J. G., Gómez M., Hempel M., Ivanov V. D., Kurtev R., Lucas P. W., Moni-Bidin C., Pullen J., Ramírez Alegría S., Saito R. K., Valenti E., New VVV Survey Globular Cluster Candidates in the Milky Way Bulge, ApJ, 2017, vol. 849, p. L24

Minniti D., Hempel M., Toledo I., Ivanov V. D., Alonso-García J., Saito R. K., Catelan M., Geisler D., Jordán A., Borissova J., Zoccali M., Kurtev R., Carraro G., Barbuy B., Clariá J., Rejkuba M., Emerson J., Moni Bidin C., Discovery of VVV CL001. A low-mass globular cluster next to UKS 1 in the direction of the Galactic bulge, A&A, 2011, vol. 527, p. A81

Miyamoto M., Nagai R., Three-dimensional models for the distribution of mass in galaxies., PASJ, 1975, vol. 27, p. 533

Modigliani A., Mulas G., Porceddu I., Wolff B., Damiani F., Banse B. K., The FLAMES-UVES Pipeline, The Messenger, 2004, vol. 118, p. 8

Montalbán J., Mackereth J. T., Miglio A., Vincenzo F., Chiappini C., Buldgen G., Mosser B., Noels A., Scuflaire R., Vrard M., Willett E., Davies G. R., Hall O. J., Nielsen

M. B., Khan S., Rendle B. M., van Rossem W. E., Ferguson J. W., Chaplin W. J., Chronologically dating the early assembly of the Milky Way, Nature Astronomy, 2021, vol. 5, p. 640

Monty S., Puzia T. H., Miller B. W., Carrasco E. R., Simunovic M., Schirmer M., Stetson P. B., Cassisi S., Venn K. A., Dotter A., Goudfrooij P., Perina S., Pessev P., Sarajedini A., Taylor M. A., The GeMS/GSAOI Galactic Globular Cluster Survey (G4CS). I. A Pilot Study of the Stellar Populations in NGC 2298 and NGC 3201, ApJ, 2018, vol. 865, p. 160

Moreno E., Fernández-Trincado J. G., Pérez-Villegas A., Chaves-Velasquez L., Schuster W. J., Orbits of globular clusters computed with dynamical friction in the Galactic anisotropic velocity dispersion field, MNRAS, 2022, vol. 510, p. 5945

Moreno-Hilario E., Martinez-Medina L. A., Li H., Souza S. O., Pérez-Villegas A., The influence of globular cluster evolution on the specific frequency in dwarf galaxies, MNRAS, 2024, vol. 527, p. 2765

Muraveva T., Delgado H. E., Clementini G., Sarro L. M., Garofalo A., RR Lyrae stars as standard candles in the Gaia Data Release 2 Era, MNRAS, 2018, vol. 481, p. 1195

Nardiello D., Libralato M., Piotto G., Anderson J., Bellini A., Aparicio A., Bedin L. R., Cassisi S., Granata V., King I. R., Lucertini F., Marino A. F., Milone A. P., Ortolani S., Platais I., van der Marel R. P., The Hubble Space Telescope UV Legacy Survey of Galactic Globular Clusters - XVII. Public Catalogue Release, MNRAS, 2018, vol. 481, p. 3382

Nardiello D., Milone A. P., Piotto G., Marino A. F., Bellini A., Cassisi S., Observing multiple stellar populations with VLT/FORS2. Main sequence photometry in outer regions of NGC 6752, NGC 6397, and NGC 6121 (M 4), A&A, 2015, vol. 573, p. A70

Nardiello D., Piotto G., Milone A. P., Marino A. F., Bedin L. R., Anderson J., Aparicio A., Bellini A., Cassisi S., D'Antona F., Hidalgo S., Ortolani S., Pietrinferni A., Renzini A., Salaris M., Marel R. P. v. d., Vesperini E., The Hubble Space Telescope UV Legacy Survey of Galactic Globular Clusters - IV. Helium content and relative age of multiple stellar populations within NGC 6352, MNRAS, 2015, vol. 451, p. 312

Nataf D. M., Gonzalez O. A., Casagrande L., Zasowski G., Wegg C., Wolf C., Kunder A., Alonso-Garcia J., Minniti D., Rejkuba M., Saito R. K., Valenti E., Zoccali M., Poleski R., Pietrzyński G., Skowron J., Soszyński I., Szymański M. K., Udalski A., Ulaczyk K., Wyrzykowski Ł., Interstellar extinction curve variations towards the inner Milky Way: a challenge to observational cosmology, MNRAS, 2016, vol. 456, p. 2692

Navarro J. F., Frenk C. S., White S. D. M., A Universal Density Profile from Hierarchical Clustering, ApJ, 1997, vol. 490, p. 493

Nepal S., Chiappini C., Guiglion G., Steinmetz M., Pérez-Villegas A., Queiroz A. B., Miglio A., Dohme P., Khalatyan A., Insights from super-metal-rich stars: Is the Milky Way bar young?, A&A, 2024, vol. 681, p. L8

Ness M., Freeman K., Athanassoula E., Wylie-de-Boer E., Bland-Hawthorn J., Asplund M., Lewis G. F., Yong D., Lane R. R., Kiss L. L., ARGOS - III. Stellar populations in the Galactic bulge of the Milky Way, MNRAS, 2013, vol. 430, p. 836

Ness M., Lang D., The X-shaped Bulge of the Milky Way Revealed by WISE, AJ, 2016, vol. 152, p. 14

Neumayer N., Seth A., Böker T., Nuclear star clusters, A&A Rev., 2020, vol. 28, p. 4

Nguyen C. T., Costa G., Girardi L., Volpato G., Bressan A., Chen Y., Marigo P., Fu X., Goudfrooij P., PARSEC V2.0: Stellar tracks and isochrones of low- and intermediate-mass stars with rotation, A&A, 2022, vol. 665, p. A126

Niederhofer F., Georgy C., Bastian N., Ekström S., Apparent age spreads in clusters and the role of stellar rotation, MNRAS, 2015, vol. 453, p. 2070

Nogueras-Lara F., Kinematic data rebuild the nuclear star cluster as the most metal-rich region of the Galaxy, A&A, 2022, vol. 666, p. A72

Nogueras-Lara F., Schultheis M., Najarro F., Sormani M. C., Gadotti D. A., Rich R. M., Evidence of an age gradient along the line of sight in the nuclear stellar disc of the Milky Way, A&A, 2023, vol. 671, p. L10

Nomoto K., Kobayashi C., Tominaga N., Nucleosynthesis in Stars and the Chemical Enrichment of Galaxies, ARA&A, 2013, vol. 51, p. 457

Oliveira R. A. P., Maia F. F. S., Barbuy B., Dias B., Santos J. F. C., Souza S. O., Kerber L. O., Bica E., Sanmartim D., Quint B., Fraga L., Armond T., Minniti D., Parisi M. C., Katime Santrich O. J., Angelo M. S., Pérez-Villegas A., De Bórtoli B. J., The VISCACHA survey - VII. Assembly history of the Magellanic Bridge and SMC Wing from star clusters, MNRAS, 2023, vol. 524, p. 2244

Oliveira R. A. P., Ortolani S., Barbuy B., Kerber L. O., Maia F. F. S., Bica E., Cassisi S., Souza S. O., Pérez-Villegas A., Precise distances from OGLE-IV member RR Lyrae stars in six bulge globular clusters, A&A, 2022, vol. 657, p. A123

Oliveira R. A. P., Souza S. O., Kerber L. O., Barbuy B., Ortolani S., Piotto G., Nardiello D., Pérez-Villegas A., Maia F. F. S., Bica E., Cassisi S., D'Antona F., Lagioia E. P., Libralato M., Milone A. P., Anderson J., Aparicio A., Bedin L. R., Brown T. M., King I. R., Marino A. F., Pietrinferni A., Renzini A., Sarajedini A., van der Marel R., Vesperini E., The Hubble Space Telescope UV Legacy Survey of Galactic Globular Clusters. XX. Ages of Single and Multiple Stellar Populations in Seven Bulge Globular Clusters, ApJ, 2020, vol. 891, p. 37

Origlia L., Massari D., Rich R. M., Mucciarelli A., Ferraro F. R., Dalessandro E., Lanzoni B., The Terzan 5 Puzzle: Discovery of a Third, Metal-poor Component, ApJ, 2013, vol. 779, p. L5

Origlia L., Rich R. M., Ferraro F. R., Lanzoni B., Bellazzini M., Dalessandro E., Mucciarelli A., Valenti E., Beccari G., Spectroscopy Unveils the Complex Nature of Terzan 5, ApJ, 2011, vol. 726, p. L20

Ortolani S., Bica E., Barbuy B., Two reddened globular clusters projected close to the galactic center: Palomar 6 and Djorgovski 1., A&A, 1995, vol. 296, p. 680

Ortolani S., Bica E., Barbuy B., B, V and I photometry of the intermediate metallicity bulge globular clusters NGC 6325 and NGC 6355, A&A, 2003, vol. 402, p. 565

Ortolani S., Bica E., Barbuy B., AL 3 (BH 261): A New Globular Cluster in the Galaxy, ApJ, 2006, vol. 646, p. L115

Ortolani S., Cassisi S., Salaris M., Interstellar Reddening Effect on the Age Dating of Population II Stars, Galaxies, 2017, vol. 5, p. 28

Ortolani S., Held E. V., Nardiello D., Souza S. O., Barbuy B., Pérez-Villegas A., Cassisi S., Bica E., Momany Y., Saviane I., Another relic bulge globular cluster: ESO 456-SC38 (Djorgovski 2), A&A, 2019, vol. 627, p. A145

Ortolani S., Nardiello D., Pérez-Villegas A., Bica E., Barbuy B., Halo intruders in the Galactic bulge revealed by HST and Gaia: the globular clusters Terzan 10 and Djorgovski 1, A&A, 2019, vol. 622, p. A94

Osborn W., Two new CN-strong globular cluster stars, The Observatory, 1971, vol. 91, p. 223

Pallanca C., Lanzoni B., Ferraro F. R., Casagrande L., Saracino S., Purohith Bhaskar Bhat B., Leanza S., Dalessandro E., Vesperini E., A New Identity Card for the Bulge Globular Cluster NGC 6440 from Resolved Star Counts, ApJ, 2021, vol. 913, p. 137

Pancino E., Pasquini L., Hill V., Ferraro F. R., Bellazzini M., High-Resolution Spectroscopy of Metal-rich Giants in ω Centauri: First Indication of Type Ia Supernova Enrichment, ApJ, 2002, vol. 568, p. L101

Parisi M. C., Geisler D., Carraro G., Clariá J. J., Costa E., Grocholski A. J., Sarajedini A., Leiton R., Piatti A. E., Age Determination of 15 Old to Intermediate-age Small Magellanic Cloud Star Clusters, AJ, 2014, vol. 147, p. 71

Parisi M. C., Geisler D., Clariá J. J., Villanova S., Marcionni N., Sarajedini A., Grocholski A. J., Ca II Triplet Spectroscopy of Small Magellanic Cloud Red Giants. III. Abundances and Velocities for a Sample of 14 Clusters, AJ, 2015, vol. 149, p. 154

Parisi M. C., Gramajo L. V., Geisler D., Dias B., Clariá J. J., Da Costa G., Grebel E. K., Ca II triplet spectroscopy of Small Magellanic Cloud red giants. V. Abundances and velocities for 12 massive clusters, A&A, 2022, vol. 662, p. A75

Parisi M. C., Grocholski A. J., Geisler D., Sarajedini A., Clariá J. J., Ca II Triplet Spectroscopy of Small Magellanic Cloud Red Giants. I. Abundances and Velocities for a Sample of Clusters, AJ, 2009, vol. 138, p. 517

Parisi M. C., Oliveira R. A. P., Angelo M. S., Dias B., Maia F. F. S., Saroon S., Feinstein C., Santos J. F. C., Bica E., Ferreira B. P. L., Fernández-Trincado J. G., Westera P.,

Minniti D., Garro E. R., Santrich O. J. K., De Bortoli B. J., Souza S. O., Kerber L., Pérez-Villegas A., The VISCACHA survey - IX. The SMC Southern Bridge in 8D, MNRAS, 2024, vol. 527, p. 10632

Pedregosa F., Varoquaux G., Gramfort A., Michel V., Thirion B., Grisel O., Blondel M., Prettenhofer P., Weiss R., Dubourg V., Vanderplas J., Passos A., Cournapeau D., Brucher M., Perrot M., Duchesnay E., Scikit-learn: Machine Learning in Python, Journal of Machine Learning Research, 2011, vol. 12, p. 2825

Peebles P. J. E., A Model for Continuous Clustering in the Large-Scale Distribution of Matter, Ap&SS, 1974, vol. 31, p. 403

Pérez-Villegas A., Barbuy B., Kerber L. O., Ortolani S., Souza S. O., Bica E., Globular clusters in the inner Galaxy classified from dynamical orbital criteria, MNRAS, 2020, vol. 491, p. 3251

Pérez-Villegas A., Portail M., Gerhard O., The stellar halo in the inner Milky Way: predicted shape and kinematics, MNRAS, 2017, vol. 464, p. L80

Pérez-Villegas A., Rossi L., Ortolani S., Casotto S., Barbuy B., Bica E., Orbits of Selected Globular Clusters in the Galactic Bulge, PASA, 2018, vol. 35, p. e021

Perren G. I., Piatti A. E., Vázquez R. A., Astrophysical properties of star clusters in the Magellanic Clouds homogeneously estimated by ASteCA, A&A, 2017, vol. 602, p. A89

Pfeffer J., Kruijssen J. M. D., Crain R. A., Bastian N., The E-MOSAICS project: simulating the formation and co-evolution of galaxies and their star cluster populations, MNRAS, 2018, vol. 475, p. 4309

Pfeffer J., Lardo C., Bastian N., Saracino S., Kamann S., The accreted nuclear clusters of the Milky Way, MNRAS, 2021, vol. 500, p. 2514

Piatti A. E., Revisiting a detached stellar structure in the outer north-eastern region of the Small Magellanic Cloud, MNRAS, 2022, vol. 509, p. 3462

Piatti A. E., Santos J. F. C., Clariá J. J., Bica E., Sarajedini A., Geisler D., Ages and metallicities of five intermediate-age star clusters projected towards the Small Magellanic Cloud, MNRAS, 2001, vol. 325, p. 792

Pietrinferni A., Cassisi S., Salaris M., Castelli F., A Large Stellar Evolution Database for Population Synthesis Studies. II. Stellar Models and Isochrones for an α-enhanced Metal Distribution, ApJ, 2006, vol. 642, p. 797

Pillepich A., Madau P., Mayer L., Building Late-type Spiral Galaxies by In-situ and Ex-situ Star Formation, ApJ, 2015, vol. 799, p. 184

Piotto G., Milone A. P., Bedin L. R., Anderson J., King I. R., Marino A. F., Nardiello D., Aparicio A., Barbuy B., Bellini A., Brown T. M., Cassisi S., Cool A. M., Cunial A., Dalessandro E., D'Antona F., Ferraro F. R., Hidalgo S., Lanzoni B., Monelli M., Ortolani S., Renzini A., Salaris M., Sarajedini A., van der Marel R. P., Vesperini E., Zoccali M., The Hubble Space Telescope UV Legacy Survey of Galactic Globular Clusters. I. Overview of the Project and Detection of Multiple Stellar Populations, AJ, 2015, vol. 149, p. 91

Piskunov N. E., Kupka F., Ryabchikova T. A., Weiss W. W., Jeffery C. S., VALD: The Vienna Atomic Line Data Base., A&AS, 1995, vol. 112, p. 525

Planck Collaboration Ade P. A. R., Aghanim N., Arnaud M., Ashdown M., Aumont J., Baccigalupi C., Banday A. J., Barreiro R. B., Bartlett J. G., et al. Planck 2015 results. XIII. Cosmological parameters, A&A, 2016, vol. 594, p. A13

Platais I., Melo C., Quinn S. N., Clem J. L., de Mink S. E., Dotter A., Kozhurina-Platais V., Latham D. W., Bellini A., The Effects of Differential Reddening and Stellar Rotation on the Appearance of Multiple Populations in Star Clusters: The Case of Trumpler 20, ApJ, 2012, vol. 751, p. L8

Plummer H. C., On the problem of distribution in globular star clusters, MNRAS, 1911, vol. 71, p. 460

Pols O., Stellar Structure and Evolution. Astronomical Institute Utrecht, 2011

Portail M., Gerhard O., Wegg C., Ness M., Dynamical modelling of the galactic bulge and bar: the Milky Way's pattern speed, stellar and dark matter mass distribution, MNRAS, 2017, vol. 465, p. 1621

Portail M., Wegg C., Gerhard O., Peanuts, brezels and bananas: food for thought on the orbital structure of the Galactic bulge., MNRAS, 2015, vol. 450, p. L66

Prantzos N., Charbonnel C., On the self-enrichment scenario of galactic globular clusters: constraints on the IMF, A&A, 2006, vol. 458, p. 135

Queiroz A. B. A., Anders F., Chiappini C., Khalatyan A., Santiago B. X., Nepal S., Steinmetz M., Gallart C., Valentini M., Dal Ponte M., Barbuy B., Pérez-Villegas A., Masseron T., Fernández-Trincado J. G., Khoperskov S., Minchev I., Fernández-Alvar E., Lane R. R., Nitschelm C., StarHorse results for spectroscopic surveys and Gaia DR3: Chrono-chemical populations in the solar vicinity, the genuine thick disk, and young alpha-rich stars, A&A, 2023, vol. 673, p. A155

Queiroz A. B. A., Anders F., Chiappini C., Khalatyan A., Santiago B. X., Steinmetz M., Valentini M., Miglio A., Bossini D., Barbuy B., Minchev I., Minniti D., García Hernández D. A., Schultheis M., Beaton R. L., Beers T. C., Bizyaev D., Brownstein J. R., Cunha K., Fernández-Trincado J. G., Frinchaboy P. M., Lane R. R., Majewski S. R., Nataf D., Nitschelm C., Pan K., Roman-Lopes A., Sobeck J. S., Stringfellow G., Zamora O., From the bulge to the outer disc: StarHorse stellar parameters, distances, and extinctions for stars in APOGEE DR16 and other spectroscopic surveys, A&A, 2020, vol. 638, p. A76

Queiroz A. B. A., Chiappini C., Perez-Villegas A., Khalatyan A., Anders F., Barbuy B., Santiago B. X., Steinmetz M., Cunha K., Schultheis M., Majewski S. R., Minchev I., Minniti D., Beaton R. L., Cohen R. E., da Costa L. N., Fernández-Trincado J. G., Garcia-Hernández D. A., Geisler D., Hasselquist S., Lane R. R., Nitschelm C., Rojas-Arriagada A., Roman-Lopes A., Smith V., Zasowski G., The Milky Way bar and bulge revealed by APOGEE and Gaia EDR3, A&A, 2021, vol. 656, p. A156

Ramírez-Siordia V. H., Bruzual G., Cervantes Sodi B., Bitsakis T., Parameter estimation for scarce stellar populations, MNRAS, 2019, vol. 486, p. 5567

Razera R., Barbuy B., Moura T. C., Ernandes H., Pérez-Villegas A., Souza S. O., Chiappini C., Queiroz A. B. A., Anders F., Fernández-Trincado J. G., Friaça A. C. S., Cunha K., Smith V. V., Santiago B. X., Schiavon R. P., Valentini M., Minniti D., Schultheis M., Geisler D., Sobeck J., Placco V. M., Zoccali M., Abundance analysis of APOGEE spectra for 58 metal-poor stars from the bulge spheroid, MNRAS, 2022, vol. 517, p. 4590

Recio-Blanco A., Piotto G., de Angeli F., Cassisi S., Riello M., Salaris M., Pietrinferni A., Zoccali M., Aparicio A., A homogeneous set of globular cluster relative distances and reddenings, A&A, 2005, vol. 432, p. 851

Renzini A., On the many uses of globular cluster luminosity functions, Mem. Soc. Astron. Italiana, 1986, vol. 57, p. 357

Renzini A., Rethinking globular clusters formation, Mem. Soc. Astron. Italiana, 2013, vol. 84, p. 162

Renzini A., D'Antona F., Cassisi S., King I. R., Milone A. P., Ventura P., Anderson J., Bedin L. R., Bellini A., Brown T. M., Piotto G., van der Marel R. P., Barbuy B., Dalessandro E., Hidalgo S., Marino A. F., Ortolani S., Salaris M., Sarajedini A., The Hubble Space TelescopeUV Legacy Survey of Galactic Globular Clusters - V. Constraints on formation scenarios, MNRAS, 2015, vol. 454, p. 4197

Rich R. M., Shara M., Fall S. M., Zurek D., Two Groups of Nearly Coeval Star Clusters in the Small Magellanic Cloud, AJ, 2000, vol. 119, p. 197

Richer H. B., Heyl J., Anderson J., Kalirai J. S., Shara M. M., Dotter A., Fahlman G. G., Rich R. M., A Dynamical Signature of Multiple Stellar Populations in 47 Tucanae, ApJ, 2013, vol. 771, p. L15

Riello M., De Angeli F., Evans D. W., Montegriffo P., Carrasco J. M., Busso G., Palaversa L., Burgess P. W., Diener C., Davidson M., Rowell N., Fabricius C., Jordi C., Bellazzini M., Pancino e. a., Gaia Early Data Release 3. Photometric content and validation, A&A, 2021, vol. 649, p. A3

Rivinius T., Carciofi A. C., Martayan C., Classical Be stars. Rapidly rotating B stars with viscous Keplerian decretion disks, A&A Rev., 2013, vol. 21, p. 69

Romano D., Ferraro F. R., Origlia L., Portegies Zwart S., Lanzoni B., Crociati C., Massari D., Dalessandro E., Mucciarelli A., Rich R. M., Calura F., Matteucci F., Modeling the Chemical Enrichment History of the Bulge Fossil Fragment Terzan 5, ApJ, 2023, vol. 951, p. 85

Romero-Colmenares M., Fernández-Trincado J. G., Geisler D., Souza S. O., Villanova S., Longa-Peña P., Minniti D., Beers T. C., Bidin C. M., Perez-Villegas A., Moreno E., Garro E. R., Baeza I., Henao L., Barbuy B., Alonso-García J., Cohen R. E., Lane R. R., Muñoz C., CAPOS: The bulge Cluster APOgee Survey. II. The intriguing "Sequoia" globular cluster FSR 1758, A&A, 2021, vol. 652, p. A158

Rosenberg A., Saviane I., Piotto G., Aparicio A., Galactic Globular Cluster Relative Ages, AJ, 1999, vol. 118, p. 2306

Rossi L. J., NIGO: A Numerical Integrator of Galactic Orbits, Astronomy and Computing, 2015, vol. 12, p. 11

Ryabchikova T., Piskunov N., Kurucz R. L., Stempels H. C., Heiter U., Pakhomov Y., Barklem P. S., A major upgrade of the VALD database, Physica Scripta, 2015, vol. 90, p. 054005

Saito R. K., Hempel M., Minniti D., Lucas P. W., Rejkuba M., Toledo I., Gonzalez O. A., Alonso-García J., Irwin M. J., Gonzalez-Solares E., Hodgkin S. T., Lewis J. R., Cross N., Ivanov V. D., Kerins E., Emerson J. P., Soto e. a., VVV DR1: The first data release of the Milky Way bulge and southern plane from the near-infrared ESO public survey VISTA variables in the Vía Láctea, A&A, 2012, vol. 537, p. A107

Salaris M., Pietrinferni A., Piersimoni A. M., Cassisi S., Post first dredge-up [C/N] ratio as age indicator. Theoretical calibration, A&A, 2015, vol. 583, p. A87

Salaris M., Weiss A., Cassarà L. P., Piovan L., Chiosi C., Detailed AGB evolutionary models and near-infrared colours of intermediate-age stellar populations: tests on star clusters, A&A, 2014, vol. 565, p. A9

Salinas R., Pajkos M. A., Strader J., Vivas A. K., Contreras Ramos R., The Overlooked Role of Stellar Variability in the Extended Main Sequence of LMC Intermediate-age Clusters, ApJ, 2016, vol. 832, p. L14

Sandage A., Wildey R., The Anomalous Color-Magnitude Diagram of the Remote Globular Cluster NGC 7006, ApJ, 1967, vol. 150, p. 469

Schaye J., Crain R. A., Bower R. G., Furlong M., Schaller M., Theuns T., Dalla Vecchia C., Frenk C. S., McCarthy I. G., Helly J. C., Jenkins A., Rosas-Guevara Y. M., White S. D. M., Baes M., Booth C. M., Camps P., Navarro J. F., Qu Y., Rahmati A., Sawala T., Thomas P. A., Trayford J., The EAGLE project: simulating the evolution and assembly of galaxies and their environments, MNRAS, 2015, vol. 446, p. 521

Schiavon R. P., Zamora O., Carrera R., Lucatello S., Robin A. C., Ness M., Martell S. L., Smith V. V., García-Hernández D. A., Manchado A., Schönrich R., Bastian N., Chiappini C. e. a., Chemical tagging with APOGEE: discovery of a large population of N-rich stars in the inner Galaxy, MNRAS, 2017, vol. 465, p. 501

Schönrich R., Binney J., Dehnen W., Local kinematics and the local standard of rest, MNRAS, 2010, vol. 403, p. 1829

Shapley H., Shapley M. B., Studies based on the colors and magnitudes in stellar clusters. XIV. Further remarks on the structure of the galactic system., ApJ, 1919, vol. 50, p. 107

Simmerer J., Sneden C., Cowan J. J., Collier J., Woolf V. M., Lawler J. E., The Rise of the s-Process in the Galaxy, ApJ, 2004, vol. 617, p. 1091

Siqueira-Mello C., Chiappini C., Barbuy B., Freeman K., Ness M., Depagne E., Cantelli E., Pignatari M., Hirschi R., Frischknecht U., Meynet G., Maeder A., Looking for imprints of the first stellar generations in metal-poor bulge field stars, A&A, 2016, vol. 593, p. A79

Skrutskie M. F., Cutri R. M., Stiening R., Weinberg M. D., Schneider S., Carpenter J. M., Beichman C., Capps R., Chester T., Elias J., Huchra J., Liebert J., Lonsdale C., Monet D. G., Price S., Seitzer P., Jarrett T., Kirkpatrick J. D., Gizis J. E., Howard E., Evans T., Fowler J., Fullmer L., Hurt R., Light R., Kopan E. L., Marsh K. A., McCallon H. L., Tam R., Van Dyk S., Wheelock S., The Two Micron All Sky Survey (2MASS), AJ, 2006, vol. 131, p. 1163

Smith R., Flynn C., Candlish G. N., Fellhauer M., Gibson B. K., Simple and accurate modelling of the gravitational potential produced by thick and thin exponential discs, MNRAS, 2015, vol. 448, p. 2934

Sneden C., Cowan J. J., Gallino R., Neutron-capture elements in the early galaxy., ARA&A, 2008, vol. 46, p. 241

Sormani M. C., Sanders J. L., Fritz T. K., Smith L. C., Gerhard O., Schödel R., Magorrian J., Neumayer N., Nogueras-Lara F., Feldmeier-Krause A., Mastrobuono-Battisti A., Schultheis M., Shahzamanian B., Vasiliev E., Klessen R. S., Lucas P., Minniti D., Self-consistent modelling of the Milky Way's nuclear stellar disc, MNRAS, 2022, vol. 512, p. 1857

Soszyński I., Udalski A., Wrona M., Szymański M. K., Pietrukowicz P., Skowron J., Skowron D., Poleski R., Kozłowski S., Mróz P., Ulaczyk K., Rybicki K., Iwanek P., Gromadzki M., Over 78 000 RR Lyrae Stars in the Galactic Bulge and Disk from the OGLE Survey, Acta Astron., 2019, vol. 69, p. 321

Soto M., Barbá R., Gunthardt G., Minniti D., Lucas P., Majaess D., Irwin M., Emerson J. P., Gonzalez-Solares E., Hempel M., Saito R. K., Gurovich S., Roman-Lopes A., Moni-Bidin C., Santucho M. V., Borissova J., Kurtev R., Toledo I., Geisler D., Dominguez M., Beamin J. C., Milky Way demographics with the VVV survey. II. Color transformations and near-infrared photometry for 136 million stars in the southern Galactic disk, A&A, 2013, vol. 552, p. A101

Souza S. O., Ernandes H., Valentini M., Barbuy B., Chiappini C., Pérez-Villegas A., Ortolani S., Friaça A. C. S., Queiroz A. B. A., Bica E., Chrono-chemodynamical analysis of the globular cluster NGC 6355: Looking for the fundamental bricks of the Bulge, A&A, 2023, vol. 671, p. A45

Souza S. O., Kerber L. O., Barbuy B., Pérez-Villegas A., Oliveira R. A. P., Nardiello D., Self-consistent Analysis of Stellar Clusters: An Application to HST Data of the Halo Globular Cluster NGC 6752, ApJ, 2020, vol. 890, p. 38

Souza S. O., Valentini M., Barbuy B., Pérez-Villegas A., Chiappini C., Ortolani S., Nardiello D., Dias B., Anders F., Bica E., Photo-chemo-dynamical analysis and the origin of the bulge globular cluster Palomar 6, A&A, 2021, vol. 656, p. A78

Spite M., Nouvelle détermination des paramètres physiques et chimiques de l'atmosphère de l'étoile γ Serpentis, Annales d'Astrophysique, 1967, vol. 30, p. 685

Spitoni E., Recio-Blanco A., de Laverny P., Palicio P. A., Kordopatis G., Schultheis M., Contursi G., Poggio E., Romano D., Matteucci F., Beyond the two-infall model. I. Indications for a recent gas infall with Gaia DR3 chemical abundances, A&A, 2023, vol. 670, p. A109

Spoo T., Tayar J., Frinchaboy P. M., Cunha K., Myers N., Donor J., Majewski S. R., Bizyaev D., García-Hernández D. A., Jönsson H., Lane R. R., Pan K., Longa-Peña P., Roman-Lopes A., The Open Cluster Chemical Abundances and Mapping Survey. VII. APOGEE DR17 [C/N]-Age Calibration, AJ, 2022, vol. 163, p. 229

Springel V., Frenk C. S., White S. D. M., The large-scale structure of the Universe, Nature, 2006, vol. 440, p. 1137

Stassun K. G., Oelkers R. J., Pepper J., Paegert M., De Lee N., Torres G., Latham D. W., Charpinet S., Dressing C. D., Huber D., Kane S. R., Lépine S., Mann A., Muirhead P. S., Rojas-Ayala B., Silvotti R., Fleming S. W., Levine A., Plavchan P., The TESS Input Catalog and Candidate Target List, AJ, 2018, vol. 156, p. 102

Stetson P. B., Pancino E., DAOSPEC: An Automatic Code for Measuring Equivalent Widths in High-Resolution Stellar Spectra, PASP, 2008, vol. 120, p. 1332

Sun W., de Grijs R., Deng L., Albrow M. D., Stellar Rotation and the Extended Main-sequence Turnoff in the Open Cluster NGC 5822, ApJ, 2019, vol. 876, p. 113

Tailo M., Di Criscienzo M., D'Antona F., Caloi V., Ventura P., The mosaic multiple stellar populations in ω Centauri: the horizontal branch and the main sequence, MNRAS, 2016, vol. 457, p. 4525

Tokovinin A., Cantarutti R., Tighe R., Schurter P., Martinez M., Thomas S., van der Bliek N., SOAR Adaptive Module (SAM): Seeing Improvement with a UV Laser, PASP, 2016, vol. 128, p. 125003

Tremmel M., Fragos T., Lehmer B. D., Tzanavaris P., Belczynski K., Kalogera V., Basu-Zych A. R., Farr W. M., Hornschemeier A., Jenkins L., Ptak A., Zezas A., Modeling the Redshift Evolution of the Normal Galaxy X-Ray Luminosity Function, ApJ, 2013, vol. 766, p. 19

Truran J. W., A new interpretation of the heavy element abundances in metal-deficient stars., A&A, 1981, vol. 97, p. 391

Valenti E., Ferraro F. R., Origlia L., Near-Infrared Properties of 24 Globular Clusters in the Galactic Bulge, AJ, 2007, vol. 133, p. 1287

van den Bergh S., UBV photometry of globular clusters., AJ, 1967, vol. 72, p. 70

Vandenberg D. A., Bolte M., Stetson P. B., Measuring Age Differences among Globular Clusters Having Similar Metallicities: A New Method and First Results, AJ, 1990, vol. 100, p. 445

VandenBerg D. A., Brogaard K., Leaman R., Casagrand e L., The Ages of 55 Globular Clusters as Determined Using an Improved VĤB_TO Method along with Color-Magnitude Diagram Constraints, and Their Implications for Broader Issues, ApJ, 2013, vol. 775, p. 134

Vasiliev E., AGAMA: action-based galaxy modelling architecture, MNRAS, 2019, vol. 482, p. 1525

Vasiliev E., Baumgardt H., Gaia EDR3 view on galactic globular clusters, MNRAS, 2021, vol. 505, p. 5978

Vásquez S., Zoccali M., Hill V., Gonzalez O. A., Saviane I., Rejkuba M., Battaglia G., Calcium triplet metallicity calibration for stars in the Galactic bulge, A&A, 2015, vol. 580, p. A121

Vidotto A. A., Gregory S. G., Jardine M., Donati J. F., Petit P., Morin J., Folsom C. P., Bouvier J., Cameron A. C., Hussain G., Marsden S., Waite I. A., Fares R., Jeffers S., do Nascimento J. D., Stellar magnetism: empirical trends with age and rotation, MNRAS, 2014, vol. 441, p. 2361

Wagner-Kaiser R., Sarajedini A., von Hippel T., Stenning D. C., van Dyk D. A., Jeffery E., Robinson E., Stein N., Anderson J., Jefferys W. H., The ACS survey of Galactic globular clusters - XIV. Bayesian single-population analysis of 69 globular clusters, MNRAS, 2017, vol. 468, p. 1038

Weatherford N. C., Kıroğlu F., Fragione G., Chatterjee S., Kremer K., Rasio F. A., Stellar Escape from Globular Clusters. I. Escape Mechanisms and Properties at Ejection, ApJ, 2023, vol. 946, p. 104

White S. D. M., Rees M. J., Core condensation in heavy halos: a two-stage theory for galaxy formation and clustering., MNRAS, 1978, vol. 183, p. 341

Woosley S. E., Heger A., Weaver T. A., The evolution and explosion of massive stars, Reviews of Modern Physics, 2002, vol. 74, p. 1015

Woosley S. E., Weaver T. A., The Evolution and Explosion of Massive Stars. II. Explosive Hydrodynamics and Nucleosynthesis, ApJS, 1995, vol. 101, p. 181

Wylie S. M., Clarke J. P., Gerhard O. E., The Milky Way's middle-aged inner ring, A&A, 2022, vol. 659, p. A80

Zinn R., West M. J., The globular cluster system of the Galaxy. III. Measurements of radial velocity and metallicity for 60 clusters and a compilation of metallicities for 121 clusters., ApJS, 1984, vol. 55, p. 45

Appendix

Appendix A

Complete publication list

- **The VISCACHA survey - IX. The SMC Southern Bridge in 8D**
  Parisi, M. C., R. A. P. Oliveira, M. S. Angelo, B. Dias, F. F. S. Maia, S. Saroon, C. Feinstein, J. F. C. Santos, E. Bica, B. P. L. Ferreira, J. G. Fernández-Trincado, P. Westera, D. Minniti, E. R. Garro, O. J. K. Santrich, B. J. De Bortoli, **S. O. Souza**, L. Kerber, & A. Pérez-Villegas MNRAS, 527, 10632 (2024)
  https://ui.adsabs.harvard.edu/abs/2024MNRAS.52710632P

- **The influence of globular cluster evolution on the specific frequency in dwarf galaxies**
  Moreno-Hilario, E., L. A. Martinez-Medina, H. Li, **S. O. Souza**, & A. Pérez-Villegas MNRAS, 527, 2765 (2024)
  https://ui.adsabs.harvard.edu/abs/2024MNRAS.527.2765M

- **Light elements Na and Al in 58 bulge spheroid stars from APOGEE**
  Barbuy, B., A. C. S. Friaça, H. Ernandes, T. Moura, T. Masseron, K. Cunha, V. V. Smith, D. Souto, A. Pérez-Villegas, **S. O. Souza**, C. Chiappini, A. B. A. Queiroz, J. G. Fernández-Trincado, P. da Silva, B. X. Santiago, F. Anders, R. P. Schiavon, M. Valentini, D. Minniti, D. Geisler, V. M. Placco, M. Zoccali, M. Schultheis, C. Nitschelm, T. C. Beers, & R. Razera MNRAS, 526, 2365 (2023)
  https://ui.adsabs.harvard.edu/abs/2023MNRAS.526.2365B

- **The VISCACHA survey - VII. Assembly history of the Magellanic Bridge and SMC Wing from star clusters**
  Oliveira, R. A. P., F. F. S. Maia, B. Barbuy, B. Dias, J. F. C. Santos, **S. O. Souza**, L. O. Kerber, E. Bica, D. Sanmartim, B. Quint, L. Fraga, T. Armond, D. Minniti,

M. C. Parisi, O. J. Katime Santrich, M. S. Angelo, A. Pérez-Villegas, & B. J. De Bórtoli MNRAS, 524, 2244 (2023)

https://ui.adsabs.harvard.edu/abs/2023MNRAS.524.2244O

- **Chrono-chemodynamical analysis of the globular cluster NGC 6355: Looking for the fundamental bricks of the Bulge**

  Souza, S. O., H. Ernandes, M. Valentini, B. Barbuy, C. Chiappini, A. Pérez-Villegas, S. Ortolani, A. C. S. Friaça, A. B. A. Queiroz, & E. Bica A&A, 671, A45 (2023)

  https://ui.adsabs.harvard.edu/abs/2023A&A...671A..45S

- **Abundance analysis of APOGEE spectra for 58 metal-poor stars from the bulge spheroid**

  Razera, R., B. Barbuy, T. C. Moura, H. Ernandes, A. Pérez-Villegas, **S. O. Souza**, C. Chiappini, A. B. A. Queiroz, F. Anders, J. G. Fernández-Trincado, A. C. S. Friaça, K. Cunha, V. V. Smith, B. X. Santiago, R. P. Schiavon, M. Valentini, D. Minniti, M. Schultheis, D. Geisler, J. Sobeck, V. M. Placco, & M. Zoccali MNRAS, 517, 4590 (2022)

  https://ui.adsabs.harvard.edu/abs/2022MNRAS.517.4590R

- **The VISCACHA survey - V. Rejuvenating three faint SMC clusters**

  Bica, E., F. F. S. Maia, R. A. P. Oliveira, B. Dias, J. F. C. Santos, J. P. Rocha, L. Kerber, J. F. Gardin, T. Armond, M. C. Parisi, **S. O. Souza**, & B. Barbuy MNRAS, 517, L41 (2022)

  https://ui.adsabs.harvard.edu/abs/2022MNRAS.517L..41B

- **Reconstructing the Disrupted Dwarf Galaxy Gaia-Sausage/Enceladus Using Its Stars and Globular Clusters**

  Limberg, G., **S. O. Souza**, A. Pérez-Villegas, S. Rossi, H. D. Perottoni, & R. M. Santucci ApJ, 935, 109 (2022)

  https://ui.adsabs.harvard.edu/abs/2022ApJ...935..109L

- **The VISCACHA survey - IV. The SMC West Halo in 8D**

  Dias, B., M. C. Parisi, M. Angelo, F. Maia, R. A. P. Oliveira, **S. O. Souza**, L. O. Kerber, J. F. C. Santos, A. Pérez-Villegas, D. Sanmartim, B. Quint, L. Fraga, B.

Barbuy, E. Bica, O. J. K. Santrich, J. A. Hernandez-Jimenez, D. Geisler, D. Minniti, B. J. De Bórtoli, L. P. Bassino, & J. P. Rocha MNRAS, 512, 4334 (2022)
https://ui.adsabs.harvard.edu/abs/2022MNRAS.512.4334D

- **Precise distances from OGLE-IV member RR Lyrae stars in six bulge globular clusters**
  Oliveira, R. A. P., S. Ortolani, B. Barbuy, L. O. Kerber, F. F. S. Maia, E. Bica, S. Cassisi, **S. O. Souza**, & A. Pérez-Villegas A&A, 657, A123 (2022)
  https://ui.adsabs.harvard.edu/abs/2022A&A...657A.123O

- **Photo-chemo-dynamical analysis and the origin of the bulge globular cluster Palomar 6**
  Souza, S. O., M. Valentini, B. Barbuy, A. Pérez-Villegas, C. Chiappini, S. Ortolani, D. Nardiello, B. Dias, F. Anders, & E. Bica A&A, 656, A78 (2021)
  https://ui.adsabs.harvard.edu/abs/2021A&A...656A..78S

- **UVES analysis of red giants in the bulge globular cluster NGC 6522**
  Barbuy, B., E. Cantelli, L. Muniz, **S. O. Souza**, C. Chiappini, R. Hirschi, G. Cescutti, M. Pignatari, S. Ortolani, L. Kerber, F. F. S. Maia, E. Bica, & E. Depagne A&A, 654, A29 (2021)
  https://ui.adsabs.harvard.edu/abs/2021A&A...654A..29B

- **CAPOS: The bulge Cluster APOgee Survey. II. The intriguing "Sequoia"globular cluster FSR 1758**
  Romero-Colmenares, M., J. G. Fernández-Trincado, D. Geisler, **S. O. Souza**, S. Villanova, P. Longa-Peña, D. Minniti, T. C. Beers, C. M. Bidin, A. Perez-Villegas, E. Moreno, E. R. Garro, I. Baeza, L. Henao, B. Barbuy, J. Alonso-García, R. E. Cohen, R. R. Lane, & C. Muñoz A&A, 652, A158 (2021)
  https://ui.adsabs.harvard.edu/abs/2021A&A...652A.158R

- **Abundance Patterns of α and Neutron-capture Elements in the Helmi Stream**
  Limberg, G., R. M. Santucci, S. Rossi, A. B. A. Queiroz, C. Chiappini, **S. O. Souza**, H. D. Perottoni, A. Pérez-Villegas, & F. O. Barbosa ApJL, 913, L28 (2021)
  https://ui.adsabs.harvard.edu/abs/2021ApJ...913L..28L

- **Gemini/Phoenix H-band analysis of the globular cluster AL 3**

  Barbuy, B., H. Ernandes, **S. O. Souza**, R. Razera, T. Moura, J. Meléndez, A. Pérez-Villegas, M. Zoccali, D. Minniti, B. Dias, S. Ortolani, & E. Bica A&A, 648, A16 (2021)

  https://ui.adsabs.harvard.edu/abs/2021A&A...648A..16B

- **APOGEE discovery of a chemically atypical star disrupted from NGC 6723 and captured by the Milky Way bulge**

  Fernández-Trincado, J. G., T. C. Beers, D. Minniti, L. Carigi, V. M. Placco, S.-H. Chun, R. R. Lane, D. Geisler, S. Villanova, **S. O. Souza**, B. Barbuy, A. Pérez-Villegas, C. Chiappini, A. B. A. Queiroz, B. Tang, J. Alonso-García, A. E. Piatti, T. Palma, A. Alves-Brito, C. Moni Bidin, A. Roman-Lopes, R. R. Muñoz, H. P. Singh, R. Kundu, L. Chaves-Velasquez, M. Romero-Colmenares, P. Longa-Peña, M. Soto, & K. Vieira A&A, 647, A64 (2021)

  https://ui.adsabs.harvard.edu/abs/2021A&A...647A..64F

- **The VISCACHA survey. III. Star clusters counterpart of the Magellanic Bridge and Counter-Bridge in 8D**

  Dias, B., M. S. Angelo, R. A. P. Oliveira, F. Maia, M. C. Parisi, B. De Bortoli, **S. O. Souza**, O. J. Katime Santrich, L. P. Bassino, B. Barbuy, E. Bica, D. Geisler, L. Kerber, A. Pérez-Villegas, B. Quint, D. Sanmartim, J. F. C. Santos, & P. Westera A&A, 647, L9 (2021)

  https://ui.adsabs.harvard.edu/abs/2021A&A...647L...9D

- **VVV CL001: Likely the Most Metal-poor Surviving Globular Cluster in the Inner Galaxy**

  Fernández-Trincado, J. G., D. Minniti, **S. O. Souza**, T. C. Beers, D. Geisler, C. Moni Bidin, S. Villanova, S. R. Majewski, B. Barbuy, A. Pérez-Villegas, L. Henao, M. Romero-Colmenares, A. Roman-Lopes, & R. R. Lane ApJL, 908, L42 (2021)

  https://ui.adsabs.harvard.edu/abs/2021ApJ...908L..42F

- **The enigmatic globular cluster UKS 1 obscured by the bulge: H-band discovery of nitrogen-enhanced stars**

  Fernández-Trincado, J. G., D. Minniti, T. C. Beers, S. Villanova, D. Geisler, **S. O.**

Souza, L. C. Smith, V. M. Placco, K. Vieira, A. Pérez-Villegas, B. Barbuy, A. Alves-Brito, C. M. Bidin, J. Alonso-García, B. Tang, & T. Palma A&A, 643, A145 (2020)
https://ui.adsabs.harvard.edu/abs/2020A&A...643A.145F

- **The Hubble Space Telescope UV Legacy Survey of Galactic Globular Clusters. XX. Ages of Single and Multiple Stellar Populations in Seven Bulge Globular Clusters**
  Oliveira, R. A. P., **S. O. Souza**, L. O. Kerber, B. Barbuy, S. Ortolani, G. Piotto, D. Nardiello, A. Pérez-Villegas, F. F. S. Maia, E. Bica, S. Cassisi, F. D'Antona, E. P. Lagioia, M. Libralato, A. P. Milone, J. Anderson, A. Aparicio, L. R. Bedin, T. M. Brown, I. R. King, A. F. Marino, A. Pietrinferni, A. Renzini, A. Sarajedini, R. van der Marel, & E. Vesperini ApJ, 891, 37 (2020)
  https://ui.adsabs.harvard.edu/abs/2020ApJ...891...37O

- **Self-consistent Analysis of Stellar Clusters: An Application to HST Data of the Halo Globular Cluster NGC 6752**
  Souza, S. O., L. O. Kerber, B. Barbuy, A. Pérez-Villegas, R. A. P. Oliveira, & D. Nardiello ApJ, 890, 38 (2020)
  https://ui.adsabs.harvard.edu/abs/2020ApJ...890...38S

- **Globular clusters in the inner Galaxy classified from dynamical orbital criteria**
  Pérez-Villegas, A., B. Barbuy, L. O. Kerber, S. Ortolani, **S. O. Souza**, & E. Bica MNRAS, 491, 3251 (2020)
  https://ui.adsabs.harvard.edu/abs/2020MNRAS.491.3251P

- **Another relic bulge globular cluster: ESO 456-SC38 (Djorgovski 2)**
  Ortolani, S., E. V. Held, D. Nardiello, **S. O. Souza**, B. Barbuy, A. Pérez-Villegas, S. Cassisi, E. Bica, Y. Momany, & I. Saviane A&A, 627, A145 (2019)
  https://ui.adsabs.harvard.edu/abs/2019A&A...627A.145O

- **A deep view of a fossil relic in the Galactic bulge: the Globular Cluster HP 1**
  Kerber, L. O., M. Libralato, **S. O. Souza**, R. A. P. Oliveira, S. Ortolani, A. Pérez-Villegas, B. Barbuy, B. Dias, E. Bica, & D. Nardiello MNRAS, 484, 5530 (2019)

https://ui.adsabs.harvard.edu/abs/2019MNRAS.484.5530K

- **The VISCACHA survey - I. Overview and first results**

  Maia, F. F. S., B. Dias, J. F. C. Santos, L. de O. Kerber, E. Bica, A. E. Piatti, B. Barbuy, B. Quint, L. Fraga, D. Sanmartim, M. S. Angelo, J. A. Hernandez-Jimenez, O. J. Katime Santrich, R. A. P. Oliveira, A. Pérez-Villegas, **S. O. Souza**, R. G. Vieira, & P. Westera MNRAS, 484, 5702 (2019)

  https://ui.adsabs.harvard.edu/abs/2019MNRAS.484.5702M

Appendix B

Line lists

B.1 Palomar 6

Table B.1 - Equivalent widths for FeI and FeII lines.

Ion	λ [Å]	χ_{ex} [eV]	loggf	star 730	star 243	star 030	star 785	star 145	star 401
						[mÅ]			
FeII	5991.38	3.15	−3.65	32.60	39.20	25.5	—	32.3	—
FeII	6084.11	3.20	−3.97	35.20	26.20	25.6	28.7	14.3	18.70
FeII	6149.25	3.89	−2.69	63.80	43.50	22.3	31.1	24.0	—
FeII	6247.56	3.89	−2.52	—	—	27.3	25.9	49.4	35.20
FeII	6416.93	3.89	−2.64	68.90	36.90	27.1	—	35.4	29.10
FeII	6432.68	2.89	−3.57	22.70	31.90	10.2	34.7	28.3	30.10
FeII	6456.39	3.90	−2.31	—	37.30	29.6	23.3	47.4	54.00
FeII	6516.08	2.89	−3.31	62.20	59.2	30.8	43.1	26.7	47.80
FeI	5902.48	4.59	−1.81	—	5.10	2.6	—	8.7	—
FeI	5905.67	4.65	−0.73	40.90	—	28.5	—	31.9	—
FeI	5905.69	4.65	−0.73	—	40.60	—	46.7	—	43.90
FeI	5909.97	3.21	−2.78	—	84.90	—	32.7	—	59.80
FeI	5916.25	2.45	−2.97	59.50	—	—	—	—	—
FeI	5916.26	2.45	−2.99	—	91.10	30.9	25.1	32.0	72.10
FeI	5927.79	4.65	−1.09	38.50	37.70	44.4	46.7	—	—
FeI	5929.67	4.55	−1.41	45.50	44.90	31.3	—	—	30.70
FeI	5930.18	4.65	−0.23	51.70	—	—	—	—	—
FeI	5930.19	4.65	−0.23	—	78.70	—	68.3	—	68.70

Tabela B.1 – continued

Ion	λ	χ_{ex}	loggf	star 730	star 243	star 030	star 785	star 145	star 401
FeI	5934.65	3.93	−1.17	34.30	—	54.0	—	70.4	—
FeI	5934.67	3.93	−1.17	—	76.40	—	28.8	—	62.30
FeI	5952.73	3.98	−1.44	48.50	50.40	—	30.8	52.7	40.10
FeI	5956.69	0.86	−4.60	42.10	—	37.5	—	—	—
FeI	5956.71	0.86	−4.61	—	79.10	—	—	—	82.50
FeI	5975.35	4.84	−0.69	36.80	—	15.6	—	42.3	—
FeI	5983.69	4.55	−1.47	30.80	52.80	17.2	—	20.1	43.90
FeI	5987.06	4.80	−0.43	43.30	—	27.0	—	—	—
FeI	5987.07	4.79	−0.15	—	62.90	—	—	—	59.60
FeI	6003.01	3.88	−1.12	44.80	—	—	—	—	—
FeI	6003.02	3.88	−1.12	—	90.40	25.4	44.3	63.7	76.00
FeI	6005.54	2.59	−3.61	40.50	—	34.4	—	43.6	—
FeI	6008.56	3.88	−0.99	31.50	—	25.3	—	57.2	—
FeI	6020.17	4.61	−0.27	38.10	—	29.2	—	64.5	—
FeI	6024.05	4.55	−0.12	31.20	90.40	2.00	73.9	45.0	69.90
FeI	6027.06	4.08	−1.09	80.00	79.70	29.7	43.2	32.5	59.10
FeI	6054.08	4.37	−2.31	46.50	16.50	—	—	—	—
FeI	6056.01	4.73	−0.46	—	62.30	35.7	41.9	23.8	41.70
FeI	6065.48	2.61	−1.53	66.00	—	—	—	—	—
FeI	6065.49	2.61	−1.53	—	132.60	—	—	—	101.5
FeI	6078.49	4.80	−0.32	57.70	—	—	—	—	—
FeI	6078.50	4.79	−0.40	—	65.90	18.0	49.5	41.5	65.40
FeI	6079.00	4.65	−1.13	—	—	—	—	44.2	36.90
FeI	6079.01	4.65	−1.12	57.10	—	—	—	—	—
FeI	6082.71	2.22	−3.57	31.20	—	—	—	—	—
FeI	6082.72	2.22	−3.57	—	69.20	—	72.2	—	65.10
FeI	6093.64	4.61	−1.50	25.10	—	11.3	—	41.9	—
FeI	6093.67	4.60	−1.51	—	15.50	—	—	—	25.70
FeI	6094.36	4.65	−1.94	46.10	18.80	—	—	—	—
FeI	6096.66	3.98	−1.93	—	43.00	—	39.1	—	—

Tabela B.1 – continued

Ion	λ	χ_{ex}	loggf	star 730	star 243	star 030	star 785	star 145	star 401
FeI	6105.15	4.54	−2.07	—	16.50	—	—	—	10.40
FeI	6137.70	2.59	−1.40	40.00	142.10	—	—	—	146.5
FeI	6151.62	2.18	−3.30	59.50	114.00	56.4	48.4	37.3	110.8
FeI	6157.73	4.08	−1.25	—	67.10	27.9	37.8	35.1	58.30
FeI	6159.38	4.61	−1.97	26.40	—	—	—	—	—
FeI	6165.36	4.14	−1.47	43.50	64.90	43.1	—	17.7	—
FeI	6173.34	2.22	−2.88	—	122.80	—	46.9	—	96.80
FeI	6180.21	2.73	−2.59	56.30	89.50	36.3	—	58.5	63.90
FeI	6187.99	3.94	−1.72	63.80	60.10	34.2	48.4	—	62.90
FeI	6200.32	2.61	−2.44	—	88.40	—	—	—	80.40
FeI	6213.44	2.22	−2.48	88.90	129.90	39.5	—	—	105.50
FeI	6219.29	2.20	−2.43	96.80	134.10	—	—	—	116.50
FeI	6220.78	3.88	−2.46	65.00	—	—	—	—	24.60
FeI	6226.73	3.88	−2.22	47.40	32.00	—	18.4	—	—
FeI	6229.23	2.84	−2.97	—	83.70	11.7	58.5	31.3	52.30
FeI	6240.65	2.22	−3.21	—	97.30	17.9	44.6	40.6	77.20
FeI	6246.33	3.60	−0.88	—	34.30	—	89.4	—	87.30
FeI	6252.57	2.40	−1.69	54.20	162.20	—	137.8	—	110.40
FeI	6254.25	2.28	−2.44	24.30	—	—	—	—	—
FeI	6265.14	2.18	−2.55	61.90	119.90	—	121.9	—	105.40
FeI	6270.23	2.86	−2.46	36.70	61.10	21.2	32.4	90.8	61.50
FeI	6271.28	3.32	−2.70	23.20	40.70	19.0	36.4	24.6	39.70
FeI	6297.80	2.22	−2.74	—	130.10	—	58.6	84.8	101.60
FeI	6301.51	3.65	−0.72	138.40	118.20	—	127.7	—	—
FeI	6302.50	3.69	−0.91	—	94.40	—	148.5	—	—
FeI	6311.50	2.83	−3.14	85.60	81.20	—	26.2	63.2	36.50
FeI	6315.31	4.14	−1.23	51.70	79.10	5.7	42.9	25.1	53.60
FeI	6315.81	4.08	−1.71	35.30	48.60	22.4	58.1	37.2	50.10
FeI	6322.69	2.59	−2.43	—	80.80	—	36.9	—	92.80
FeI	6330.84	4.73	−1.74	—	44.60	—	—	—	—

Tabela B.1 – continued

Ion	λ	χ_{ex}	loggf	star 730	star 243	star 030	star 785	star 145	star 401
FeI	6335.34	2.20	−2.18	43.4	143.30	1.5	88.4	—	119.30
FeI	6336.83	3.69	−1.05	—	105.70	38.7	84.5	60.5	102.80
FeI	6344.16	2.43	−2.92	87.20	127.10	22.8	75.8	82.3	90.70
FeI	6355.04	2.84	−2.29	—	128.30	—	—	—	92.70
FeI	6358.69	0.86	−4.47	—	160.90	—	—	—	149.70
FeI	6380.75	4.19	−1.38	50.80	42.00	15.9	23.8	36.2	50.30
FeI	6392.54	2.28	−4.03	52.50	63.10	11.7	—	—	—
FeI	6393.61	2.43	−1.43	46.5	158.70	—	—	—	—
FeI	6408.03	3.69	−1.00	—	101.50	—	—	74.9	95.80
FeI	6411.11	4.73	−1.92	40.10	13.70	—	—	—	5.0
FeI	6411.66	3.65	−0.60	48.50	121.10	—	—	105.	98.70
FeI	6419.94	4.73	−0.24	44.40	78.70	15.6	75.9	44.2	80.60
FeI	6421.35	2.28	−2.03	71.10	158.20	—	—	107.	113.50
FeI	6430.86	2.18	−2.01	51.30	174.20	—	—	—	123.40
FeI	6469.21	4.83	−0.77	73.50	84.00	—	56.5	27.7	—
FeI	6475.63	2.56	−2.94	63.00	127.30	18.3	70.5	31.2	—
FeI	6481.88	2.28	−2.98	—	140.40	16.6	55.1	70.5	97.50
FeI	6494.99	2.40	−1.27	143.20	—	57.1	—	—	—
FeI	6498.95	0.96	−4.70	—	123.10	—	33.8	—	109.60
FeI	6518.37	2.83	−2.30	—	83.60	—	51.1	—	81.30
FeI	6533.93	4.56	−1.45	—	31.30	2.00	—	29.5	—
FeI	6546.25	2.75	−1.54	106.10	159.90	63.3	—	—	141.80
FeI	6556.81	4.79	−1.72	—	19.00	—	28.1	—	—
FeI	6569.22	4.73	−0.42	99.40	77.60	31.6	—	55.9	69.30
FeI	6574.25	0.99	−5.02	—	116.30	—	26.7	—	93.60
FeI	6575.04	2.59	−2.71	—	121.80	—	—	—	80.90
FeI	6581.21	1.48	−4.68	85.20	97.20	—	32.0	23.1	65.70
FeI	6591.31	4.59	−2.07	28.10	10.70	1.00	—	—	11.50
FeI	6593.87	2.43	−2.42	39.60	136.20	69.4	—	—	103.70
FeI	6597.56	4.80	−1.07	45.70	36.50	26.7	—	—	36.00

Tabela B.1 – continued

Ion	λ	χ_{ex}	loggf	star 730	star 243	star 030	star 785	star 145	star 401
FeI	6608.04	2.28	−4.03	74.30	62.60	10.0	—	49.4	45.40
FeI	6609.12	2.56	−2.69	73.40	132.60	24.5	73.0	—	131.60
FeI	6627.54	4.55	−1.68	36.80	42.40	5.1	—	9.9	—
FeI	6678.00	2.69	−1.42	45.00	157.60	—	—	—	118.10
FeI	6699.14	4.59	−2.10	24.40	24.20	2.70	—	—	—
FeI	6705.11	4.61	−1.06	—	—	16.3	—	30.8	—
FeI	6726.67	4.59	−1.09	—	—	28.0	—	16.0	—

Table B.2 - Line-by-line abundances ratios in the six UVES sample stars for the CNO, odd-Z (Na and Al), alpha- (Mg, Si, Ca, and Ti), and heavy-elements (Y, Zr, Ba, La, and Eu).

Species	λ [Å]	χ_{ex} [eV]	loggf	star 730	star 243	star 030	star 785	star 145	star 401
				[X/Fe]					
NaI	5682.633	2.10	−0.71	+0.07	+0.28	−0.09	+0.27	—	—
NaI	6154.230	2.10	−1.56	—	+0.48	+0.43	+0.42	+0.42	—
NaI	6160.753	2.10	−1.26	+0.51	+0.51	—	+0.13	+0.37	+0.10
AlI	6696.185	4.02	−1.58	+0.47	+0.37	+0.59	+0.09	+0.08	+0.33
AlI	6698.673	3.14	−1.65	+0.42	+0.14	+0.39	+0.29	+0.15	+0.47
MgI	5528.405	5.11	−2.10	—	—	—	+0.14	—	—
MgI	6318.720	5.11	−2.36	+0.41	+0.48	+0.58	+0.34	+0.49	+0.24
MgI	6319.242	5.11	−2.80	+0.45	+0.45	+0.53	—	+0.40	+0.40
MgI	6765.450	5.75	−1.94	—	+0.27	+0.47	+0.27	+0.55	+0.25
SiI	5665.555	4.92	−2.04	+0.48	+0.19	+0.38	+0.60	+0.51	+0.61
SiI	5666.690	5.62	−1.74	+0.41	+0.59	+0.50	+0.20	—	+0.44
SiI	5690.425	4.93	−1.87	+0.07	+0.58	+0.12	—	+0.43	+0.60
SiI	5948.545	5.08	−1.30	+0.21	+0.18	+0.13	+0.15	+0.54	+0.39
SiI	6142.494	5.62	−1.50	+0.24	+0.22	—	+0.50	+0.02	+0.29
SiI	6145.020	5.61	−1.45	+0.49	+0.19	—	—	+0.23	+0.42
SiI	6155.142	5.62	−0.85	+0.05	+0.40	+0.20	+0.30	+0.09	+0.25
SiI	6237.328	5.61	−1.01	+0.43	+0.48	+0.31	+0.29	+0.43	+0.48
SiI	6243.823	5.61	−1.30	+0.53	+0.46	—	+0.42	+0.46	+0.06
SiI	6414.987	5.87	−1.13	+0.12	+0.45	+0.42	+0.51	+0.67	+0.64
SiI	6721.844	5.86	−1.17	+0.60	+0.43	+0.52	+0.49	+0.40	+0.31
CaI	5601.277	2.53	−0.52	−0.33	+0.07	—	—	—	+0.22
CaI	5867.562	2.93	−1.55	+0.50	+0.02	+0.49	+0.40	+0.41	+0.40
CaI	6156.030	2.52	−2.39	—	—	—	+0.40	+0.56	+0.44
CaI	6161.295	2.51	−1.02	+0.26	—	+0.50	−0.10	−0.09	+0.48
CaI	6166.440	2.52	−0.90	+0.37	+0.53	−0.39	+0.30	+0.27	+0.11
CaI	6169.044	2.52	−0.54	+0.45	+0.43	—	+0.00	+0.11	+0.28
CaI	6169.564	2.52	−0.27	+0.55	+0.44	—	—	+0.15	+0.42

Tabela B.2 – continued

Species	λ	χ_{ex}	loggf	star 730	star 243	star 030	star 785	star 145	star 401
CaI	6439.080	2.52	+0.30	+0.24	+0.55	—	—	—	+0.50
CaI	6455.605	2.52	−1.35	+0.47	+0.48	+0.43	+0.10	+0.40	+0.47
CaI	6464.679	2.52	−2.10	—	—	—	+0.49	+0.37	+0.55
CaI	6493.788	2.52	−2.44	−0.07	+0.14	—	—	—	−0.10
CaI	6499.654	2.52	−0.85	+0.36	+0.58	+0.15	—	+0.20	+0.43
CaI	6572.779	0.00	−4.32	—	—	−0.16	+0.20	+0.32	+0.08
CaI	6717.687	2.71	−0.61	+0.46	—	−0.23	−0.10	+0.33	+0.43
TiI	5689.459	2.29	−0.44	+0.39	+0.39	+0.42	+0.49	+0.44	+0.58
TiI	5866.449	1.07	−0.84	+0.36	+0.51	+0.12	+0.09	+0.48	+0.29
TiI	5922.108	1.05	−1.46	—	+0.43	+0.32	+0.40	+0.27	+0.35
TiI	5941.750	1.05	−1.50	+0.49	+0.28	+0.50	+0.30	+0.23	+0.35
TiI	5965.825	1.88	−0.42	+0.54	+0.53	+0.47	+0.20	+0.30	+0.33
TiI	5978.539	1.87	−0.53	+0.02	+0.36	+0.46	+0.60	+0.56	+0.13
TiI	6064.623	1.05	−1.94	—	+0.58	+0.48	—	+0.44	+0.35
TiI	6091.169	2.27	−0.42	+0.36	+0.43	+0.49	+0.40	+0.49	+0.33
TiI	6126.214	1.07	−1.43	+0.46	+0.57	+0.36	+0.00	+0.33	+0.22
TiI	6258.110	1.44	−0.36	+0.11	+0.31	+0.22	+0.00	−0.08	−0.22
TiI	6261.106	1.43	−0.48	+0.57	+0.45	+0.13	+0.00	−0.04	+0.06
TiI	6303.767	1.44	−1.57	+0.56	+0.56	—	+0.20	+0.57	+0.39
TiI	6312.240	1.46	−1.60	—	—	+0.09	+0.50	—	+0.26
TiI	6336.113	1.44	−1.74	—	+0.25	—	—	—	+0.56
TiI	6508.150	1.43	−2.05	—	+0.60	—	—	—	+0.28
TiI	6554.238	1.44	−1.22	−0.10	+0.47	+0.33	+0.20	+0.37	+0.38
TiI	6556.077	1.46	−1.07	+0.25	—	+0.42	+0.40	+0.46	+0.59
TiI	6599.113	0.90	−2.09	+0.52	+0.50	+0.46	+0.60	+0.68	+0.40
TiI	6743.127	0.90	−1.73	+0.39	+0.47	+0.10	+0.40	+0.49	+0.52
TiII	5418.751	1.58	−2.13	—	—	−0.23	—	+0.20	+0.27
TiII	6491.580	2.06	−2.10	+0.18	+0.38	+0.23	−0.10	+0.00	+0.41
TiII	6559.576	2.05	−2.35	+0.14	+0.26	+0.48	+0.10	+0.26	—

Tabela B.2 – continued

Species	λ	χ_{ex}	loggf	star 730	star 243	star 030	star 785	star 145	star 401
TiII	6606.970	2.06	−2.85	+0.26	+0.39	+0.02	+0.40	+0.36	+0.23
YI	6435.004	0.07	−0.82	+0.02	+0.44	+1.12	+0.78	+0.89	−0.01
YII	6795.414	1.74	−1.19	+0.33	+0.23	+0.48	+0.84	+0.57	+0.09
ZrI	6127.475	0.15	−1.06	+0.71	+0.74	+0.58	+0.60	+0.85	+0.29
ZrI	6134.585	0.00	−1.42	+0.86	+0.37	+0.84	—	+0.33	+0.48
ZrI	6140.535	0.52	−1.60	—	+0.86	—	—	+0.95	+0.92
ZrI	6143.252	0.07	−1.10	+0.71	+0.75	+0.54	+0.63	+0.84	−0.04
BaII	5853.675	0.60	−1.10	—	+0.52	—	—	—	+0.36
BaII	6496.897	0.60	−0.32	—	+0.65	—	+0.23	—	+0.62
LaII	6172.721	0.13	−2.25	+0.72	+0.03	+0.86	+0.78	+0.81	+0.32
LaII	6262.287	0.40	−1.60	+0.55	+0.30	—	—	+0.37	+0.16
LaII	6296.079	1.25	−0.84	+0.37	—	—	—	—	+0.19
LaII	6320.376	0.17	−1.56	+0.37	+0.29	+0.19	+0.52	+0.79	+0.21
LaII	6390.477	0.32	−1.41	+0.31	+0.10	+0.67	+0.77	+0.75	+0.30
EuII	6437.640	1.32	−0.32	+0.55	+0.50	+0.62	+0.65	+0.77	+0.57
EuII	6645.064	1.38	+0.12	+0.31	+0.12	+0.37	+0.82	+0.72	+0.59

B.2 NGC6355

Table B.3 - Equivalent widths for FeI and FeII lines.

Ion	λ [Å]	χ_{ex} [eV]	loggf	star 1539	star 1363	star 1176	star 133
				[m Å]			
FeII	5991.38	3.10	−3.65	—	21.1	33.4	17.0
FeII	6084.11	3.20	−3.97	—	16.8	13.2	11.8
FeII	6149.25	3.80	−2.69	—	62.4	28.1	17.5
FeII	6247.56	3.80	−2.30	41.6	—	47.1	29.9
FeII	6416.93	3.80	−2.64	29.7	34.6	25.5	18.1

Tabela B.3 – continued

Ion	λ	χ_{ex}	loggf	star 1539	star 1363	star 1176	star 133
FeII	6432.68	2.80	−3.57	42.2	42.4	40.2	33.1
FeII	6456.39	3.90	−2.31	—	48.2	61.7	40.8
FeII	6516.08	2.80	−3.31	53.8	17.1	47.0	42.7
FeI	5905.67	4.60	−0.73	—	30.3	—	27.2
FeI	5916.25	2.40	−2.97	87.1	—	55.6	—
FeI	5927.79	4.60	−1.09	—	23.7	17.1	19.3
FeI	5929.67	4.50	−1.41	23.9	17.7	14.4	16.0
FeI	5930.18	4.60	−0.23	66.3	62.6	46.7	49.9
FeI	5934.65	3.90	−1.17	70.3	—	49.0	54.2
FeI	5952.73	3.90	−1.44	50.9	49.2	38.9	43.3
FeI	5956.69	0.80	−4.60	119.8	—	78.4	—
FeI	5975.35	4.80	−0.69	33.6	35.7	23.6	—
FeI	5983.69	4.50	−1.47	—	44.4	34.0	—
FeI	5987.06	4.80	−0.43	39.7	—	25.3	—
FeI	6003.01	3.80	−1.12	74.9	74.5	54.2	65.3
FeI	6005.54	2.50	−3.61	37.8	41.6	19.2	24.9
FeI	6008.56	3.80	−0.99	84.3	—	60.1	67.0
FeI	6020.17	4.60	−0.27	73.3	—	50.0	54.5
FeI	6024.05	4.50	−0.12	82.2	85.0	67.4	72.0
FeI	6027.06	4.00	−1.09	55.7	57.8	34.0	38.6
FeI	6054.08	4.30	−2.31	—	—	—	—
FeI	6065.48	2.60	−1.53	148.7	—	124.5	—
FeI	6078.49	4.80	−0.32	43.5	45.5	26.9	37.8
FeI	6079.01	4.60	−1.12	21.2	23.2	13.6	17.0
FeI	6082.71	2.20	−3.57	67.4	69.1	33.1	50.0
FeI	6093.64	4.60	−1.50	20.3	14.6	20.1	12.8
FeI	6137.70	2.50	−1.40	—	—	137.6	—
FeI	6151.62	2.10	−3.30	82.6	—	53.7	72.7
FeI	6165.36	4.10	−1.47	32.4	30.1	16.6	17.6

Tabela B.3 – continued

Ion	λ	χ_{ex}	loggf	star 1539	star 1363	star 1176	star 133
FeI	6180.21	2.70	−2.59	82.4	84.8	49.6	64.2
FeI	6187.99	3.90	−1.72	40.0	37.3	22.4	31.8
FeI	6213.44	2.20	−2.48	122.4	—	96.4	—
FeI	6219.29	2.20	−2.43	131.7	—	109.2	—
FeI	6220.78	3.80	−2.46	10.3	—	—	—
FeI	6226.73	3.80	−2.22	17.5	23.1	13.8	16.1
FeI	6252.57	2.40	−1.69	—	—	134.3	—
FeI	6254.25	2.20	−2.44	133.7	—	114.8	—
FeI	6265.14	2.10	−2.55	128.2	—	110.6	—
FeI	6270.23	2.80	−2.46	71.7	76.1	42.6	58.0
FeI	6271.28	3.30	−2.70	27.4	27.3	15.2	16.9
FeI	6301.51	3.60	−0.72	104.0	—	86.7	—
FeI	6311.50	2.80	−3.14	43.6	42.7	23.3	28.9
FeI	6315.31	4.10	−1.23	45.3	41.9	28.3	—
FeI	6315.81	4.00	−1.71	29.2	28.7	10.3	18.2
FeI	6335.34	2.20	−2.18	142.7	—	122.2	—
FeI	6344.16	2.40	−2.92	91.2	—	62.8	72.9
FeI	6380.75	4.10	−1.38	42.2	35.9	26.3	33.5
FeI	6392.54	2.20	−4.03	36.9	37.5	—	—
FeI	6393.61	2.40	−1.43	—	—	140.8	—
FeI	6411.66	3.60	−0.60	115.8	—	98.5	101.7
FeI	6419.94	4.70	−0.24	57.5	55.9	40.6	45.1
FeI	6421.35	2.20	−2.03	—	—	132.5	—
FeI	6430.86	2.10	−2.01	—	—	132.8	—
FeI	6469.21	4.80	−0.77	—	—	—	—
FeI	6475.63	2.50	−2.94	82.5	—	52.8	68.5
FeI	6546.25	2.70	−1.54	136.6	—	116.3	—
FeI	6569.22	4.70	−0.42	54.3	55.8	42.5	46.4
FeI	6581.21	1.40	−4.68	52.6	63.0	16.7	39.1
FeI	6593.87	2.40	−2.42	125.9	—	98.8	—

Tabela B.3 – continued

Ion	λ	χ_{ex}	loggf	star 1539	star 1363	star 1176	star 133
FeI	6597.56	4.80	−1.07	21.0	21.1	—	14.9
FeI	6608.04	2.20	−4.03	37.5	37.9	—	—
FeI	6609.12	2.50	−2.69	97.6	—	64.0	81.1
FeI	6627.54	4.50	−1.68	—	14.5	—	11.2
FeI	6678.00	2.60	−1.42	—	—	134.5	—

Table B.4 - Line-by-line abundances ratios in the six UVES sample stars for the odd-Z (Na and Al), alpha- (Mg, Si, Ca) + Ti, iron-peak (V, Mn, Co, Cu, and Zn), and heavy elements (Y, Zr, Ba, La, Nd, and Eu).

Species	λ [Å]	χ_{ex} [eV]	loggf	star 1539	star 1363	star 1176	star 133
				[X/Fe]			
MgI	6318.720	5.11	−2.36	+0.35	+0.47	+0.38	+0.47
MgI	6319.242	5.11	−2.80	+0.32	+0.41	—	—
SiI	5665.555	4.92	−2.04	+0.20	+0.20	+0.25	+0.40
SiI	5666.690	5.62	−1.74	—	—	+0.56	+0.10
SiI	5690.425	4.93	−1.87	+0.35	+0.33	+0.40	+0.30
SiI	5948.545	5.08	−1.30	+0.30	+0.30	+0.30	+0.35
SiI	6142.494	5.62	−1.50	+0.45	+0.30	—	−0.40
SiI	6145.020	5.61	−1.45	+0.30	+0.50	+0.15	+0.50
SiI	6155.142	5.62	−0.85	+0.25	+0.19	+0.35	+0.30
SiI	6237.328	5.61	−1.01	+0.06	+0.14	+0.25	+0.35
SiI	6243.823	5.61	−1.30	+0.26	+0.21	+0.35	+0.35
SiI	6414.987	5.87	−1.13	+0.23	+0.06	+0.56	+0.10
SiI	6721.844	5.86	−1.17	—	—	+0.10	+0.69
CaI	5601.277	2.53	−0.52	+0.43	+0.47	+0.09	+0.68
CaI	5867.562	2.93	−1.55	+0.26	+0.31	+0.35	+0.45
CaI	6156.030	2.52	−2.39	—	—	—	—

Tabela B.4 – continued

Species	λ	χ_{ex}	loggf	star 1539	star 1363	star 1176	star 133
CaI	6102.723	1.88	−0.79	+0.60	+0.50	+0.70	+0.70
CaI	6122.217	1.89	−0.20	+0.50	+0.50	+0.70	+0.70
CaI	6161.295	2.51	−1.02	+0.36	+0.44	+0.20	+0.44
CaI	6162.167	1.90	−1.09	+0.30	+0.30	+0.70	+0.50
CaI	6166.440	2.52	−0.90	+0.15	+0.30	+0.09	+0.30
CaI	6169.044	2.52	−0.54	+0.61	+0.50	+0.05	+0.55
CaI	6169.564	2.52	−0.27	+0.65	+0.58	+0.15	+0.71
CaI	6439.080	2.52	+0.30	+0.75	+0.55	+0.70	+0.75
CaI	6455.605	2.52	−1.35	+0.30	+0.44	+0.20	+0.53
CaI	6464.679	2.52	−2.10	+0.60	+0.70	+0.55	+0.70
CaI	6493.788	2.52	−2.44	+0.50	+0.50	+0.55	+0.50
CaI	6499.654	2.52	−0.85	+0.50	+0.50	+0.10	+0.50
CaI	6572.779	0.00	−4.32	+0.60	+0.49	−0.01	+0.55
CaI	6717.687	2.71	−0.61	+0.50	+0.50	+0.25	+0.50
TiI	5922.108	1.05	−1.46	+0.51	+0.55	+0.18	+0.48
TiI	5941.750	1.05	−1.50	+0.36	+0.40	+0.28	+0.33
TiI	5965.825	1.88	−0.42	+0.30	+0.45	+0.08	+0.34
TiI	5978.539	1.87	−0.53	+0.40	+0.30	+0.13	+0.37
TiI	6064.623	1.05	−1.94	+0.31	+0.30	+0.05	+0.28
TiI	6091.169	2.27	−0.42	+0.14	+0.26	—	+0.23
TiI	6126.214	1.07	−1.43	+0.30	+0.40	+0.10	+0.30
TiI	6258.110	1.44	−0.36	+0.10	+0.15	+0.19	+0.10
TiI	6261.106	1.43	−0.48	+0.30	+0.50	+0.10	+0.30
TiI	6312.240	1.46	−1.60	+0.24	+0.40	+0.09	+0.35
TiI	6336.113	1.44	−1.74	+0.20	+0.34	+0.26	+0.18
TiI	6554.238	1.44	−1.22	+0.10	+0.15	+0.06	+0.26
TiI	6556.077	1.46	−1.07	+0.30	+0.40	+0.22	+0.32
TiI	6599.113	0.90	−2.09	+0.28	+0.30	+0.10	+0.30
TiI	6743.127	0.90	−1.73	+0.20	+0.26	−0.19	+0.20
TiII	5418.751	1.58	−2.13	+0.30	+0.38	+0.30	+0.43

Tabela B.4 – continued

Species	λ	χ_{ex}	loggf	star 1539	star 1363	star 1176	star 133
TiII	6491.580	2.06	−2.10	+0.30	+0.38	+0.30	+0.43
TiII	6559.576	2.05	−2.35	+0.26	+0.30	+0.23	+0.36
TiII	6606.970	2.06	−2.85	+0.35	+0.30	+0.31	+0.30
NaI	5682.633	2.10	−0.71	−0.32	−0.30	−0.00	+0.31
NaI	5688.194	2.10	−1.40	−0.35	−0.30	−0.30	+0.20
NaI	6154.230	2.10	−1.56	−0.15	−0.00	—	+0.30
NaI	6160.753	2.10	−1.26	−0.35	−0.00	−0.35	+0.00
AlI	6696.185	4.02	−1.58	−0.30	−0.30	$<+0.30$	$<+0.30$
AlI	6698.673	3.14	−1.65	−0.29	+0.00	$<+0.30$	$<+0.30$
VI	5703.560	1.05	−0.21	+0.05	+0.17	—	+0.14
VI	6081.440	1.05	−0.58	−0.02	+0.17	—	+0.02
VI	6090.220	1.08	−0.16	+0.05	+0.14	−0.32	+0.08
VI	6119.520	1.06	−0.47	−0.05	+0.08	−0.26	−0.05
VI	6199.190	0.29	−1.48	+0.05	+0.17	—	−0.11
VI	6243.100	0.30	−0.88	+0.11	+0.38	—	+0.05
VI	6251.820	0.29	−1.44	+0.11	+0.32	−0.41	−0.05
VI	6274.650	0.27	−1.72	−0.05	+0.11	—	−0.08
MnI	5394.669	0.00	−3.55	−0.40	−0.50	−0.40	−0.50
MnI	6013.513	3.07	−0.40	−0.30	−0.25	−0.30	−0.30
MnI	6016.640	3.07	−0.22	−0.35	−0.50	−0.60	−0.40
MnI	6021.800	3.08	−0.10	−0.30	−0.45	−0.25	−0.50
CoI	5212.691	3.51	−0.11	—	+0.15	—	+0.15
CoI	5301.047	1.71	−2.00	+0.00	+0.10	—	+0.10
CoI	5342.708	4.02	+0.69	+0.05	+0.05	—	+0.00
CoI	5454.572	4.07	+0.24	—	+0.10	+0.20	+0.10
CoI	5647.234	2.28	−1.56	+0.05	+0.05	+0.00	+0.30
CoI	6188.996	1.71	−2.45	+0.00	+0.00	+0.00	+0.30
CuI	5105.537	1.39	−1.52	−0.40	−0.15	−0.30	−0.35
CuI	5218.197	3.82	+0.00	−0.30	+0.00	+0.05	+0.00

Tabela B.4 – continued

Species	λ	χ_{ex}	loggf	star 1539	star 1363	star 1176	star 133
ZnI	6362.339	5.79	−0.30	−0.30	−0.20	+0.30	−0.10
YI	6435.004	0.07	−0.82	−0.30	−0.32	−0.30	+0.00
YII	6795.414	1.74	−1.19	+0.20	+0.00	+0.00	—
ZrI	6127.475	0.15	−1.06	−0.08	+0.05	—	−0.08
ZrI	6134.585	0.00	−1.42	+0.05	+0.20	—	+0.23
ZrI	6140.535	0.52	−1.60	—	—	—	−0.50
ZrI	6143.252	0.07	−1.10	−0.14	+0.02	—	−0.08
BaII	5853.675	0.60	−1.10	+0.92	+1.00	+1.00	+1.05
BaII	6141.713	0.70	−0.08	+0.60	+0.80	+0.65	+0.80
BaII	6496.897	0.60	−0.32	+1.00	+1.00	+1.10	+1.20
LaII	6262.287	0.40	−1.60	+0.00	+0.00	+0.17	+0.26
LaII	6320.376	0.17	−1.56	+0.00	+0.00	+0.14	+0.30
LaII	6390.477	0.32	−1.41	+0.25	+0.17	+0.00	+0.26
NdII	6740.078	0.06	−1.53	+0.45	+0.15	+0.17	−0.30
NdII	6790.372	0.18	−1.77	+0.55	+0.40	+0.00	−0.30
NdII	6549.525	0.06	−2.01	+0.40	+0.30	+0.00	—
EuII	6437.640	1.32	−0.32	+0.55	+0.55	+0.65	+0.50
EuII	6645.064	1.38	+0.12	+0.50	+0.55	+0.50	+0.70